CUSTOMIZED CONJUGATION: TAILORED Π-SYSTEMS FOR ORGANIC ELECTRONIC APPLICATIONS

A Dissertation
Presented to
The Academic Faculty

by

Natasha B. Teran

In Partial Fulfillment
of the Requirements for the Degree
Doctor of Philosophy in the
School of Chemistry and Biochemistry

Georgia Institute of Technology
December 2015

CUSTOMIZED CONJUGATION: TAILORED Π-SYSTEMS FOR ORGANIC ELECTRONIC APPLICATIONS

Approved by:

Dr. John R. Reynolds, Advisor
School of Chemistry and Biochemistry;
School of Materials Science and Engineering
Georgia Institute of Technology

Dr. Elsa Reichmanis
School of Chemical and Biochemical Engineering
Georgia Institute of Technology

Dr. David Collard
School of Chemistry and Biochemistry
Georgia Institute of Technology

Dr. Stefan France
School of Chemistry and Biochemistry
Georgia Institute of Technology

Dr. Mohan Srinivasarao
School of Materials Science and Engineering
Georgia Institute of Technology

Date Approved: October 20, 2015

To my mother and father

ACKNOWLEDGEMENTS

In scientific research, or any great undertaking, “we are like dwarfs standing on the shoulders of giants.” So if I have seen further, it is because of giant minds: brilliant scientists, young and old, whose work became the foundation of my research; and giant hearts: sympathetic allies, whose trials became mine, and who equally shared in my many struggles. I would like to express my profound gratitude to them.

First, I thank Prof. John Reynolds, for accepting me into his research group, and introducing me to many admirable students and professors who have also helped me along the way. I am grateful, as well, for the way he has pushed me to give my best in my work, with his delving questions, and imaginative perspectives. I thank him for the many doors he has opened for me to grow as a scientist, a professional, and an educator. The move from the University of Florida to Georgia Tech was one we grumbled over many times, but it has enriched my education in extraordinary ways, and I thank him for this unique opportunity. I am also thankful of his uncredited sixth sense. My strong need to be self-reliant has hindered me many trying times from knocking on his office door, but most of those days he would call or pop over by my desk, seemingly out of nowhere, and his kind words and advice, shrouded in stories, always put me back on track.

I also thank the many other educators who have contributed to my scientific training. I am grateful to my committee members, Dr. Elsa Reichmanis, Dr. Stefan France, Dr. David Collard, and Dr. Mohan Srinivasarao for their scientific input throughout formal and informal consultations. I also thank my professors from UF, particularly Dr. Stephen Miller, and Dr. Ronald Castellano, whose physical organic

courses were a joy. I am also deeply grateful to Dr. Erwin Enriquez, my adviser from Ateneo de Manila University, who introduced me to materials science, and whose childlike wonder at the field is truly inspiring.

I also thank the professors, post docs, and graduate students whom I have collaborated with: Dr. Yanrong Shi and Dr. Tobin Marks at Northwestern University; Dewei Zhu, Dr. Alexander Baev, Dr. Guang He, Dr. Mark Swihart, and Dr. Paras Prasad at SUNY-Buffalo; and Samuel Ho, Ying Chen, and Dr. Franky So, and Jason Zemain, and Dr. Kirk Schanze at the University of Florida. I also thank Keith Johnson for his help with Matlab, and electrochromic polymer characterizations. I am also grateful to the many funding agencies that have supported my research throughout the years: the Air Force Office of Scientific Research (AFOSR), and Wintek Corporation.

Stepping into organic materials research with barely any background was a daunting experience in my first year, but the generous senior graduate students of the Reynolds group gave me the boost I needed to overcome this hurdle. Special thanks go to Dr. Romain Stalder, who was a thorough and patient mentor, for sharing his formula for handling the inevitable despair that visits any organic synthetic chemist: crossing over to the Faraday cage to watch your materials do cool things. I also thank Dr. Toan Pho, Dr. Leandro Estrada, Dr. Chad Amb, Dr. Frank Arroyave, Dr. Dan Patel, Dr. Mike Craig, and Dr. Pengjie Shie, who at one time or other helped me solve a synthesis problem or two.

One of the most treasured gifts I have received from graduate school is the enduring friendships I have built. I thank Dr. Caroline Grand for all our shared experiences, in and out of lab, from New Orleans to Prague. I owe a great deal of gratitude to Dr. Coralie Richard for her wisdom and encouragement, for being my

constant companion in the lab, and being my relentless cheerleader. I also thank Kin Lo, who I can talk to about anything, and who has been tremendously helpful in making my east coast-west coast balancing act work. I am also pleased to have shared this experience with the duo of Rylan Wolfe and Toan Pho, who made late nights and weekends in lab tolerable; and Dr. Ray Bulloch, who has a gift for blunt delivery of undeniable truths. I also thank the "upstairs folk:" Dr. Anna Österholm, Dr. Eric Shen, Dr. Aubrey Dyer, and Dr. Gaëlle Deshayes for their pragmatic perspectives, and scientific guidance. I also thank my friends, Joanna San Pedro, Helen Cativo, and Badeth Henares for their support.

I am also indebted to the people who have helped me through the maze of grad school: the graduate coordinators, Dr. Ben Smith and Lori Clark (UF), Dr. Cam Tyson, and Dr. Kenyetta Johnson (GT); and the administrative assistants, Cheryl Googins, Sarah Klossner, Annyetta Douglas (UF), and Aeryal Herrod and Venese Blake-Leggett (GT).

My most heartfelt thanks go to my family. I am deeply grateful for my mother, Elizabeth, the wisest and strongest person I know. Thank you for teaching me to speak my truth quietly and clearly, and to always keep my mind open to the stories of others. I am equally thankful for my father, Antonio, whose quiet persistence, perseverance, and permanence betray an indomitable strength. I also thank my sisters, Andrea and Samantha, who I share everything with, tribulations and triumphs alike. Finally, I give profound thanks to Justin, who is my counterpoint and my match, and keeps me at equilibrium. Thank you for sharing your family with me.

TABLE OF CONTENTS

LIST OF TABLES

LIST OF FIGURES

LIST OF SCHEMES

LIST OF CHARTS

LIST OF SYMBOLS AND ABBREVIATIONS

α	Linear or first order polarizability
A	Acceptor
AFM	Atomic force microscopy
β	Second order polarizability
BLA	Bond length alternation
BTD	2,1,3-Benzothiadiazole
γ	Third order polarizability
CV	Cyclic voltammetry
δ	Chemical shift
D	Donor
DPV	Differential pulse voltammetry
DSC	Differential scanning calorimetry
EA	Electron affinity
E_B	Exciton binding energy
E_g	Energy gap
E_{ij}	Transition energy (i to j excitation)
$E_{g,opt}$	Optical energy gap
ΔE_{inj}	Injection barrier
ΔE_{ST}	Singlet-triplet splitting
$E_{S0\text{-}S1}$	Singlet ground state to singlet excite state energy gap
E_T	Triplet energy
EDOT	3,4-ethylenedioxythiophene
EBL	Electron blocking layer

ECP	Electrochromic polymer
EIL	Electron injection layer
EML	Emissive layer
EOD	Electron only device
EQE	External quantum efficiency
ETL	Electron transport layer
ETM	Electron transporting material
FIrpic	bis(3,5-difluoro-2-(2-pyridyl)phenyl-(2-carboxypyridyl)iridium(III)
HBL	Hole blocking layer
HIL	Hole injection layer
HOD	Hole only device
HOMO	Highest Occupied Molecular Orbital
HTL	Hole transport layer
HTM	Hole transporting material
ICT	Intramolecular charge transfer
IP	Ionization potential
$Ir(mppy)_3$	tris[2-(*p*-tolyl) pyridine] iridium(III)
ITO	Indium tin oxide
K_d	Dimerization constant
LUMO	Lowest Unoccupied Molecular Orbital
M_{if}	Transition Dipole Moment (i to f state excitation)
$\Delta\mu$	Dipole moment change
NBS	*N*-Bromosuccinimide
NLO	Nonlinear optics
OLED	Organic Light Emitting Diode

OTTLE	Optically transparent thin layer electrode
PAH	Polycyclic aromatic hydrocarbon
Pd_2dba_3	tris(dibenzylideneacetone)-dipalladium(0)
PDI	Polydispersity index
ProDOT	Propylenedioxythiophene
Pt	Platinum
SOS	Sum-over-states
SPhos	Dicyclohexyl(2',6'-dimethoxy-[1,1'-biphenyl]-2-yl)phosphane
$TBAPF_6$	Tetrabutylammonium hexafluorophosphate
T_c	Crystallization temperature
T_d	Decomposition temperature
TEG	*fac*-tris(2-(3-*p*-xylyl) phenyl)pyridine iridium(III)
T_g	Glass transition temperature
TGA	Thermogravimetric analysis
THF	Tetrahydrofuran
TICT	Twisted intramolecular charge transfer
TLC	Thin layer chromatography
T_m	Melting temperature

SUMMARY

The versatility of the conjugated π-system allows it to be structurally tailored and imbued with properties relevant for organic electronic applications. Judicious selection of synthons and synthetic methodologies enables the modular construction of small to large conjugated materials at high synthetic efficiency. In this dissertation, three examples highlight the successful implementation of these design concepts, leading to high performance materials for three different prospective device applications.

The first chapter of the dissertation gives an overview of the theoretical basis for the tunability of the π-conjugated system and the different electronic processes enabled by such a system, followed by a brief review of the different methods for structural control of optoelectronic and macroscopic properties of the π-system. The second chapter then gives the methods by which these properties are characterized in the dissertation.

Chapter 3 first gives a brief introduction to the device architecture and physics in organic light emitting devices, followed by a limited survey of OLED organic materials to highlight key structural elements, and structure-property relationships. Special focus is given to transporting and host materials. Then the structural design and synthesis of three triphenylene-based π-conjugated materials is reported. The careful selection of synthons and synthetic techniques allowed the synthesis of these materials in few steps and high overall yields. Optoelectronic, thermal and morphological characterization of the materials showed successful design implementation, giving rise to large energy gaps, sufficient triplet energies, moderate transport characteristics, excellent thermal properties, and stable amorphous morphologies. The materials were then studied in OLEDs, and

yielded high efficiency green devices, comparable in performance to well-established host materials in the literature.

In Chapter 4, materials for third-order nonlinear optics are explored. The chapter begins with an introduction to NLO and NLO materials. Then a theoretical background to twisted intramolecular charge transfer is given, highlighting the key structural elements, and mechanisms by which NLO properties are enhanced. A family of 18 structures was proposed, and computationally screened, allowing key structure-property relationships to be developed, and three candidates for synthesis to be identified. The design and synthesis of the three chromophores is presented, emphasizing the judicious selection of the 3-hexylthiophene-2-boronic acid pinacol ester as a key synthon that incorporates three design elements (steric bulk, electron donating ring, and solubility). The synthesis of the chromophores is thoroughly discussed to emphasize the approach taken to address synthetic challenges. The rigorous structural characterization of the chromophores is then presented, emphasizing the role of steric and electronic effects in determining structure, and showing the responsiveness of the π-systems to the medium. Optical absorption studies and electrochemistry allowed the measurement of key material parameters, ground-to-excited state transition energy, change in dipole moment, and transition dipole. All twisted chromophores showed significantly lower E_{ge}, enhanced M_{ge}, and large $\Delta\mu$, resulting in promising third-order polarizabilities for optical switching applications.

In Chapter 5, donor-acceptor systems with well-defined π-conjugation lengths were studied in their neutral and charged states for potential use as high-contrast electrochromic materials. The chapter begins with a discussion of the physicochemical basis for electrochromism, and presents a survey of charge carriers and their electronic

and magnetic properties, with examples from the literature. Then the design and synthesis of dioxythiophene-based donor-acceptor small molecules is presented. The development of an efficient synthetic approach for one-step D-A-D trimer synthesis is discussed. Then a thorough characterization of the neutral and charged state optoelectronic properties of both small molecules is presented, showing well-defined optical and electrochemical transitions, reflecting the discrete nature of the π-systems. The structure of the charge carriers in these molecules are then determined from a battery of spectroelectrochemical experiments, stoichiometric analyses, and electron paramagnetic resonance spectroscopy. The small molecules showed polaronic transitions that were assigned to polaron pairs and their π-dimers. Then, the discrete chromophore in one small molecule is built into a polymeric structure, with non-conjugated linkers. Well-defined optical and electrochemical transitions, and enhanced thermal properties ($\boldsymbol{T_g}$, $\boldsymbol{T_d}$) are observed in the polymer neutral state, as intended. The charged state of the polymer is shown to have optical transitions ascribable to a strong contribution from dimer structures. Spectroelectrochemistry of the polymer film then showed strong π-π stacking interactions yielding broadened transitions. Morphology studies of the polymer showed fibrillar structures, attributed to the rod-coil nature of the polymer repeat unit.

Finally, in Chapter 6, the conclusions of this dissertation are presented, emphasizing the structure-property relationships developed throughout Chapters 3 to 5. Then, ideas for further improving the tailored properties of each family of molecules, based on the conclusions from each chapter, are presented.

CHAPTER 1

INTRODUCTION

1.1. Conjugated Organic Materials and Their Electronic Structure

The use of organic materials in electronics applications has been a rich field of research for several decades, and has seen application in real-world devices that are already commonplace. The immense structural versatility in organic materials denotes a wide array of potential functions and properties. These are attractive not only for practical applications, but also for the fundamental study of the interactions of electric and electromagnetic fields with traditionally insulating materials. The myriad techniques and methods of organic synthetic chemistry enable the design of precision organic compounds for a variety of electronic functions.

The unifying feature in organic electronic materials is their π-conjugated system. Their structure can be broken down into two major parts. First, a framework of σ-bonds arising from the sp^x-sp^y orbital interactions (where x and y can be 1, or 2) connect adjacent carbon (or hetero-) atoms in σ-bonds. Here, the electron density is localized along the shared inter-nuclear axis between two atoms, leading to electrons that are tightly bound, and to a scaffold that holds the molecule rigidly together. With two or three electrons used in σ-bonds, the four-valent carbon atom is left with one or two electrons in *p*-orbitals. The lobes of the *p*-orbitals are directed perpendicular to the plane of the σ-bonds, so the interaction between *p*-orbitals (a π-bond) leads to electron density above and below the plane. While electrons in a σ-bond are tightly held by the nuclei, electrons in π-bonds are only *loosely* held. This simple disparity forms the foundation for

the unique and useful photophysical properties of π-conjugated materials, as illustrated in the succeeding section.

1.1.1. Evolution of Electronic Structure

An understanding of the technologically relevant properties of conjugated materials must begin with an insight into their electronic energy level structure. To start, the example of ethylene is examined (Figure 1.1a). For the sake of simplicity, only the orbitals on the carbon atoms are considered.

The carbon atoms of ethylene each have three sp^2 orbitals used to form one C-C, and two C-H σ-bonds. Since the electrons in the sp^2 orbitals are more tightly bound to the carbon nucleus, a bonding interaction (σ) between them is strongly stabilized. Conversely, an antibonding interaction (σ*) leads to a strong destabilization, leading to significant splitting between the two. The *p*-orbitals form a π-bond, having electron density being above and below the internuclear plane. The π-bond level is slightly stabilized, whereas the antibonding π* level is slightly destabilized. The pairwise occupation of the σ- and π- orbitals leads to an overall gain in stability. The bonding π-orbital in ethylene is the highest occupied molecular orbital (HOMO), and the antibonding π-orbital is the lowest unoccupied molecular orbital (LUMO). As with the valence orbitals of isolated atoms, the peculiar yet practical chemistry of conjugated systems involves these *frontier* orbitals.

When three or more adjacent *p*-orbitals (such as in alternating single and double bonds) are parallel and interacting, as in 1,3-butadiene (Figure 1.1b), the electron density can be shared or *delocalized* across all *p*-orbitals, shown by the four resonance structures. The occupied bonding, and unoccupied antibonding orbitals lead to a gain in stability, an

effect of conjugation. An analogous evolution of electron molecular orbital levels is found for cyclic conjugated systems. Systems that can attain aromaticity can benefit from enhanced stability arising from full occupation of a continuous ring of bonding π-orbitals in a closed shell configuration.

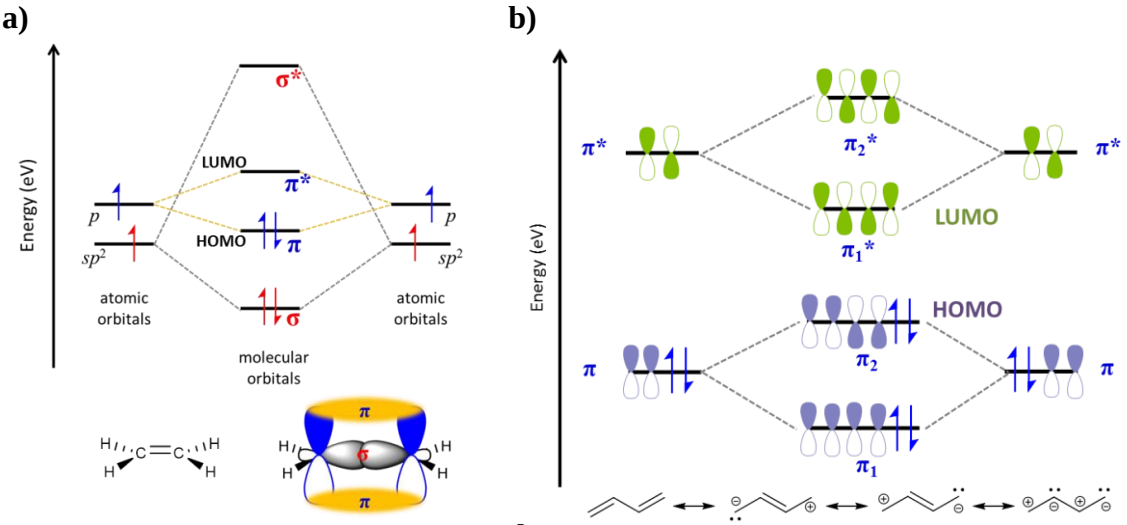

Figure 1.1. Interactions between (a) sp^2 and p orbitals in ethylene, leading to σ- and π-bonding and antibonding orbitals; (b) π and π* orbitals in 1,3-butadiene, to create new bonding and antibonding orbitals, and the resultant HOMO and LUMO orbitals.

As the number of interacting *p*-orbitals increase, i.e. as the conjugation length increases, the energy gap between the HOMO and LUMO decreases (Figure 1.2). At the limit of an infinite number of conjugated *p*-orbitals, the energy gap should ideally disappear, leading to a metallic type of band structure, and metallic conductivity. This condition would be true only if all π-bonds were equivalent. But in such a highly symmetric system, additional stabilization can be attained by breaking the symmetry, a phenomenon known as Peierls distortion, or Jahn-Teller distortion.[1-4] The lower symmetry configuration is accessed by an interaction with the vibrations of nuclei, i.e. the stretching of C-C bonds. This creates an alternating structure of long and short bonds in

the π-system, known as bond length alternation (BLA). The stabilization from symmetry breaking leads to a HOMO level that has lower energy, and a LUMO level that has higher energy, than otherwise predicted by a fully symmetrical structure. Thus, a gap opens in the energy level structure, leading to semiconducting properties (Figure 1.2b).

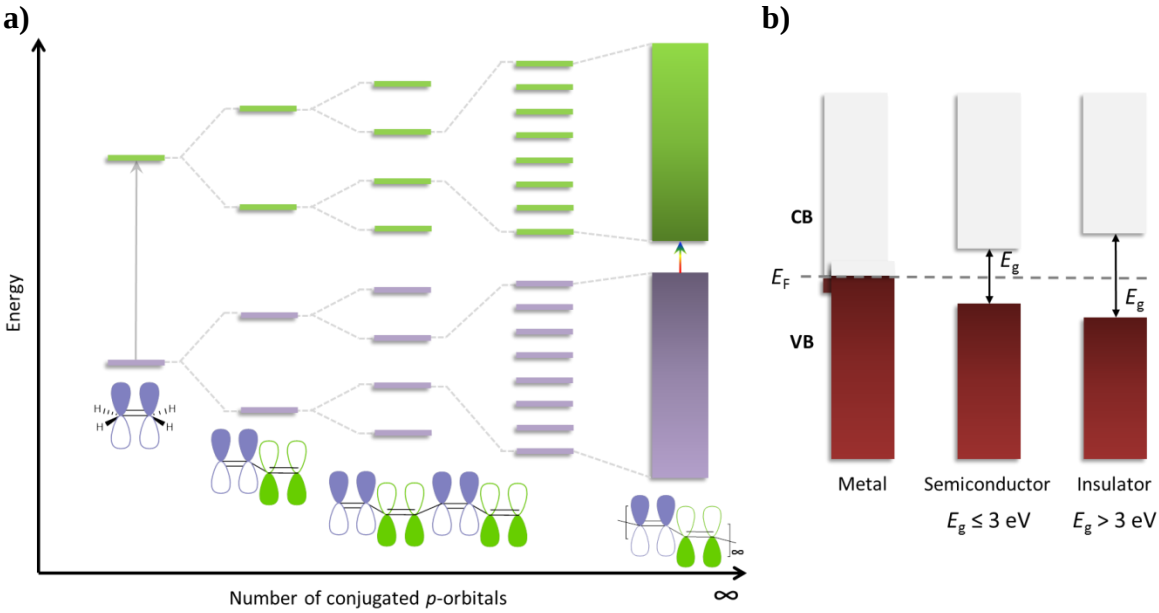

Figure 1.2. (a) Schematic diagram of the development of band-like energetic structure in long polyenes and conjugated polymers, and the finite energy gap that exists even in infinitely long systems. (Adapted from reference [4].) (b) Comparison of band structures in metals, semiconductors, and insulators, and their relative energy gaps (E_F is the Fermi level).[5]

Again, this gap arose from a vibrational mode that causes symmetry breaking. The Jahn-Teller distortion is a manifestation of strong electron-phonon coupling, a central theme in π-conjugated organic systems.

1.1.2. Optoelectronic Processes and Excited States in Conjugated Systems

Conjugated materials find application as active materials in transistors, photovoltaics, light emitting diodes, electrochromic displays, optical switching, and others. As semiconducting materials, their useful properties tend to emerge when they are

in excited states, whether neutral or charged. Their reduced energy gaps allow them to undergo optical (electrical) excitation at moderate wavelengths (voltages). The fate of that excitation, whether by decay into emitted photons, or by generating charge carriers, is exploited in the aforementioned devices. The subsequent sections are devoted to the optoelectronic processes that are most relevant to this dissertation.

1.1.2.1. Light Absorption and Emission

Light absorption in conjugated systems generates neutral excited states when photons of sufficient energy impinge on the molecule in its ground state. The resulting transitions are depicted with a Jablonski diagram (Figure 1.3).[6,7] The ground state of conjugated molecules are generally in a closed-shell, singlet configuration (all spins paired), and thus, shown as S_0. The excited states can be singlet (S_1, S_2, …, S_n) or triplet (T_1, T_2, …, T_n), and have vibrational (ν_0, ν_1, ν_2, …, ν_m), and rotational (not shown) sublevels. Absorption of light leads to promotion of a ground state electron to an excited state (generally in the singlet manifold). Absorption takes place according to the Franck-Condon principle, so that the nuclear positions do not change during the electronic transition, and a higher vibrational level can be occupied if its vibration mode coincides with that of the ground state. The relaxation to the S_1 ν_0' level occurs via internal conversion, accompanied by phonon emission. A molecule then undergoes radiative transition from this state to the ground state, with concomitant emission of photons via fluorescence. Intersystem crossing, in which a non-radiative transition from the singlet state to the triplet state (T_n), can allow the molecule to relax to the ground state via phosphorescence. However, the spin-orbit coupling that allows significant intersystem

crossing is poor in many conjugated organic molecules, and thus, its rate and probability are low, unless mediated by heavy atoms.

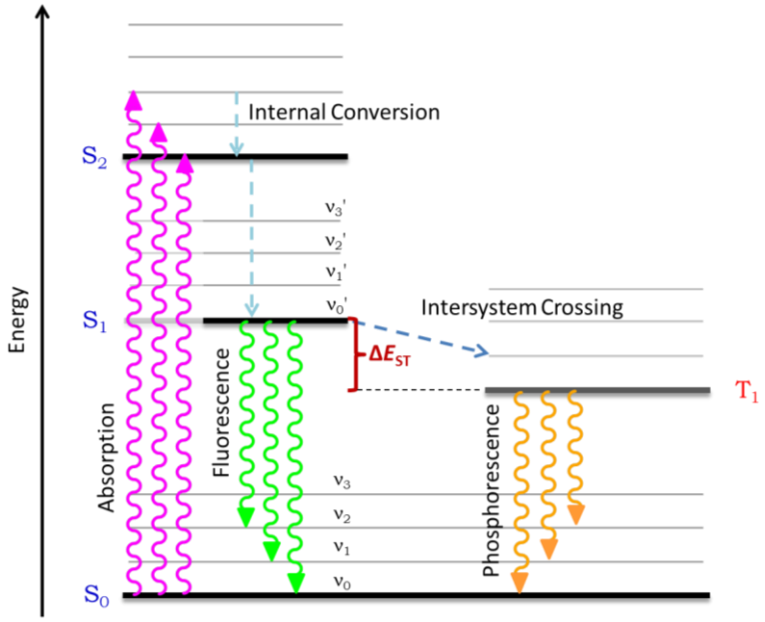

Figure 1.3. Jablonski diagram (for nuclei in fixed positions) showing the optical transitions that a conjugated system can undergo (radiative transitions are shown as wavy arrows, and non-radiative transitions as dashed arrows). (Adapted from ref.[6])

In characterizing conjugated systems, the absorption and emission (fluorescence and phosphorescence) spectra yield information regarding the energy gap between the ground and neutral excited states, and for certain molecules, the energy gap between vibronic modes. The former (termed the *optical gap*) is determined from the onset of the lowest energy peak ($E_{\text{onset,abs}}$, *vide infra*), while the latter is determined from the peak-to-peak separation of vibronic overtones (when observed). The intensity of the absorption peaks also provides information regarding the strength of the transition, and gives a measure of the degree of spatial overlap between the initial and final states (usually correlated to the HOMO and LUMO wavefunctions). The intensity depends on how strongly the electron cloud of a molecule is perturbed by its interaction with a photon (of

sufficient energy). This is quantified by the transition dipole moment (M_{if}, where i and f are the initial and final states), i.e. the transient charge separation (dipole) in the electron cloud that develops upon interaction with the photon. Experimentally, this is determined from the oscillator strength (f), which is approximated from the area under the absorption peak (plotted as the molar extinction coefficient (ε) against the energy (ν) in wavenumbers), according to the equation:

$$\boldsymbol{f \, \alpha \, M_{if}^2} \tag{1.1a}$$

$$\boldsymbol{f \equiv 4.3 \times 10^{-9} \int \varepsilon(\nu) \, d\nu} \tag{1.1b}$$

The light absorption process can be seen as a resonant oscillation of the π-electrons of the conjugated system to the oscillating electric field of light. The instantaneous π-electron re-distribution results in *polarization*, which is linearly proportional to the light's electric field. The induced dipole creates an internal electric field in the molecule, which can add to the applied electric field, and contribute to the ensuing polarization response of the molecules.[8] This latter contribution becomes important when high intensities of light are impinging on a material, and a nonlinear relationship between polarizability and the applied electric field is generated.

It must also be noted that in molecular systems, the optically-promoted transition to the singlet or triplet excited state leads to a Coulombically bound electron-hole pair in one molecule (called a Frenkel exciton).[9] The electrostatic interaction remains strong due to the low dielectric constant of organic molecules, arising from their strong electron-phonon, and electron-electron correlation interactions.[10] The exciton binding energy ($\boldsymbol{E_B}$) gives a measure of the strength of these interactions, and in conjugated systems, can range from a few tenths of an eV to above 1 eV.[9,11] This is significantly higher than those

in inorganic semiconductors, in which the higher dielectric constant leads to $\boldsymbol{E_B}$ of a few meV.[12] Since $\boldsymbol{E_B}$ in inorganic semiconductors is much lower than thermal energy at 25 °C (k_BT = 26 meV), light absorption leads directly to free charge carriers.[13]

Related to $\boldsymbol{E_B}$ is the singlet-triplet exchange energy ($\boldsymbol{\Delta E_{ST}}$, Figure 1.3),[14] which is the energy gap between the singlet and triplet states. A large $\boldsymbol{\Delta E_{ST}}$ denotes that the singlet and triplet states are described by very different wavefunctions, i.e. the singlet and triplet excitons are localized in different parts of the molecule.[15] It also denotes a large $\boldsymbol{E_B}$ due to localization of the electron-hole pair in a small part of the molecule. The $\boldsymbol{\Delta E_{ST}}$ is obtained from the energy difference between the high-energy fluorescence and phosphorescence peaks.[14]

1.1.2.2. Doping and Charge Injection

Charged excited states can also be generated in conjugated organic materials by chemical or electrochemical redox reactions (doping), charge injection from metal electrodes, or by the dissociation of the optically induced neutral exciton (generally through charge transfer).[16,17] Because these processes generate *charged states*, their energetic costs are different from the optical gap shown in Figure 1.3.

The process of generating positive (p-doping) and negative (n-doping) charge carriers are schematically illustrated in Figure 1.4. In p-doping, an electron acceptor (Ox^+) extracts an electron from the HOMO level of the organic molecule (M), leaving a hole (h^+) in its place. In n-doping, an electron donor transfers an electron to the LUMO level (actually to the lower level of the midgap states, *vide infra*) of the dopand molecule. It is clear from this picture that the energy levels of the organic material and the oxidant or reductant must be properly aligned in order for the electron transfer to be exothermic.

Furthermore, the doping process leads to a significant change in the energy level structure (appearance of midgap states) of the organic material, due to its strong electron-phonon coupling (*vide infra*).

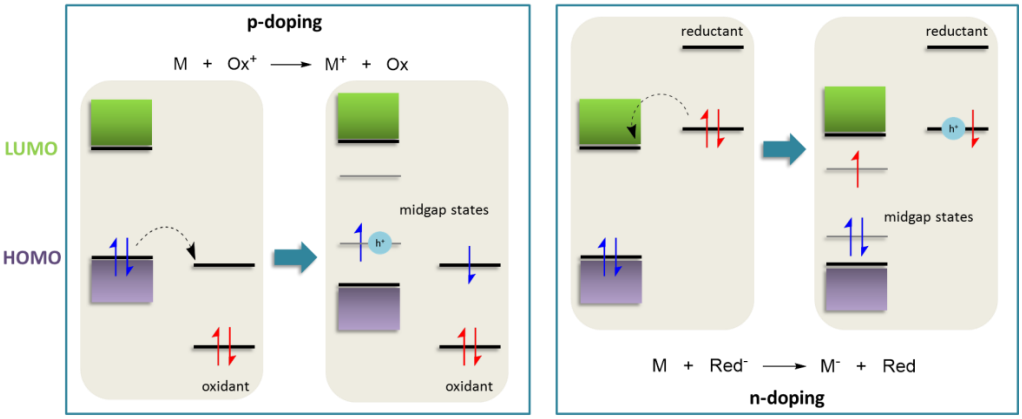

Figure 1.4. Simplified schematic diagram of the electron transfer processes in doping an organic material (dopand) with oxidizing and reducing agents (dopant).

In organic materials, p-doping can be induced chemically with an oxidizing agent such as I_2, $SbCl_5$, Ag^+, or NO^+, or electrochemically with the application of a positive voltage. The process is different in inorganic semiconductors, where doping is accomplished by substituting host atoms in the lattice (e.g. Si) with an element with fewer valence electrons (e.g. B).[18] A crucial consequence of this difference is that while a neutral lattice is maintained in inorganic systems, p-doping generates positive charge carriers in organic materials, necessitating the presence of charge-balancing counterions. Thus, the dopant in organic materials occupies interstitial positions in the conjugated matrix, and may still be Coulombically bound to the charge carrier in the π-system.[19] Depending on the strength of their interaction, the dopant can perturb the energetic landscape of the π-system.

Charged state generation in organic systems leads to considerable geometric deformations in the π-system, which is a demonstration of their strong electron-phonon coupling. This deformation manifests as a change in the BLA pattern to create a π-electron distribution that stabilizes a charge better. For oligo- or poly- (hetero)aromatic systems, the charged state favors the quinoidal resonance form over the aromatic form, due to its lower ionization potential, and higher electron affinity.[20]

The energetic cost of charged state formation is graphically illustrated in Figure 1.5, with oligothiophene as an example. The ground state configuration favors the aromatic resonance form, due to its enhanced stability. The charged state generation can be envisioned to proceed as a vertical (Franck-Condon) ionization process (step 1, red arrow), with energetic cost equivalent to the ionization energy from the undeformed state (IE_{ud}). Then, the molecule undergoes a geometric relaxation (deformation) to the quinoidal state (step 2, red arrow), with concomitant stabilization amounting to the relaxation energy E_{rel}. Similarly, the ionization can also proceed by first deforming the aromatic system to a vibrational mode corresponding to a quinoidal type of geometry (step 1, blue arrow), with an energetic cost equivalent to the distortion energy, E_{dis}. Since the molecule is in a quinoidal state, which has lower ionization potential and higher electron affinity, the ionization energy required (step 2, blue arrow), IE_d, is lower. Thus, the charged state π-system has significantly different band structure and energetic landscape (e.g. evolution of midgap states shown in Figure 1.5). This charged state coupled to a geometric deformation is called a *polaron*, which has different optical and electronic properties, as will be elucidated in a later chapter. The n-doping of conjugated systems takes place through an analogous process.

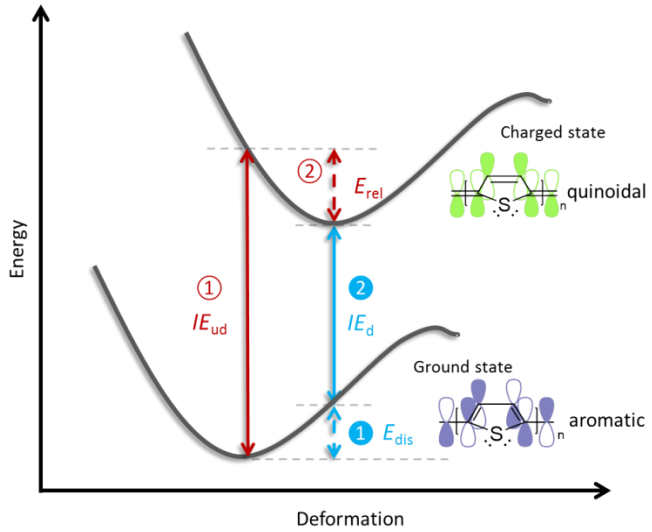

Figure 1.5. Schematic diagram of the coupled ionization and geometric deformation in organic conjugated systems, with aromatic and quinoidal forms of oligothiophene as an example. (Adapted from ref.[21])

The deformation to the quinoidal form upon ionization has been shown in oligothiophenes by X-ray crystallography of their radical cation salts.[22,23] An example of the change in BLA pattern from aromatic to quinoidal in a thiophene ring[22] is shown in Figure 1.6. The quinoidalization is apparent in the significant decrease of the inter-aryl bond length. The extent of this deformation is strongly dependent on the π-system, and the medium in which the charged state is created.

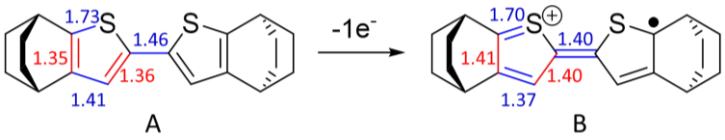

Figure 1.6. Changes in BLA pattern in thiophene rings as determined from X-ray crystallography of the neutral molecule (A) and the salt of its radical cation (B). Values are in Å, and taken from ref. [22].

Although doping and charge injection both involve electron transfer processes that generate charge carriers, charge injection as a term tends to be used frequently to denote interfacial charge transfer, commonly with metal electrodes. Here, charge

injection does not involve counterions, but charge balance is maintained by the simultaneous injection of charge carriers of opposite sign from a second organic material/metal electrode interface. Interfacial charge injection is thus an important process in transistors, photovoltaics, and light emitting diodes, in which the organic semiconducting material tends to be sandwiched between metallic cathode and/or anode materials.

The process of interfacial charge injection is affected by many factors, not least of which is the nature of the interaction between metal and organic material at the surface.[24] A thorough treatment of these is available in the literature, and the reader is encouraged to consult these for an exhaustive discussion.[25-29] Differences in the mechanism of charge injection from metals to inorganic versus organic semiconductors arise from the amorphous and disordered nature of organic materials, with weak van der Waals interactions in the condensed phase, and the significant effects of impurities. Nevertheless, the metal-organic charge injection process can still be approximated by the schematic diagram in Figure 1.4, with the understanding that the energy levels shift and bend due to the interactions (e.g. dipoles) at the surface.

1.1.2.3. Charge Transport

Charge injection and transport are processes that are firmly associated, dominated by the weak interaction (van der Waals) and disorder in amorphous organic materials. Because of the covalent bonding, high degree of order, and repetitive structure in an inorganic crystal, transport in inorganic semiconductors occurs through a wave- or band-like motion of charge carriers, leading to high mobility values in tens or hundreds $cm^2 V^{-1} s^{-1}$. In organic materials, the inherent disorder leads to a statistical distribution of

environments for each molecule, and to a spread of energies. Thus, transport in organic materials is limited to a hopping mechanism (Figure 1.7).[16,30-35] The charges must hop from molecule to molecule that interact via van der Waals forces, in a series of charge transfer events. Charge transfer, as will be explored further in a later chapter, depends on the electronic coupling between participating molecules (the transfer integral), and the reorganization energy related to forming the charged state (λ_{rel} – E_{rel} in Figure 1.5). Again, for a thorough discussion of the charge transport mechanism, the reader is directed to the reviews from Bredas, *et al.*,[31,33,36] Bässler,[16,25] Stafström,[34] and Baranovski,[35] among others.

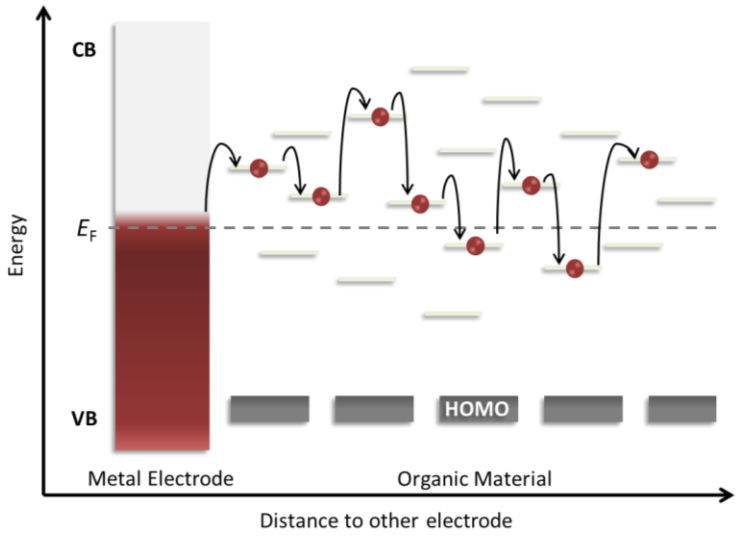

Figure 1.7. Schematic representation of hopping transport in disordered organic materials. (Adapted from ref.[35])

1.2. Structural Control of Optoelectronic Properties

The diverse utility of π-conjugated materials in electronic devices arises from the precise control of properties that are accessible from mere structural variations. Properties such as energy gap, oxidation and reduction potentials, charge transfer and transport characteristics, and polarizability can all be tuned with appropriate functional groups.

These can be assembled in a cooperative fashion to obtain synergistic responses, or in a non-cooperative fashion to obtain antagonistic properties, in one molecule.

1.2.1. Conjugation Length

The foregoing discussions have demonstrated that the optoelectronic properties of conjugated materials derive from the interacting *p*-orbitals. As the number of these orbitals increase, the energy gap decreases, so that while the energy gap of ethylene is 10 eV,[37] and that of 1,3-butadiene is 9.0 eV,[37] polyacetylene has a gap of around 1.5 eV.[38] Thus, in sufficiently long π-systems, excited states can be accessed with near-UV, visible, and near-IR energies.

Many examples in the literature have shown that in a series of oligomers, the absorption maximum of the lowest energy transition undergoes a gradual red-shift in wavelength with increasing number of repeat units. The absorption energy (*E* in eV) has been shown to roughly follow a linear trend with the reciprocal of the number of repeat units (*n*) in several polyaromatic systems.[39-43] A more exact relationship developed by Meier *et al*.[39] allows the determination of the effective conjugation length, the value for *n* at which a property (here, the absorption wavelength) saturate for a given repeat unit structure:

$$\boldsymbol{E(n) = E_{\infty} + (E_1 - E_{\infty})e^{-a(n-1)}} \qquad (1.2)$$

where *a* describes how fast the equation converges to the limit for a particular polyaromatic system, and E_1 and E_{∞} refer to the monomer and infinite polymer absorption energies, respectively. Thus, the energy of the lowest excited state decreases with increasing conjugation length, due to the narrowing of the energy gap shown in section 1.1.1.

Both linear and nonlinear polarizabilities also show a dependence on conjugation length, with increasing sensitivity shown by nonlinear polarizabilities.[44-46] These relationships can be rudimentarily rationalized based on the linear relationship between dipole moment and the displacement between the centers of positive and negative charge. A longer π-system can yield a larger separation distance between the optically-induced positive and negative charge centers, and thereby to larger polarizations.

A linear relationship between the reciprocal of conjugation length (or number of rings) and oxidation potential has also been observed in a number of oligo-heterocycles.[40,41,43,47] This observation can easily be understood in terms of the energy level structure in Figure 1.2, where the HOMO energy increases with conjugation length. The higher HOMO will correspond to a lower ionization potential, and a lower voltage necessary to extract an electron from the π-system.

Relationships between doped polymer conjugation length and hopping conductivity (both along the chain and between chains) have also been developed in the work of Baughmann and Shacklette.[48,49] They showed that parallel (intrachain, σ_1) and perpendicular (interchain, σ_2) conductivity varies with the conjugation length according to:

$$\frac{\boldsymbol{\sigma_1}}{\boldsymbol{\sigma_2}} = \frac{\boldsymbol{L^2}}{\boldsymbol{6d^2F}} \tag{1.3}$$

where *L* is the conjugation length, *d* is the interchain distance, and F is a geometric factor that gives a measure of the fraction of nearest-neighbor chains that are parallel to the transport direction. The predictions from the equation compared well with experimental observations from poly-*p*-phenylene, polyacetylene, and polythiophene. This relationship between hopping conductivity and conjugation length can be fundamentally traced to the

effect of conjugation length on the ionization potential or electron affinity, because the frequency of hops depends on the ease with which charge transfer (i.e. a redox event between two chains or chain segments) can occur.

1.2.2. Torsional Effects and Conjugation Breaking

In the alternating single and double bond motif of conjugated systems, the overlap of p-orbitals that is crucial for generating useful optoelectronic properties depends on the dihedral twist angle around single bonds. In conjugated polymers, the dihedral twist angle can be modulated by steric factors introduced by side chains,[50] fused ring systems,[51] secondary interactions such as hydrogen bonding,[52] sulfur-oxygen interactions,[53] among others.

An example of the effect of torsion angle on optoelectronic properties was reported by Breza, *et al*.[54] They showed that in a series of oligothiophenes, the calculated absorption maximum (λ_{max}) varied significantly with the torsion angle between thiophene rings (Figure 1.8). The torsion angle can be modulated by side chains around the inter-ring bond, as shown by a comparison of the results to solution spectra of methyl- and ethyl-substituted bithiophenes. These trends have been replicated in longer oligothiophenes,[55] and other oligomers. Increases in calculated energy gap, and ionization potentials with increasing torsion angle (0 – 90°) were also demonstrated in poly-*p*-phenylene, polypyrrole, and polythiophene.[56] The changes in ionization potential with conformation can also affect charge injection barriers.[57] The effect of torsion angle on energy gap and charge transfer integral (and thereby charge transport mobility) in oligomers of 3-hexylthiophene was studied by Darling via theoretical calculations.[58] The

increase in energy gap and decrease in transfer integral was shown to be more substantial in shorter oligomers relative to longer ones.

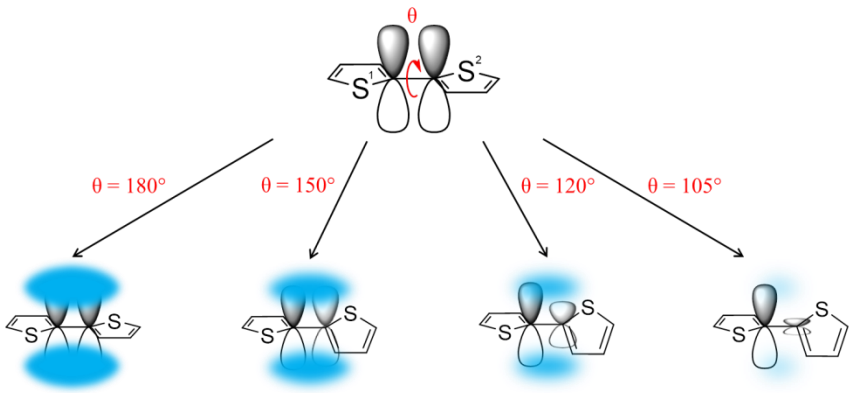

θ	λ_{max} calc	λ_{max} exp	Exp'tal structure
180 ± 15°	373 – 374	310	
148 – 155°	368 – 371	302	
1 3 – 135°	365 – 376	279	
90 ± 15°	313 - 318	270	

Figure 1.8. The effect of torsion-angle modulated π-overlap on absorption maxima in a series of alkyl-substituted bithiophenes. (Data obtained from ref.[54])

A substantially more pronounced effect of torsion angle is observed in molecules in which the twist is accompanied by electron transfer, so called, twisted intramolecular charge transfer (TICT).[59] Here, a large torsion angle is induced by rotation around a single bond linking a donor and an acceptor unit, and interrupts conjugation between the two. This mechanism has been exploited for near-complete charge transfer and the induction of large dipole moments, and linear and nonlinear polarizability after

photoexcitation in donor-acceptor molecules.[60,61] This mechanism will be fully discussed in a later chapter.

1.2.3. Electron Density of the Conjugated System and the Donor-Acceptor Approach

A well-established approach toward modulating optoelectronic properties in conjugated systems is by tuning the electron richness of the π-system. On the one hand, heterocycles that have substituents that can donate electron density to the π-system (called donors) can raise its HOMO (lower the ionization potential). On the other hand, heterocycles that have substituents that can withdraw electron density from the conjugated system (called acceptors) can lower its LUMO (increase its electron affinity).[62]

One of the most ubiquitous heterocycles employed in the field of organic electronics is 3,4-ethylenedioxythiophene (EDOT). Many of its advantageous properties derive from the oxygen substituents on the β-positions of the thiophene ring, which increase the electron density in the thiophene ring, allowing its monomer and polymer to have low oxidation potentials, moderate energy gaps, and stable radical cations and dications.[63-65] The electron donation by oxygen also enhances the reactivity of the α-positions, while simultaneously blocking the β-positions from participating in reactions. Other notable electron-rich (donor) heterocycles are other dioxythiophenes such as acyclic dialkoxythiophenes, and 3,4-propylenedioxythiophene (ProDOT), dialkoxybenzenes, carbazoles, triarylamines, and fused ring systems such as dithienosilole, dithienogermole, among others.

Electron-accepting heterocycles, on the other hand, have substituents such as carbonyl groups, amides, imides, imines, and azoles, all of which can form mesomers that withdraw electron density from the π-system. Some commonly employed acceptors are 2,1,3-benzothiadiazole (BTD), isoindigo (iI), diketopyrrolopyrrole (DPP), benzotriazole (BTz), and naphthalene diimide (NDI).[62] These heterocycles can increase the electron affinity of the π-system, and stabilize its radical anions and dianions.

Covalently linking a donor, and an acceptor moiety induces an intramolecular charge transfer interaction, in which the donor transfers electron density toward the acceptor, generating a significant contribution from a charge-separated mesomer.[66-69] This concept, outlined in Figure 1.9, has been implemented successfully to obtain low energy gap materials that have found pervasive application in low energy light absorption for solar cells,[62] and large polarizabilities for nonlinear optics.[70,71] The reduction in energy gap is attributed to the HOMO and LUMO of the resulting donor-acceptor compound being tied to the HOMO of the donor, and the LUMO of the acceptor, respectively (Figure 1.9a). The charge transfer interaction can also induce a contribution of the quinoidal mesomer (Figure 1.9b), which delocalizes the electron density across the two moieties. The versatility of this approach lies in the many different electron-rich and electron-poor heterocycles, which have varying ionization potentials, electron affinities, and different levels of localization of their HOMO and LUMO wavefunctions, that can be combined. All these parameters interact together to determine how the resulting energy gap of the donor-acceptor conjugate correlates with the individual constituent moieties.[69]

The donor-acceptor concept has also been used to generate materials with a dual band absorption, with a low energy band arising from the charge-transfer interaction, and

a higher energy band that tends to correlate with the extent of conjugation in the π-system.[69] This dual band absorption has been used to obtain a variety of intensely colored polymers for electrochromics,[72,73] including green,[74] and broadly-absorbing polymers.[75,76]

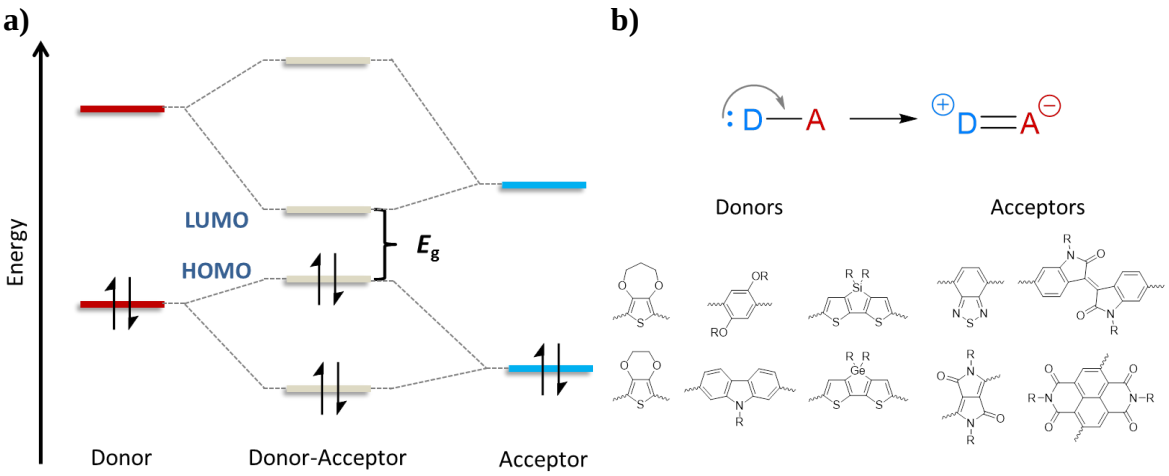

Figure 1.9. Schematic diagram of orbital mixing that gives reduced energy gaps in donor-acceptor systems (a). The charge-transfer interaction between donors and acceptors, and structures of common electron –rich and –poor heterocycles (b).

1.2.4. Aromatic and Quinoidal Mesomers

Another approach to tuning the energy gap in conjugated systems is by modulating the contributions of aromatic and quinoidal forms of the heterocycles to the ground state structure, and the HOMO and LUMO energies.[2,77-80] A classic demonstration of this concept is highlighted in the difference in energy gaps between polythiophene and polyisothianapthene.[2,81,82] As shown in the schematic potential energy surfaces and structures in Figure 1.10, polythiophene has a ground state structure that is better described by the aromatic canonical resonance form, whereas polyisothianaphthene is better described by the quinoidal canonical structure. The latter case can be rationalized from a comparison of the aromatic stabilities of thiophene and benzene. The aromatic mesomer of polyisothianaphthene has thiophene in an aromatic configuration, whereas its

quinoidal mesomer has benzene in the aromatic form. Since benzene has a stronger resonance stabilization energy than thiophene, polyisothianaphthene favors the quinoidal form in its ground state.[2] The quinoidal contribution in polyisothianaphthene enhances delocalization across the polymer chain, and reduces the energy gap of this polymer to 1.0 eV,[82] versus 2.1 eV from polythiophene.[2]

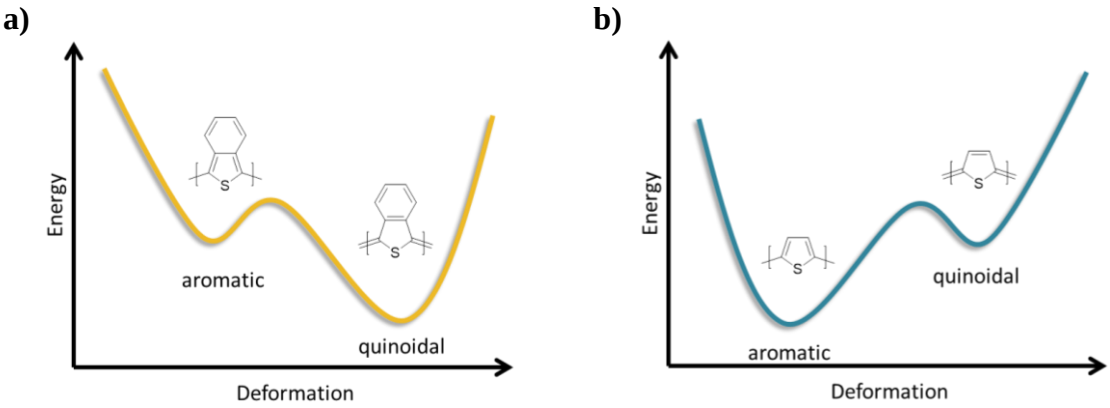

Figure 1.10. Schematic representation of the relative energies of the aromatic and quinoidal mesomers of polyisothianapthene (a) and polythiophene (b).

In substance, tuning the contribution of aromatic and quinoidal resonance forms to the ground state structure is simply a method by which to manipulate the BLA of a conjugated system. The donor-acceptor approach accomplishes the same, with a concomitant charge transfer. Reducing the energy gap can be accomplished by finding the right balance between the contributing resonance forms. Additionally, balancing of aromatic/quinoidal contributions is another approach for creating systems that have low reorganization energy, and thereby enhanced charge transfer and transport characteristics.[79]

The balance of aromatic and quinoidal contributions has also been exploited in tuning the polarizabilities of conjugated materials. For example, Andreu, *et al.*[83] have

used quinoidal heterocycles that attain an aromatic structure upon charge transfer to imbue a charge-separated structure with enhanced resonance stabilization energy.

1.2.5. Aggregation and Intermolecular Effects

In optoelectronic devices, the organic conjugated materials are generally in the condensed phase, making the study of their intermolecular assembly crucial to understanding their performance characteristics.[84] In some applications, the intermolecular effects are favorable, in other cases they are detrimental, and so a mechanism for their control is also a necessary component of material design. Optoelectronic processes such as charge transfer and hopping transport strongly depend on the intermolecular interactions and π-π wavefunction overlap in the solid state.[85] Interactions are generally favored in these cases, and are promoted by enhancing the planarity of the π-system, for example through the use of highly crystalline structures, fused rings, secondary interactions, and proper placement of side chains. Optoelectronic processes that require absorption (or emission) of specific wavelengths of light (such as color tuning in electrochromics, or optically-induced polarization in nonlinear optics) favor disruption of these interactions, which can be implemented with amorphous structures, and branched side chains. Another approach of preventing interactions is by dispersing the active material into a matrix.

Interactions between molecules are frequently determined from shifts in absorption or emission bands. These interactions lead to a Davydov splitting[86-88] of the excited state, and thereby new possible transitions, allowed or forbidden depending on the relative orientations of the transition dipole moments in the arrangement of molecules. Three dominant types of intermolecular arrangements can be envisaged: 1) a

cofacial parallel orientation termed H-aggregate; 2) a head-to-tail or "brickwork" orientation called J-aggregate; and 3) a tilted orientation, called oblique (Figure 1.11).

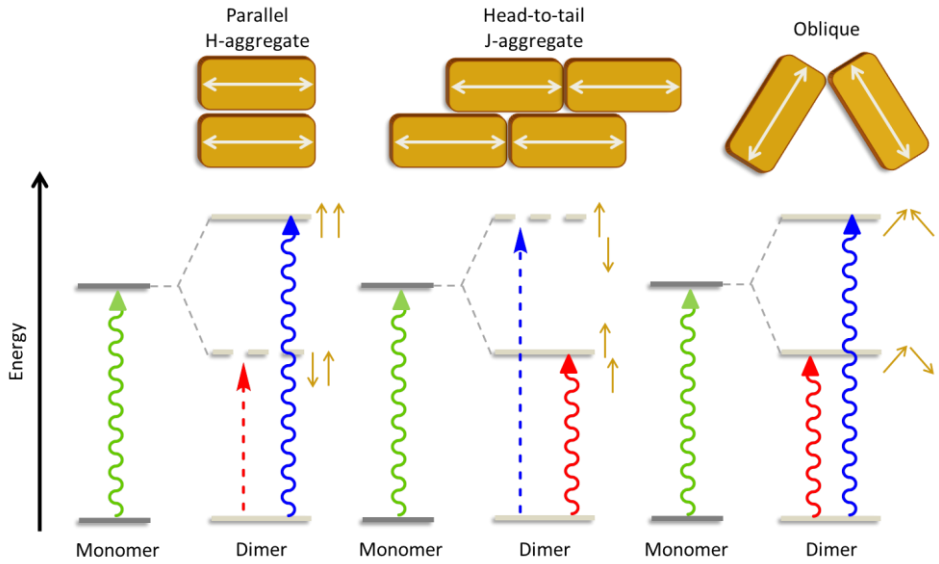

Figure 1.11. Davydov splitting of different intermolecular orientations and the resulting allowed (wavy arrows), and forbidden (dashed arrows) transitions. The orientations of transition dipoles are shown beside the excited state energy levels. (Adapted from refs.[87-89])

In H-aggregates, the allowed interaction of the transition dipoles leads to a transition to the upper level excited state, and a higher energy or blue-shifted (hypsochromic) absorption. The transition to the lower level involves a forbidden interaction of the transition dipoles, and is not observed. In J-aggregates, the allowed transition is to the lower level excited state, leading to a bathochromic or red-shifted absorption. Finally, in oblique interactions, both transitions are allowed as the interaction of the transition dipole moments lead to finite probabilities. In this latter case, the absorption will only undergo an observable shift (broadening) if the splitting is significant.

The change from isolated to condensed phase in long oligomers or polymer chains also tends to be accompanied by conformation changes that favor planarization of the π-system. These changes enhance both intra- and inter- molecular π-overlap, and lead to lower energy transitions observed as a red-shift of the absorption band in going from the solution state to the film state.[90,91] In well-ordered materials, the shift to the film state can also be accompanied by an enhancement of the vibronic resolution in absorption bands.

1.3. Structural Control of Macroscopic Properties

Material design for organic electronic devices for the most part focuses on structural control of optoelectronic properties, but must also take into account the requirements of fabrication processing and device stability. One of the touted advantages of organic materials is the ease with which their structure can be synthetically modified. A modular approach to material design can confer multiple crucial, sometimes disparate, properties in one molecule. Thus, the required optoelectronic properties can be designed into the π-conjugated backbone of the material, whereas secondary properties such as solubility, thermal, and mechanical stability can be added with peripheral functionalities.

1.3.1. Solubility

Soluble organic materials are amenable to low-cost processing techniques such as spray- or spin- casting, inkjet printing, and other roll-to-roll compatible methods. But, the π-conjugated backbone by itself leads to additive π-π stacking interactions that render unsubstituted materials intractable and infusible. For the material to be soluble, appropriate side chains must be affixed to the backbone. These side chains will disrupt the π-π stacking interactions, but a compromise can be made between making the

material sufficiently processable, and still have significant π-π stacking to maintain desired optoelectronic properties.

The nature of side chains chosen for a material depends on what the expected processing and fabrication conditions will require. Nonpolar alkyl chains allow solubility in and processability from organic solvents. The length of the chains necessary to confer solubility depends on the size of the π-system. Since π-π stacking interactions are additive, larger π-systems tend to have stronger interactions, and will require longer alkyl chains that have larger conformational entropy. The chains can also be linear or branched, with branched chains requiring more entropic volume, and preventing close-approach of π-stacks. Other functionalities such as oligoether chains, or carboxylate- or phosphonic acid- terminated alkyl chains can confer solubility in polar solvents (even water). The choice between nonpolar- or polar- soluble materials depends on the device fabrication conditions, and the substrate on which the material is to be deposited. Orthogonal solubilities are favored for contiguous layers in a device. Another approach is the use of cleavable side chains, solubilizing groups that can be removed post-deposition with thermal treatments.[92] The side chains can also be designed to cross-link post-deposition to render the material layer infusible, and amenable to patterning.[93]

1.3.2. Thermal Properties and Film Stability

Thermal stability is crucial for materials that find use in devices that may be subject to localized heating. For example, active materials for photovoltaics are expected to withstand ambient heat from the sun, materials for biomedical applications must withstand heat sterilization, and transistor materials are continually exposed to elevated temperatures during device operation. Furthermore, small molecule organic materials are

sometimes processed into films via thermal evaporation under vacuum, requiring temperatures well above 150 °C.

Thermal stability is commonly quantified in two terms: 1) the temperature at which chemical decomposition occurs, T_d (observed as a loss in material mass); and 2) the temperature range in which the material retains morphological stability. The latter is related to the glass transition temperature, T_g: the temperature at which the material (usually amorphous) changes from a hard and brittle glass, to a soft and elastic solid, commonly through the motions of moieties or groups of atoms in the material.[94] Whereas T_d depends on the collective number and nature of bonds in the material, T_g depends on the flexibility of groups of atoms (moieties) in the material. Both transition temperatures tend to increase with increasing molecular weight, but T_g can be improved with bulky and rigid moieties that have small rotational moments, such as aryl groups, bicyclic groups, and spiro-linkages.

The T_g is a particularly important parameter in amorphous materials, which is characteristic of the solid phase of many organic conjugated polymers and small molecules. The amorphous state offers many advantageous properties for organic electronic applications. Amorphous films tend to have better homogeneity than crystalline films, have fewer grain boundaries, and lead to more uniform transport characteristics, and less light scattering.[95] High T_g's allow amorphous materials, which are not at thermodynamic equilibrium, to maintain their glassy state, and prevent crystallization throughout fabrication processes such as annealing, and normal device operation.[96]

In composite active layers where one material is dispersed in another, such as those used in bulk heterojunction photovoltaics, and phosphorescent organic light emitting diodes, the amorphous film must also maintain the microscopic domain distribution and the overall morphology of the film. The stability of the morphology depends on the T_g of the matrix, because a firmer matrix will restrict the diffusion of dopant molecules through the film.

1.4. Thesis of This Dissertation

In this dissertation, three independent projects highlight the careful and purposeful design and synthetic control of conjugation to imbue materials with application-directed properties. In each chapter, an introduction of the physicochemical processes for each application is given. These serve as a background of the conceptualization of molecules to meet design requirements for specific roles in electronic applications. The three-pronged approach of targeted design and pragmatic synthesis, rigorous characterization, and in-depth structure-property analyses is a unifying theme of this dissertation.

In Chapter 3, triphenylene-based materials with *meta*-linkage disrupted conjugated π-systems are presented. The notable synthetic methods used that allowed access to the materials in few steps and at high yields are discussed. The conjugation-breaking substitution pattern gives rise to large energy gaps without prohibiting charge transport in the polyaromatic systems. Both crystalline and amorphous materials are obtained, dependent on whether solubilizing side chains are present. The thermal and film characteristics of the materials are presented, and a new method of attaining morphological stability is reported. These materials are then presented as suitable hosts in

phosphorescent organic light emitting devices with high efficiencies. The performance characteristics of the materials are analyzed based on their carefully determined optoelectronic properties.

In Chapter 4, molecules in which the conjugation across electron-rich and electron-poor rings is carefully diminished with appropriately positioned peripheral functionalities are presented. The design of molecules was directed not only by the intended properties, but also for synthetic efficiency, and this coupled approach is discussed. The steric and electronic control of charge transfer that gives rise to large polarization is comprehensively characterized, both from a structural and an optoelectronic standpoint. Material parameters related to nonlinear polarizability were determined from optical and electrochemical techniques, and correlated with the structure. The thermodynamics of aggregation were also studied for one permitting case. The molecules exhibited nonlinear polarizabilities that show promise for optical switching applications.

In Chapter 5, discrete conjugated systems based on donor and acceptor heterocycles are exhaustively studied in their neutral and doped states. Both chemical and electrochemical techniques, coupled with electronic and magnetic spectroscopy, are employed to define the structure of the charge carrier at the mono- and di- cation states. The evolution of, and interaction between charged states are studied to guide the design of active materials for high contrast electrochromics. A polymeric derivative is synthesized utilizing an appropriate linker to maintain the discrete conjugated system. The neutral and charged states, thermal properties, and film forming characteristics of the polymer are studied and compared with its small molecule equivalent.

CHAPTER 2

CHARACTERIZATION TECHNIQUES AND EXPERIMENTAL METHODS

The work presented in this dissertation involved collaborations with multiple groups from different universities. OLED device fabrication and characterizations (Chapter 3), as well as AFM film studies were done by Szuheng Ho from the group of Prof. Franky So at the University of Florida. Emission spectra of OLED host materials (Chapter 3) were taken by Charles Zeman IV from the group of Prof. Kirk Schanze at the University of Florida. Theoretical calculations (Chapter 4) were conducted by Dr. Alexander Baev from the group of Prof. Paras Prasad at State University of New York at Buffalo. Nonlinear optical (z-scan) measurements (Chapter 4) were done by Dr. Guang He from Prof. Prasad's group. Mixed solvent spray-casting of electrochromic polymer films on phosphonic-acid treated ITO substrates, and their electrochemistry and microscopy (Chapter 5) were performed by Keith Johnson from the Reynolds group. AFM film studies of electrochromic materials (Chapter 5) were performed by Dr. Caroline Grand from the Reynolds group. Their results are acknowledged and credited in the respective sections in which they appear.

2.1. Materials and Reagents

All reagents were purchased from various commercial sources and used as received without further purification, unless otherwise noted. Toluene, tetrahydrofuran, dichloromethane, acetonitrile, and propylene carbonate (PC) were obtained from a solvent purification system, and stored over activated 4Å molecular sieves under Ar a few hours prior to use (if not used inside a glovebox). Solvents used for carbon-carbon

cross coupling reactions, and for electrochemical and chemical doping experiments were further degassed with at least three freeze-pump-thaw cycles prior to use. When necessary, solvents were tested for water content on a Mettler Toledo Coulometric C20 Karl Fischer Titrator, and the solvent was dried over molecular sieves when water content exceeded 10 ppm.

2.2. Synthetic Methods and Structural Characterizations

Synthetic approaches and optimization of procedures are discussed in the respective chapters, as appropriate. But the importance of organic synthesis in enabling organic electronics research cannot be overemphasized.[97-100] Many of the synthetic challenges encountered throughout this work were addressed by catalysts and ligands recently developed for carbon-carbon cross coupling and C-H activation methodologies. The reader is encouraged to consult the following references for an introduction to the commonly used methods in this field: Suzuki-Miyaura coupling,[101-106] Stille coupling,[107,108] C-H activation,[109,110] direct arylation,[111-116] and other transition metal-catalyzed techniques.[98,100] For an introduction to the practical approach to conjugated material synthesis, the reader is also encouraged to consult the Ph.D. dissertation of Dr. Justin Kerszulis.[117]

FTIR spectra were obtained in the solid state on a Shimadzu IRAffinity-1 spectrometer on a MIRacle Single Reflection Horizontal ATR sampling accessory, with a DLATGS detector. ^{1}H and ^{13}C NMR spectra were recorded on a Varian Mercury 300 MHz spectrometer. Multidimensional and ^{11}B NMR spectra were recorded on a Bruker DRX 500 MHz spectrometer, with the help of Dr. Les Gelbaum. Chemical shifts are referenced to the residual solvent peaks (reported with the spectra for each compound).

Low resolution mass spectra were recorded on a Micromass Quattro LC Triple Quadrupole HPLC/MS/MS mass spectrometer, while high resolution mass spectra were recorded on a Waters Autospec M Three Sector Tandem mass spectrometer, performed at the Bioanalytical Mass Spectrometry Facility of the Georgia Institute of Technology. Elemental analysis was carried out by Atlantic Microlab, Inc. Gel-Permeation Chromatography (GPC) of **Poly EPBPE** was performed at 35 °C in THF on a Waters column (4.6 mm × 300mm; Styragel HR 5E), a Waters HPLC pump 1515, using a Refractive Index Detector 2414. The GPC was calibrated to narrow molecular weight polystyrene standards. The polymer was dissolved to a concentration of 1 mg mL^{-1} in THF, and filtered through a 0.45 μm PTFE filter, and 20 μL of the polymer solution was injected for analysis. Molecular weights were calculated using Waters Breeze II software.

2.3. Optoelectronic Characterizations

Many of the optoelectronic characterizations performed for the materials in this dissertation are standard in the Reynolds group.[117] Thus, focus is given only to methods that are less commonly applied, such as spectroelectrochemistry *via* chemical and electrochemical doping in solution.

2.3.1. A Note on Frontier Orbital Levels and Energy Gap Determinations

It is easy to confuse terminologies relating to the energies associated with excitation and charge generation processes in organic materials, a common case in organic electronics literature, as pointed out recently by Bredas.[10] Add to this the fact that while theoretical calculations, and conceptualizations of the processes tend to consider isolated molecules (gas phase), practical measurements always involve materials in the

condensed phase. The limits of experimental measurements also force researchers to make estimations of quantities, the details of which can get lost in the discussion. While the onus of accurate measurement and reporting strongly rests on the researcher, the reader also needs to be cognizant of these shortcomings. The succeeding discussion is provided to clarify the choice of terms used in the subsequent chapters, for which different excitation processes are relevant.

The first issue that needs to be clarified is the difference between orbitals and states.[7] HOMO and LUMO orbital energies from theoretical calculations are usually erroneously equated with ground and excited state energies, when the former are calculated as one-electron wavefunctions, whereas the latter is described by a superposition or linear combination of different configurations. Thus, while the HOMO and ground state energies are correlated with a closed shell configuration (for most organic compounds), the excited state is described by a manifold of closed shell configurations (S_n), and another manifold of open shell configurations (T_n), with contributions from different distributions of electrons in the HOMO, LUMO, HOMO − n, LUMO + m orbitals. Thus, often the theoretically-derived HOMO-LUMO energy gap is only roughly approximated by the energy difference between the ground and first excited state, with the electron-electron, electron-hole, and spin pairing interactions neglected. Furthermore, each electronic state is coupled to manifolds of different vibrational modes, so the energy also varies with the movements of the nuclei (many vibrational modes strongly affect the π-system, such as C=C stretching modes, aromatic ring modes).

In practice, the energy gap between the ground and excited state is determined from lowest energy band from optical absorption spectra taken from low concentration

solutions (10^{-7} to 10^{-4} M) or films of the material. As much as possible, the choice of whether to use solution or film results (in estimating other energy values) depends on the state of the active material in the intended application. Since the bands are broadened by vibrational and rotational levels, the optical energy gap ($\boldsymbol{E_{g,opt}}$) is taken from the onset of the lowest energy absorption band ($E_{onset,abs}$).

Whereas optical transitions lead to neutral excitons in organic materials, charge injection and transfer processes require the consideration of ionized states. In these processes, the ionization potential (IP) and electron affinity (EA) are the relevant energetic quantities. IP is defined as the energy required to completely remove an electron from a gas phase molecule in its ground state, to create a free positively charged system (usually a radical cation in organic systems). Here, this quantity is experimentally determined from the first electrochemical oxidation potential ($E_{ox,ec}$) in film or solution states, referenced to a standard (the ferrocene/ferrocenium redox couple, generally taken to have $E_{½,ox} = -5.1$ eV vs. vacuum[118]). Similarly, EA is defined as the energy required to add an electron to the LUMO of the organic molecule in the gas phase. It is approximated by the first electrochemical reduction potential ($E_{red,ec}$). Note that the electrochemical methods deviate greatly from the gas-phase conditions that the definition requires; other experimental methods are available that better approach this condition (photoelectron spectroscopy[119]). The difference between the IP and EA gives the fundamental energy gap, $E_{g,fund}$. This quantity is taken to be nearly equivalent to the transport gap, $E_{transport}$.

The relationships between these energetic quantities and their related experimental approximations are schematically illustrated in Figure 2.1. In this

dissertation, both IP and EA values are reported as negative quantities, whereas the $\boldsymbol{E_{g,opt}}$ is reported as a positive quantity.

For nonlinear optical materials (Chapter 4), in which optically induced excited states are relevant, $\boldsymbol{E_{g,opt}}$ is appropriate to correlate with $\boldsymbol{E_{ge}}$, the ground to first excited state energy gap (see section 4.1 and 4.5.3). As discussed in Chapter 1, the optical excitation leads to a neutral exciton, so that $\boldsymbol{E_{g,opt}}$ fails to take into account $\boldsymbol{E_B}$. Thus, for systems in which charged states are important, as in OLED host materials (Chapter 3), and in electrochromics (Chapter 5), different treatments are done.

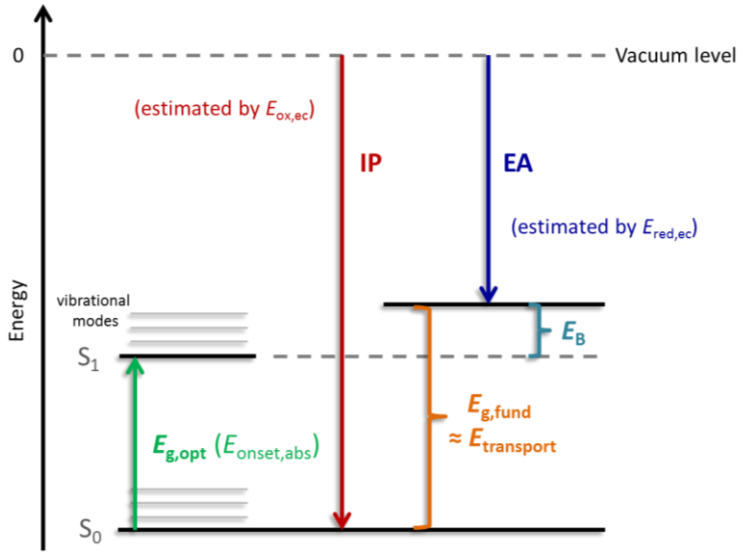

Figure 2.1. Schematic diagram of the different energy gaps probed in conjugated organic materials, and the experimental quantities used in this dissertation to approximate them (in parentheses). Brackets delineate quantities that are derived from two separate experiments. (Adapted from ref.[10])

For OLEDs (Chapter 3), charge injection, charge transfer, and energy transfer are the dominant processes occurring in the device. For charge injection, the relevant processes are the removal of an electron (to vacuum) from a neutral molecule, and the addition of an electron (from vacuum) to a neutral molecule. The energies associated with

these processes are IP, and EA, respectively. In this dissertation, these values are approximated from electrochemical techniques. As much as possible, values from film measurements are used, but the poor electrochemical stability of the films prevented reliable data from being obtained. Furthermore, reduction waves were not observed in electrochemical experiments, so that EA was approximated from the difference between IP and $\boldsymbol{E}_{\mathbf{g,opt}}$. However, the failure to account for $\boldsymbol{E}_{\mathbf{B}}$ is explicitly stated in the discussion.

It must also be noted that electrochemical methods involve counterions, arising from the electrolyte solution. The Coulombic interaction between the active material and these dopant ions, as well as the solvent medium, will also vary the energetic landscape, and is drastically different from the processes that occur in OLED devices. Unfortunately, the corrections necessary for a large array of forces are not fully understood. Thus, the reader should keep in mind the approximate nature of the electrochemically derived IP and EA values.

For electrochromics (Chapter 5), the application processes are closely related with the experimental techniques used to study the active materials, i.e. electrochemical switching. Thus, the measured oxidation ($E_{\mathrm{ox,ec}}$) and reduction ($E_{\mathrm{red,ec}}$) potentials are used to estimate the IP and EA, respectively. When the reduction potential cannot be experimentally obtained (due to limits of potential window of the electrolyte solution), the EA is again obtained from the difference between IP and $\boldsymbol{E}_{\mathbf{g,opt}}$. In this application, in which the active materials are studied in their neutral and oxidized states, the EA value is less relevant than the IP.

Finally, in regard to electrochemical methods, two types of voltammetric techniques are employed, cyclic voltammetry (CV) and differential pulse voltammetry

(DPV). The difference between the two techniques lies in how the potential is applied.[120] In CV, the voltage is linearly increased with time (sweep), whereas in DPV, the voltage is applied according to a square wave function (pulses). In DPV, the current is sampled twice during the experiment, which allows for the reduction of the contribution of the capacitive current (to charge the electrolytic double layer) to the measured current. Thus, whenever possible, DPV results are used to report $E_{ox,ec}$ and $E_{red,ec}$.

2.3.2. Electrochemistry and Doping Experiments

Solution and film electrochemical experiments were done on a EG&G Princeton Applied Research 273 A potentiostat/galvanostat using a three-electrode cell inside an Ar-filled glovebox with a 0.02 cm^2 platinum (Pt) button working electrode (for solution and Pt-button film experiments), a 1 × 1 cm^2 Pt mesh electrode (for solution OTTLE experiments), or a 7 × 50 × 0.7 mm^3 ITO-coated glass electrode (purchased from Delta Technologies, Ltd.; sheet resistance R_s 8-12 Ω sq^{-1}), a Pt wire counter electrode and a $Ag/AgNO_3$ reference electrode, at a scan rate of 50mV s^{-1}, unless otherwise indicated. All electrochemistry were done with 0.1 M (in CH_2Cl_2 solution) or 0.5 M (in acetonitrile or PC) tetrabutylammonium hexafluorophosphate ($TBAPF_6$) as the supporting electrolyte. The Ag/Ag^+ reference electrode was calibrated against a ferrocene/ferrocenium standard, the $E_{½,ox}$ for which is taken to be 5.1 eV below vacuum level. The reader is referred to the Cardona, *et al*.[118] for discussions regarding this value. Solution electrochemistry experiments were done at 1 *mM* concentrations of analyte, unless otherwise noted (e.g. for OTTLE experiments). Film experiments on Pt button were done on films drop-cast from 0.5 to 1 mg mL^{-1} chloroform (toluene for **DTPBP** in Chapter 3) solutions of the analyte. Polymer film experiments on ITO electrode were

done on films spray- cast from 50 mg mL^{-1} toluene solutions (or other solvent mixtures, as indicated) of the polymer, filtered through 0.45 μm PTFE syringe filters. Spray-casting was done using Anest Iwata airbrushes with nitrogen carrier gas at 25 psi. The airbrush was disassembled, and cleaned with copious amounts of toluene, and acetone, until all traces of color were removed. The ITO-coated glass electrodes were cleaned on both conducting and non-conducting sides by rinsing and wiping with isopropyl alcohol, acetonitrile, acetone, and toluene sequentially, and dried with a stream of nitrogen gas from the airbrush.

Optical absorption spectra were collected at room temperature using an Agilent Cary 5000 UV-vis-NIR spectrophotometer, using 10 mm path length quartz cells for solution chemical doping measurements, an OTTLE cuvette for electrochemical doping experiments, and an ITO slide for film experiments. A constant gentle flow of Ar was delivered to the spectrometer throughout all experiments.

2.3.2.1. Chemical Doping

All chemical doping experiments were performed in CH_2Cl_2 solutions. The solvent was obtained from a solvent purification system, degassed with at least three freeze-pump-thaw cycles, and stored in the glovebox in the dark. The solvent used was never more than a week old. Chemical oxidants used were $AgPF_6$, $NOBF_4$, and Mo(tfd-$CO_2Me)_3$.[121,122] Both chemicals are sensitive to light and moisture, and were thus dispensed exclusively in the glovebox and protected from light.

Solutions of the π-conjugated molecule were prepared at various known concentrations in CH_2Cl_2. The solid material was weighed in a tared vial outside the glovebox, and transferred to the glovebox (after degassing in the antechamber). Stock

solutions (1 to 3 μM) were prepared in the glovebox and stored under light protection. To dispense the chemical oxidant, a capped vial filled with Ar was weighed outside the glovebox, transferred to the glovebox, filled with a small amount of oxidant, capped, then transferred outside the glovebox under Ar for weighing. Then the vial was again transferred to the glovebox, and dissolved in the appropriate volume of solvent to obtain the concentrations on the order of mM. The oxidant and π-conjugated molecule solutions were then transferred to two separate amber vials, capped with rubber septa, sealed with thick layers of parafilm, and transferred outside of the glovebox. The vials were kept under a blanket of Ar and protected from light throughout the experiment.

A known volume of the molecule solution (2.00 mL) was transferred via syringe (previously rinsed with CH_2Cl_2 three to five times, and purged with Ar) to an Ar filled cuvette with a septum-lined screw-cap. The same volume of CH_2Cl_2 was transferred to two other cuvettes to serve as a reference solutions. While not inside the spectrophotometer, the vials were kept in the dark. The oxidant solution was then gradually titrated into the molecule solution and the reference solution, at 0.01 mL increments, with a syringe (rinsed and purged as previous). All syringes were kept plugged into a septum-capped vial full of Ar when not in use. Blank spectra were obtained with the pure solvent solution and the doped solvent (without the active molecule) for every titration point. Results were reported with the absorption values corrected for volume changes with titration.

As a side note, cuvettes that have been contaminated with the oxidants must be cleaned thoroughly as minute amounts of dopant can still react with fresh solutions. This was done by washing with water and detergent (provided by Spectrasil), and soaking the

cuvettes in the Spectrasil recommended solution overnight. Then the cuvettes were rinsed with copious amounts of deionized water, then isopropyl alcohol, acetonitrile, acetone, and dichloromethane, allowed to air dry, then purged with (a gentle stream of) Ar prior to use.

Electron Paramagnetic Resonance (EPR) spectroscopy was also performed on neutral and chemically doped solutions, with a Bruker X-Band instrument at room temperature, and 9.848 GHz, with the help of Dr. Robert Braga. EPR sample tubes (Wilmad 715-PQ-250M) were purged with Ar prior to use. Solutions of π-conjugated small molecules (1 *mM*) were doped with $AgPF_6$ in CH_2Cl_2. The volumes (~500 μL) were kept constant through each solution studied.

2.3.2.2. Electrochemical Doping on Optically Transparent Thin Layer Electrode (OTTLE)

In order to simultaneously observe the changes in optical transitions of a π-conjugated molecule during electrochemical switching in solution, an OTTLE was used. A discussion of this technique is provided in Bard and Faulkner.[120] The OTTLE is a Pt mesh working electrode (WE) that is fitted in a specially designed cuvette, with a Pt counter electrode (CE), and reference electrode (RE). The setup is depicted in Figure 2.2a. The optical path length of the cell is only slightly thicker than the mesh electrode, so that absorption spectrum taken is only of the electrochemically oxidized analyte within the mesh. It was observed, however, that there were limits to how close the reference and counter electrodes could be placed due to the confines of the optical path dimensions (Figure 2.2b). As will be discussed in section 5.4.2.2.1.2, these parameters from the setup gave rise to observable differences in electrochemical behavior, relative to the normal

electrochemical setup with a Pt button working electrode, coiled Pt wire counter electrode, and closely-placed $Ag/AgNO_3$ reference electrode.

The concentration of analyte in CH_2Cl_2 used for OTTLE experiments were between 30 to 150 μM. The solutions were prepared and transferred to the OTTLE cuvettes in the glovebox. The cuvettes were kept under an Ar blanket outside the glovebox. The caps were sealed with thick layers of Teflon tape, and the slot for the reference electrode was similarly sealed. It must be noted that these steps tended to move the electrodes, and so short circuits between the electrodes had to be carefully avoided.

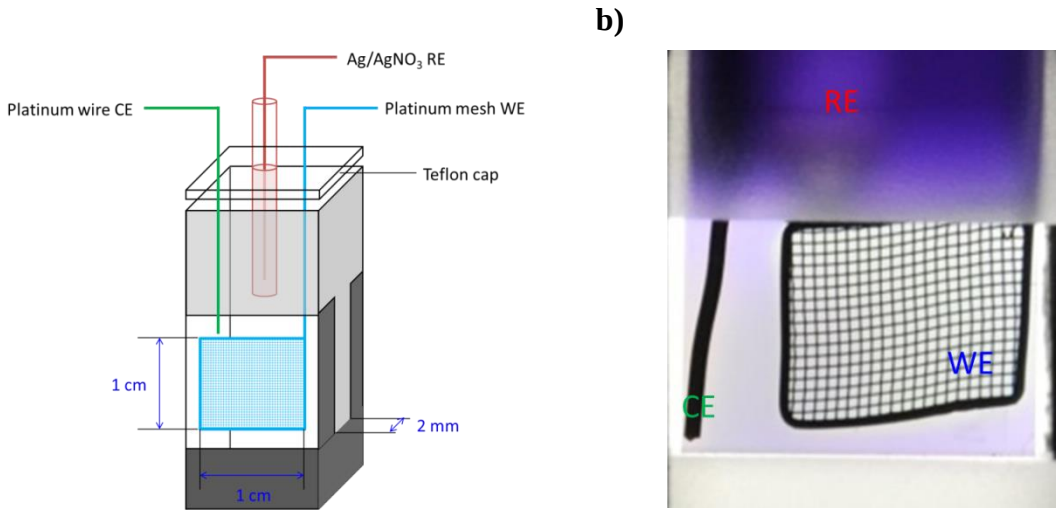

Figure 2.2. (a) Setup of an OTTLE cell and cuvette. (b) Photograph of the optical path, and actual relative positions of the electrodes.

The OTTLE cell was then placed inside the spectrometer and connected to the potentiostat, and kept from further exposure to ambient light until the experiment was completed. A reference cell filled with electrolyte solution was also used, and the relative positions of the electrodes in this cell were adjusted until a flat baseline could be achieved. It must be noted that slight differences between the reference and analyte cell setups gave rise to "jumps" in the spectra at the detector change-overs. Potentiostatic

experiments were then conducted, and optical spectra were obtained after the potential has been applied to the solution for 30 s, and 720 s (separate experiments).

2.3.2.3. Spectroelectrochemistry on Films

For polymer films, the study of changes in optical transitions upon electrochemical oxidation were done on films spray-cast on ITO coated glass substrates from 50 mg mL^{-1} toluene solutions (or other solvent mixtures, as indicated) of the polymer, filtered through 0.45 μm PTFE syringe filters. Spray-casting was done with an airbrush as described.

The electrochemical oxidation of the polymer films were conducted inside a quartz cuvette filled with 0.5 M $TBAPF_6$ and PC as the supporting electrolyte. A Pt wire served as the counter electrode, and $Ag/AgNO_3$ as the reference electrode. Static potential was applied to the polymer film at 50 mV steps, and the optical spectra were recorded after at least 30 s of voltage application.

2.3.3. Optical Spectroscopic Methods

Optical absorption spectra were collected at room temperature using an Agilent Cary 5000 UV-vis-NIR spectrophotometer, using 10 mm path length quartz cells for solution measurements, and 1 × 1 in^2 quartz or ITO substrates for film measurements. Spectrometer grade solvents were used at all times, and for solvatochromic experiments, were dried over molecular sieves when necessary. Film spectra for Chapter 3 were taken from spin-cast films of the analytes from 1 to 5 mg mL^{-1} solutions. Molar extinction coefficients in solution were obtained by performing a concentration dependent study, and determined from the slope of the regression line.

2.4. Thermal Characterization

Thermogravimetric analysis of 3 to 5 mg of molecules and polymers were performed on a Perkin Elmer Pyris 1 under nitrogen atmosphere (20 mL min^{-1} flow rate) at a heating rate of 10 °C min^{-1}, on a Pt pan from 50 °C to 500 °C. Decomposition temperatures ($\boldsymbol{T_d}$) are reported as the temperature at which 5 % of the initial sample weight is lost. Differential scanning calorimetry (DSC) was performed on a TA Q200 instrument under nitrogen atmosphere (50 mL min^{-1} flow rate), using 6 to 10 mg of sample. The sample was pulverized as finely as possible, and an even coating on the aluminum pan was obtained by tapping the bottom surface of the pan against a clean and padded surface. The heating/cooling rate was adjusted from 10 to 20 °C min^{-1} until a glass transition temperature was detected. Three cycles were done; the first is done to erase any thermal history of the sample, and only the second and/or third cycles are reported. All results, unless otherwise indicated, are reported from experiments done at 10 °C min^{-1}. First order transitions, such as melting ($\boldsymbol{T_m}$) and crystallization ($\boldsymbol{T_c}$) temperatures are reported as the temperature at the peak of the transition. Second order transitions, such as the glass transition temperature ($\boldsymbol{T_g}$), are reported by taking the peak temperature of the first derivative of the transition.

2.5. Film Morphology Characterization

Optical microscopy was done at room temperature with an Olympus BX51 Polarizing Microscope, under transmitted light. Polarized light microscopy was done with M-Plan Fluorite objectives (10X, 20X, 50X), and a U-PO3 polarizer. Images were captured with a QImaging MicroPublisher 5.0 RTV camera, and processed with the Linksys 32DV software. The colors visualized with the software were adjusted manually

until a similar color to that observed from the eyepiece was obtained (as perceived by the user). Polarized light microscopy was performed by setting the analyzer and polarizer perpendicular to each other, and orienting the long axis of the sample (when possible) 45° relative to either N-S or E-W directions with the rotatable stage. A U-P521 first order retardation plate (530 nm) was used to enhance contrast when high magnifications (low light) are used.

CHAPTER 3

TRIPHENYLENE-BASED DERIVATIVES AS HOSTS AND CHARGE TRANSPORT MATERIALS FOR ORGANIC LIGHT EMITTING DEVICES

3.1. Introduction to OLEDs

Electroluminescence, the phenomenon in which emission occurs from a material through which a current or voltage is passed, has been known to occur in certain organic materials since the 1950's.[123] In 1965, Helfrich and Schneider[124] reported blue fluorescence from extremely pure anthracene single crystals subjected to a current flowing through electrodes and anthracene-ion-containing electrolyte solutions. A linear relationship was established between the light intensity and the applied voltage (10 to 10,000 V), and the measured current with the same applied voltage, indicating that the luminous intensity depended on the number of charges injected. However, the voltages required to induce this emission from the organic materials (single crystalline acridine orange and anthracene) are notably high (on the order of 100 V); thus, no practical light output could be derived from these single crystalline materials. Using films of anthracene less than a micron thick, Vincett *et al.*[125] were able to reduce the required voltage for electroluminescence to 30 V. But the more significant development came in 1987 from C. W. Tang and S. A. VanSlyke when they substantially reduced these voltages with a change in device architecture.[126] Instead of a thin film of organic material sandwiched between two electrodes, they created a diode using a double layer of two organic materials between the anode and cathode, enabling each organic layer to transport only one type of charge carrier. Through this novel architecture, green electroluminescence

was obtained at a brightness of 1000 cd/m^2 with a voltage *below* 10 V, making practical devices attainable. Adachi and coworkers[127,128] further improved on this design by separating the charge transport layers from the emitter layer in a three-layer device. Nowadays, the OLED architecture is much more complex, making use of multilayer structures, as discussed in the succeeding section.

3.1.1. Device Architecture and Physics

The variability of device architectures, simple or complex, for OLEDs currently reported in the literature belies the general operating mechanism that is involved in all these devices: an externally applied electric field generates charges (holes and electrons) in metal electrodes, that are then injected into organic semiconductors interposed between them, are transported through these layers, recombine in an organic or metal-organic material, and emit light. A schematic of the architecture of a multilayer OLED device is shown in Figure 3.1a, and the relative energy levels of the component layers that allow the mechanism for emission to occur are shown in Figure 3.1b.[129]

When an electric field is applied across the cathode and the anode, electrons (e^-) and holes (h^+) are injected from the respective electrodes into the respective transport layers. Thin interfacial layers (HIL/EIL) may be applied to each electrode to improve contact between the metal electrodes and the organic layers deposited on them. This leads to improved film morphologies and energy level matching, thereby promoting charge injection. The charge injection process can be summarized as follows:[31] an electron is removed from the HOMO level of the organic material in contact with the anode (creating a hole in the organic material), whereas the cathode reduces the adhered organic material by adding an electron to its LUMO. The energy difference between the Fermi

a)

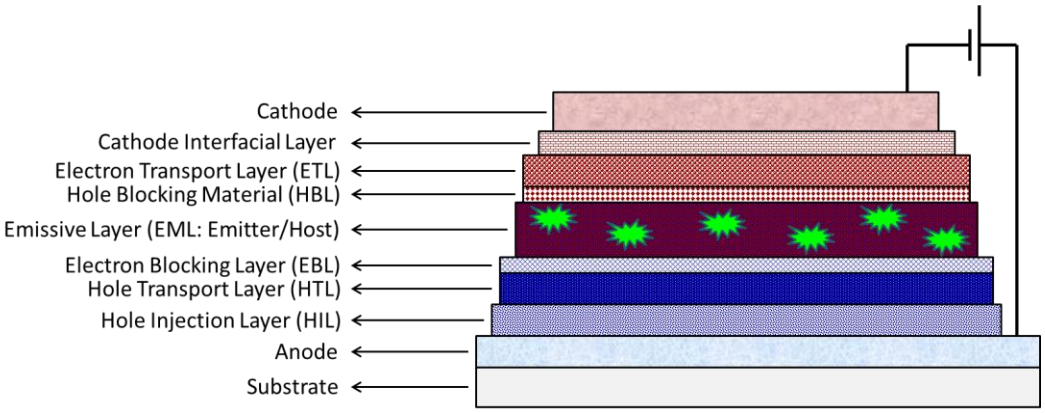

b)

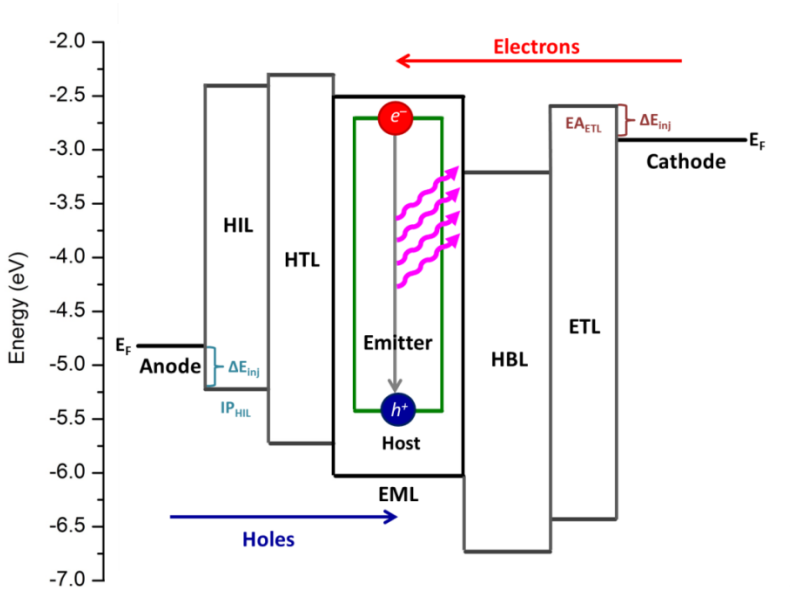

Figure 3.1. Schematic of a multilayer OLED device architecture (a), and its operating mechanism (b).

level (E_F) of each electrode and the IP (or EA) of the organic material in contact provides a measure of the energetic barrier (ΔE_{inj}) that must be surmounted to inject charge carriers into the organic semiconductor. The comparative energetic levels serve as a rough guide in choosing appropriate pairs of electrodes and organic interfacial and transport layers to incorporate in a device. The individual charge carriers injected into the organic layers then drift under the influence of the applied electric field through the transport layers (HTL/ETL) until they meet in the emissive/emitter layer (EML), where

they recombine to form excitons that eventually decay with a concomitant emission of light *via* fluorescence or phosphorescence.

The energetic alignments of the individual layers, the charge balance between holes and electrons, and the degree of confinement of excitons in the EML are crucial in determining the overall charge injection, and light emission efficiencies. The observed improvement in efficiency in multilayer devices, as opposed to single- or double- layer devices that has been discussed above, arises from the reduction in injection barriers provided by well-suited interfacial and transport layers, as well as the confinement of charge carriers in the emissive layer by the blocking layers. Thus, efficient OLED device operation depends on both material selection and architecture.

3.1.2. Device Characterization

The primary method of characterization of an OLED device is done by applying a fixed voltage on a device of a specific area, and measuring the current and light generated, giving a current density (J) – voltage (V) – luminance (L) plot, such as shown in Figure 3.2.[130,131] The current density, and not the current itself, is plotted to take the active area of the OLED device into consideration. A typical curve will consist of three discernible regions: the subthreshold, the turn-on, and the saturated regimes. Upon application of a low voltage, a small current is generated from charges that are injected, but exciton formation is limited, and no light emission occurs. This is the subthreshold regime (voltage < 2.7 V). As the voltage is increased, the turn-on regime (2.7 V < voltage < 3.6 V) is reached, in which there are sufficient charges injected into, and migrating through the device to form excitons that can radiatively decay, and generate light output. Here, a drastic increase in light emission occurs, and the current density shows a power

law dependence on the voltage. The turn-on voltage is identified as the voltage at which the transition from subthreshold to turn-on regimes occurs, and is normally taken as the voltage at which 1 cd m^{-2} of luminance is generated. At the turn-on regime, however, many of the injected charges occupy trap states. The saturation regime is reached when these traps are filled, and a steady-state current is observed.

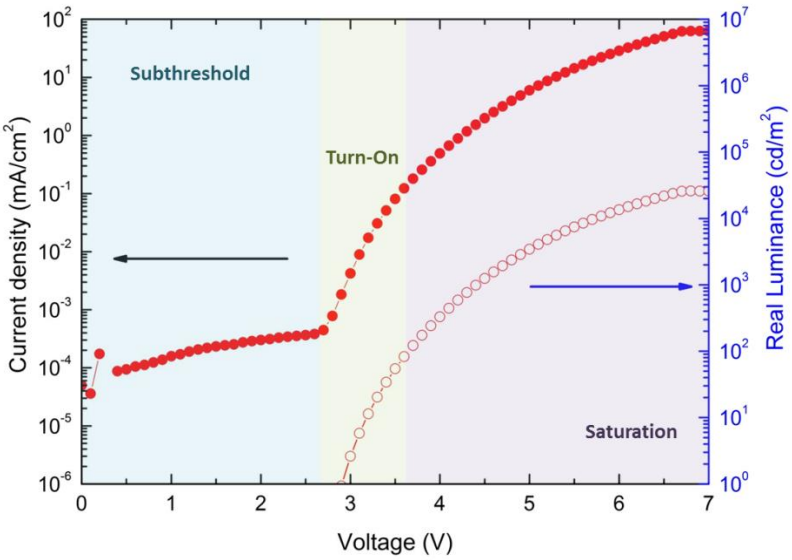

Figure 3.2. Current density – Voltage – Luminance plot of a typical OLED device.

The efficiency of an OLED device can be quantified through many parameters, such as the current or luminous (η_L), and luminous power (η_P) efficiencies, as well as the external quantum efficiency (η_{ext}).[131-133] The current or luminous efficiency is formally defined as:

$$\boldsymbol{\eta_L = \frac{AL}{I}} \tag{3.1}$$

where A is the device active area (in m^2), L is the luminance (in cd m^{-2}, or [nits]), and I is the OLED current (in A). η_L is determined from the ratio of the luminance over the

current density, and is readily obtained from the *J*−*V*−*L* plot. It has units of candelas per amp (cd A^{-1}). The luminous power efficiency or luminosity is defined as:

$$\boldsymbol{\eta_P = \frac{L_P}{IV}} \tag{3.2}$$

where L_P is the luminous power given in lumens (lm), and *IV* is the electrical power required to drive the device at a particular voltage V, and has units of watts (W). Thus, η_P has units of lm W^{-1}. It gives a measure of the light output per unit electrical input. Finally, the external quantum efficiency (EQE) is given by the ratio of the number photons emitted (N_ϕ) to the number of electrons injected (N_e):

$$\boldsymbol{EQE = \eta_{ext} = \frac{N_\phi}{N_e}} \tag{3.3}$$

and, thus, gives a measure how well the device converts the current generated into light. The optical characteristics of an OLED device are also important parameters in determining its potential for application.[134] In this respect, the emission spectra and chromaticity (standardized by the Commission International de l'Eclairage (CIE)) of the OLED device are also determined. Finally, the long-term stability of devices are also characterized based on brightness decay over time.[131]

3.2. Organic Materials for OLEDs

The main electrode materials used in OLEDs remain inorganic, with indium tin oxide (ITO) serving as the dominant anode material, and low work function metals such as lithium, calcium, and magnesium serving as cathode materials.[129] All the other layers sandwiched between them can be made entirely out of organic π-conjugated materials. Organic materials can be easily tailored with appropriate functional groups and structural elements to confer desired properties such as charge injecting, charge transporting, and

emitting character, and can, thus, perform the different functions required from the interposed layers.

3.2.1. Charge Transport Materials

Charge transport in disordered organic materials occurs through a hopping mechanism due to the inherent disorder in amorphous organic materials. This disorder creates localized states, precluding a coherent motion that leads to band-like transport.[135] The most common measure of charge transport characteristics in organic materials is the carrier mobility, μ, which under an applied electric field, E, is given by:

$$\boldsymbol{\mu = \frac{v}{E} = \frac{eD}{k_B T}} \tag{3.4}$$

where v is the charge velocity, e is the electron charge, D is the diffusion coefficient, k_B is Boltzmann's constant, and T is the temperature.[33] The unit for μ is usually given as $cm^2 V^{-1} s^{-1}$ (from the first relation in eq. 3.4), and is field-dependent. The total carrier mobility has two contributions arising from tunneling and hopping, with the former dominating at low temperature, and the latter at high temperature. Only the hopping contribution is considered for operating OLED devices, which occurs at elevated temperatures. The hopping mobility is related to the diffusion coefficient by the rate of electron transfer, k_{ET}, by the equation:

$$\boldsymbol{D = a^2 k_{ET}} \tag{3.5}$$

where a denotes the intermolecular spacing.

The effect of the rate of electron-transfer can be understood by considering the transport mechanism as a process in which the charged species undergoes a series of

sequential incoherent redox interactions with adjacent neutral molecules,[31,33,136-138] as illustrated by the following equations:

$$M_a + M_b^+ \rightarrow M_a^+ + M_b \quad (3.6)$$

$$M_a + M_b^- \rightarrow M_a^- + M_b \quad (3.7)$$

These self-exchange charge transfer reactions dominate the charge transport mechanism in organic materials due to their inherent strong electron-phonon coupling that localizes the charge carriers in a single geometric distortion.[21] This same description also applies to the energy transfer process involved in creating excited states in phosphorescent OLEDs (*vide infra*).[139] Being a thermally-activated process, the rate of electron transfer (k_{ET}) follows an Arrhenius type relationship provided by Marcus theory:[140]

$$\boldsymbol{k_{ET} = \frac{4\pi^2}{h}\, t^2 \sqrt{\frac{1}{4\pi\lambda k_B T}} \exp\left[\frac{-(\Delta G^o + \lambda)^2}{4\lambda k_B T}\right]} \quad (3.8)$$

Here, h is Planck's constant, $\Delta G°$ is the Gibbs free energy of the exchange reaction, t is the transfer integral, and λ is the reorganization energy. Two quantities from this equation can be identified that guide material selection for charge transport: (1) λ gives the effect of the difference in equilibrium geometry between charged and neutral states, with a smaller difference favoring faster transfer rates; and (2) t gives the effect of the electronic coupling between HOMO (LUMO) wavefunctions in adjacent molecules for hole (electron) transport, with stronger coupling leading to higher rates. Thus, the key structural parameters to consider are the electron delocalization, intermolecular orbital overlap, and the geometric distortion upon excitation and ionization.

A dominant structural factor influencing charge mobility is the molecular packing, as can be illustrated with the following observations: (1) single crystalline materials have mobility values several orders of magnitude higher than their polycrystalline counterparts;[141] (2) charge carrier mobilities of single crystalline materials are anisotropic, with variations in values measured from different crystallographic directions.[142,143] This effect of molecular packing on mobility can be traced back to its influence on the transfer integral.[33] A maximum wavefunction overlap can be envisioned for a packing motif in which the π-systems are cofacially stacked, and have the smallest distance possible. As the distance between the π-systems, and the displacement from cofacial geometry increase, the transfer integral will decrease, leading to lower mobilities. Of course the cofacial configuration also leads to the highest repulsion. Given these observations, it is easy to understand why organic materials with high mobilities (oligoacenes,[143] discotic polyaromatic hydrocarbons,[144] fullerenes[145]) tend to have rigid, π-extended structures.

The following sections cover a survey of popular transport materials. Mobilities are qualitatively compared across families of structurally related molecules, but it must be noted that absolute comparisons are usually precluded by different experimental methods and device architectures used to determine these values.

3.2.1.1. Hole Transport Materials

As Figure 3.1b shows, the hole transport layer serves to conduct positive charge carriers from the anode to the emissive layer (EML). Thus, hole transport materials (HTMs) must have low IPs, ideally isoenergetic with the work function of the anode or the hole injection layer (HIL) that it is in contact with, such that the injection barrier is

low. If there is no separate electron blocking layer (EBL), the HTM must also have a lower EA than that of the EML to prevent electrons from escaping the EML. Since they provide a pathway for holes to the EML, their radical cations must also be stable, and have high hole mobilities. Aside from these electronic properties, they should also have high purity to reduce traps, and form thermally stable thin films with good morphology (high glass transition temperatures, T_g).

Some common HTMs are given in Table 3.1, along with some of their important properties. Triarylamines, and carbazoles are common structural moieties due to the electron-donating properties of amines, and the easy oxidizability that the nitrogen lone pair provides. The radical cations of these materials are also stable due to delocalization from the phenyl rings. Modifications by annelation, and spiro derivatives give rise to improved thermal properties (e.g. spiro-TAD).

Table 3.1. Some common HTMs and their pertinent properties.[129,146-151]

Hole Transport Material	IP (HOMO) (eV)	EA (LUMO) (eV)	μ_h[a] (cm^2/Vs)	T_g (°C)
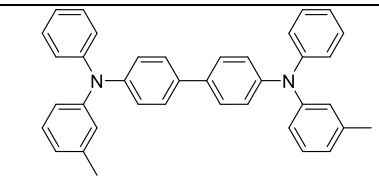 TPD	−5.50	−2.30	1.0×10^{-3}	65
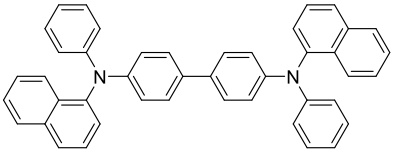 NPB	−5.70	−2.60	8.8×10^{-4}	95
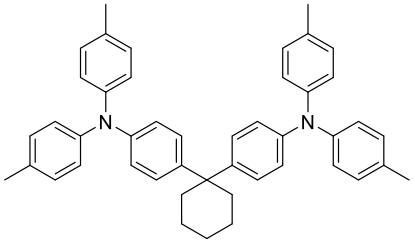 TAPC	−5.60	−2.0	1.0×10^{-3}	78

Table 3.1. continued

Hole Transport Material	IP (HOMO) (eV)	EA (LUMO) (eV)	μ_h [a] (cm^2/Vs)	T_g (°C)
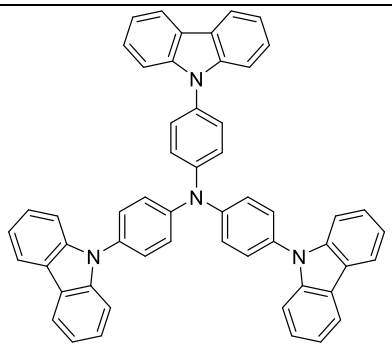 TCTA	−5.70	−2.4	2.0×10^{-5}	151
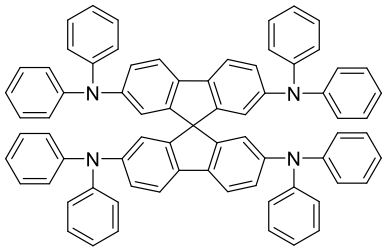 Spiro-TAD	*b*	*b*	1.6×10^{-2}	133

[a] At electric fields of ~ 10^5 V/cm for most of these. [b] Assumed to be nearly equivalent to TPD.

3.2.1.2. Electron Transport Materials

The ETL performs a converse function to that of the HTL. It serves to receive and transport electrons from the cathode. Its EA must be close to the work function of the cathode, and the EA of the EML to reduce the charge injection barrier. Conversely, its IP must be sufficiently high to help confine holes in the EML (especially if it also serves the purpose of an HBL). It should have reasonable electron mobilities, and have a stable radical anion. Similarly, it must have high thermal stabilities, and good film morphologies for its thin films. Some common ETMs are shown in Table 3.2. Electron-withdrawing groups such as oxadiazole, imine, and cyano groups are a common motif. Of these, TPBi is one of the most commonly used.[129] Metal chelated compounds, such as Alq_3,[126] are also common, but are not covered here.

Table 3.2. Some common ETMs and their pertinent properties.[129,146-152]

Electron Transport Material	IP (HOMO) (eV)	EA (LUMO) (eV)	μ_e[a] (cm^2/Vs)	T_g (°C)
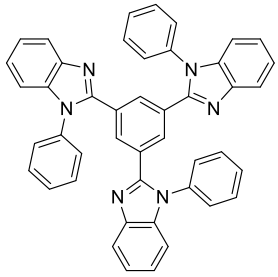 TPBi	−6.2 to −6.7	−2.7	10^{-6} to 10^{-5}	124
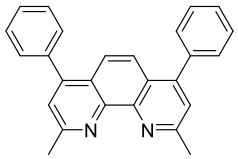 BCP	−6.7	−3.2	7×10^{-6}	83
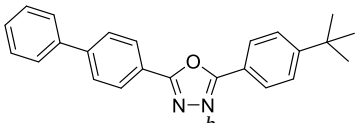 PBD[b]	−6.2	−2.4	2×10^{-5}	60
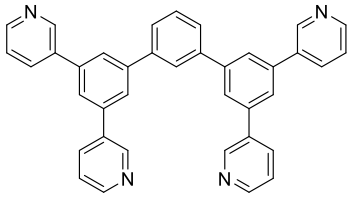 BmPyPB	−6.2	−2.6	1×10^{-4}	106

[a] At electric fields of ~ 10^5 V/cm. [b] At electric fields of ~ 10^6 V/cm

3.2.2. Emissive Layer Materials

While OLED light emitting materials can either be fluorescent or phosphorescent emitters, the former tend to deliver lower emission efficiencies due to the limitations of spin statistics.[6] In the latter, metal complexes are used to harvest both singlet and triplet excited states, leading to theoretical internal quantum efficiencies (IQE) of 100 %. The use of phosphorescent emitters was demonstrated in the work of Baldo *et al*. in 1999,[153] in which the green emitting *fac*-tris(2-phenylpyridine) iridium [$Ir(ppy)_3$] metal organic complex resulted in devices demonstrating high external quantum efficiencies (EQE) of

8.0 %. In 2001,[154] IQEs approaching 100 % were achieved, resulting in EQEs near 20 %, from an iridium-based emitter that showed near quantitative phosphorescence efficiency. Because the excited-state lifetimes in phosphorescent emitters are long (10^{-6} s), they are susceptible to bimolecular quenching by triplet-triplet annihilation at high concentration.[150,155,156] To mitigate these phenomena, these phosphorescent emitters are dispersed into a host material.

The emission process in phosphorescent guest-host systems can be outlined by the following steps (Figure 3.3):[129,139,147] (1) holes and electrons are injected from the corresponding transport layers into the host material to create singlet (S_1) or triplet (T_1 *via* intersystem crossing (ISC)) excitons; (2) the excited states can either decay radiatively from the host (orange arrow, undesired), or undergo a charge or energy transfer process to the guest (desired; Förster (black electrons, singlet) or Dexter (black electron – singlet; gray electron – triplet)) energy transfer to create singlet or triplet excited states in the guest molecule, and return the host to its ground state; (3) the triplet excited state in the guest molecule undergoes recombination and radiative decay (green arrow) leading to light emission. When there is an appreciable offset between the frontier energy levels of the host and guest, the charge carriers can also be directly trapped in the guest from the electrodes, leading to direct creation of excited states in the guest emitter.[139,147,151]

The rates of the energy transfer processes that are involved in the host-guest interaction, especially the Dexter process, can be described by Marcus theory (eq. 3.8). Thus, the activation energy for the transfer of excited states between host and guest is related to: (1) the reorganization energies (λ), or changes in molecular geometry in going from ground to triplet excited states, and *vice versa*, with rigid molecules having smaller

λ; and (2) the driving force (Δ*G*°), or the energetic offset between IP and EA energies of the host and guest.

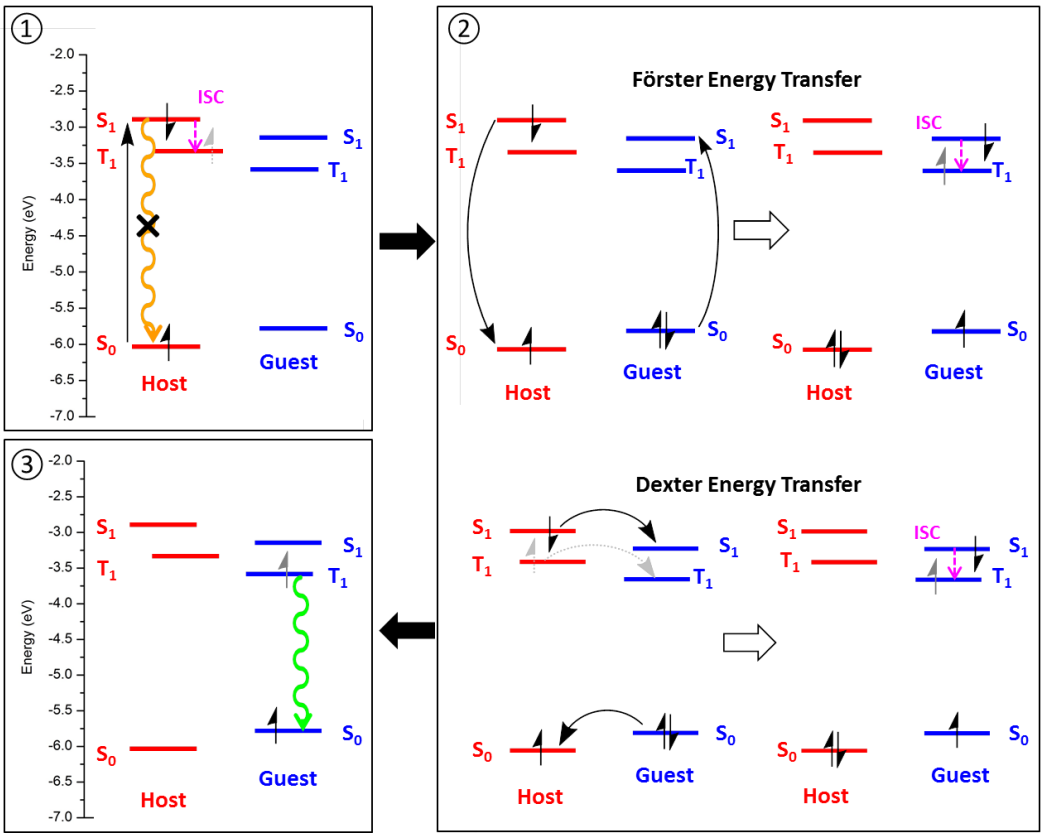

Figure 3.3. The emission process in a host-guest system (steps 1-3), involving desired energy transfer processes for emission to occur solely from the guest.

Other energetic considerations that must be met in order for the host-guest energy transfer process to be efficient are:[129,147,150,157,158] (1) the host should have a wide enough IP-EA gap (transport gap) so that holes and electrons are favorably transported to, and exclusively recombine in the guest emitter, and for the material to remain transparent; (2) the host should have a triplet energy ($\boldsymbol{E}_{\mathbf{T}}$) larger than that of the guest emitter so that triplet excitons of the guest cannot undergo back energy transfer, and be quenched by the host. The IP and EA of the host must also be well-aligned with the corresponding energies of the transport layers to reduce charge injection barriers. The energy gap cannot

be too large to maintain a small driving voltage for the device. These requirements mean that the singlet-triplet splitting (exchange energy) ΔE_{ST}, should also be as small as possible.

Aside from these energetic requirements, the host material should be able to conduct both holes and electrons (i.e. capable of ambipolar charge transport) so that charge balance in the emitting layer is met, and emission is confined in the guest (to generate better color purity). This can be mediated by the use of charge blocking layers.[159] Host materials should also have good thermal properties, with amorphous character and high glass transition temperatures to form stable film morphologies past the device annealing temperature (> 100 °C), and to enhance device lifetimes. Finally, the guest should be phase compatible with the host to maintain homogeneity across the emitter layer.

3.2.2.1. Host Materials

With all the requirements outlined in the previous section, it is readily apparent that the design of host materials necessitates a rigorous balancing act of interconnected material properties. The requisite wide energy gap tends to create mismatched energy levels with transport layers and electrode work functions, and demands a large driving voltage. The desired high triplet energy implies a high singlet energy, leading to pronounced barriers for electron injection from many cathodes. The condition of ambipolar transport suggests incorporation of both electron-donating and electron-withdrawing groups without activating a donor-acceptor interaction that can significantly reduce the energy gap. The need for stable amorphous films entails suppression of crystallinity, yet the latter is a prevalent characteristic of high mobility materials.

In order to integrate as many of the desired properties as possible in one host material, a "lego" approach can be implemented, with key functionalities and structural moieties expected to confer these properties assembled in one small molecule (Figure 3.4). Electron-donating heterocycles (D), such as carbazoles, and arylamines, enable hole transporting ability.[147,150,160] Electron-accepting moieties (A), such as *N*-heterocyclic arenes (pyridine, triazine), phosphine oxide groups, and oxadiazoles, imbue the host with electron transporting character.[150,160] These are coupled together so that ambipolar charge transport character can be obtained, but the conjugation between these two moieties must be interrupted to suppress the donor-acceptor intramolecular charge transfer that leads to lower energy gap and triplet energy.[147,160] This can be induced through the introduction of steric torsion (θ), *meta*-linkages (*m*), or non-sp^2-hybridized groups (σ), such as silicon, phosphine oxide, or aliphatic linkages.[147] The desired thermal properties are then obtained with appropriate rigid, and bulky groups, and spiro-linkages.

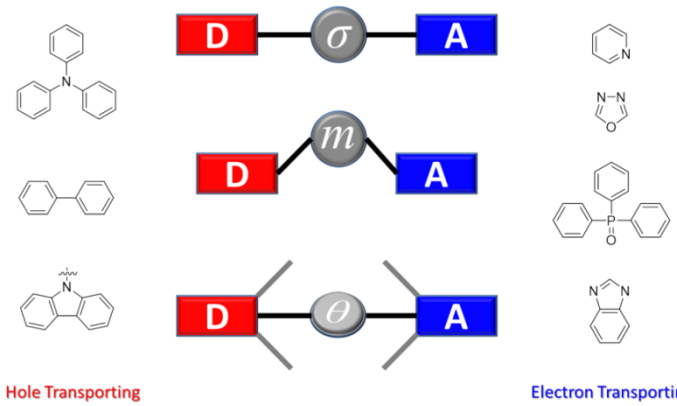

Figure 3.4. The typical donor and acceptor heterocycles used in OLED host materials and the structural linkages used to suppress their intramolecular charge transfer interaction.

Table 3.3 shows some typical host materials and their properties. Carbazoles and biphenyl moieties are ubiquitous because of their high triplet energies (>2.6 eV).[161] The

lego approach has been successfully applied in CBP derivatives, as shown in entries 1-3. CBP has extended conjugation from a biphenyl moiety that is *para*-linked to carbazole groups, which results in a moderate to high energy gap and triplet energy, but not sufficiently high for blue emitters. Changing the linking group to a single phenyl group with a *meta*-orientation in mCP significantly raises the EA and triplet energies. Both host materials only have moderate glass transition temperatures. SimCP, which incorporates the tetraphenylsilane moiety from UGH2, provides significant bulkiness with aryl rings, and the silicon linkage prevents extension of π-conjugation that would otherwise detrimentally reduce the triplet energy and energy gap. Entries 5 and 6 show two examples of ambipolar charge transporting hosts (similar hole and electron mobilities), obtained from incorporating both electron-donating (hole transporting) and electron-withdrawing (electron transporting) moieties coupled through non-conjugated pathways.

Table 3.3. Some common host materials and their pertinent properties.[129,146-152,162]

Host Material	IP (eV)	EA (eV)	E_T (eV)	μ_h[a] (10^{-5} cm^2/Vs)	μ_e[a] (10^{-5} cm^2/Vs)	T_g (°C)
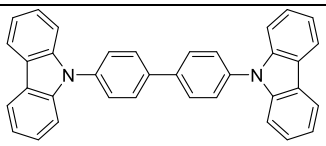 CBP	−6.3	−3.0	2.67			62
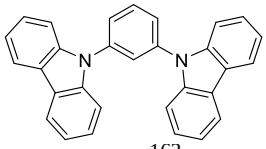 mCP[163]	−6.15	−2.4	3.0	12	3.4	55
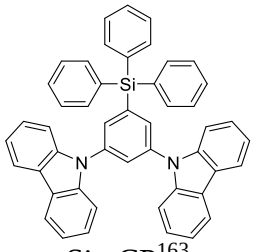 SimCP[163]	−6.12	−2.56	3.0	24	13	101

Table 3.3 continued

Host Material	IP (eV)	EA (eV)	E_T (eV)	μ_h [a] (10^{-5} cm^2/Vs)	μ_e [a] (10^{-5} cm^2/Vs)	T_g (°C)
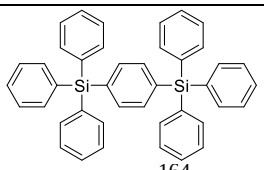 UGH2[164]	−7.2	−2.8	3.5			345[b]
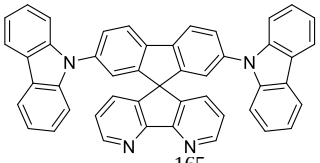 CSC[165]	−5.63	−2.36	3.27	0.41	0.5	179
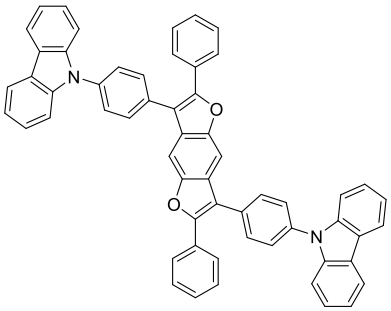 CZBDF[166]	−5.52	−2.20	3.32	370	440	162

[a] At electric fields of ~ 10^5 V/cm. [b] Melting point.

3.3. Triphenylene-Based Host Materials

Triphenylene has a planar 18-π-electron structure that is composed of four benzene rings fused into a rigid and highly symmetric D_{3h} point group. This planar delocalized structure allows for strong intermolecular electronic overlap, or π-π stacking interactions (appreciable transfer integral), and the rigid fused polycyclic system prevents appreciable deformation upon charge injection (small reorganization energy).[158,167-170] These structural characteristics give triphenylene the ability to self-assemble into ordered stacks of aromatic rings, where the discotic shape of triphenylene, when combined with appropriate substituents, leads to mesogenic character. This self-assembly has been exploited in its derivatives to form columnar mesophases, and has been explored for unidirectional charge transport.[84,144,170-173] Symmetric derivatives have shown both

electron and hole mobilities that can vary over three or more decades, depending on the liquid crystalline phase, reaching values on the order of 10^{-1} cm^2 V^{-1} s^{-1}.[174,175]

Triphenylene also has a high triplet energy at ~2.9 eV.[176,177] The fused polyaromatic structure of triphenylene also gives it high thermal and chemical stability.[178] These optoelectronic properties make the triphenylene core a promising moiety to explore for OLED host materials. Indeed, it has recently been coupled to electron-donating,[158,179,180] and electron-withdrawing[168] heterocycles, and studied as host materials for red, green, and blue emitters. High gap materials were obtained, with triplet energies ranging from 2.3 to 2.7 eV. High glass transition temperatures (T_g > 100 °C) were obtained in some derivatives, whereas others show high melting temperatures, with no T_g observed. Transport characteristics as studied from electron-only and hole-only devices are tuned by the nature of the substituents, with some ambipolar characteristics obtained for a bis-dibenzothiophene derivative,[179] and an mCP-based[180] derivative.

3.3.1. Design and Synthesis of Triphenylene-Based Hosts

A vacuum-processed triphenylene-based host material was recently reported in a patent by Adamovich, *et al.*[181] to give long lifetime devices in a graduated architecture. To understand the promising results observed in these devices, the same host material was synthesized here for a thorough characterization of its optoelectronic, thermal and film forming properties, and its performance in OLEDs. Two derivatives with solubilizing alkyl chains were also synthesized, and characterized in solution-processed devices. The structures of the materials are shown in Chart 3.1. In these materials, the triphenylene cores provide the rigid π-system for both hole and electron transport, and the conjugation between the two is broken by the *meta*-linkage provided by the biphenyl

moiety. Thus, wide band gap materials, with high triplet energies, and favorable transport characteristics are expected. The bulky aromatic framework is predicted to yield high glass transition temperatures. The effect of the alkyl chains in the two soluble derivatives on the intermolecular π-system interactions, and thereby the solid-state optoelectronic properties, as well as the thermal and film-forming properties are also examined.

Chart 3.1.

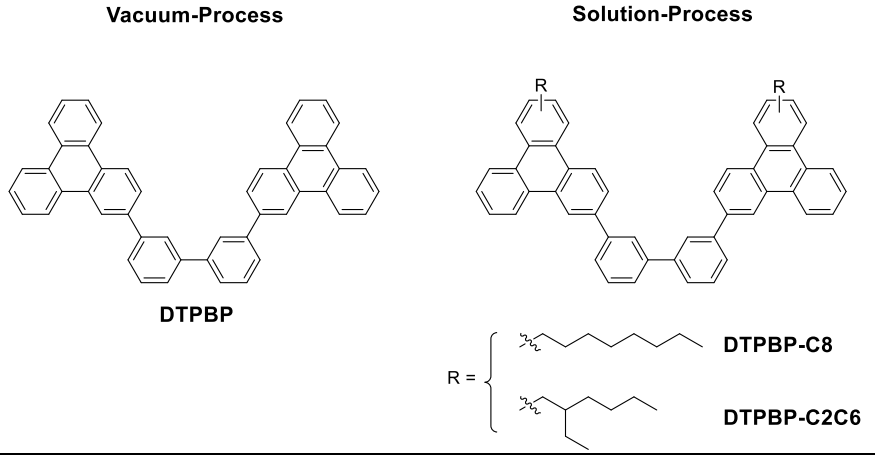

The syntheses of these materials are outlined in Schemes 3.1, and 3.2. The biphenyl moiety (**3.1**) is constructed from 1,3-dibromobenzene from an Ullman-type coupling using a Lipshutz cuprate generated from the lithiated species, and CuCN.[182] Alkylation of triphenylene (**3.4a** and **3.4b**) was achieved through a Friedel-Crafts acylation, followed by a Wolff-Kishner reduction with hydrazine. Steric and electronic factors coincide to regio-specifically alkylate the triphenylene core only at its 2-position. The deactivation of the aromatic ring to further acylation induced by the electron-withdrawing carbonyl group ensures mono-alkylation of the triphenylene ring at near-quantitative yields. The final step is a Suzuki coupling utilizing an electron-rich and highly-hindered ligand to allow the moderately sterically cumbersome coupling to occur

in excellent yields (see section 4.5.1 for a thorough discussion). The borylation step is discussed in greater detail in the succeeding section.

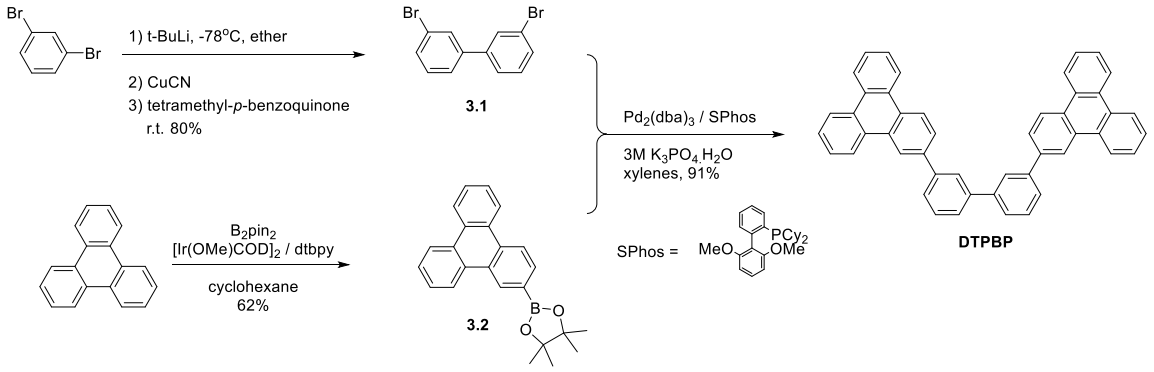

Scheme 3.1. Synthesis of **DTPBP**.

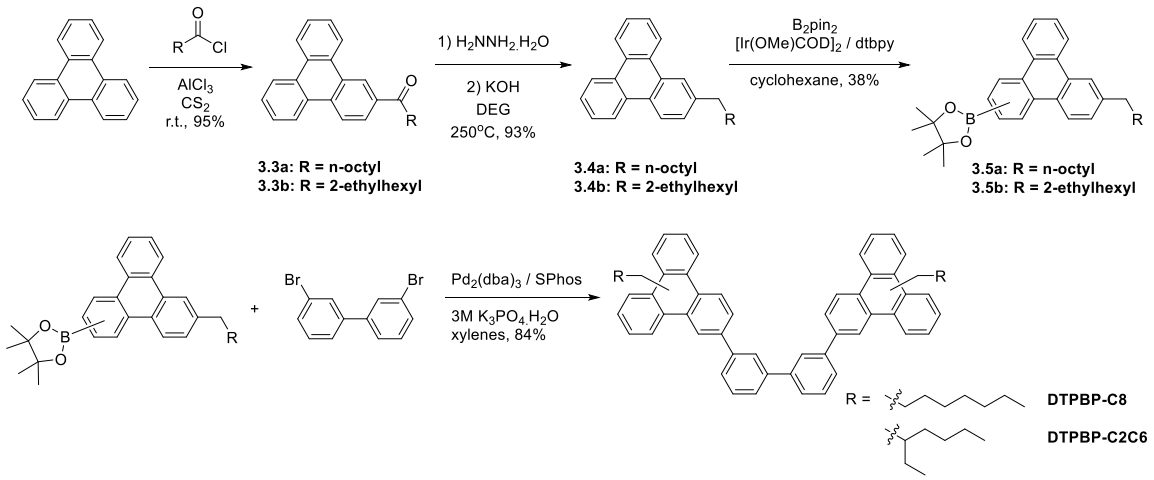

Scheme 3.2. Synthesis of alkylated derivatives **DTPBP-C8** and **DTPBP-C2C6**.

3.3.1.1. Regio-specific Iridium-Catalyzed Borylation of Triphenylene

The synthesis of derivatives of triphenylene, especially unsymmetrical ones, usually requires the construction of the polycyclic ring system from smaller rings such as phenyl, biphenyl, terphenyl, naphthyl, and phenanthryl rings.[183-186] These methods become tedious and costly if structures of higher complexity such as oligomeric or polymeric structures are to be obtained with triphenylene as a building block.

In the last decade, significant progress has been made on the direct borylation of polycyclic aromatic hydrocarbons (PAHs) using an iridium-catalyzed C-H activation approach.[109] With careful selection of the catalytic system and accompanying ligands, regio-specific borylation of PAHs has been accomplished in moderate to high yields. For the active catalyst prepared from the reaction of $[Ir(OMe)(COD)]_2$ (COD = 1,5-cyclooctadiene) and 4,4'-di-*tert*-butyl-2,2'-bipyridine (dtbpy) *in situ*, regiospecificity is predominantly dictated by steric factors, avoiding borylation at positions adjacent to ring junction carbons.[109,187,188] This regiospecificity has been attributed to the sterically crowded five-coordinate species $[Ir(dtbpy)(Bpin)_3]$ (pin = $OCMe_2CMe_2O$) that undergoes the key C-H activation step.

In triphenylene, with its D_{3h} symmetry, only two unique positions are available for mono-functionalization. Of these two positions, the 2 (3, 6, 7, 10, or 11) -position is less-sterically hindered, and also more electron rich.[189] Thus, the direct borylation of this position using the sterically-directing Ir-based catalyst system was pursued to construct the **DTPBP**-based host materials. The reaction leads to a mixture of the starting material, mono-, and di-borylated products, as observed from thin layer chromatography, and NMR spectroscopy. The conversion yield of the desired mono-borylated species was optimized by careful control of the stoichiometry of the reaction, with 1.1 equivalents of the boron source giving the highest conversion. Fewer equivalents of the boron source did not give rise to an improvement of the conversion to the mono-borylated species over the di-borylated species.

To improve the recovery of the product *via* column chromatography, the silica gel used was saturated with boric acid prior to use. The boric acid method allows greater

recovery of the product by preventing retention (without degradation) of the boronic ester on silica gel.[190] The desired mono-borylated (**3.2**) product was obtained at a yield of 62 %, which is similar to those obtained with other PAHs such as naphthalene and perylene.[191]

NMR spectroscopy (^{1}H, ^{13}C, ^{11}B) and high resolution mass spectrometry confirmed the successful mono-borylation of triphenylene. As expected from the sterically crowded nature of the catalytic system, ^{1}H-NMR spectroscopy of the pure product showed borylation occurring only at the 2-position, as determined from the splitting pattern of the aromatic protons. The regiochemistry was further substantiated with two-dimensional techniques (COSY, HSQC, HMBC), as well as 1D-NOESY ^{1}H-, and DEPT-135 ^{13}C-NMR spectroscopy, allowing all protons, and protonated carbons to be structurally assigned. The correlations obtained from these NMR analyses are summarized in Table 3.4.

The same borylation conditions applied to the alkylated triphenylene derivatives **3.3a** and **3.3b** did not yield regiospecific mono-boronic esters. The regiospecific alkylation of triphenylene breaks the original D_{3h} symmetry (Figure 3.5a), and creates 11 unique sites for the succeeding borylation reaction. Only four of these are sterically accessible, and have higher electron density (Figure 3.5b). These isomers are inseparable, and the final product yields a mixture of regio-isomers, as observed by ^{1}H-NMR (Figure 3.5c). Their distribution is reflected in the Bpin CH_3 proton peak, which gives three resonances, with an integration ratio of 1:1:2. The overlap of the resonance for two isomers can be understood from the structural similarity in these two isomers (Figure 3.5b, boxed). Because **3.5a** and **3.5b** are a mixture of isomers, the resulting alkylated

derivatives **DTPBP-C8** and **DTPBP-C2C6** are also a mixture of isomers, with the same **DTPBP** core (Chart 3.2).

Table 3.4. Results of 1D- and 2D-NMR analyses of **3.2**.

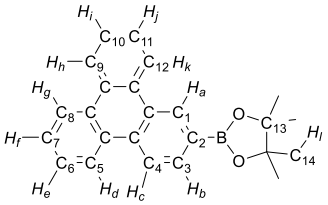

^{13}C δ (ppm)	DEPT	^{1}H δ (ppm)	mult.	*J* (Hz)	NOESY	COSY	HSQC Correlations	HMBC
25.12	CH_3	1.45	s				$H_l \rightarrow C_{14}$	
84.16	Q							
122.57	CH	8.66	m				$H_{c,g,h} \rightarrow C_{4,8,9}$	$H_b \rightarrow C_4$
123.29	CH	8.66	m					$H_{f,i} \rightarrow C_{8,9}$
123.41	CH	8.66	m					
123.83	CH (2)	8.71, 8.84	m			1 → 3,4	$H_{d,k} \rightarrow C_{5,12}$	$H_{e,j} \rightarrow C_{5,12}$
127.29	CH (2)		m			5,8 → 6,7	$H_{e,f,i,j} \rightarrow C_{6,7,10,11}$	$H_{h,k} \rightarrow C_{10,11}$
127.33	CH	7.67						$H_g \rightarrow C_7$
127.75	CH				1→12			$H_d \rightarrow C_6$
129.12	Q					9,12 → 10,11		
129.77	Q							$H_{a,c,d,g,h,k} \rightarrow Q_C$
129.79	Q							
130.03	Q					3 → 4		
130.43	Q							
130.67	CH	9.17	s				$H_a \rightarrow C_1$	$H_b \rightarrow C_1$
132.15	Q							$H_{a,b,c} \rightarrow Q_C$
132.92	CH	8.08	d	1.23, 8.18			$H_b \rightarrow C_3$	$H_a \rightarrow C_3$

Chart 3.2. Isomers of DTPBP-C8 and DTPBP-C2C6

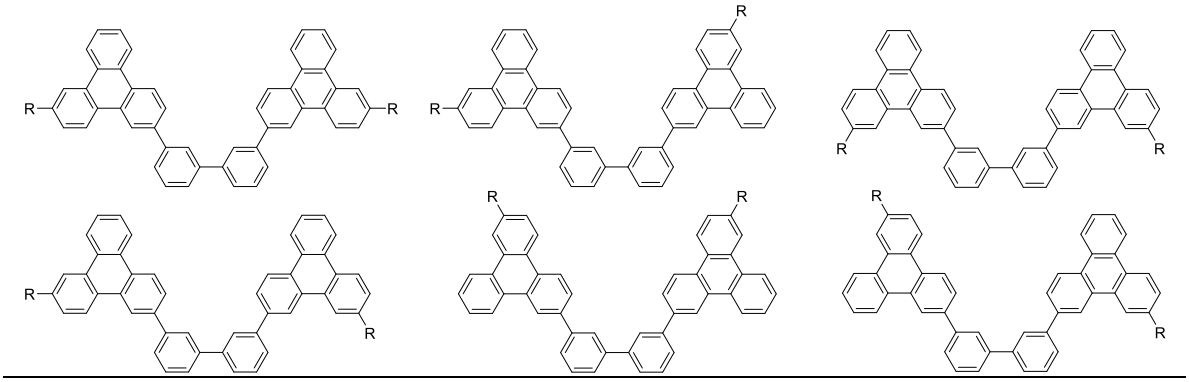

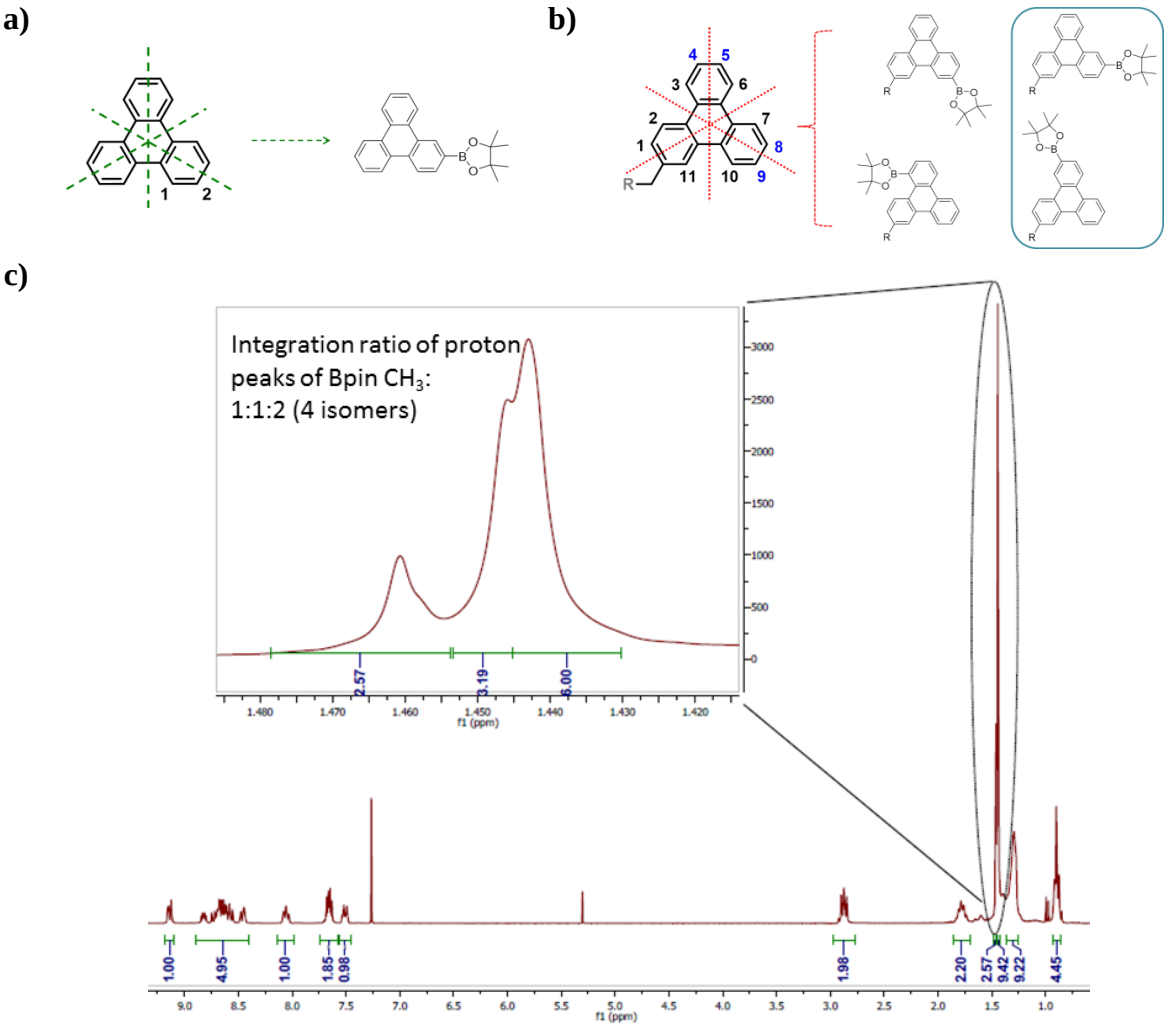

Figure 3.5. (a) The D_{3h} symmetry of triphenylene, leading to two unique sites and the regiospecific borylation in the sterically and electronically favored 2-position; (b) The broken symmetry of the alkylated derivative, leading to four unique sites, and four distinct isomers; and (c) The ^{1}H-NMR spectra of an alkylated triphenylene boronic ester showing the isomeric mixture from the Bpin CH_3 ^{1}H resonance.

3.3.2. Optoelectronic Characteristics of Triphenylene-Based Hosts

The structure of the host materials studied are based on two fused-benzene-ring systems connected in a non-conjugative fashion *via* a 3,3'-biphenyl moiety. There is no electron excess or deficiency in the π-system. Thus, little absorption in the visible, large energy gaps, and high oxidation potentials are expected from these materials, despite the large π-framework.

3.3.2.1. Photophysical Properties

The film and solution (CH_2Cl_2) absorption spectra for the host materials are shown in Figure 3.6, and the λ_{max}, λ_{onset}, and molar absorptivity ε are summarized in Table 3.5. The electronic absorption spectra show a strong peak around 275 nm, and a shoulder around 310 nm. The absorptions have strong oscillator strengths, with $\varepsilon \sim 10^5$ M^{-1} cm^{-1} for the main peak, and $\varepsilon \sim 10^4$ M^{-1} cm^{-1} for the shoulder peak. The solution spectra for all derivatives differ only marginally in both λ_{max}, and ε, which can be ascribed to the uniformity of the molecular π-system that gives rise to the π-π* transition observed. In the film absorption spectra, the shoulder peak red-shifts, whereas the main peak maintains the position of its maximum. These changes can be attributed to the contribution from intermolecular interactions that are present in the condensed state. While the onset of film absorption for all host materials red-shift relative to the solution onset, the most significant change occurs for the unalkylated **DTPBP**. Without any intervening alkyl chains, **DTPBP** is expected to π-stack better than the alkylated derivatives. Alkyl chains are expected to increase any deviation from cofacial stacking, to reduce steric interactions between the chains.[36] Thus, **DTPBP** displays a substantial 20 nm shift. The absorption onsets of the materials fall outside of the visible range, giving colorless solutions and films. All materials have a wide optical gap ($\boldsymbol{E_{g,opt}}$), making them promising materials as hosts for phosphorescent emitters in OLEDs. The values are very similar to what is reported for triphenylene (3.65 eV).[177] The slight decrease may be due to a small contribution from a more extended π-system from the *p*-terphenyl fragment formed with the biphenyl linker, as shown in Figure 3.7.

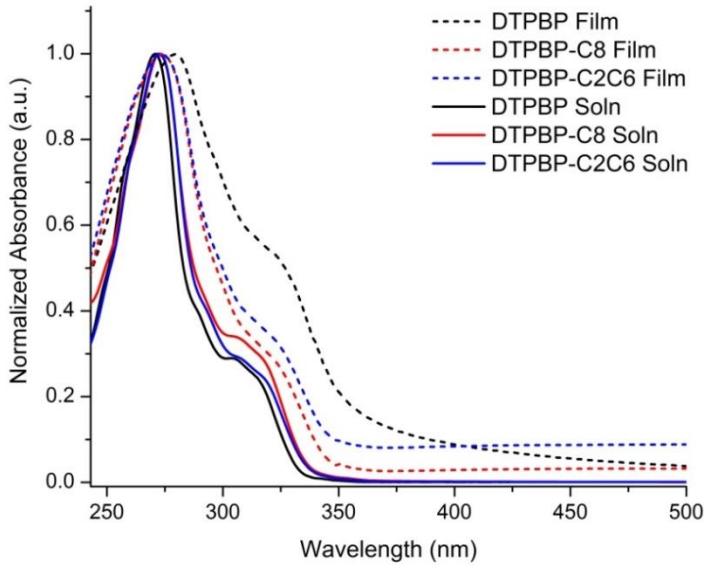

Figure 3.6. Solution (in CH_2Cl_2) and film absorption spectra of the host materials.

Table 3.5. Photophysical properties of triphenylene-based host materials.

	λ_{max} (nm)		Sol'n ε ($\times 10^5$ M^{-1} cm^{-1})		λ_{onset} (nm)		$E_{g,opt}$ (eV)		$E_{S0\text{-}S1}$ [a] (eV)	E_T [b] (eV)	ΔE_{ST} [c] (eV)
	Film	Soln	275 nm	310 nm	Film	Soln	Film	Soln			
DTPBP	280	271	1.3	0.36	353	331	3.51	3.75	3.48	2.62	0.87
DTPBP -C8	274	273	1.2	0.42	344	336	3.60	3.69	3.47	2.61	0.85
DTPBP -C2C6	273	273	1.4	0.40	343	336	3.62	3.69	3.47	2.61	0.85

[a] Taken from the λ_{max} of the highest energy fluorescence peak. [b] Taken from the λ_{max} of the highest energy phosphorescence peak. [c] Estimated from the energy difference between the singlet and triplet emissions at 80 K.

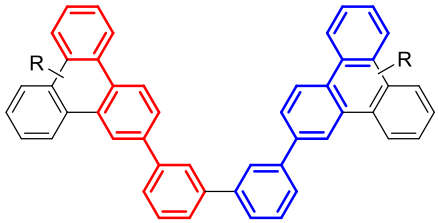

Figure 3.7. The *p*-terphenyl π-system created in the **DTPBP** molecule.

The emission spectra (Figure 3.8) of the host materials were obtained from dilute solutions in methyl THF at room temperature, and 80 K (by Charles Zeman IV from Prof. Kirk Schanze's group at the University of Florida). All compounds show fluorescence

(singlet) emission in the 350 to 450 nm region, with an improvement in vibronic resolution at lower temperature. A vibronic spacing of ~ 10 nm (0.08 eV) is found for the fluorescence emission, and strong intensities for the 0→0 and 0→1 transitions, reflecting the rigidity of the conjugated systems leading to the π-π* transition.[6] Phosphorescence is observed from these systems at low temperature in the 450 to 650 nm range, with distinct vibronic resolution having spacing of ~ 35 nm (0.16 eV). The triplet energies of the host materials are taken from the λ_{max} of the highest energy vibronic peak in the phosphorescence region, and are summarized in Table 3.5.

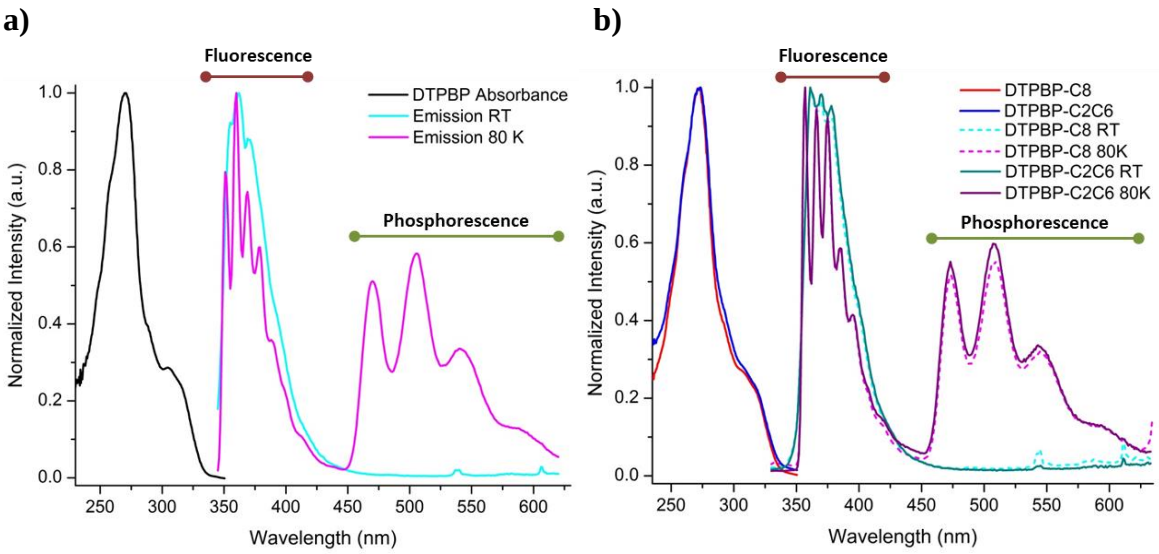

Figure 3.8. Fluorescence and phosphorescence emission spectra of **DTPBP** (a), and alkylated derivatives (b) at room temperature and 80 K.

As discussed in previous sections, the triplet energy of the host must be higher than that of the phosphorescent guest emitter so that exothermic energy transfer from host to guest occurs, and back energy transfer from guest to host does not. Based on the triplet energy values obtained for these triphenylene-based host materials, their energies are well- situated for red and green iridium-based phosphorescent dopants that tend to have

triplet energies $\boldsymbol{E_T}$ < 2.60 eV.[129] The triplet energy values are significantly lower than that for triphenylene (2.9 eV),[176,177] and are closer to that for *p*-terphenyl (2.53 eV).[177]

The singlet-triplet splitting ($\boldsymbol{\Delta E_{ST}}$) of the host materials were estimated from the difference between the highest energy fluorescence ($\boldsymbol{E_{S0\text{-}S1}}$), and phosphorescence peaks ($\boldsymbol{E_T}$) at 80 K,[14,192] and are summarized in Table 3.5. $\boldsymbol{\Delta E_{ST}}$ of the triphenylene-based hosts are around 0.8 eV, similar to many small molecules, which have splittings of 0.7 – 1 eV.[11,193] The substantial splitting can be attributed to the lack of electron-withdrawing or electron-donating moieties in the structure that can induce an intramolecular charge transfer (ICT) transition. These transitions tend to lead to less localization of the singlet transition in a different part of the molecule from the triplet transition.[193-196] In triphenylene-based polymers, a large $\boldsymbol{\Delta E_{ST}}$ has been observed due to localization of the triplet state in the triphenylene ring, and localization of the singlet state in the extended conjugation along the polymer chain.[192,197]

3.3.2.2. Electrochemistry and Frontier Energy Levels

Cyclic and differential pulse voltammetry of the alkylated materials in CH_2Cl_2 solution, and on films deposited on Pt buttons were used to determine their oxidation potentials (with reference to the ferrocene/ferrocenium redox couple), and electrochemical stability. The results are shown in Figure 3.9 and Figure 3.10. **DTPBP** was insoluble in many organic solvents, so its electrochemistry could only be studied on films cast on Pt buttons (Figure 3.11). The derived energy levels are summarized in Table 3.6.

As Figures 3.9 to 3.11 show, the triphenylene-based host materials have oxidation potentials above 1.00 V, leading to large IPs. The oxidation traces of the alkylated

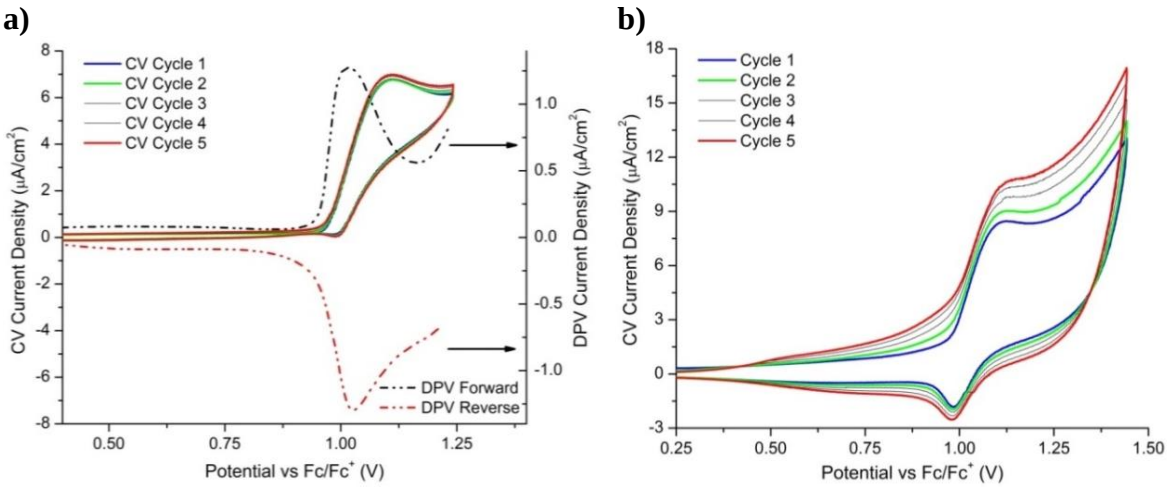

Figure 3.9. Cyclic and differential pulse voltammograms of **DTPBP-C8** (a), and electrochemical stability at higher potentials (b).

derivatives are reversible within a limited applied potential window (< 1.55 V). Above this potential, the current increases for each anodic sweep of the voltage, and the onset of the oxidation wave decreases (Figure 3.9b and 3.10b). This may be attributed to oligomerization reactions between radical cations formed.

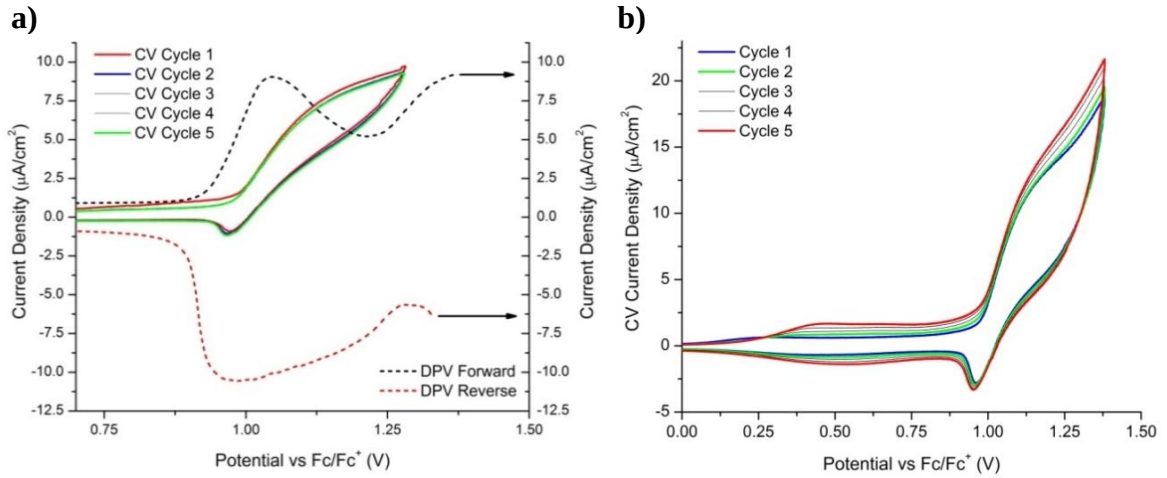

Figure 3.10. Cyclic and differential pulse voltammograms of **DTPBP-C2C6** (a), and electrochemical stability at higher potentials (b).

The unalkylated derivative **DTPBP** could not be studied in solution, and the films formed on Pt buttons were crystalline and not uniform. The anodic sweeps from cyclic

voltammetry (Figure 3.11) gave rise to onsets of oxidation, but increasing the applied potential led to a decay of the measured current. The oxidation potential was thus obtained from differential pulse voltammetry performed on fresh films. This method may have artificially increased the measured oxidation potential of the material, relative to the alkylated derivatives, due to the additional energy required for the electrolyte solution to permeate the film.

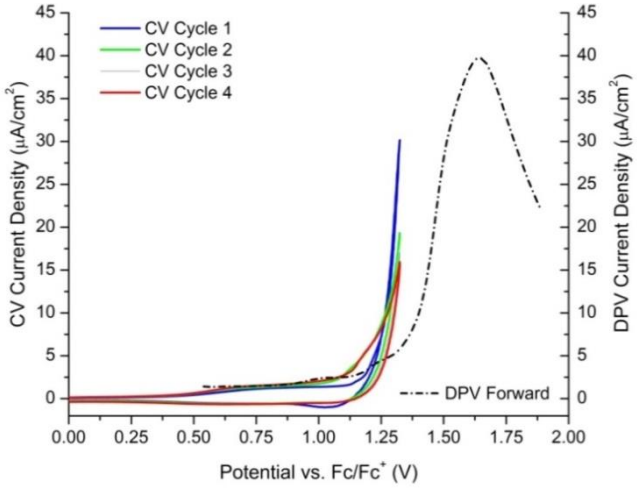

Figure 3.11. Cyclic and differential pulse voltammograms of **DTPBP**.

Table 3.6. Electrochemical properties of triphenylene-based host materials.

	$E_{ox,DPV}$[a] (V)	IP[c] (eV)	EA[d] (eV)	E_g (eV)
DTPBP	1.48[a]	−6.60	−3.09	3.51
DTPBP-C8	1.02[b]	−6.14	−2.54	3.60
DTPBP-C2C6	1.04[b]	−6.16	−2.54	3.62

[a]DPV peak potential; values referenced to ferrocene ($E_{½}$ = 0.076 V vs. Ag/Ag^+ in CH_3CN). [b]DPV peak potential; values referenced to ferrocene ($E_{½}$ = 0.25 V vs. Ag/Ag^+ in CH_2Cl_2). [c]Values reported relative to vacuum (-5.12 eV). [d]Calculated from the sum of IP and $E_{g,opt}$, thus E_B is not accounted for.

No reduction waves were observed for any of the host materials, so the EAs were obtained by taking the sum of the IP obtained from electrochemistry, and the optical gap measured from absorption spectroscopy (Table 3.6). It must be emphasized, however, that this method of estimating the EA does not account for the exciton binding energy,

and thus, the calculated energy gap $\boldsymbol{E_g}$, is significantly lower than the actual transport gap (where free and mobile charge carriers are created). The difference arises from the optical gap measuring a transition involving an electrostatically bound electron-hole pair, whereas the IP and EA are concerned with ionized states. The energy difference, which is $\boldsymbol{E_B}$, can range from hundreds of meV to 1 eV, [10] and the $\boldsymbol{E_g}$ calculated here is expected to be underestimated by this difference.

The energy levels of these triphenylene-based host materials are similar to the carbazole derivatives CBP, mCP, and SimCP, making them suitable materials for electron and hole injection from common anode and electrode materials, and electron and hole transporting materials (Figure 3.12). Their wide energy gaps make them suitable hosts for many phosphorescent emitters.

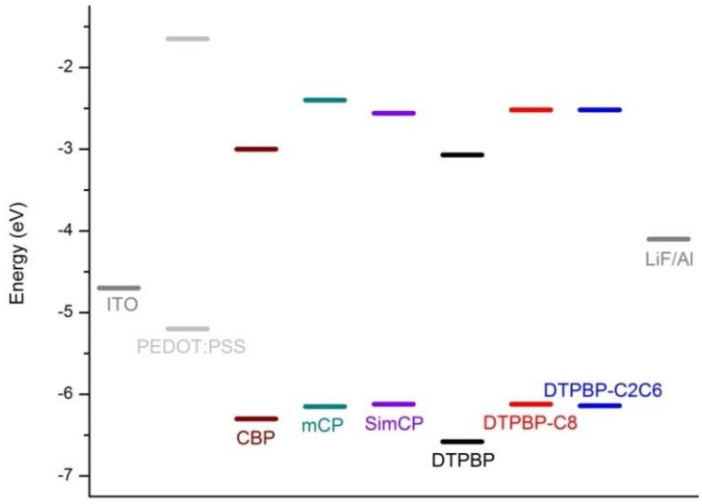

Figure 3.12. Ionization potentials and electron affinities of carbazole- and triphenylene-based host materials, compared with common electrode materials.

3.3.3. Thermal Properties: Control of Crystallinity and Glass Transition Temperature

The thermal properties of the host materials were studied by means of thermogravimetric analysis (TGA) to determine their decomposition temperatures, and differential scanning calorimetry (DSC) to determine their transition temperatures. The results are shown in Figure 3.13, and summarized in Table 3.7. All host materials have high thermal stability, with high decomposition temperatures (defined as the temperature at which ~ 5 % of the sample weight is lost), $\boldsymbol{T_d}$ > 400 °C. The stability can be ascribed to the fused polycyclic structure of triphenylene, and the lack of heteroatoms. All host materials show a glass transition temperature. For the unalkylated derivative **DTPBP**, $\boldsymbol{T_g}$ > 100 °C, whereas for the alkylated derivatives $\boldsymbol{T_g}$ < 60 °C. The alkylated derivatives have moderate $\boldsymbol{T_g}$'s due to the disorder introduced by the isomeric mixture. A closer inspection of the DSC curves shows some possible glass transitions at higher temperatures, with significantly lower changes in heat capacity (Figure 3.13b, inset, circled). These may be due to isomers that allow for more entanglements of the alkyl chains. The disorder in these materials also suppresses crystallization, which can aid the formation of stable amorphous films. The unalkylated derivative, on the other hand, shows crystallization and melting temperatures, due to the lack of alkyl chains that interrupt the stacking of triphenylene moieties. It also displays a liquid crystal phase transition (*vide infra*) at a slightly lower temperature than its melting temperature. The high decomposition temperatures of the host materials are promising for enhanced stability in OLED device operating conditions. Their glass transitions indicate that they can be deposited as amorphous films.

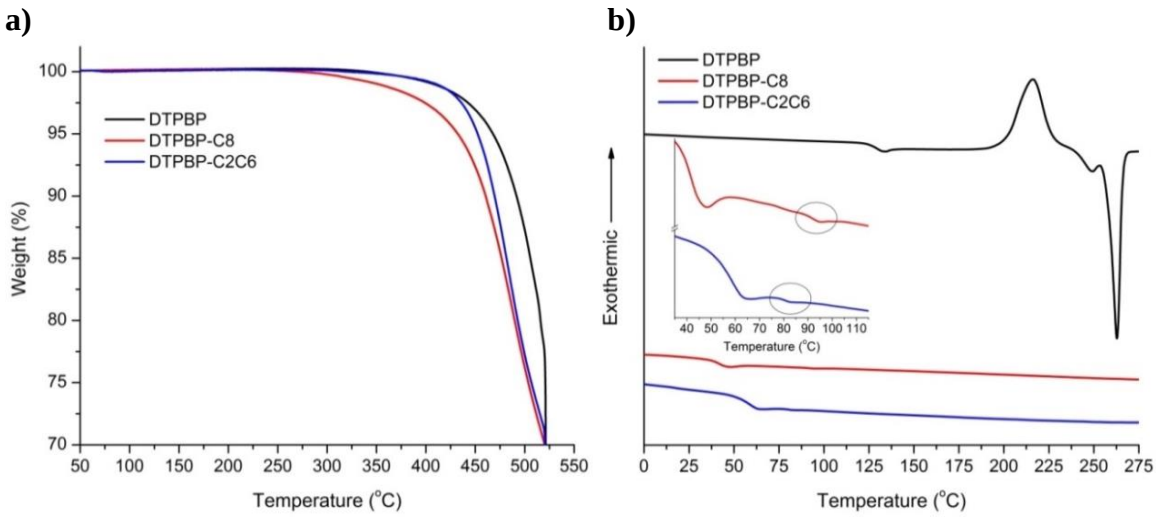

Figure 3.13. Thermal properties of the triphenylene-based host materials as studied by TGA (a), and DSC (b) (Inset: expanded DSC thermograms of the alkylated derivatives).

Table 3.7. Thermal properties of the triphenylene-based host materials.

	T_g	T_c	T_m	T_d
DTPBP	130	217; 249[a]	263	468
DTPBP-C8	43	-	-	432
DTPBP-C2C6	59	-	-	452

[a] Liquid crystalline transition.

3.3.3.1. Processability, Film Morphology, and Stability

The processability of the triphenylene-based host materials is markedly different due to the substantial solubility of the alkylated derivatives, relative to the unmodified **DTPBP**. The former are soluble to a large extent in many organic solvents (CH_2Cl_2, $CHCl_3$, toluene) at concentrations greater than 100 mg/mL. **DTPBP**, on the other hand, can only be dissolved to appreciable extents in high-boiling solvents, such as 1,1,2,2-tetrachloroethane (5-10 mg/mL), *o*-dichlorobenzene (2 mg/mL), and toluene (< 1 mg/mL).

Films of the host materials were cast from appropriate solvents, and studied *via* microscopic techniques. Atomic force microscopy was performed on the spin-cast films

of the alkylated derivatives by Szuheng Ho (from Prof. Franky So's group at the University of Florida). Polarized and non-polarized optical microscopy was done on spin-cast and drop-cast films of the unalkylated **DTPBP**. The micrographs are shown in Figures 3.14 to 3.16.

The alkylated derivatives can be processed from solution and spun coat into thin films (100 – 3000 nm thickness) with uniformly smooth, and pinhole-free surfaces. The roughness of the films, measured as $\mathbf{R_{rms}}$ (root mean square roughness, where a large value correlates with a rougher surface), are approximately 0.5 nm, well below the 1.0 nm roughness target[157] for host materials, especially when serving as substrates for further deposition of organic layers in a device. Notably, the film morphologies are stable and uniform even after annealing at temperatures well above their glass transitions ($\mathbf{\Delta R_{rms}}$ ~ 0.06 nm). This can be attributed to the disorder inherent in the isomeric mixture, preventing any aggregation or crystallization from occurring, even with sufficient thermal energy. Thus, stable amorphous films can be obtained from the alkylated derivatives despite their moderate glass transition temperatures, and their uniformity is expected to remain stable even in devices operating at elevated temperatures. This is an unprecedented advantage arising from the isomeric mixture generated by the synthetic approach, and a novel design strategy that can be pursued to simultaneously impart high solubility, and favorable film forming characteristics in host materials.

The unalkylated **DTPBP**, on the other hand, did not uniformly coat substrates when spin- or drop-cast from solutions, due to the substantially low concentrations attainable in even high boiling solvents (toluene, *o*-dichlorobenzene). Optical microscopy of these films shows the strong propensity of this material to crystallize. In drop-cast

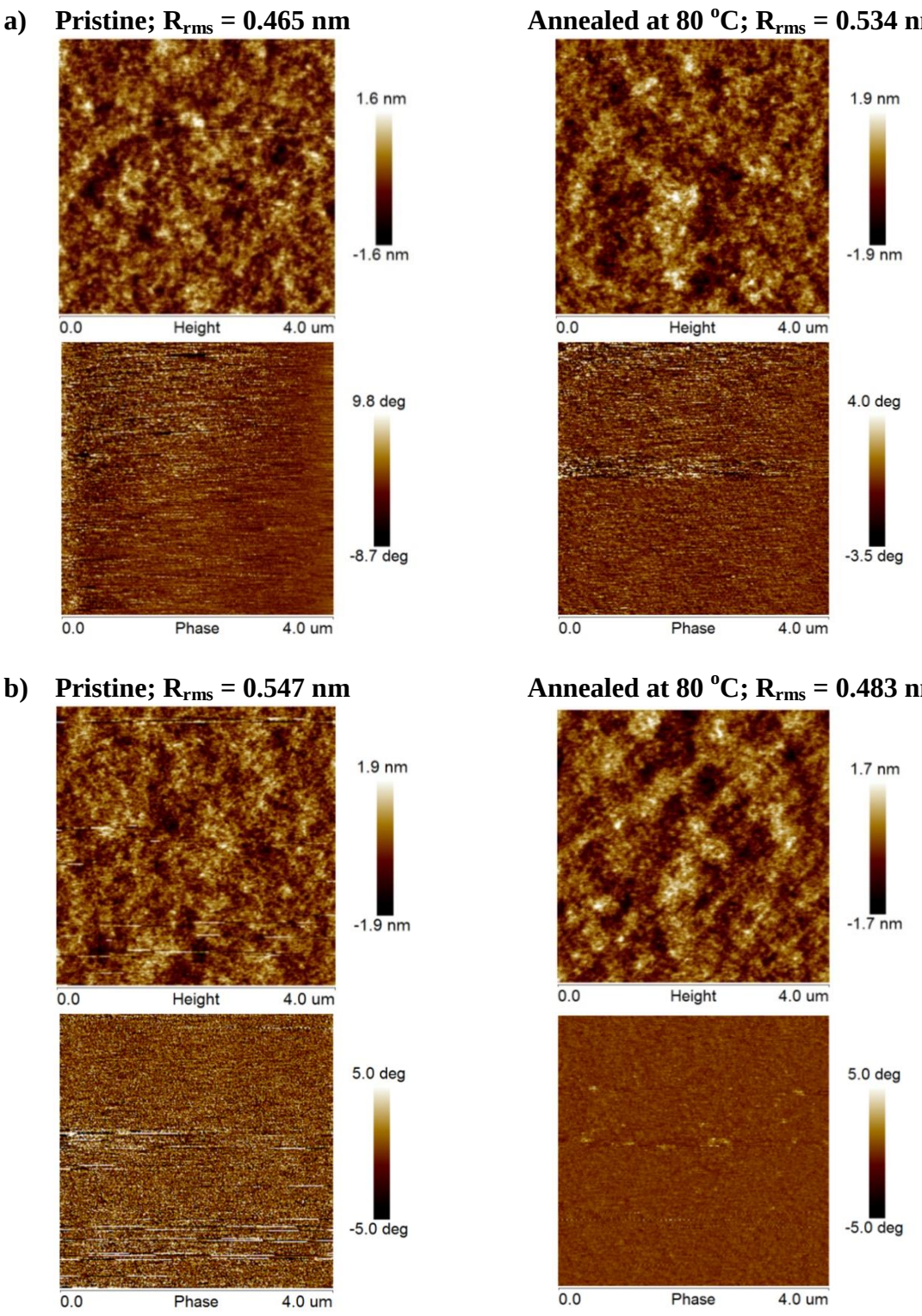

Figure 3.14. Atomic force micrographs (phase and height) of spin-cast films of **DTPBP-C8** (a), and **DTPBP-C2C6** (b), and their calculated roughness. (Images provided by Szuheng Ho, So group, University of Florida.)

films, fibers of high aspect ratios are observed, with lengths above two millimeters (Figure 3.15a), and showing strong birefringence. Spin-cast films, on the other hand, give short needles with furcated structures that show marked anisotropy under cross polarization (Figure 3.15b). These variations in morphology can be ascribed to the kinetic differences of the processing techniques, wherein long crystallization times are possible in drop-cast films, whereas only short periods are allowed in spin-casting.

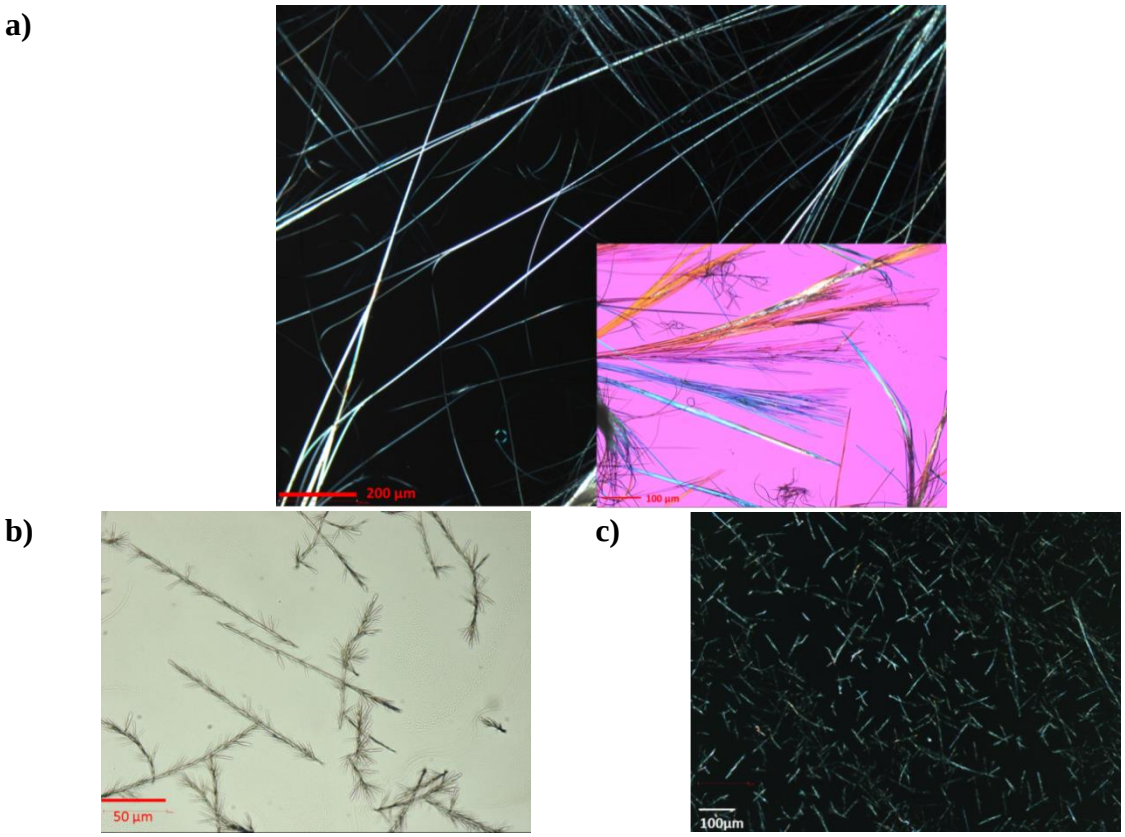

Figure 3.15. Polarized and unpolarized optical micrographs of **DTPBP** showing long birefringent fibers in drop-cast films (a) (Inset: birefringent fibers visualized with 530 nm waveplate compensator), and birefringent short furcated needles in spin-cast films (b) films.

The mesogenic properties of the triphenylene cores are also evident in the liquid crystalline textures observed from solvent vapor-annealed (Figure 3.16a) and thermally quenched (Figure 3.16b) films. Maltese cross patterns are observed in solvent vapor-

annealed films, and arise from spherulitic structures, ranging in size from 8 to 200 μm in diameter. The spherulites form due to the needles that grow radially outward from a single crystallization nucleus (Figure 3.16a, upper right image). This self-assembly can be attributed to the disc shape of triphenylene, and its strong π-stacking interactions, possibly forming a columnar lamellar arrangement that leads to the various spherulitic structures observed.[167] When the **DTPBP** solution is not allowed enough time for self-assembly, but rather deposited on a heated substrate that induces rapid evaporation of the casting solvent, no well-defined ordered structure is observed. Instead, a mosaic-like texture is formed (Figure 3.16b).

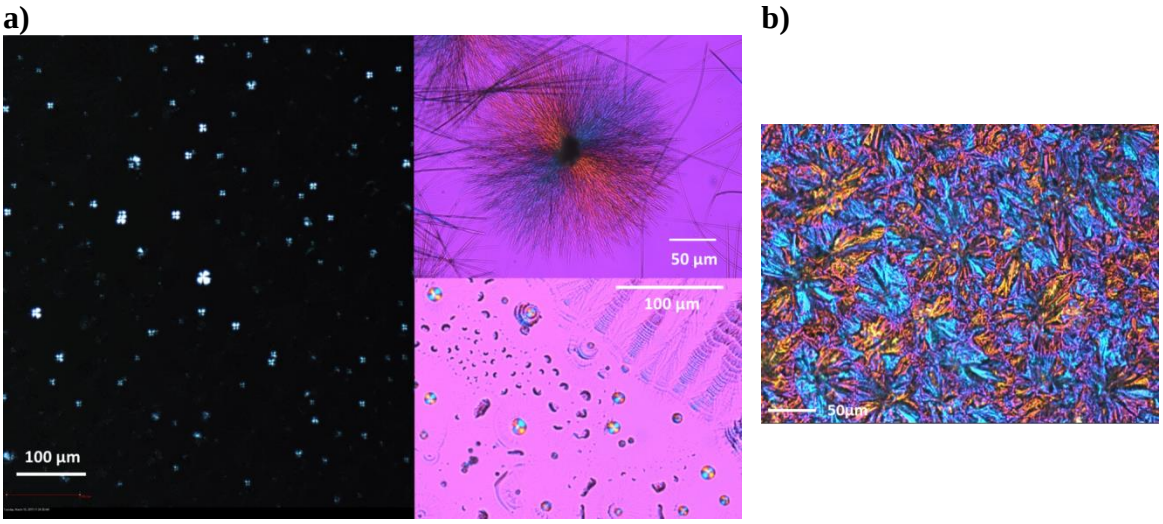

Figure 3.16. Polarized optical micrographs of **DTPBP** drop-cast films showing maltese cross patterns, and larger spherulitic structures (a), and mosaic-like liquid crystalline textures (b).

The competing forces that form these mesophases are not immediately apparent from the structure of **DTPBP**, but may arise from the strong unidirectional interactions between the triphenylene cores, and the disorder introduced by the sterically-promoted twisting of the biphenyl linker. The ability of the unalkylated derivative to form high

aspect ratio crystalline fibers, and liquid crystalline phases depending on the processing conditions can be potentially exploited for improving its charge transport characteristics.

3.3.4. Triphenylene-Based Device Characterizations

The optoelectronic and thermal characteristics of the triphenylene-based materials make them suitable hosts for phosphorescent emitters in OLEDs. Their OLED devices, and the related devices for measuring charge transport mobilities were fabricated and characterized at the University of Florida by Szuheng Ho from the group of Prof. Franky So. The emitter layers were vacuum-processed for the unalkylated derivative, and solution-processed for the alkylated derivatives.

With the triplet energies of the triphenylene-based host materials at ~2.6 eV, OLED devices were fabricated and characterized with tris[2-phenylpyridinato-C2,N] iridium(III) ($Ir(ppy)_3$), tris[2-(*p*-tolyl) pyridine] iridium(III) ($Ir(mppy)_3$), and *fac*-tris(2-(3-*p*-xylyl) phenyl)pyridine iridium(III) (TEG), phosphorescent emitters with triplet energy below 2.4 eV. A blue OLED device was also fabricated with the unalkylated derivative **DTPBP**, with bis(3,5-difluoro-2-(2-pyridyl)phenyl-(2-carboxypyridyl)iridium(III) (FIrpic) as the dopant emitter. The performance of **DTPBP** is also compared with **CBP**, and **mCP**, well-established host materials for green and blue emitters, respectively.

3.3.4.1. Vacuum-Processed DTPBP-Based Devices

The charge-carrier transport characteristics of vacuum processed **DTPBP** were studied with hole-only and electron-only devices. The mobility dependence on electric field, and the device architectures for each type of carrier are shown in Figure 3.17. The electron mobility of **DTPBP** is one to two orders of magnitude lower than the hole

mobility, which is a behavior exhibited by many organic materials,[170] and is also observed in many other host materials containing the triphenylene moiety.[179,180] The strong dependence of mobility values on the device architecture, and the techniques used to measure them make comparison with other host materials problematic.

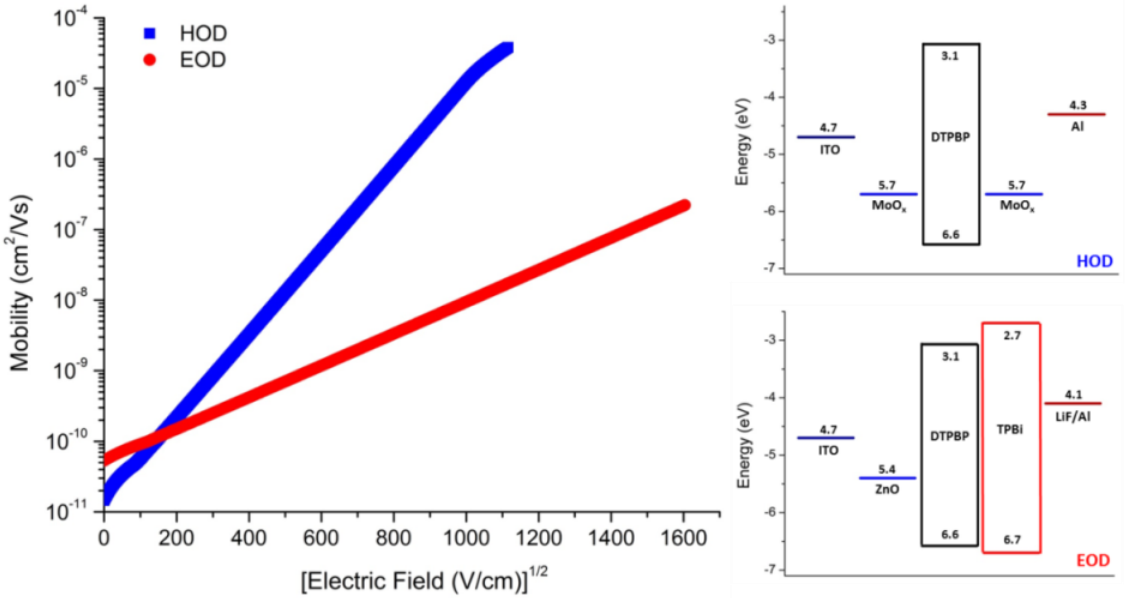

Figure 3.17. Charge transport characteristics of **DTPBP** as determined from hole-only-device (HOD) and electron-only-device (EOD) with architectures shown on the right.[129,198]

3.3.4.1.1. DTPBP in Green OLED Device

The performance of **DTPBP** and **CBP** were compared as vacuum-processed host materials for $Ir(ppy)_3$. The device architecture is shown in Figure 3.18. The frontier energy levels for ITO, PEDOT:PSS, TAPC, CBP, TPBi, and LiF/Al were taken from the literature.[129,198,199] The significantly deeper IP of **DTPBP** relative to **CBP** can be expected to provide a higher barrier to hole injection. **DTPBP**'s IP level is also closer to TPBi, which prevents TPBi from serving simultaneously as a hole blocker and an electron transporting material. By comparison, **CBP** has energy levels that are better

matched with both the hole and electron transporting materials. In terms of electron injection, both **DTPBP** and **CBP** provide minimal barrier from TPBi. TAPC, on the other hand, has a sufficiently less negative EA level to serve as an electron blocking material for both hosts.

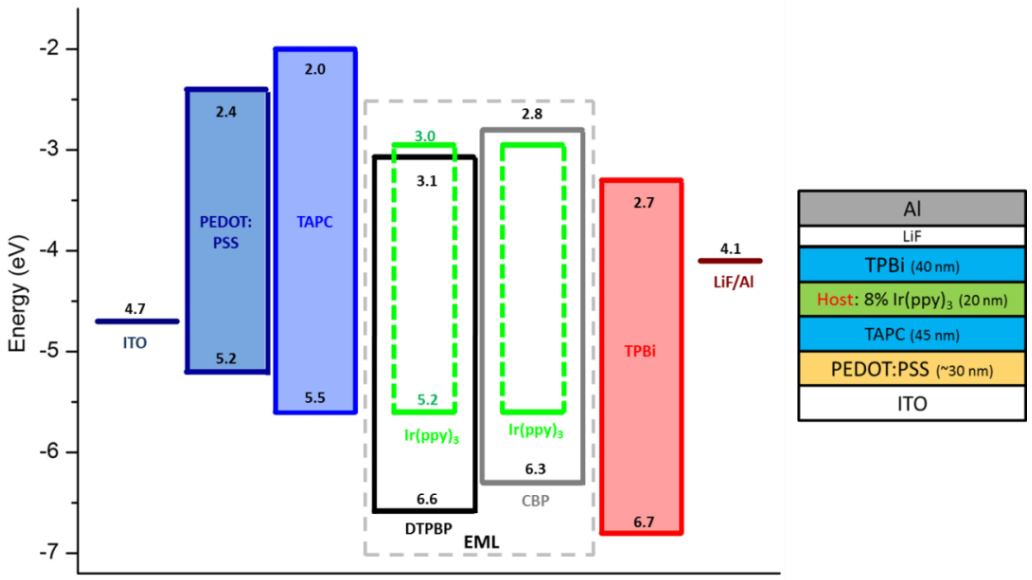

Figure 3.18. Vacuum-processed **DTPBP** and **CBP** green device architecture and energy diagram.[129,150,198,199]

The *J-V-L* curves of the **DTPBP**- and the **CBP**- based device are shown in Figure 3.19. The two devices show similar characteristiscs, with turn-on voltages just below 3 V, and reaching luminance values of 1000 cd m^{-2} at driving voltages just above 5 V. The current density in the **CBP** device is slightly higher than in the **DTPBP** device at turn-on, and may be attributed to the higher charge transport mobilities in the former host material. However, the luminance and current densities in the **DTPBP** device are slightly higher than those of **CBP** at high voltages.

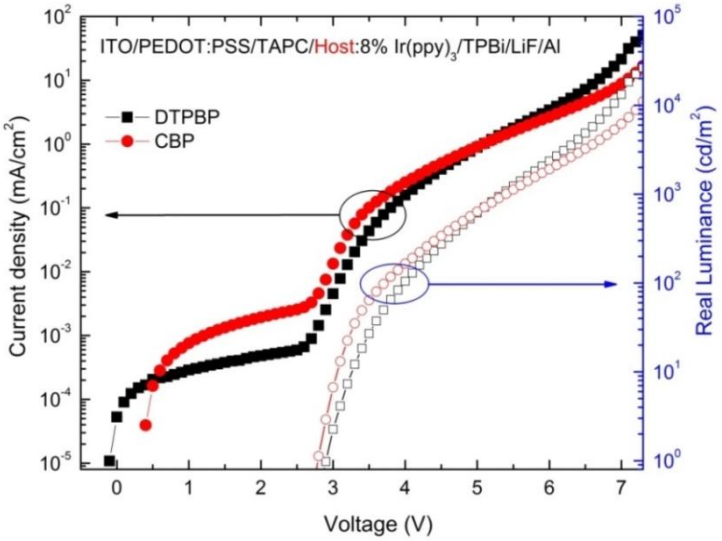

Figure 3.19. Current-density-voltage characteristics of green OLED devices with **DTPBP** and **CBP** as host materials.

The current and luminous power efficiencies of both devices are shown in Figures 3.20a and 3.20b, respectively. Both materials give high current efficiencies, maximizing at about 70 cd A^{-1} with brightness of 1000 – 3000 cd m^{-2}. Power efficiencies of 55 – 60 lm W^{-1} are achieved at brightness well below 100 cd m^{-2}, and decreases to around 40 lm W^{-1} at a brightness of 1000 cd m^{-2}. The power efficiency roll-off displayed by both devices may be attributed to the higher probability of triplet-triplet annihilation at higher current densities.[200] These performance characteristics are comparable to many host materials that have electron-donating and/or electron-withdrawing units in the literature (including **CBP**).[147]

The electroluminescence spectra for both **DTPBP** and **CBP** devices are shown in Figure 3.21. The emission predominantly arises from $Ir(ppy)_3$, although the slight difference observed for **DTPBP** may arise from a small emission from the host material. The spectra do indicate near-complete charge and/or energy transfer from the host to the emitter, and strong confinement of the excitons in the emitting layer. These results are

notable in light of charge carrier imbalance expected in **DTPBP**, due to its significantly lower electron mobility, relative to its hole mobility. Tentatively, the confinement of the emission in the emitter layer may be due to the higher hole injection barrier created by the deep IP of **DTPBP** relative to the hole transporting TAPC. These two factors may balance out the charge carriers in the emitter layer.

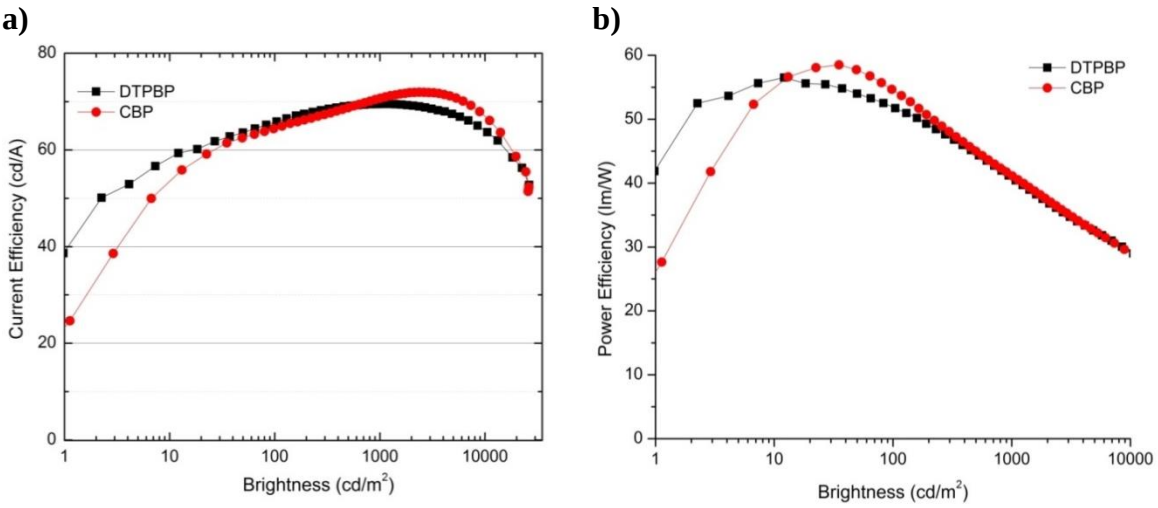

Figure 3.20. Current efficiencies (a) and power efficiencies of green OLED devices with **DTPBP** and **CBP** as host materials.

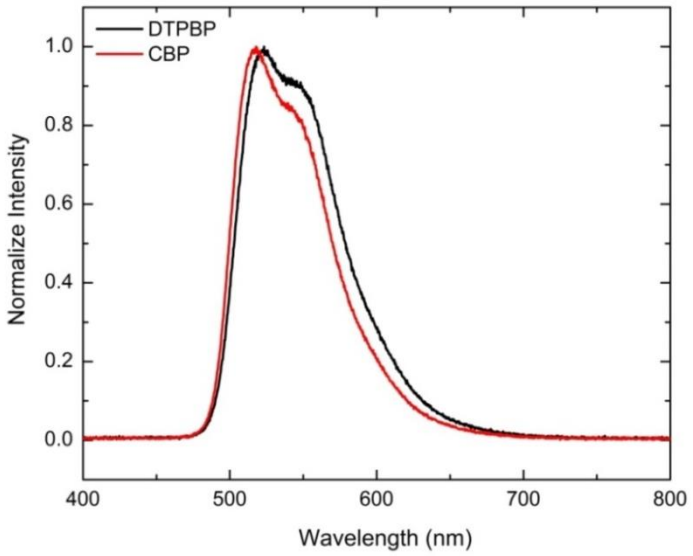

Figure 3.21. Emission spectra of green OLED devices with **DTPBP** and **CBP** as host materials.

It must also be noted that the strongly similar performance of **DTPBP** and **CBP**, despite their significantly different energy levels and mobilities, may indicate that the exciton formation occurs by direct charge transfer to the dopant from the transport layers. An investigation of this phenomenon, however, requires further device studies on the effect of dopant concentration, and is outside the scope of this work.

3.3.4.1.2. DTPBP in Blue OLED Device

The performance of **DTPBP** as a potential host for blue emitters was studied with FIrpic, and compared with **mCP**. The device architecture used is shown in Figure 3.22. The electron transport layer used was 3TPYMB, the structure for which shown in the same figure. The energy levels for all materials besides **DTPBP** were taken from the literature.[129,199,201,202] As the figure shows, the energy levels of **mCP** are well-aligned with the emitter, whereas **DTPBP** has a lower EA than FIrpic. The deep IP of **DTPBP**

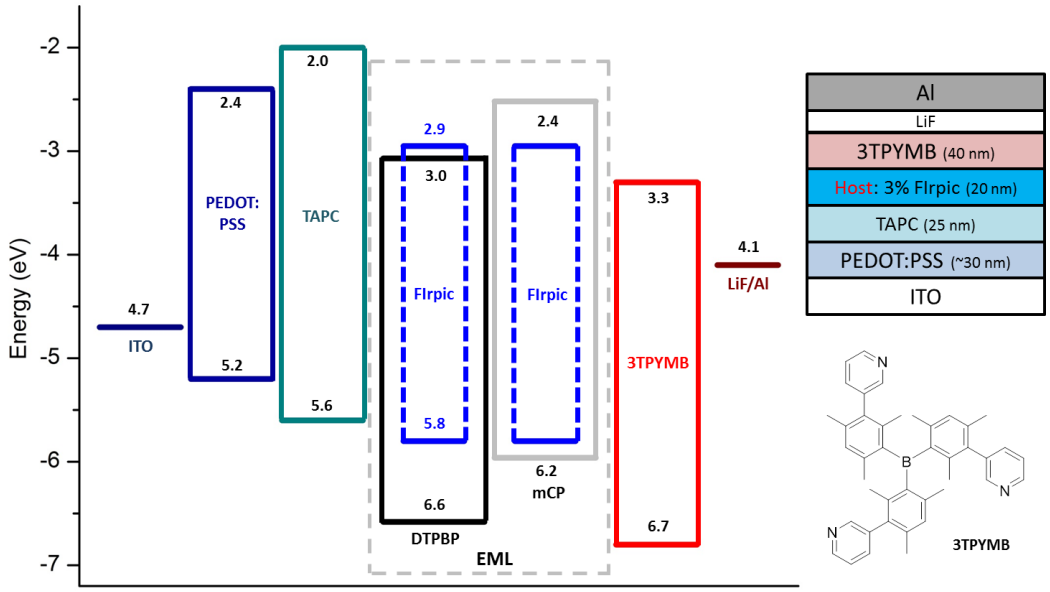

Figure 3.22. Vacuum-processed **DTPBP** and **mCP** blue device architecture and energy diagram.[129,199,201,202]

also provides a significant hole injection barrier from the transport layer TAPC, whereas **mCP** does not. The electron injection barrier from 3TPYMB is greater for **mCP** than it is for **DTPBP**. Both TAPC and 3TPYMB can serve as carrier blocking layers for **mCP**, whereas only TAPC can serve as an electron blocking layer for **DTPBP**. 3TPYMB has an IP energy level close to that of **DTPBP**, and does not provide a significant barrier to serve as a hole blocking material.

The *J-V-L* curves for the blue devices are shown in Figure 3.23. The turn-on voltage for the **mCP** device is about 3.4 V, whereas that for **DTPBP** is about 3.9 V. The driving voltages to reach a luminance of 1000 cd m^{-2} are around 6.4 V for **mCP**, and 7.6 V **DTPBP**. At higher voltages, the current densities for **DTPBP** are slightly higher than those for **mCP**, but the luminance is substantially higher for **mCP**.

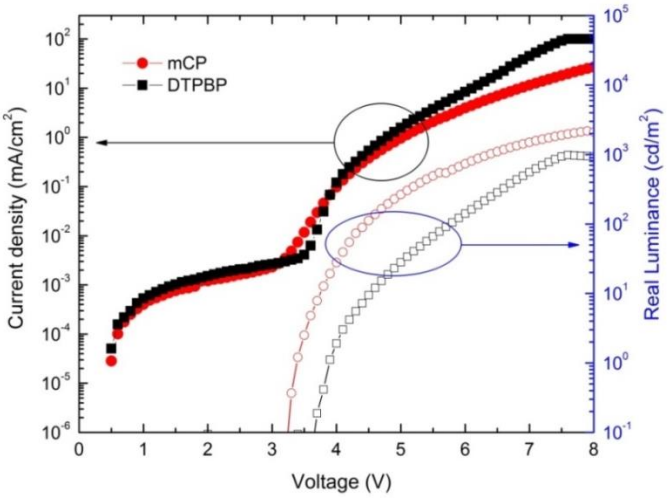

Figure 3.23. Current-density-voltage characteristics of blue OLED devices with **DTPBP** and **mCP** as host materials.

The current and power efficiencies of the devices are shown in Figures 3.24a and 3.24b. The values for **DTPBP** are insignificant, whereas **mCP** shows a maximum current

efficiency of 30 cd A^{-1} at just below 100 cd m^{-2} brightness, with a maximum power efficiency of about 25 lm W^{-1}.

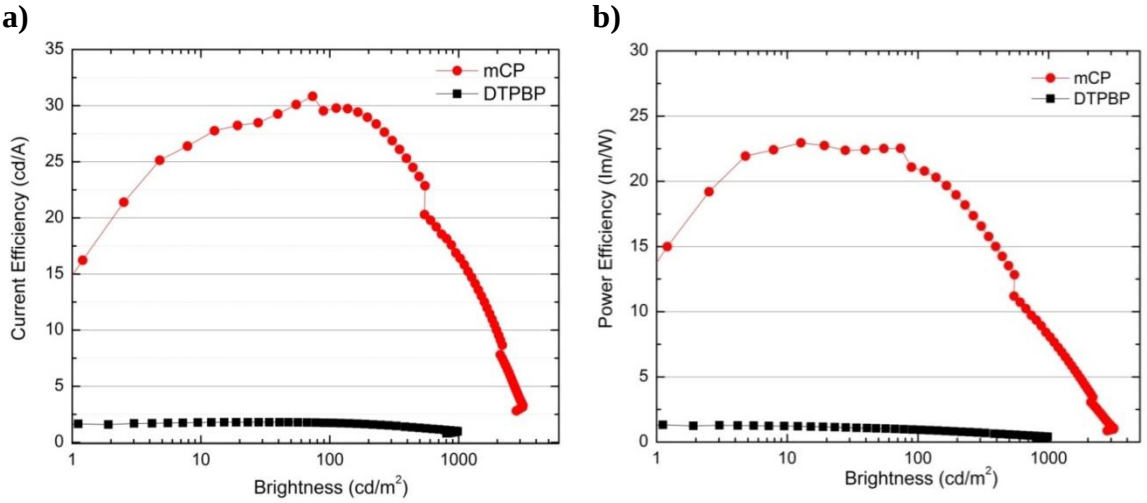

Figure 3.24. Current efficiencies (a) and power efficiencies (b) of blue devices with **DTPBP** and **mCP** as host materials for FIrpic.

The electroluminescence spectra of both devices, shown in Figure 3.25, suggest a cause for the substantially inferior performance of **DTPBP** relative to **mCP** as host for a blue emitter. As the figure shows, the emission detected is poorly derived from the triplet emitter, and likely comes from the host material itself. This is likely due to the significantly lower triplet level of **DTPBP** (2.6 eV) relative to FIrpic (2.7 eV), and **mCP** (3.0 eV). It is likely that energy/charge transfer does not occur between **DTPBP** and the triplet emitter, leading to decay (radiative and non-radiative) of excitons in the host, rather than the emitter. This can also explain the *J-V-L* behavior (Figure 3.23), where **DTPBP** and **mCP** give similar current densities at different voltages, but **mCP** gives a higher luminance than **DTPBP**. The charges generated in **DTPBP** do not give rise to triplet excitons in the emitter, and thus lower light emission is observed.

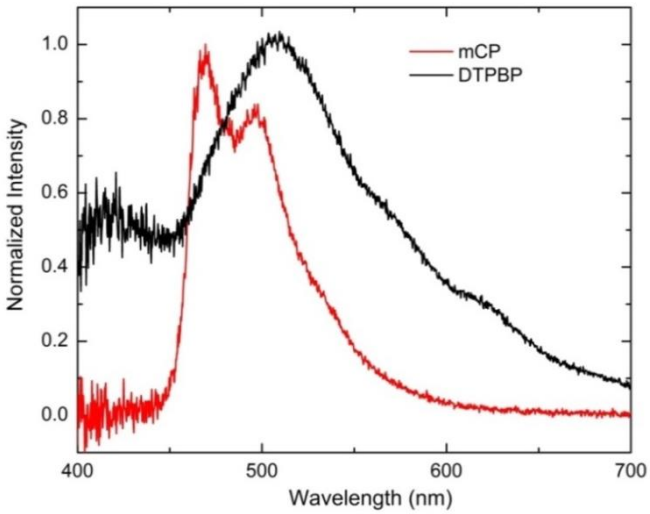

Figure 3.25. Emission spectra of blue OLED devices with **DTPBP** and **mCP** as host materials.

3.3.4.2. Solution-Processed Alkylated DTPBP-Based Devices

With the high solubility of the alkylated derivatives, active layers of the neat and emitter-doped alkylated derivatives were spin-cast from organic solvents, and deposited on aqueous-soluble or cross-linked HTLs. The charge transport properties of **DTPBP-C8** were studied in an electron-only device and compared with TPBi, a well-known electron transporting material. The results for **DTPBP-C8** were assumed to be similar to the charge transport properties of **DTPBP-C2C6** due to their similar electronic cores resulting in similar electronic energy levels, and their multi-isomeric composition leading to similar intermolecular interactions.

The electron-only device architecture, and electric field dependence of the mobility of neat **DTPBP-C8,** and **DTPBP-C8** doped with different amounts of the green emitter TEG, along with neat TPBi, are shown in Figure 3.26. Under fields of [800 – 1000 V/cm]^{½}, TPBi gives mobilities on the order of 10^{-8} to 10^{-7} cm^2 V^{-1} s^{-1}. These values are significantly lower than what is reported in the literature, which is on the order

of 10^{-6} to 10^{-5} cm^2 V^{-1} s^{-1}.[150] These inconsistencies may be attributed to differences in device architecture, processing, and operating conditions (e.g. temperature) that may lead to differences in injection barriers and trap concentrations. Under the same architecture and processing conditions, neat **DTPBP-C8** gives mobilities on the order of 10^{-8} cm^2 V^{-1} s^{-1}, and shows strong field dependence. The low electron mobility in **DTPBP-C8** may be attributed to the disorder introduced by the isomeric mixture present in the material, and the lack of electron-withdrawing moieties that can stabilize a radical anion structure. At higher fields, **DTPBP-C8** gives higher mobilities than TPBi, and may be due to the electric field being sufficient to overcome injection barriers. The figure also shows that of the dopant further decrease the mobility. It is likely that the dopant serves as a trap doping **DTPBP-C8** with TEG lowers its electron mobility, and increasing concentrations center, and impedes the hopping of electrons across the device. The hole mobility of the alkylated derivatives are still under study.

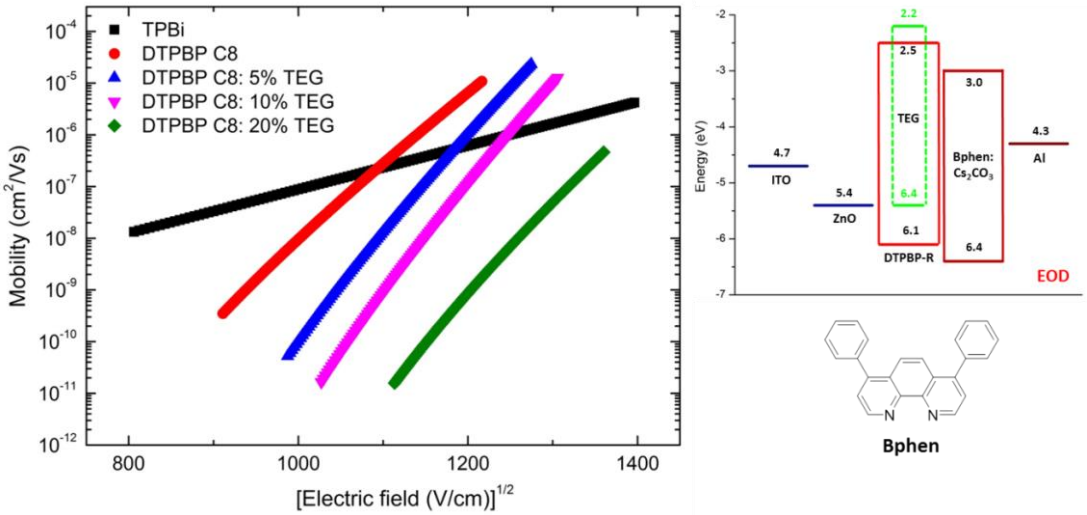

Figure 3.26. Electron mobility of neat and TEG-doped **DTPBP-C8** compared with TPBi. The device architecture used to measure mobility is shown on the right, along with the structure for Bphen, the material used as part of the electron transport layer.

The ability of the alkylated derivatives to serve as host materials was tested with the solution-processed green emitters, $Ir(mppy)_3$ and TEG. The device architectures are shown in Figure 3.27. During device fabrication, the organic solution processed emitter layer is deposited on top of the hole injection and/or hole transporting layers, which must be insoluble in the processing solvent of the emitter layer. This requirement thus limits the materials that can be used for these layers to aqueous soluble (PEDOT-PSS) or cross-linkable (PLEXCORE® HTL) materials. As shown in Figure 3.27, the IP levels of both materials introduce a significant hole injection barrier toward the alkylated **DTPBP** layer, but not to either emitter. It is thus likely that direct hole injection to the emitter will occur. The EA levels of the hole injection and/or transport layers are not sufficiently high so as to provide a significant barrier to electron injection, and simultaneously serve as electron blocking layers. The electron transport layer TPBi has an EA level that is sufficiently high to reduce the electron injection barrier. TPBi also has a sufficiently low IP level to provide hole blocking capabilities and help confine excitons in the emitter

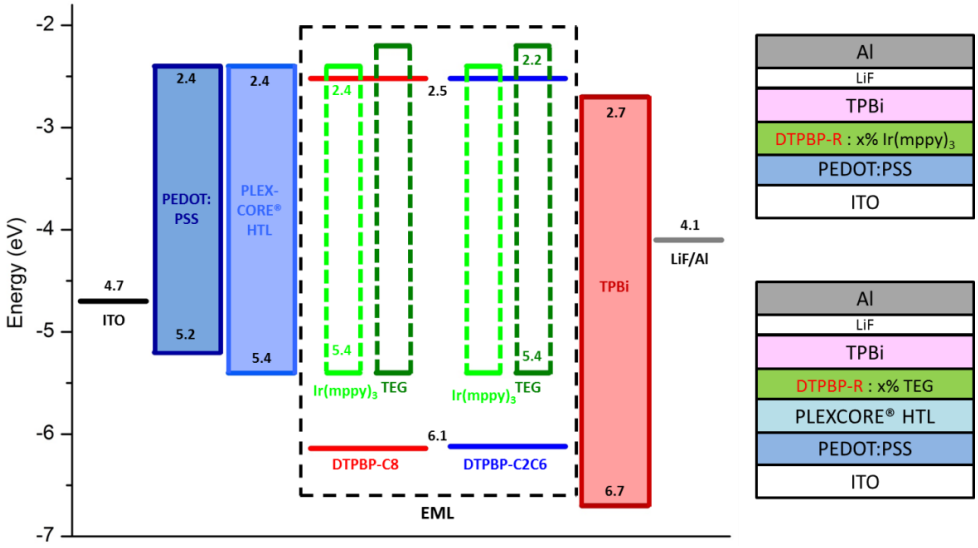

Figure 3.27. Solution-processed alkylated **DTPBP** device architectures and energy diagram.[129,150,198]

layer. The lower EA of the alkylated **DTPBP** hosts relative to the emitters may lead to electron injection to the host materials, but may be impeded by their poor electron mobility (Figure 3.26).

For the $Ir(mppy)_3$ emitter, devices with two different dopant concentrations, at 10 % and 30 %, and two deposition conditions of the emitter layer, 500 rpm and 1000 rpm, were studied. The *J-V-L* curves for these devices are shown in Figure 3.28. For **DTPBP-C8**, the devices with higher emitter doping concentration had turn-on voltages at 2.9 – 3.0 V, whereas those with lower doping had turn-on voltages at 4.6 – 5.4 V. The devices with **DTPBP-C2C6**, on the other hand, had turn-on voltages at 2.8 V for the higher emitter doping levels, and 4.4 – 5.2 V for the lower doping levels. The driving voltages to attain luminance values of 1000 cd m^{-2} are around 5.0 – 6.2 V for **DTPBP-C8** and 4.5 – 5.7 V for **DTPBP-C2C6**, in the 30 % $Ir(mppy)_3$-doped devices. Both current densities and luminance values are significantly higher for the 30 % $Ir(mppy)_3$-doped devices, than the 10 % $Ir(mppy)_3$-doped devices. The higher doping levels may lead to improvement of charge transport in the host materials,[203] giving rise to better performance characteristics. It is also possible that the better-matched energy levels of the dopant emitter (to the HTL) relative to the host material (Figure 3.27) for hole injection may lead to direct creation of triplet excited states in the emitter, rather than through energy transfer from the host materials. The active layers deposited at 1000 rpm also gave consistently higher current densities and luminance values for both types of alkylated **DTPBP** hosts. The 1000 rpm deposition is expected to yield thinner films, which may lead to lower local fields that can impede charge injection and transport.

a)

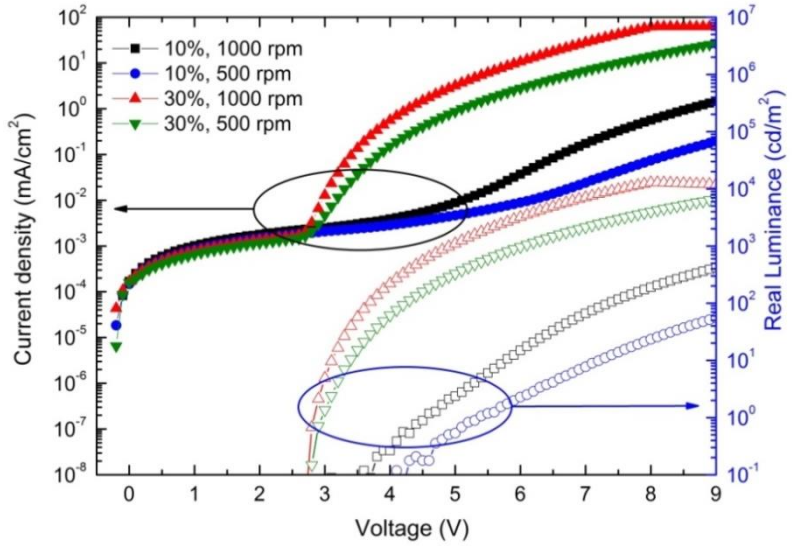

b)

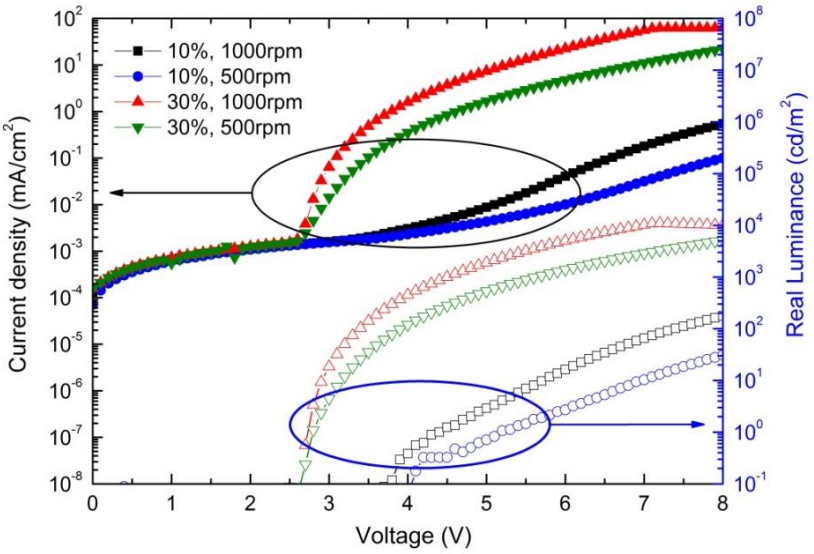

Figure 3.28. Current-voltage-luminance characteristics of the devices based on the alkylated host materials **DTPBP-C8** (a) and **DTPBP-C2C6** (b) for the green emitter $Ir(mppy)_3$ at different doping levels.

The current efficiencies of the $Ir(mppy)_3$ devices are shown in Figure 3.29. For **DTPBP-C8**, all devices showed maximum values of about 40 cd A^{-1}, except for the 10 % $Ir(mppy)_3$-doped device deposited at 500 rpm, which had a maximum of around 30 cd A^{-1}. The higher efficiencies obtained with the devices with higher doping concentrations may be due to more efficient triplet exciton generation from direct charge injection to the dopant. The higher-doped devices also showed lower efficiency roll-off at higher

brightness. For **DTPBP-C2C6**, the highest current efficiency is 40 cd A^{-1} for the 10 % $Ir(mppy)_3$-doped device deposited at 1000 rpm. As with **DTPBP-C8**, the higher doped devices with **DTPBP-C2C6** showed lower efficiency roll-off. This may indicate that the emitter improves the transport characteristics of the host material, which allows it to support higher charge densities at higher brightness. It may also be due to the charges injected into the host material at lower doping levels being unable to undergo charge transfer to the triplet emitter, likely from a mismatch of the EA levels of dopant and host. The lower doping concentration likely increases the probability of charge injection to the host, which may not lead to triplet exciton formation in the emitter.

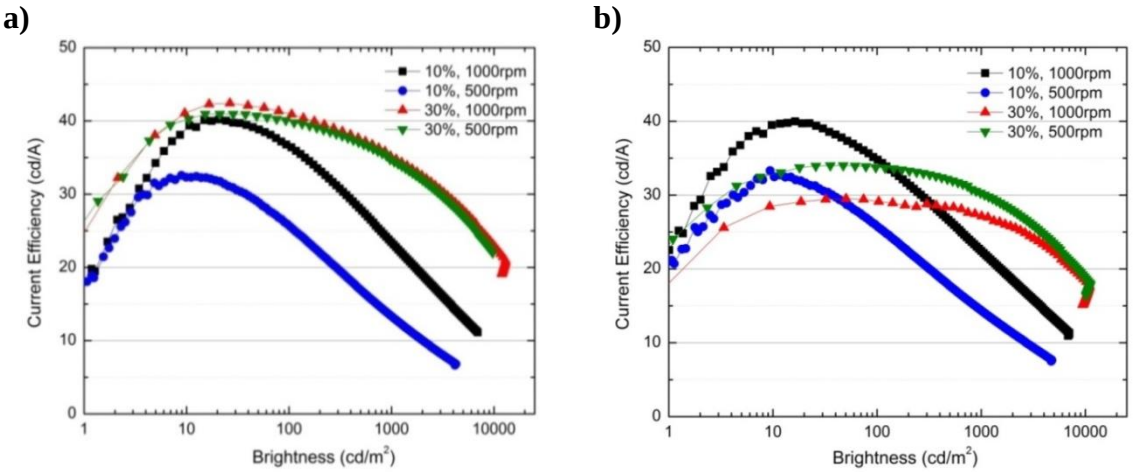

Figure 3.29. Current efficiencies of the devices based on the alkylated host materials **DTPBP-C8** (a) and **DTPBP-C2C6** (b) for the green emitter $Ir(mppy)_3$ at different doping levels.

The performance characteristics for both alkylated derivatives compare well with a spin-cast **CBP**-based $Ir(mppy)_3$ device that has been reported in the literature.[198] This device has a similar architecture to the devices studied here: ITO/PEDOT:PSS/CBP:6 % $Ir(mppy)_3$/BPhen/LiF/Al. The device gave a peak current efficiency of 26 cd A^{-1}, and a

peak power efficiency of 14 lm W^{-1}. The device also showed a similar efficiency roll-off behavior as the alkylated **DTPBP** hosts.

The electroluminescence spectra for all $Ir(mppy)_3$ devices are shown in Figure 3.30. The emission from $Ir(mppy)_3$ peaks at 510 nm, and most devices show a maximum around this wavelength. As expected from the *J-V-L*, and the current efficiency plots, the devices with lower dopant concentration did not show pure emission from $Ir(mppy)_3$. A slight contribution from the host material can be observed at 550 nm, and may be attributed to charges being injected into the host that directly emit from the host's triplet excitons, rather than the emitter's. This, again, may arise from the incomplete energy transfer from host to emitter, due to the mismatch of the EA levels of the two materials.

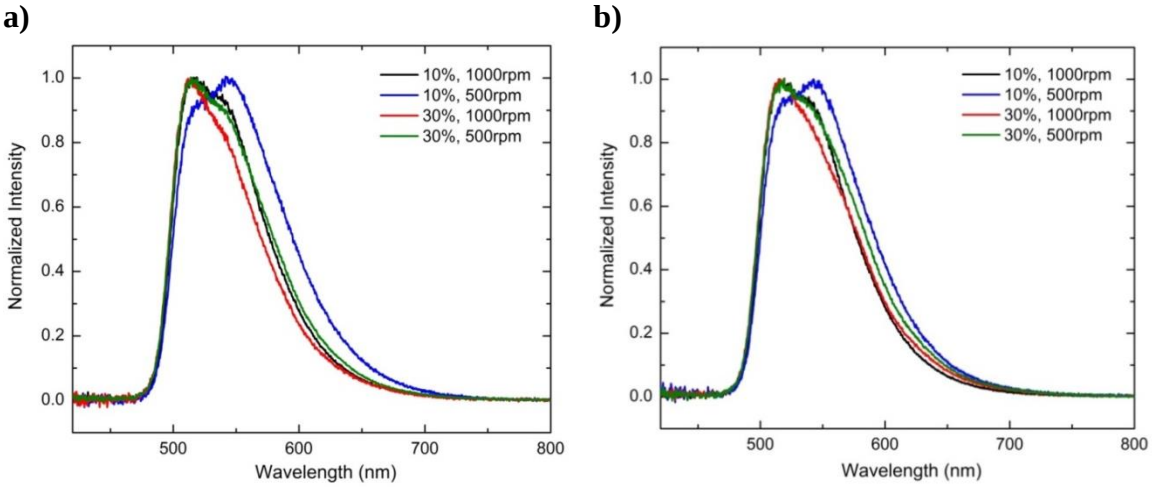

Figure 3.30. Electroluminscence spectra of the devices based on the alkylated host materials **DTPBP-C8** (a) and **DTPBP-C2C6** (b) for the green emitter $Ir(mppy)_3$ at different doping levels.

The alkylated **DTPBP** materials were also tested as hosts for TEG. The *J-V-L* characteristics of these devices are shown in Figure 3.31. The turn-on voltages for the TEG devices are between 2.4 – 2.9 V. A luminance of 1000 cd m^{-2} is reached with driving voltages above 9 V. The significantly higher driving voltage may be due to the

larger energy gap of TEG, and may indicate direct injection of charge carriers from the transport layers to the emitters rather than to the host. As with $Ir(mppy)_3$, the higher doped devices give higher current densities, and higher luminance values at each driving voltage, for both types of host material. Since the charge transport characteristics of the host materials do not improve with increased TEG-doping (Figure 3.26), this effect can be attributed to more efficient emission by direct charge injection into the dopant at higher concentrations, rather than better charge injection or transport in the host. However, the difference in *J-V-L* characteristics of the 30 % TEG-doped devices relative to the 10 % TEG-doped devices is much smaller than it is for the $Ir(mppy)_3$ devices.

The current efficiencies of the TEG-doped devices are shown in Figure 3.32a. The performance of all devices show little dependence on the doping level at low brightness levels, due to the similarity in *J-V-L* behavior at low luminance values. At higher brightness, the 10 % TEG-doped devices show faster efficiency roll-off. This effect may be due to poor energy transfer of charges injected in the host material to the emitter, again due to a mismatch of their EA levels. The peak efficiencies of the devices ranged from 35 to 45 cd A^{-1}. At 1000 cd m^{-2}, the efficiencies drop to 25 to 30 cd A^{-1}. These characteristics are significantly lower than the 55 cd A^{-1} reported for a TEG device with a phosphine oxide-based host material.[203] However, the architecture for the latter device makes use of an HTL material (*N*,*N*'-bis(4-(6-(3-ethyloxetan-3-y)methoxy))-hexylphenyl)-*N*,*N*'-diphenyl-4,4'-diamin; OTPD), that has a sufficiently high EA level to simultaneously serve as electron blocking layer. This may be a particularly significant architectural enhancement that can improve the performance of the devices reported here due to the poor electron mobility of the alkylated **DTPBP** host materials.

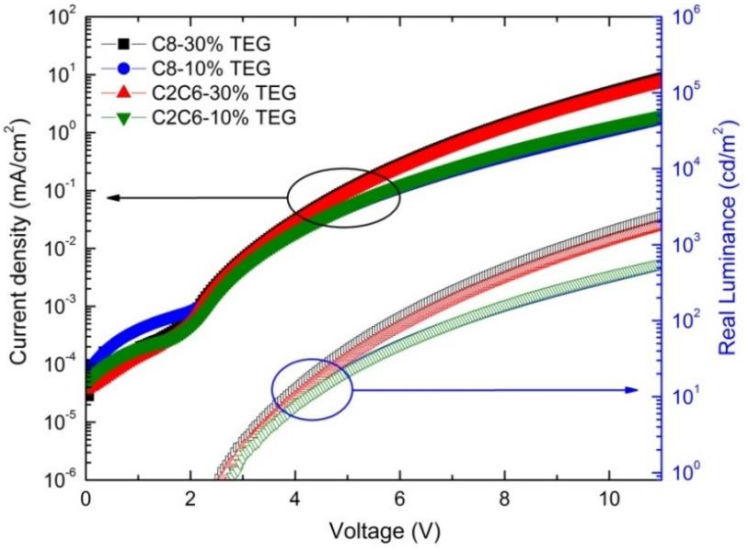

Figure 3.31. Current-voltage-luminance characteristics of the alkylated host materials **DTPBP-C8** and **DTPBP-C2C6** for the green emitter TEG at different doping levels.

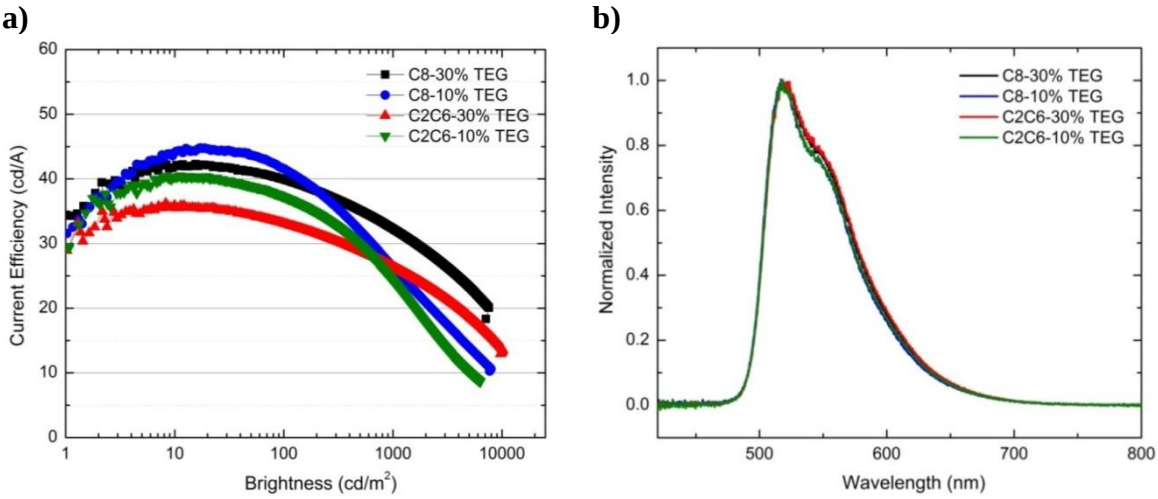

Figure 3.32. Current efficiency (a) and electroluminscence spectra (b) of the devices based on the alkylated host materials **DTPBP-C8** and **DTPBP-C2C6** for the green emitter TEG at different doping levels.

The electroluminescence spectra of all TEG-based devices are shown in Figure 3.32b. The peak at 525 nm can be attributed to the emission from TEG, and the devices with higher TEG-doping show a peak around this wavelength, whereas the lower doped devices peak just below 520 nm. There is little emission contribution from the host

materials, which may be attributed to direct charge injection to the emitter, and favorable energy transfer of excited states created in the host to TEG.

3.4. Summary

The triphenylene-based host materials were synthesized in less than five steps and with high overall yields. The synthetic approach took advantage of Ir-catalyzed C-H activation, leading to one-step borylations that gave high yields. This method gave rise to regiospecific borylation of highly symmetric triphenylene, but gave rise to a mixture of isomers in alkylated triphenylene derivatives. The resulting alkylated host materials were also regioisomeric mixtures, and resulted in an unprecedented approach to stabilizing amorphous film morphologies in low glass transition materials.

The material properties and device performance characteristics of the triphenylene-based host materials are summarized in Table 3.8. The planarity and rigidity of the triphenylene core in **DTPBP** induces crystallinity in the unalkylated derivative, giving rise to fibers with high aspect ratios formed from solution. The conformational flexibility around the biphenyl and triphenyl-biphenyl linkage, along with the triphenylene core, gave rise to a balance between order and disorder, leading to high T_g, and liquid crystalline textures. The alkylated derivatives gave uniformly smooth ($\mathbf{R_{rms}}$ < 1 nm), and morphologically stable films, even after annealing at elevated temperatures. The lack of electron-donating and electron-withdrawing moieties in the structure of these host materials gave rise to deep IP and high EA levels, but the π-extension from the *p*-terphenyl fragment in the structure leads to a moderate triplet energy, despite the high energy gap. The lack of electron- donating or withdrawing moieties, along with the disorder in the materials, also resulted in low charge transport mobilities. The reported

mobilities, however, are strongly dependent on device architecture, and may be improved with better energy level alignment between electrodes and hosts.

Table 3.8. Summary of material properties and OLED device performance characteristics of triphenylene-based host materials.

	IP (eV)	EA (eV)	E_T (eV)	T_g (°C)	μ^a (cm^2/Vs) μ_h	μ_e	Emitter	CE[b] (cd/A)	PE[b] (lm/W)
DTPBP	6.6	3.1	2.6	130	10^{-5}	10^{-8}	$Ir(ppy)_3$	70	57
DTPBP-C8	6.1	2.5	2.6	43		10^{-8}	$Ir(mppy)_3$ TEG	42 45	
DTPBP-C2C6	6.1	2.5	2.6	59			$Ir(mppy)_3$ TEG	40 40	

[a]Measured at [1000 V/cm]^{½}. [b]CE – Current Efficiency, PE – Power efficiency; Peak values for best device architectures.

All **DTPBP** materials were studied as host materials for green emitters and gave comparable performance characteristics to other host materials reported in the literature.

3.5. Synthetic Details

3,3'-dibromo-1,1'-biphenyl (3.1). This procedure was adapted from reference. [182] 1,3-dibromobenzene (10 mmol, 2.36 g) was dissolved in anhydrous THF in a two-neck round bottom flask fitted with a stir bar. The solution was cooled to −78 °C in a dry ice/isopropanol bath and stirred for 30 mins. Then t-BuLi (1.7 M, 11 mmol, 6.5 mL) was added dropwise and the reaction mixture stirred at −78 °C for 1.5 hrs. Then dry and degassed CuCN (5 mmol, 0.45 g) was added and stirred until dissolved. Then duroquinone (15 mmol, 2.46 g) was added and the reaction stirred and allowed to come to r.t. over 4 hrs. The reaction mixture was then quenched with 2 *M* HCl (aq.) (1000 mL). Then THF was evaporated under vacuum. Then the organics were extracted with ether (3 × 500 mL). The organics were separated and then washed with water (1000 mL), and

brine (1000 mL). The organic layer was dried over $MgSO_4$ and concentrated under vacuum. Product was purified with column chromatography and eluted with hexanes to yield 1.27 g (81%) of the pure product. ^{1}H NMR (300 MHz, $CDCl_3$): δ 7.70 (t, J = 1.9 Hz, 2H), 7.54 – 7.44 (m, 4H), 7.31 (s, J = 8.7 Hz, 2H).). ^{13}C NMR (75 MHz, $CDCl_3$): δ 141.94, 131.00, 130.58, 130.34, 125.92, 123.19. HRMS (EI, $[M+H]^+$) *m/z* calcd. for $C_{12}H_8Br_2$ 309.8993; found 309.8997.

4,4,5,5-tetramethyl-2-(triphenylen-2-yl)-1,3,2-dioxaborolane (3.2). Triphenylene (10 mmol, 2.2831 g), B_2pin_2 (11 mmol, 2.7936 g), $[Ir(COD)(OMe)]_2$ (0.2 mmol, 0.1326 g), and dtbpy (0.4 mmol, 0.1075 g) were all charged into an oven-dried schlenk tube with a stir bar. The solids were pumped under vacuum for 10 min. then purged with Ar three times. Then cyclohexane (50 mL) was added and the mixture was bubbled with Ar for 45 min. The reaction set up was then fitted with a condenser and the mixture heated to reflux (~85 ^{o}C) for 16 hours. The reaction was then cooled to room temperature and the solvent was removed in vacuo. The reaction mixture was redissolved in CH_2Cl_2 and passed through short pad of boric acid treated silica gel, and eluted with CH_2Cl_2. The solvent was then removed under vacuum and the mixture purified in batches by column chromatography on boric acid treated silica gel and eluted with 1:1 hexanes: CH_2Cl_2. The fractions containing the mono-borylated product were collected and concentrated under reduced pressure to yield 2.20 g (62 %) of the pure product. ^{1}H NMR (300 MHz, $CDCl_3$): δ 9.17 (s, 1H), 8.88 – 8.79 (m, 1H), 8.75 – 8.60 (m, 4H), 8.08 (dd, J = 8.2, 1.1 Hz, 1H), 7.75 – 7.60 (m, 4H), 1.45 (s, 12H). ^{13}C NMR (75 MHz, $CDCl_3$): δ 132.92, 132.15, 130.67, 130.43, 130.03, 129.79, 129.77, 129.12, 127.75, 127.33, 127.29, 123.83, 123.41,

123.29, 122.57, 84.16, 25.12. HRMS (EI, $[M+H]^+$) *m*/*z* calcd. for $C_{24}H_{23}BO_2$ 354.1791; found 354.1795.

General Procedure for Friedel-Crafts Acylation: $AlCl_3$ (1.05 eq.) was suspended in carbon disulfide (0.2 M). Triphenylene (1 eq.) and alkyl chloride (2 eq.) were separately dissolved in CS_2 and slowly added to the mixture. The reaction mixture was stirred for 6 hrs then quenched with 0.1 *M* HCl (aq.). The organics were then extracted with CH_2Cl_2, washed with saturated $NaHCO_3$ (aq.), then brine. The organic layer was then separated and dried over Na_2SO_4. The product was passed through a short pad of basic alumina.

1-(triphenylen-2-yl)octan-1-one (3.3a). ^{1}H NMR (300 MHz, $CDCl_3$): δ 9.01 (d, J = 1.8 Hz, 1H), 8.61 – 8.29 (m, 5H), 7.96 (dd, J = 8.6, 1.8 Hz, 1H), 7.59 (s, 4H), 3.01 (t, 2H), 1.91 – 1.69 (m, 2H), 1.57 – 1.20 (m, 8H), 1.04 – 0.85 (m, 3H). ^{13}C NMR (75 MHz, $CDCl_3$): δ 200.20, 134.96, 132.98, 130.59, 129.84, 129.50, 129.36, 128.87, 128.24, 127.69, 127.47, 127.37, 125.88, 123.95, 123.55, 123.42, 123.36, 123.30, 38.84, 31.94, 29.58, 29.43, 24.57, 22.85, 14.31. HRMS (EI, $[M+H]^+$) *m*/*z* calcd. for $C_{26}H_{26}O$ 354.1984; found 354.1981.

2-ethyl-1-(triphenylen-2-yl)hexan-1-one (3.3b). ^{1}H NMR (300 MHz, $CDCl_3$): δ 9.29 (d, J = 1.6 Hz, 1H), 8.85 – 8.51 (m, 5H), 8.19 (dd, J = 8.6, 1.7 Hz, 1H), 7.79 – 7.57 (m, 4H), 3.73 – 3.40 (m, 2H), 2.02 – 1.80 (m, 2H), 1.46 – 1.22 (m, 6H), 0.94 – 0.81 (m, 6H). ^{13}C NMR (75 MHz, $CDCl_3$): δ 204.69, 136.02, 133.29, 130.81, 130.09, 129.78, 129.76, 129.09, 128.46, 127.92, 127.72, 127.61, 126.32, 124.13, 124.07, 123.84, 123.57, 123.53, 48.01, 32.11, 30.06, 25.77, 23.19, 14.18, 12.28. HRMS (EI, $[M+H]^+$) *m*/*z* calcd. for $C_{26}H_{26}O$ 354.1984; found 354.1974.

General Procedure for Wolff-Kishner Reductions: The alkanoyl chloride was dissolved in a two neck round bottom flask fitted with a Dean-Stark trap, and dissolved in diethylene glycol (0.2 *M*). Then hydrazine hydrate (5 eq.) was added and the mixture was heated to 100 °C for 10 mins. Then the mixture was cooled to r.t. Then KOH (6 eq.) was added to the mixture and the reaction was heated to 150 °C, then 250 °C for two hrs. Then the reaction mixture was cooled to r.t., diluted with water, and quenched with 1 *M* HCl (aq.). Then the organics were extracted with CH_2Cl_2. The organic layer was then washed with water, then brine. The organic layer was then dried over $MgSO_4$, and concentrated. The product was then purified *via* column chromatography, and eluted with 95:5 hexanes:CH_2Cl_2.

2-octyltriphenylene (3.4a). ^{1}H NMR (300 MHz, $CDCl_3$): δ 8.78 – 8.62 (m, 4H), 8.58 (d, J = 8.5 Hz, 1H), 8.50 (d, J = 1.4 Hz, 1H), 7.76 – 7.61 (m, 4H), 7.52 (dd, J = 8.4, 1.7 Hz, 1H), 2.92 (t, 2H), 1.92 – 1.78 (m, 2H), 1.57 – 1.29 (m, 10H), 1.07 – 0.93 (m, 3H).). ^{13}C NMR (75 MHz, $CDCl_3$): δ 142.02, 130.14, 130.10, 130.02, 129.94, 129.62, 128.14, 127.91, 127.27, 127.17, 126.89, 123.46, 123.42, 123.41, 123.26, 122.85, 36.55, 34.93, 32.20, 31.89, 25.54, 22.97, 22.94, 14.37. HRMS (EI, $[M+H]^+$) *m*/*z* calcd. for $C_{26}H_{28}$ 354.2191; found 340.2197.

2-(2-ethylhexyl)triphenylene (3.4b). ^{1}H NMR (300 MHz, $CDCl_3$) δ 8.72 – 8.60 (m, 4H), 8.57 (d, J = 8.5 Hz, 1H), 8.42 (d, J = 1.4 Hz, 1H), 7.72 – 7.59 (m, 4H), 7.48 (dd, J = 8.4, 1.7 Hz, 1H), 2.79 (d, J = 10.5 Hz, 2H), 1.86 – 1.66 (m, 1H), 1.48 – 1.19 (m, 8H), 1.02 – 0.83 (m, 6H). ^{13}C NMR (75 MHz, $CDCl_3$): δ 141.12, 130.14, 130.10, 130.02, 129.80, 129.61, 128.91, 127.87, 127.36, 127.28, 127.23, 126.97, 123.75, 123.51, 123.46, 123.30, 41.46, 40.71, 32.62, 29.12, 25.73, 23.29, 14.40, 11.09.

General Procedure for Suzuki Coupling: The boronic ester (2.1 eq.), and 3,3'-dibromo-1,1'-biphenyl (1 eq.), SPhos (6 mol%), and Pd_2dba_3•$CHCl_3$ (3 mol%) were all charged into an oven-dried schlenk tube with a stir bar and pumped under vacuum for 30 min. then purged with Ar three times. Degassed xylenes and 3 *M* K_3PO_4 (aq.) were then added to the reagents. The schlenk tube was then fitted with a condenser and the reaction mixture heated to 150 °C and refluxed for 48 hrs. Then the reaction was cooled to room temperature, the solvent was reduced *in vacuo*, and the concentrated reaction mixture precipitated into cold MeOH (600 mL). After stirring for 3 hrs, the solids were filtered and air-dried under vacuum. The solids were then loaded onto a column of silica gel and eluted with hot CH_2Cl_2 or 3:1 hexanes:CH_2Cl_2.

3,3'-di(triphenylen-2-yl)-1,1'-biphenyl (DTPBP). Further purification by sublimation was done in batches at 350 °C and 10^{-6} torr. ^{1}H NMR (300 MHz, $C_2D_2Cl_4$, δ 6.0 ppm): δ 8.96 (d, J = 1.7 Hz, 2H), 8.85 – 8.74 (m, 4H), 8.74 – 8.63 (m, 6H), 8.18 (t, 2H), 8.03 (dd, J = 8.6, 1.6 Hz, 2H), 7.89 (d(t), J = 7.7 Hz, 2H), 7.82 (d(t), J = 7.8 Hz, 2H), 7.77 – 7.64 (m, 10H). HRMS (EI, $[M+H]^+$) *m*/*z* calcd. for $C_{48}H_{30}$ 606.2348; found 606.2349. Elem. Anal. calcd. C, 95.02; H, 4.98; found: C, 94.68; H, 4.87.

3,3'-bis(octyltriphenylen-2-yl)-1,1'-biphenyl (DTPBP-C8). ^{1}H NMR (300 MHz, $CDCl_3$): δ 8.98 – 8.87 (m, 2H), 8.82 – 8.50 (m, 8H), 8.46 (s, 2H), 8.16 (s, 2H), 8.03 – 7.59 (m, 12H), 7.50 (d, J = 8.1 Hz, 2H), 2.97 – 2.79 (m, 4H), 1.89 – 1.69 (m, 4H), 1.57 – 1.21 (m, 20H), 0.96 (d, J = 1.2 Hz, 6H). ^{13}C NMR (75 MHz, $CDCl_3$): δ 143 – 121 (mH), 36.52, 32.14, 31.86, 29.78, 29.69, 29.54, 22.92, 14.36. HRMS (MALDI, $[M+H]^+$) *m*/*z* calcd. for $C_{64}H_{62}$ 830.4852; found 830.4822. Elem. Anal. calcd. C, 92.48; H, 7.52; found: C, 92.49; H, 7.39.

3,3'-bis((2-ethylhexyl)triphenylen-2-yl)-1,1'-biphenyl (DTPBP-C2C6). ^{1}H NMR (300 MHz, $CDCl_3$) δ 8.96 – 8.88 (m, J = 5.6 Hz, 2H), 8.81 – 8.61 (m, 6H), 8.61 – 8.53 (m, 2H), 8.51 – 8.40 (m, 2H), 8.14 (s, 2H), 8.02 – 7.60 (m, 12H), 7.53 – 7.43 (m, 2H), 2.89 – 2.69 (m, 4H), 1.76 (s, 2H), 1.49 – 1.17 (m, 16H), 1.03 – 0.80 (m, 12H). ^{13}C NMR (75 MHz, $CDCl_3$): δ 143 – 121 (mH), 41.45, 40.71, 32.62, 29.12, 25.73, 23.30, 14.41, 11.07. HRMS (MALDI, $[M+H]^+$) *m*/*z* calcd. for $C_{64}H_{62}$ 830.4852; found 830.4810. Elem. Anal. calcd. C, 92.48; H, 7.52; found: C, 92.47; H, 7.30.

CHAPTER 4

TWISTED INTRAMOLECULAR CHARGE TRANSFER IN THIOPHENE-BASED AROMATIC/QUINOID CHROMOPHORES FOR THIRD-ORDER NONLINEAR OPTICS

4.1. Introduction to Nonlinear Optics

The field of nonlinear optics fundamentally deals with interactions between light and matter in which the response to the applied electromagnetic field (i.e. light) can be described by a nonlinear function. The history of nonlinear optics is often traced back to John Kerr in 1875, who is credited to be the first to describe the change in the refractive index of a material when subjected to a voltage.[204] In his work, a collimated beam of sunlight was passed through a prism and a polarizer, then directed to an isotropic sample under the influence of an electric field oriented at a 45º angle between two crossed polarizers. The resultant transmitted beam yielded an intensity which was described by a quadratic (i.e. nonlinear) function of the applied voltage, a phenomenon that later on came to be known as the Kerr Effect.

Despite this early finding, the field of nonlinear optics did not begin to expand until the advent of lasers in 1960. This is because the nonlinear response can only be observed with high intensity electromagnetic fields, and it was not until the invention of lasers that light of sufficient intensity to bring about nonlinear responses from common materials was made available. Only a year after the discovery of the laser, a major milestone that served as a springboard for the field of nonlinear optics was reported: in 1961 Franken, *et al*.[205] described the phenomenon of second-harmonic generation (SHG),

in which a ruby laser passing through a crystal of quartz gave rise to two transmitted beams: one at the same frequency as the incident beam (the incident beam simply transmitted by the crystal), the other at exactly *twice* the frequency.

How does the nonlinear response arise? When a material is subjected to an electric field the electrons of the material will begin to oscillate with the light wave, causing a distortion of its electron density distribution. The anisotropic electron density distribution creates an *induced dipole* ($\boldsymbol{\mu}^{\mathbf{ind}}$), or a polarization (induced dipole per unit volume), from the separation of high electron density (negative), and low electron density (positive) centers. This charge separation that creates the induced dipole depends on the applied electric field. Under low intensity electric fields (**E**), the distortion of the equilibrium electron distribution is proportional to the strength of the field, and the response is well-described by a linear relationship, given by*:

$$\boldsymbol{\mu}^{\mathbf{ind}} = \boldsymbol{\alpha}\mathbf{E} \tag{4.1}$$

where $\boldsymbol{\alpha}$ is the linear polarizability, and gives a measure of how easily distorted the electron distribution of a molecule is.[8] The applied electric field can be in the form of electromagnetic radiation, and when the frequency of the oscillating field is in the UV-vis-NIR (~ 10^{15} s^{-1}), only the electron density distribution is distorted fast enough to contribute to the induced dipole or polarization.

On the other hand, if a material is subjected to very intense fields, such as those delivered by lasers, the material polarization induced by the applied field is enough to create an internal electric field that *itself* can alter the applied field, and the resulting polarization. Thus, the polarization response can no longer be described by the above

* In the interest of simplifying the equations shown here and for the purposes of showing basic concepts, the frequency dependence and tensorial nature of all quantities are not shown.

linear equation (eq. 4.1), because the polarizability, **α**, of the material is no longer constant. The polarizability itself changes with the electric field! The description of the response becomes *nonlinear*, and the Taylor series is commonly employed to expand the linear description, as in:[206]

$$\mu = \boldsymbol{\mu^0} + \left(\frac{\partial \boldsymbol{\mu}}{\partial \mathbf{E}}\right)\mathbf{E} + \frac{\mathbf{1}}{\mathbf{2}!}\left(\frac{\partial^2 \boldsymbol{\mu}}{\partial \mathbf{E}\partial \mathbf{E}}\right)\mathbf{EE} + \frac{\mathbf{1}}{\mathbf{3}!}\left(\frac{\partial^3 \boldsymbol{\mu}}{\partial \mathbf{E}\partial \mathbf{E}\partial \mathbf{E}}\right)\mathbf{EEE} + \cdots \tag{4.2}$$

Each of the differential prefactors equates to different order microscopic polarizabilities, and to the corresponding macroscopic susceptibilities, shown in Table 4.1. The analogous macroscopic polarization, **P** is described by the following equation where $\mathbf{P^0}$ is the permanent polarization:

$$\mathbf{P} = \mathbf{P^0} + \boldsymbol{\chi^{(1)}}\mathbf{E} + \boldsymbol{\chi^{(2)}}\mathbf{EE} + \boldsymbol{\chi^{(3)}}\mathbf{EEE} + \cdots \tag{4.3}$$

Table 4.1. Definitions of polarizabilities and susceptibilities.

Microscopic Polarizability		**Macroscopic Susceptibility**	
$\alpha = \frac{\partial \mu}{\partial \mathrm{E}}$	Linear or First-order polarizability	$\chi^{(1)}$	First-order susceptibility
$\beta = \frac{\partial^2 \mu}{\partial \mathrm{E}^2}$	Quadratic or Second-order polarizability (First-order hyperpolarizability)	$\chi^{(2)}$	Second-order susceptibility
$\gamma = \frac{\partial^3 \mu}{\partial \mathrm{E}^3}$	Cubic or Third-order polarizability (Second-order hyperpolarizability)	$\chi^{(3)}$	Third-order susceptibility

While the foregoing definitions do not allow the direct correlation of each nonlinear coefficient to a material parameter, various quantum chemical approaches are available that enable these relations. These give solutions (at different levels of approximation) to the time-dependent Schrodinger equation that is used to describe the polarization of the wave function. For the purposes of identifying important material parameters that can be tuned to maximize nonlinearity, the sum-over-states (SOS) technique, which arises from time-independent perturbation theory, gives the most

commonly used expressions.[206] Specifically, the few-states expressions for these coefficients are:

$$\boldsymbol{\alpha} \propto \frac{\boldsymbol{M_{ge}^2}}{\boldsymbol{E_{ge}}} \tag{4.4}$$

$$\boldsymbol{\beta} \propto \frac{\boldsymbol{M_{ge}^2}\,\boldsymbol{\Delta\mu}}{\boldsymbol{E_{ge}^2}} \tag{4.5}$$

$$\boldsymbol{\gamma} \propto \frac{\boldsymbol{M_{ge}^2}\,\boldsymbol{\Delta\mu^2}}{\boldsymbol{E_{ge}^3}} - \frac{\boldsymbol{M_{ge}^4}}{\boldsymbol{E_{ge}^3}} + \frac{\boldsymbol{M_{ge}^2}}{\boldsymbol{E_{ge}^2}}\frac{\boldsymbol{M_{ge'}^2}}{\boldsymbol{E_{ge'}}} \tag{4.6}$$

where $\boldsymbol{M_{ge}}$ is the transition dipole between the ground and first excited state, $\boldsymbol{M_{ge'}}$ is the same quantity for the ground and higher excited states, $\boldsymbol{\Delta\mu}$ is the difference in static dipole moments between ground and excited state ($\boldsymbol{\mu_{ee} - \mu_{gg}}$), and $\boldsymbol{E_{ge}}$ and $\boldsymbol{E_{ge'}}$ are the transition energies between ground and first excited state, and ground and higher excited states, respectively. Thus, eq. 4.4 to 4.6 provide parameters that can be related to structural features of a molecule that can be synthetically tuned. Focusing particularly on the third-order polarizability, **γ**, the nonlinear response principally arises from three states: the ground state (*g*), a low-lying first excited state (*e*), and a second excited state (*e'*) that can be accessed from the first excited state. It is also clear that for the third-order response to be large, these inter-state excitations must have large transition dipole moments (large $\boldsymbol{M_{ij}}$), and small energy differences (small $\boldsymbol{E_{ij}}$). The $\boldsymbol{\Delta\mu}$ in the first term points to the importance of dipolar or non-centrosymmetric structures. Finally, factoring out the common term $\boldsymbol{M_{ge}^2/E_{ge}}$, which is equivalent to **α**, means that easily linearly polarized electron clouds are also desirable for enhanced third-order nonlinear properties.

Aside from the aforementioned optical Kerr effect and second harmonic generation, other nonlinear optical phenomena of interest are: (1) the intensity (I) dependence of the material refractive index that finds use in optical switching:

$$\boldsymbol{n_2(\lambda) = \frac{8\pi^2}{cn_0(\lambda)} \frac{\chi^{(3)}(\lambda)}{6}} \tag{4.7}$$

where $n_2(\lambda)$ is the nonlinear refractive index, $n_0(\lambda)$ is the intensity independent refractive index, and c is the speed of light in a vacuum; and (2) the intensity dependence of the total absorption that leads to two-, and three- photon absorption:

$$\boldsymbol{\alpha'_2(\lambda) \approx \alpha_0 + \beta_2 I + \beta_3 I} \tag{4.8}$$

where $\alpha'_2(\lambda)$ is the total absorption, α_0 is the linear absorption coefficient, β_2 is the two-photon absorption coefficient, and β_3 is the three-photon absorption coefficient. These latter parameters are of interest in optical limiting, optical storage, and two-photon fluorescence microscopy.[8,207] The optical switching and the optical limiting potential of an optical material is assessed based on the real, and imaginary parts of the third-order nonlinear susceptibility, and based on the figures of merit W, and T, respectively:

$$W = \frac{n_2(\lambda)I}{2\alpha_0\lambda} > 1 \tag{4.9}$$

$$T = \frac{2\beta_2\lambda}{n_2(\lambda)} < 1 \tag{4.10}$$

4.2. Organic Materials for Nonlinear Optics

Nonlinear optical materials that find use in current devices are still predominantly inorganic salts, such as potassium dideuterium phosphate (KDP), lithium niobate ($LiNbO_3$), barium titanate ($BaTiO_3$), cadmium sulfide, selenide and telluride, and quartz. But inorganic materials suffer from limitations such as an expensive and time-consuming

fabrication due to the requirement of single crystals, and slow response times.[207] Organic molecules are steadily gaining traction as alternative nonlinear optical materials due to their faster response times, low dielectric constants, and easy processability, leading to facile fabrication and integration into devices. Of course, organic materials are also relatively low cost, and their fabrication for device integration can take advantage of advances achieved in materials chemistry and engineering, such as polymer processing, film-forming techniques, and crystal-growth techniques.[207-209] From a chemistry perspective, they are also of great interest due to the relative ease of tuning their properties by a modular alteration of their backbone structure or substituents, and therefore lend themselves well to establishing structure-property relationships. But much work remains toward increasing the nonlinearities of organic materials so that lower field intensities can bring about practical effects in devices.

It is apparent that if the objective is to design materials that will have large polarizabilities, organic compounds with highly delocalized π-electrons would be excellent candidates.[44,210,211] Conjugated organic systems tend to have strong electron-phonon coupling, and excitation by light leads to an *instantaneous* change in the π-electron distribution that induces a coupled geometric relaxation. This enables the fast response times expected for these systems. The polarization in inorganic crystals, on the other hand, is mediated by the motion of ions, and has a predominant vibrational component, leading to slower response times.[207]

An early structure-property relationship established for conjugated systems is that their nonlinear properties are dependent on the length of the π-system. Hermann and Ducuing[44] have shown that while non-conjugated systems show γ that scale linearly with

the number of atoms, π-conjugated systems show **γ** that scaled with the fifth power of the delocalization length. Thus, several polymers, including oligo- and poly- thiophenes, and poly-*p*-phenylenevinylenes,[46,212-216] have been widely studied in nonlinear optics.

In order to take advantage of the contribution from the dipolar term (**Δ*μ***) in eq. 4.6, many extended π-electron networks containing aromatic rings were substituted with electron-donating and electron-withdrawing substituents at opposite ends.[208] This strategy allows for minimization of $\boldsymbol{E}_{\mathbf{ge}}$, while maximizing **Δ*μ*** and $\boldsymbol{M}_{\mathbf{ge}}$, thereby enhancing **γ**. Examples of these early types of nonlinear molecules are *p*-nitroaniline (**PNA**),[217] 4-(*N*,*N*-dimethylamino)-4'-nitrostilbene (**DANS**),[218] and dimethylaminoindoaniline (**DIA**) (Chart 4.1).[219]

The polarization of a polyene or polymethine system has also been modulated by the bond length alternation (BLA), or the average difference between the lengths of adjacent carbon-carbon bonds in its π-system.[219-223] It has been found that in the "cyanine" limit, where BLA approaches zero, **γ** approaches a large and negative value.[220] Here, the substituents at the ends of a polymethine chain are tuned such that: (1) the two resonance forms contributing to the polymethine ground state, the neutral and the charge-separated forms, are equivalent; and (2) there are no large changes in aromaticity from one resonance form to the other. The enhancement of **γ** in this approach relies on strong $\boldsymbol{M}_{\mathbf{ge}}$ and small $\boldsymbol{E}_{\mathbf{ge}}$ as the cyanine limit is approached, despite having a minimum contribution from **Δ*μ***.[224] One of the best performing molecules based on this design paradigm is **Se-7C** (Chart 4.1).[225] To date, this molecule has one of the largest **γ** (real part) values at 1300 nm of -2.2×10^{-31} esu.

Chart 4.1

Donor-Acceptor Functionalized π-Systems

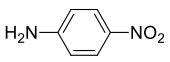

PNA

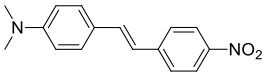

DANS

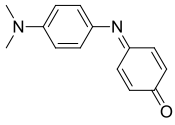

DIA

Bond-Length Alternation Tuned Chromophores

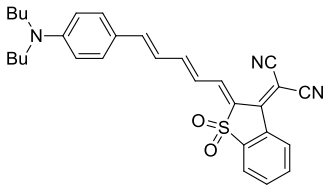

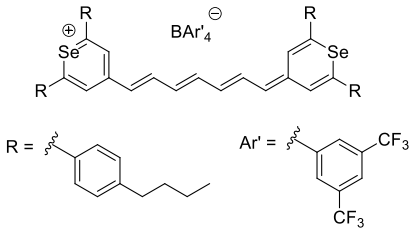

Se-7C

4.3. Twisted Intramolecular Charge Transfer (TICT) Theory and Background

In the aforementioned strategies for attaining large nonlinearities, γ depends strongly on the length of the conjugated system, and therefore these approaches rely to a great extent on further extending the π-electron system to obtain improved performance. These extended systems can suffer from limitations relating to synthetic complexity, chemical, photochemical, and thermal instabilities, and decreasing transparency in the visible and telecommunication wavelengths, and thus limit their viability in many applications.[226]

A recent approach developed by Albert *et al.*[61,227] enables the realization of substantial nonlinearities in short π-systems. The blueprint for this approach involves a forced reduction of the conjugation across a π-electron system, modulated through the dihedral angle across a donor and an acceptor moiety. Creating a large dihedral angle by twisting the system leads to a near-complete charge separation (TICT) that causes the ground state to have a zwitterionic nature. Careful selection of the donor and acceptor moieties can enhance this charge separation by introducing other stabilizing factors, for

example, by aromatization of the zwitterionic structure. This induces a large dipole moment change ($\Delta\boldsymbol{\mu}$), while enabling small excitation energies ($\boldsymbol{E}_{\mathbf{ge}}$), which, according to eqs. 4.5 and 4.6, are expected to contribute to increased nonlinearities.

The theoretical foundation for this new approach was laid using the two-level SOS expression for the first hyperpolarizability, **β**, shown in eq. 4.5. However, several chromophores developed based on this approach have also shown very large **γ**, despite their short conjugation lengths.[228,229] The evolution of **β** with the dihedral twist angle (Figure 4.1) can be traced to its effect on the transfer integral between the donor and acceptor subunits in a molecule linked by a π-bridge.[227] The transfer integral is proportional to the cosine of the twist angle, and is largest when the angle is 0°, or when the donor and acceptor subunits are coplanar. At this angle, the transition dipole between the ground and excited states, $\boldsymbol{M}_{\mathbf{ge}}$, is at a maximum, but at 90° it is zero. The change in dipole moment, $\Delta\boldsymbol{\mu}$, is at a minimum at 0°, but reaches a maximum at 90°. The energy gap, $\boldsymbol{E}_{\mathbf{ge}}$, also varies with the twist angle, and is at a maximum at 0º, but reaches a minimum at 90°. Figure 4.1b shows the progression of these three optical parameters as a function of the dihedral twist angle along a π-system. Overall, the three components combine to maximize **β** at dihedral twist angles very close to 90°. But, **β** goes to zero at 90° due to the contribution from $\boldsymbol{M}_{\mathbf{ge}}$. The same trend is seen when the model is used for donor- and acceptor- substituted biaryls (Figure 4.1a).

Other optical features that are expected from these twisted π-systems are that the linear absorption spectra for these types of molecules will comprise of three distinct peaks: two high-energy peaks corresponding to the absorptions from the two disconnected rings (called intra-subfragment excitations), and one low energy and low

a)

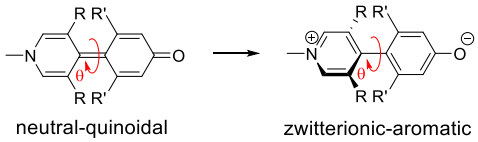

R	R'	Dihedral Twist Angle
H	H	0° [a]
H	Me	36° [b]
Me	Me	52° [b]
Me	t-Bu	68° [b]
t-Bu	t-Bu	83° [a]

b)

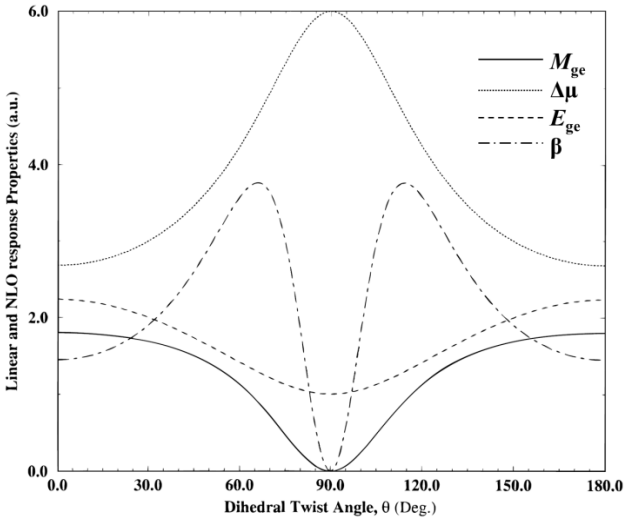

[a] Actual calculated value. [b] Estimated value from reference.

Figure 4.1. (a) Simple representative *tictoid* structures in which the optimized dihedral angle is imposed by the steric crowding around the inter-aryl bond. (b) Variation of calculated optical parameters, $\boldsymbol{E_{ge}}$ (dashed line), $\boldsymbol{M_{ge}}$ (solid line), $\boldsymbol{\Delta\mu}$ (dotted line), and the resultant two-state second-order polarizability, β (dash-dot line), as a function of the dihedral twist angle around ethylene (Figure taken from ref.[227]). (Calculated using semiempirical INDO/S Hamiltonian as implemented in the ZINDO package.) (Reprinted and adapted with permission from Albert, I. D. L.; Marks, T. J.; Ratner, M. A. *J. Am. Chem. Soc.* **1998**, *120*, 11174. Copyright (1998) American Chemical Society.[227])

oscillator strength peak from the charge-transfer absorption between the two rings (inter-subfragment excitation).[227] This offers the possibility of chromophores that give strong absorptions in the UV and IR regions, but have no or minimal absorption in the visible region, which may find potential application in optical limiting.

If a π-system based on two coupled aromatic rings is examined, the change in twist angle from 0° to 90° is found to be accompanied by a change in the π-electron delocalization between the rings. The neutral quinoid structure has the strongest delocalization between the two coplanar rings at one extreme, while the charge-separated structure has zero delocalization or conjugation, but with individual aromatic stabilization, at the opposite extreme. For these types of molecules, (called *tictoid*

molecules,) the twist angle can be used to tune the electron distribution, and the HOMO-LUMO gap ($\boldsymbol{E}_{\mathbf{ge}}$) of the chromophore simultaneously (Figure 4.2). The large change in charge distribution in going from the quinoid to the zwitterionic structure exposes the origin of the enhanced contribution of $\boldsymbol{\Delta\mu}$ to the increase in $\boldsymbol{\beta}$ as the two rings approach a perpendicular geometry (Figure 4.1b). Keinan *et al.*[230] have shown that $\boldsymbol{\beta}$ only becomes large when $\boldsymbol{\Delta\mu}$ is significant, and that this occurs at twist angles between 70 – 85°. The energy gap, on the other hand, is balanced by two counteracting stabilizing factors, aromatization and charge neutrality, which do not coincide in the same structure at a large twist angle.

From a synthetic standpoint, the dihedral angle in these twisted π-systems can be structurally modulated by the substitution pattern about the inter-ring bond. As shown in Figure 4.1a, when positions around the inter-ring bond are unsubstituted, an optimized geometry leading to a 0º calculated inter-ring angle results, while a tetra-*t*-butyl substitution gives an 83° angle.[227]

Higher level theoretical calculations on twisted π-systems with donor and acceptor substituents further reveal the participation from another resonance structure, besides the aromatic, and quinoid structures. This resonance structure takes a diradical form, which is expected to be an important contributor in the gas phase or in nonpolar environments.[231,232] This is particularly important as Nakano *et al.*[233] have shown that systems with an intermediate to large diradical character show further enhancement of $\boldsymbol{\gamma}$. In the case of archetypal twisted π-systems, such as those in Figure 4.3c, the applied field (to simulate solvent) leads to varying contributions from the canonical diradical, and zwitterionic resonance structures to the ground state.[232] When considering the behavior of

Twist Angle	Excitation Energy (eV)	HOMO	LUMO
20º	2.60	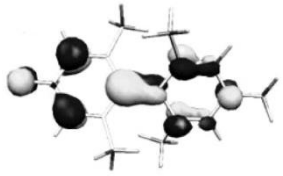	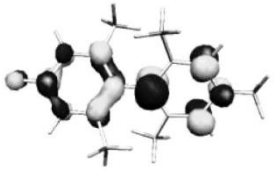
50º	1.80	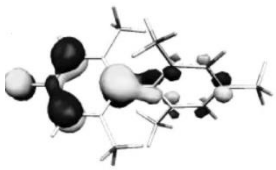	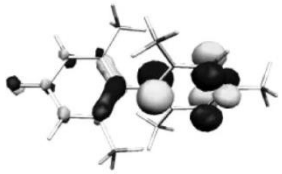
90º	0.55	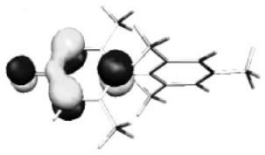	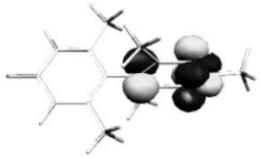

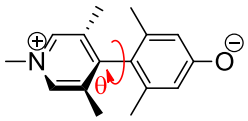

Figure 4.2. Variation in HOMO and LUMO energies and orbitals with variation in twist angle derived from INDO/S calculations. (Reprinted and adapted from *Journal of Molecular Structure: Theochem*, 633, Shahar Keinan, Egbert Zojer, Jean-Luc Brédas, Mark A. Ratner, Tobin J. Marks, Twisted π-system electro-optic chromophores. A CIS vs. MRD-CI theoretical investigation, 227, Copyright (2003), with permission from Elsevier.[230])

these twisted systems in environments of different polarity, not only does the ground state character gradually change from diradicaloid (D) in the gas phase, to zwitterionic (Z) in polar environments, but the energy gaps between these states also change, providing another method by which to tune nonlinear polarizabilities (Figure 4.3a and 4.3c). Note that this is not observed in non-twisted systems with inter-aryl angles of 0º, resulting in very little variation in the energies of the planar zwitterion (PZ) and quinoidal (Q) states (Figure 4.3a).[232] More importantly, an intermediate field strength (simulating a slightly polar solvent such as $CHCl_3$) gives rise to calculated states in which the diradical, and zwitterionic energy levels lie very closely (Figure 4.3a and 4.3c (middle diagram)).

This leads to a very small energy gap, and by the SOS expression, is expected to lead to very large **β** values, and it can be reasonably anticipated, to large **γ** values as well.

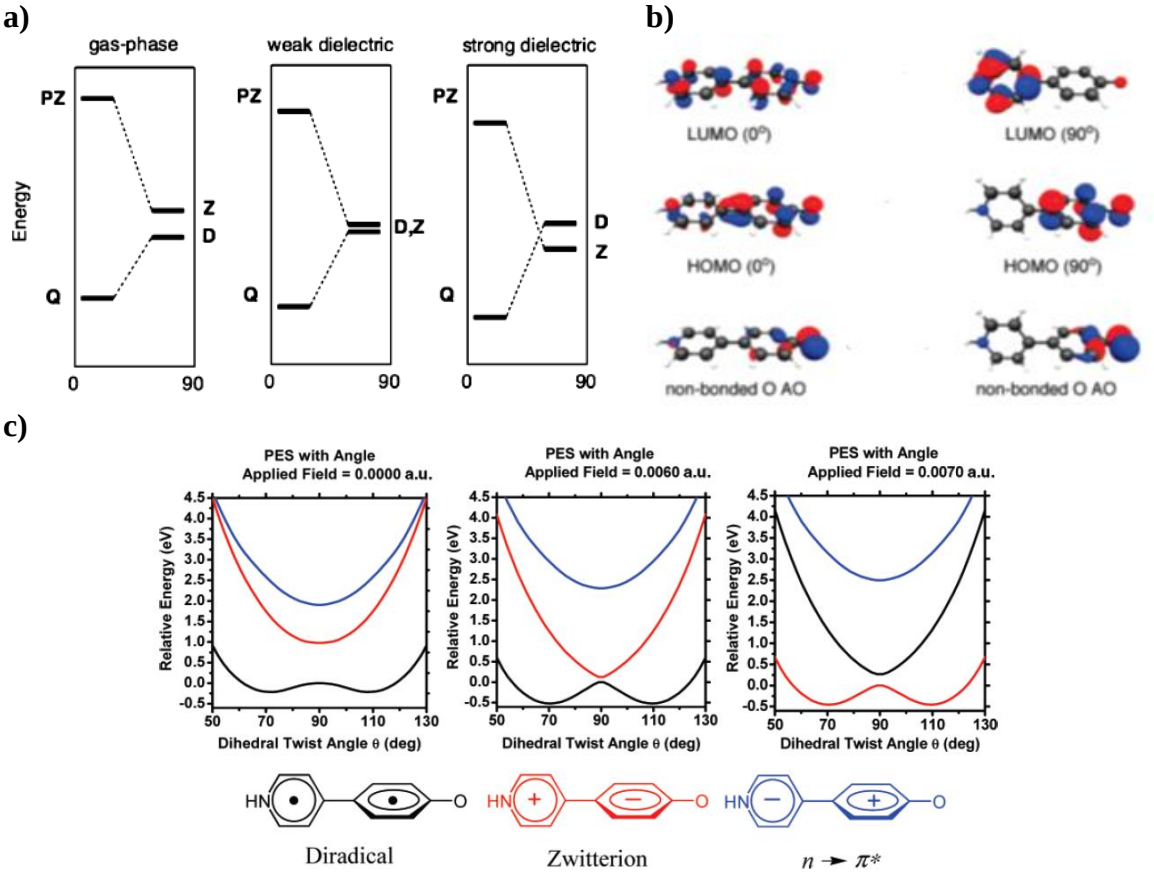

Figure 4.3. Environmental effects on state energies, ordering and electron distribution: (a) State correlation diagram as a function of twist angle and solvent polarity. (Reprinted and adapted with permission from American Chemical Society. Brown, E. C.; Marks, T. J.; Ratner, M. A. Nonlinear response properties of ultralarge hyperpolarizability twisted pi-system donor-acceptor chromophores. Dramatic environmental effects on response. *J. Phys. Chem. B* **2008**, *112*, 44. Copyright (2008) American Chemical Society.[232]) (b) Active space orbitals of a TICT chromophore as a function of twist angle. (Reprinted and adapted with permission from American Chemical Society. Kang, H.; Facchetti, A.; Jiang, H.; Cariati, E.; Righetto, S.; Ugo, R.; Zuccaccia, C.; Macchioni, A.; Stern, C. L.; Liu, Z. F.; Ho, S. T.; Brown, E. C.; Ratner, M. A.; Marks, T. J. *J. Am. Chem. Soc.* **2007**, *129*, 3267. Copyright (2007) American Chemical Society.[234]) (c) Potential energy surfaces (PES) in different simulated environments as a function of twist angle of the three most important lowest energy states shown at the bottom. (Reprinted and adapted with permission from American Chemical Society. Kang, H.; Facchetti, A.; Jiang, H.; Cariati, E.; Righetto, S.; Ugo, R.; Zuccaccia, C.; Macchioni, A.; Stern, C. L.; Liu, Z. F.; Ho, S. T.; Brown, E. C.; Ratner, M. A.; Marks, T. J. *J. Am. Chem. Soc.* **2007**, *129*, 3267. Copyright (2007) American Chemical Society.[234])

Kang *et al.*[234] synthesized a series of chromophores (Chart 4.2) that indeed show large twist angles (~ 90°) based on a tetra-*o*-methyl substitution around the inter-aryl bond linking a pyridinium acceptor, and a dicyanomethanide–substituted phenyl donor. These structures allow for a zwitterionic-aromatic ground state with a significant dipole moment, and moderate transition energy. They have shown that these properties result in significantly large **β** values. In a succeeding publication, He *et al.*[228] reported that **TMC-2** (Chart 4.2), yields **γ** (real part) at 775 nm of 1.4×10^{-33} esu, one of the largest values reported for a condensed π-system.

Chart 4.2

TMC Chromophores

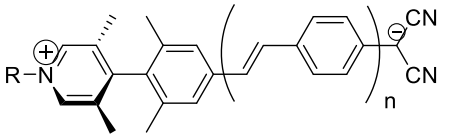

TMC-1, n = 0, R = Me

TMC-2, n = 0, R =

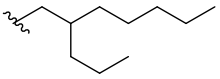

TMC-3, n = 1, R =

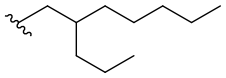

4.4. Design of Chromophores and Computational Screening

A convenient strategy to further modify these TICT systems would be to asymmetrically end cap them with stronger electron-donating and electron-withdrawing substituents to induce a greater contribution from the intramolecular charge-transfer state, which, as previously discussed, can lead to enhanced nonlinear properties.[235] One of the earliest approaches to modulating nonlinear properties devised by Oudar[218] involved functionalizing stilbene with nitro, amino, and chloro groups and a combination of these, resulting in measured **β** values ranging across two orders of magnitude. In the strategy

that involves modulating the BLA of a conjugated bridge to approach the cyanine limit, end capping of the π-bridge is done such that the resonance forms contribute equally to the ground state structure of the chromophore. The initial theoretical investigation into the relationship between BLA and the optical parameters that define **β** made use of charge-supporting amino and carbonyl groups, among others, to simulate an applied field that varies the BLA.[236,237] Later improvements to this strategy also utilized aromatic heterocycles as end groups to balance the gain and loss of aromaticity on either end in shifting from one resonance form to the other.[238] In TICT molecules in which a donor and acceptor group are bridged by a benzene ring, Sen *et al*.[60] have demonstrated that the **β** can reach a maximum only when the strengths of the donor and acceptor are an optimal combination that is proportionate to the strength of their interaction through the π-bridge.

Guided by these findings and the theoretical foundation laid by Albert *et al.*,[227] improved understanding and control of the nonlinear properties of tictoid chromophores can be studied by the use of: i) electron excessive and electron deficient heterocycles to vary the electronic distribution and aromaticity around the acceptor and donor cores; ii) annulated benzene rings to tune the contribution of aromatic and quinoidal resonance forms; iii) different π-system lengths from different heterocycles; and iv) diverse negative-charge bearing groups to further tune the charge distribution. Ultimately, these strategies expand the structure-property relationships established for tictoid systems, lead to improved understanding of the TICT mechanism, and aid in the design of molecules and materials with large nonlinearities. Thus, the families of structures shown in Chart 4.3 were proposed, and quantum mechanical calculations based on response theory at the DFT level utilizing various appropriate methods were performed by Dr. Alexander Baev

(in the group of Prof. Paras Prasad at the State University of New York at Buffalo) to estimate dihedral twist angles (**θ**), dipole moments ($\boldsymbol{\mu_{gg}}$), energy gaps ($\boldsymbol{E_{ge}}$), third-order nonlinear polarizability (**γ**), and all-optical switching figures of merit, T (<< 1) and W (>> 1). The results are shown in Table 4.2. Some structure – property relationships can be drawn from the different families of structures in Chart 4.3 and Table 4.2, and these are discussed in the succeeding sections.

Chart 4.3

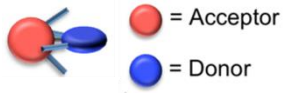
= Acceptor
= Donor

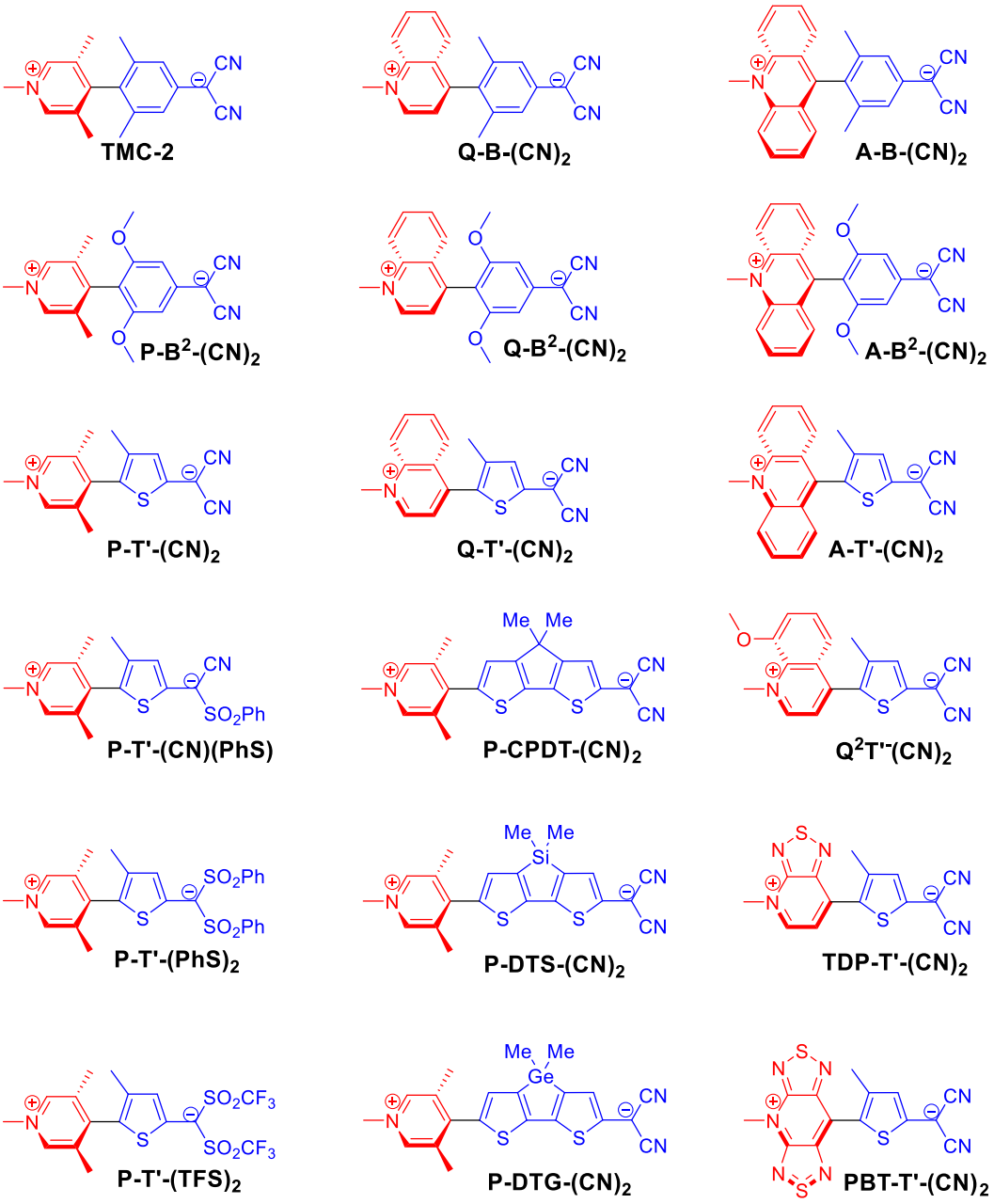
TMC-2
Q-B-(CN)2
A-B-(CN)2
P-B2-(CN)2
Q-B2-(CN)2
A-B2-(CN)2
P-T'-(CN)2
Q-T'-(CN)2
A-T'-(CN)2
P-T'-(CN)(PhS)
P-CPDT-(CN)2
Q2T''(CN)2
P-T'-(PhS)2
P-DTS-(CN)2
TDP-T'-(CN)2
P-T'-(TFS)2
P-DTG-(CN)2
PBT-T'-(CN)2

Table 4.2. Results of quantum mechanical calculations (HF/6-31G*; Dr. A. Baev, SUNY-Buffalo) in a polarizable continuous medium approximating the dielectric constant of $CHCl_3$: Twist Angle, Dipole Moment, Energy Gap, Third-Order Polarizability, and Figures of Merit T and W.

	Structure	Twist angle (θ°)	μ_{gg} (D)[a]	E_{ge} (eV)[a]	γ_{av} (10^{-33} esu) @1550 nm	$T=\alpha_2\lambda/n_2$ @1550 nm	$W=n_2I/\alpha_1\lambda$ I=10 MW/cm^2
1	**TMC-2**	89.9 (90.2)	27.0[b]	2.16[b]	0.05	0.1231	25.02
2	**Q-B-(CN)$_2$**	93.4	38.9	3.11	2.12	0.01÷0.03	1467÷915
3	**A-B-(CN)$_2$**	90.5	37.2	3.51	0.07	0.1	1.48
4	**P-B^2-(CN)$_2$**	74.0	34.9	1.49	−15.3	5.21	10.49
5	**Q-B^2-(CN)$_2$**	64.2	34.3	1.53	−17.1	--	--
6	**A-B^2-(CN)$_2$**	75.8	33.4	0.88	−5064	--	--
7	**P-T'-(CN)$_2$**	74.0 (39.6)	35.4 (20.8)	1.23 (2.5)	−9.08	2.46	2.45
8	**Q-T'-(CN)$_2$**	39.7 (18.4)	32.1 (15.8)	2.04 (2.8)	0.0002	10^4	10^{-4}
9	**A-T'-(CN)$_2$**	67.8 (9.5)	33.5 (12.0)	1.13 (3.1)	−7.22	0.4	0.93
10	**P-T'-(CN)(PhS)**	64.2	--	--	−17.1	3.89	5.05
11	**P-T'-(PhS)$_2$**	75.8	--	--	−5064	0.1	78
12	**P-T'-(TFS)$_2$**	74.7	--	--	−8.71	6.32	3.86
13	**P-CPDT-(CN)$_2$**	63.3	52.2	1.24	−32.3	21.3	2.56
14	**P-DTS-(CN)$_2$**	68.4	52.0	1.04	−5064	0.6	35.89
15	**P-DTG-(CN)$_2$**	67.9	51.7	1.06	−5064	0.1÷0.5	36.6
16	**Q^2-T'-(CN)$_2$**	40.4	32.4	2.04	0.01	10^3	10^{-3}
17	**TDP-T'-(CN)$_2$**	11.7	15.8	2.71	0.09	0.17	0.15
18	**PBT-T'-(CN)$_2$**	86.0	--	1.65	−2.26	2.00	2.84

[a] Values in parentheses show results for the same calculations done in the gas phase. [b] Values from reference [234].

4.4.1. Effect of Acceptor Strength and Benzene Annulation

In entries 1-3, 4-6, and 7-9, the acceptor ring is changed in each series from a pyridine, to a quinoline, to an acridine. In this family of acceptor rings, the electron-

withdrawing strength increases from pyridine < quinoline < acridine. The ability of each ring to stabilize a positive charge increases with increasing annulation of benzene rings, as the positive charge can be delocalized to each additional ring.

In the first series, entries 1-3, all structures have a > 90° calculated twist angle due to the three or four substituents crowding the inter-aryl bond. The magnitudes of the calculated dipole moments indicate that the zwitterionic-aromatic form dominates the ground state, in agreement with the near perpendicular conformations of the two subfragments. This conformation isolates the acceptor ring from conjugation across the inter-aryl bond, and a marked effect is seen in the energy gap, $\boldsymbol{E}_{\mathbf{ge}}$. Increasing the positive charge delocalization by annulation stabilizes the charge-separated form, leading to increasing $\boldsymbol{E}_{\mathbf{ge}}$ with increasing annulation.

In 4-6, and 7-9, the calculated twist angles are significantly lower, due to the reduced steric hindrance around the inter-aryl bond. The calculated dipole moments have values above 30 D and still point to the zwitterionic-aromatic resonance form as the greater contributor to the ground state. These lower twist angles enable some degree of delocalization, and the excited state is likely neutral-quinoidal in structure. The increasing annulation introduces aromaticity with the added rings, and this stabilizes the neutral-quinoidal form, leading to the decrease in $\boldsymbol{E}_{\mathbf{ge}}$ seen in going from pyridine to acridine.

These trends show that the annulation strategy can be used to tune the energy gap between the ground and excited states, while providing steric crowding around the inter-aryl bond.

4.4.2. Effect of Donor Strength

The electron-richness of the donor moiety can be enhanced by the addition of methoxy substituents to the benzene ring, or by changing from a benzene ring to an electron-excessive thiophene ring. Both of these changes in electron density are coupled with changes in steric bulk around the inter-aryl bond, so the trends in properties are not clear cut. However, comparing the families defined by entries (1, 4, and 7), (2, 5, and 8), and (3, 6, and 9) shows that the stronger donating strength in 3,5-dimethoxybenzene and thiophene reduces the $\boldsymbol{E_{ge}}$ values of the respective structures. This can be attributed to the ability of an electron-rich system to raise the HOMO of the conjugated system. It can also be noted that the reduced steric obstruction from these electron-rich donors significantly reduces the inter-aryl twist angle from ~ 90° to 40 – 75°. The electron-rich systems also give markedly larger $\boldsymbol{\gamma}$ values, making this approach an attractive strategy for tuning the TICT mechanism.

4.4.3. Effect of π-Extension

In entries 13-15, a significantly larger ground state dipole moment ($\boldsymbol{\mu_{gg}}$ > 50 D) is calculated for these structures. The twist angles for these systems are still large enough to allow the zwitterionic-aromatic structure to predominate in the ground state, as corroborated by the large $\boldsymbol{\mu_{gg}}$. The dipole moments are comparably large across all structures in the series, and can be attributed to the longer π-system in this series, with the addition of an extra thiophene ring into each structure. This substantial increase of the dipole moment contrasts with the trend in longer polyene/merocyanine systems where the increase in ground state dipole moments tend to be modest.[239] The TICT mechanism

likely enables this unusual $\boldsymbol{\mu_{gg}}$ enhancement in these chromophores. As a result, $\boldsymbol{\gamma}$ is also significantly larger in these series.

In the family defined by the entries 1, 10, 11, and 12, the π-extension in the donor subfragment occurs in the negative-charge bearing group. Entries 10 and 11 extend the π-system with each phenylsulfone substituent, and both structures give larger $\boldsymbol{\gamma}$ values. Thus, these negative-charge bearing groups allow for another mechanism to enhance γ, while keeping the main donor and acceptor rings (and the inter-aryl steric torsion) the same.

4.5. Thiophene-Based TICT Donor-Acceptor Chromophores

Thiophene has been a well-studied heterocycle in nonlinear optics,[70,240-243] and has been credited with enhancing nonlinear properties in many donor-acceptor chromophores. This has been attributed to its lower aromatic delocalization energy (29 kcal/mol vs. 36 kcal/mol for benzene),[243] and higher electron density in its ring carbons. The reduced aromaticity leads to a more efficient polarization and charge separation, whereas the electron excessiveness enables it to act as an auxiliary donor when coupled to an electron-donating group at its electron-rich 2- or 5- positions.[70] The contributions of thiophene to the overall nonlinear response arise from its strong effects on the dipole moment, and the transition energies, both of which are factors that determine $\boldsymbol{\beta}$ and $\boldsymbol{\gamma}$.

The structures in entries 7-9 of Table 4.2 were selected for synthesis in this study, resulting in the tictoid thiophene-based chromophores in Chart 4.4. The aim is to understand the effect of a thiophene ring on the donor subfragment on the original **TMC** chromophore (Chart 4.2) design paradigm. At the same time, the acceptor subfragment is varied by successively introducing annulated benzene rings, which is expected to vary the

contributions of the aromatic and quinoidal resonance forms to the ground and excited state structures. As can be seen from theoretical calculations, these structural modifications result in enhanced ground state dipole moments, reduced transition energies, and altered nonlinear properties.

Chart 4.4

Resonance Forms of Tictoid Thiophene-Based Chromophores

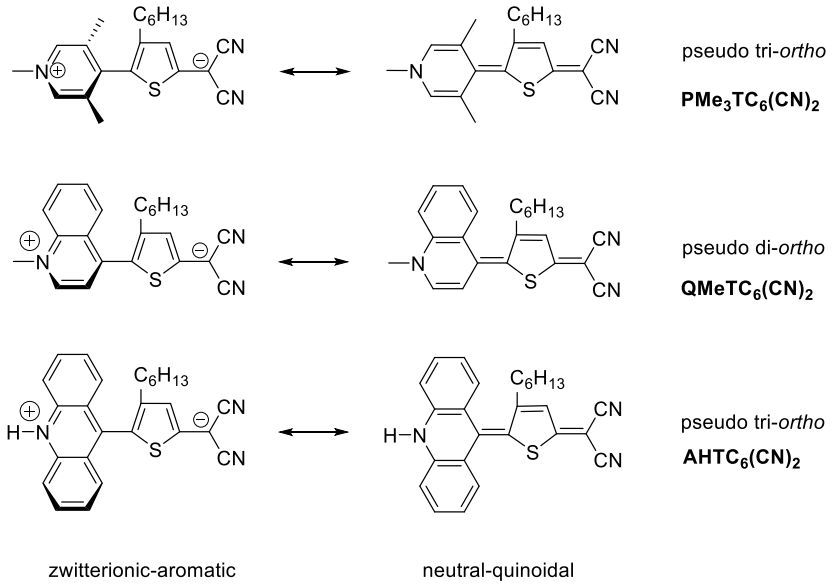

Sterically "Relaxed" Thiophene-Based Chromophore

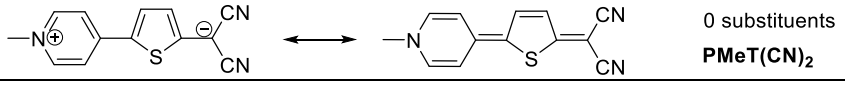

Replacing the six-membered phenyl ring of the **TMC** chromophores with the five-membered heterocycle thiophene introduces a relaxation of the steric torsion around the inter-aryl bond, due to: i) larger bond angles; and ii) smaller degree of substitution around the inter-aryl bond (tetra-*ortho* in pyridinium-phenyl vs. pseudo-tri-*ortho* in pyridinium-thiophenyl). Furthermore, the sizes of the substituents *ortho* to the inter-aryl bond in the quinoline and acridine chromophores (Chart 4.4) are smaller than a CH_3 group. Thus, smaller twist angles are expected, and calculated for these chromophores

(Table 4.2), and a key question addressed here is whether the TICT mechanism will be observed in these sterically-less-hindered chromophores.

Since both steric and electronic effects are being concomitantly induced with these structural modifications, an attempt to isolate these two effects is made by comparing the chromophores (primarily **$PMe_3TC_6(CN)_2$**) with the sterically "relaxed" derivative **$PMeT(CN)_2$** (Chart 4.4), which has been previously reported by Abbotto *et al*.[244]

4.5.1. Synthesis of Tictoid Thiophene-Based Chromophores

The key tuning element of the TICT mechanism relies on a sterically-driven twist between an electron-rich and an electron-poor aromatic ring. Many donor-acceptor synthetic strategies involve the carbon-carbon cross coupling of two aromatic rings,[98] and the steric obstruction from these tictoid chromophores presents a patent synthetic obstacle. However, recent advances in transition metal-catalyzed coupling techniques have made possible high-yielding reactions in sterically demanding substrates.[245-247] Suzuki-Miyaura chemistry was selected as the cross-coupling methodology for the tictoid chromophores due to the commercial availability of 3-hexylthiophene-2-boronic acid pinacol ester, a synthon that combines the thiophene ring with an *n*-hexyl chain as both a steric twist element, and a solubilizing group.

The synthesis of **$PMe_3TC_6(CN)_2$** is shown in Scheme 4.1. The first step is the key sterically-hindered Suzuki cross coupling that links the donor and acceptor subfragments. The starting material used was the *N*-oxide derivative of 4-bromo-3,5-lutidine, as the sluggishness induced by the steric strain demanded a more electron-deficient substrate for

oxidative addition.[234] This material was derived from the one-pot oxidation-bromination of 3,5-lutidine, following the procedure outlined by Klan.[248]

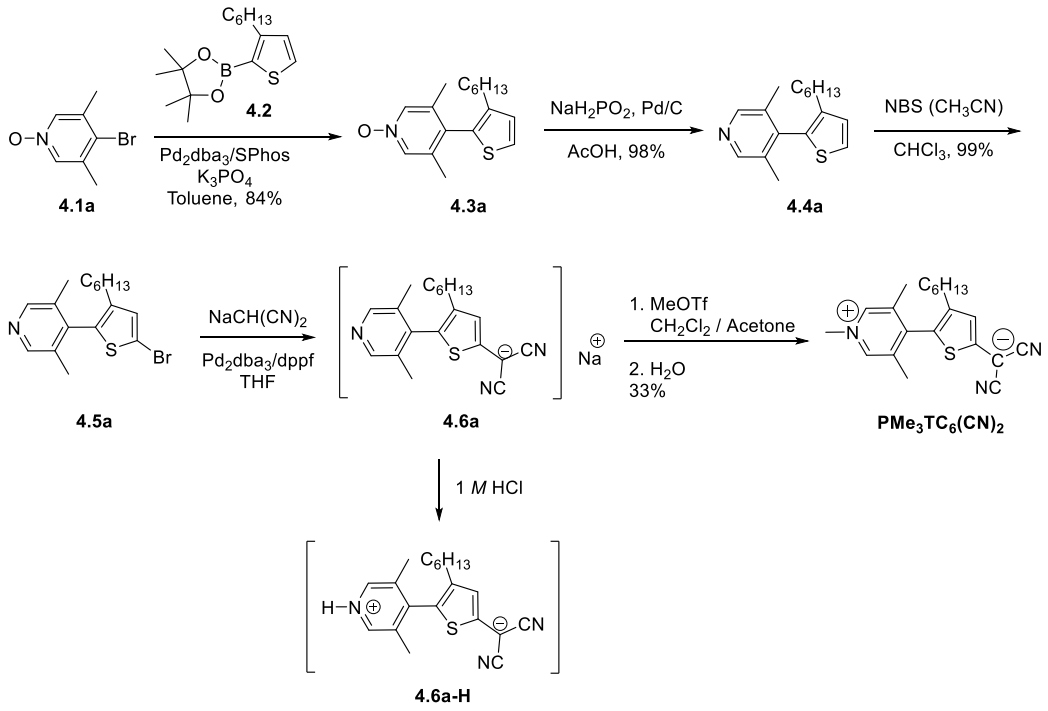

Scheme 4.1: Synthesis of **$PMe_3TC_6(CN)_2$**.

Several conditions and catalytic systems were evaluated for the Suzuki reaction as shown in Table 4.3. The Pd(0) species provided by Pd_2dba_3 was combined with three highly active, electron-rich, and sterically-bulky phosphine ligands: tri-*t*-butylphosphonium tetrafluoroborate ($P(t\text{-}Bu)_3HBF_4$), dicyclohexyl(2',6'-dimethoxy-[1,1'-biphenyl]-2-yl)phosphane (SPhos),[249] and dicyclohexyl-(2-phenanthren-9-yl)-phosphane (DCPPP).[250] Of these, SPhos gave the best yield of 84 %, even at moderate scales of 10 mmol. The activity of SPhos relies on its sterically-bulky and electron-rich nature, both of which are considered necessary contributing factors to the induction of a mechanism (Figure 4.4) involving a more reactive monoligated catalytic species ($L_1Pd(0)$), which can increase the rate of the sterically encumbered reductive elimination step from the *cis*-

Table 4.3. Optimization of the Suzuki cross-coupling step in the synthesis of **$PMe_3TC_6(CN)_2$**.

	Ligand	Base	Solvent/Temp	Scale	Yield
1	7.2mol% $P(t\text{-}Bu)_3HBF_4$	KF	Dioxane/90 °C	1 mmol	52%
2	6mol% SPhos	K_3PO_4	Toluene/100 °C	1 mmol	57%
3	7.2mol% $P(t\text{-}Bu)_3HBF_4$	KF/CsF	Dioxane/90 °C	15 mmol	6%
4	6mol% SPhos	K_3PO_4[a]	Toluene/95 °C	1 mmol	84%
5	8mol% DCPPP[b]	K_3PO_4[a]	Toluene/100 °C	1 mmol	69%
6	6mol% SPhos	K_3PO_4[a]	Toluene/95 °C	10 mmol	53%
7	6mol% SPhos	K_3PO_4[a]	Toluene/95 °C	10 mmol	84%
8	6mol% SPhos	K_3PO_4[a]	Toluene/95 °C	10 mmol	78%

[a]Base was ground into a fine powder prior to use. [b]Catalyst loading was 2 mol %.

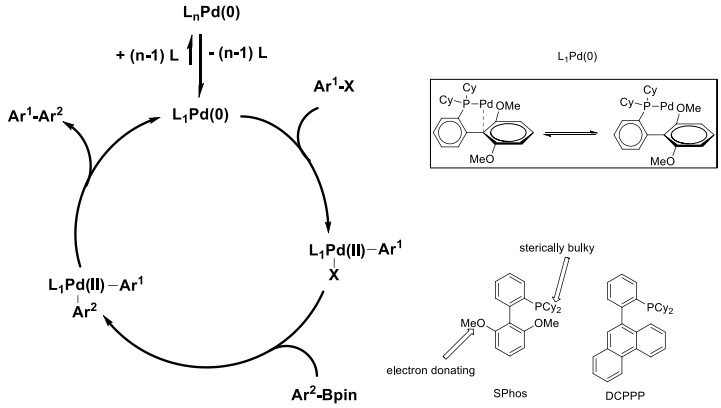

Figure 4.4. Proposed mechanism for Suzuki coupling involving an electron-rich sterically-bulky ligand like SPhos or DCPPP. Inset shows the stabilization of the monoligated species in the SPhos case by electron donation from the dimethoxybenzene ring through the Pd–C(ipso) bond (in red). (Adapted from ref. [247])

Pd(II)(Ar^1)(Ar^2) intermediate.[247,250,251] If the ligand were not sufficiently sterically bulky, the monoligated species will not be favored over the diligated species, and the resulting Pd–C(ipso) interaction would not be present.[247]

The reaction components required careful drying, and oxygen removal to reduce side reactions,[252,253] and allow the catalyst/ligand system to remain active for the duration

of the sluggish reaction. The lack of water in the reaction mixture also required grinding the inorganic base to a fine powder to aid in homogenizing the reaction mixture.

Two other key steps in this synthesis are the coupling of the negative-charge bearing moiety, and the quaternization of the pyridinium nitrogen. The negative-charge bearing group selected was the dicyanomethanide group, a stable and well-known moiety in nonlinear optical chromophores.[234,244,254,255] This was coupled to the halide **4.5a** *via* a Pd-catalyzed coupling with the CH-acid malononitrile. This reaction mechanism (Figure 4.5) required two equivalents of malononitrile, and four equivalents of the base NaH in order for the reductive elimination step of the catalytic cycle to proceed,[256] but any further excess of base was observed to reduce the halogenated derivative. Work up with water or acid resulted in protonation of the pyridinium ring nitrogen (**4.6a-H**), which has also been observed by Abbotto *et al.*[257] in similar substrates. Protonation of the ring nitrogen prevented purification by chromatographic separation (normal or reversed phase), so the final pyridine *N*-quaternization step was done on the sodium salt product **4.6a**. The salt was purified by selective dissolution and filtration in a variety of solvents and nonsolvents. In attempt to improve the efficiency of this method, the catalytic system

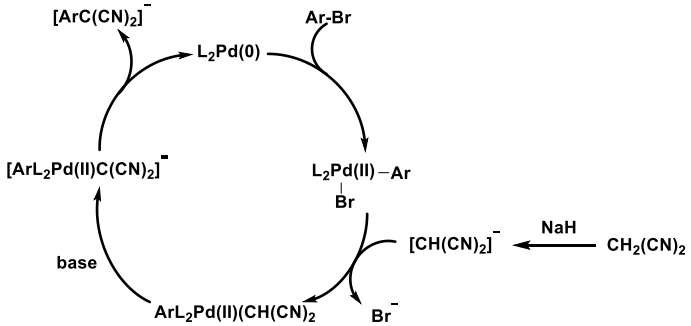

Figure 4.5. Mechanism of palladium-catalyzed coupling of CH-acids to aryl bromides. (Adapted from reference [256].)

was also changed from $Pd(PPh_3)_4$ to Pd_2dba_3/1,1′-bis(diphenylphosphino)ferrocene, the latter yielding more organic-soluble byproducts. A metathesis reaction with the sodium cation being replaced with the more organic-soluble tetraphenylphosphonium (PPh_4^+) cation was also attempted, but did not give improved results.

Quaternization of the pyridinium nitrogen was achieved from the reaction of methyl triflate with the sodium salt **4.6a**. The methyl source being a hard acid, preferentially reacted with the nitrogen lone pair over the dicyanomethanide anion, despite the latter's negative charge.[244] Purification was done *via* column chromatography on neutral alumina gel. Multiple attempts to grow crystals of the chromophores did not yield X-ray quality crystals.

The syntheses of the other thiophene-based chromophores followed a similar methodology, and are shown in Schemes 4.2 to 4.4. The synthesis of **PMeT(CN)$_2$** has been previously reported by Abbotto *et al*.[244] Notably, the other acceptor-fragment-bearing starting materials (4-bromoquinoline and 9-bromoacridine) did not require derivatization to the *N*-oxide, likely due to their reduced steric bulk, and more electron-deficient nature, leading to more facile oxidative addition. Quaternization of the nitrogen atom in the acridine derivative **4.6c** did not proceed with methyl triflate, likely due to the lower nucleophilicity of the acridine nitrogen, and steric hindrance from the protons in the 4- and 5- positions of the acridine ring. Acid treatment of the sodium salt **4.6c** did, however, yield a product that can attain a charge-separated structure by resonance.

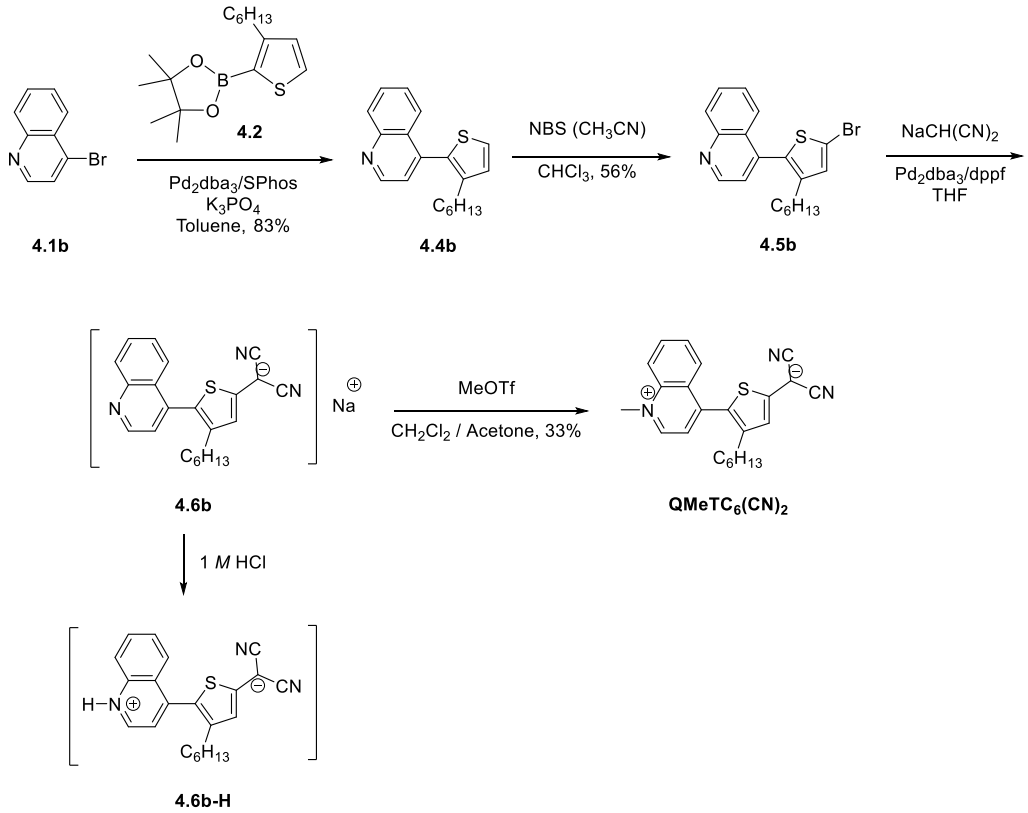

Scheme 4.2: Synthesis of **$QMeTC_6(CN)_2$**.

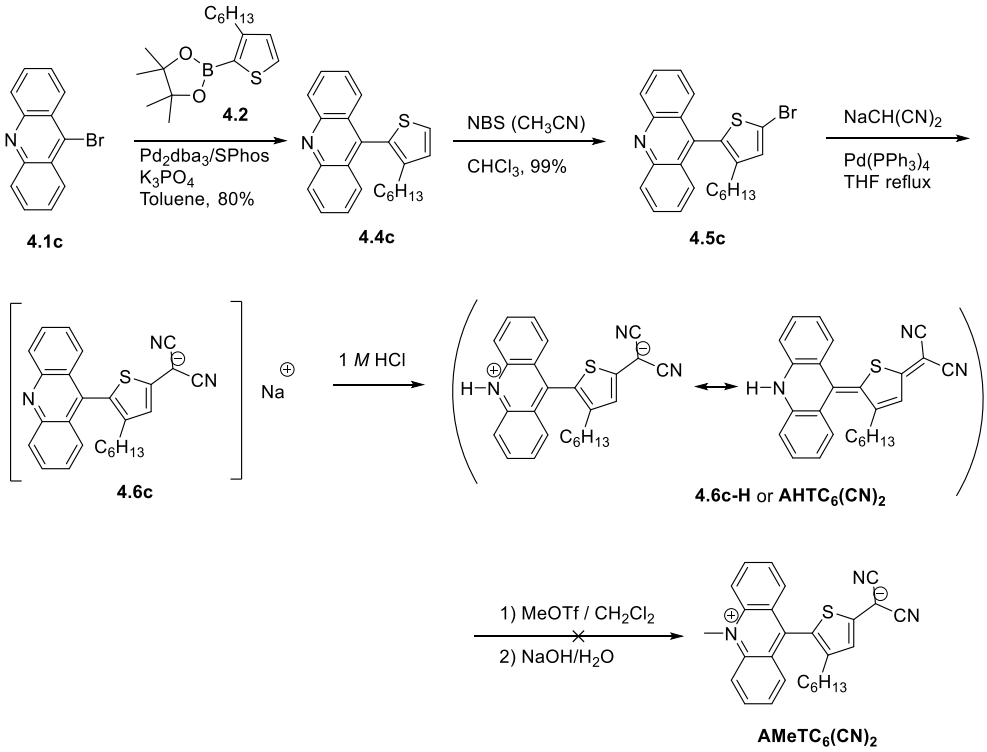

Scheme 4.3: Synthesis of **$AHTC_6(CN)_2$**.

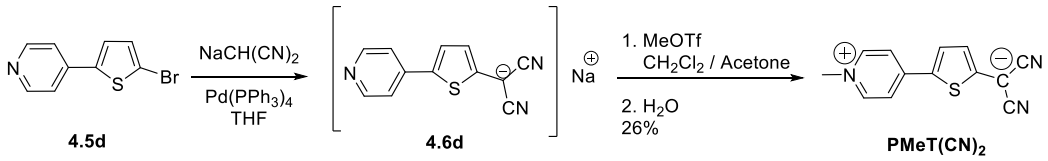

Scheme 4.4: Synthesis of **PMeT(CN)$_2$**.

The synthesis of all chromophores required no more than five steps, a marked improvement over the synthesis of the **TMC** chromophores which have the same π-conjugation length.[234] This can be attributed to the regioselective halogenation of the thiophene ring in **4.4a-c**, and the incorporation of several key structural elements on the thiophene ring (electron-rich aromatic moiety, with steric-inducing solubilizing chain).

The thiophene-based chromophores are soluble in common organic solvents of varying polarity, signifying the adequacy of the *n*-hexyl chain as a solubilizing group for these condensed π-systems. All sodium salt precursors **4.6a-d** are stable in the solid state and can be stored in the dark at −20 °C for over a year. All thiophene-based chromophores are also stable in the solid state when stored in the dark at −20 °C for over six months, and when stored in solution in the dark at room temperature over 10 days, as shown by the minimal changes in their ^{1}H-NMR spectra (Figure 4.6).

4.5.2. Structural Characterization of Charge Distribution

The TICT mechanism and the resultant linear and nonlinear properties of the chromophores strongly depend on a clear understanding of their structure, in the solid state and in solution. As Chart 4.4 details, there are two major contributors to the structure of the chromophores, a zwitterionic-aromatic form, and a neutral-quinoidal form. A potential contribution from a diradicaloid structure is also possible, especially in

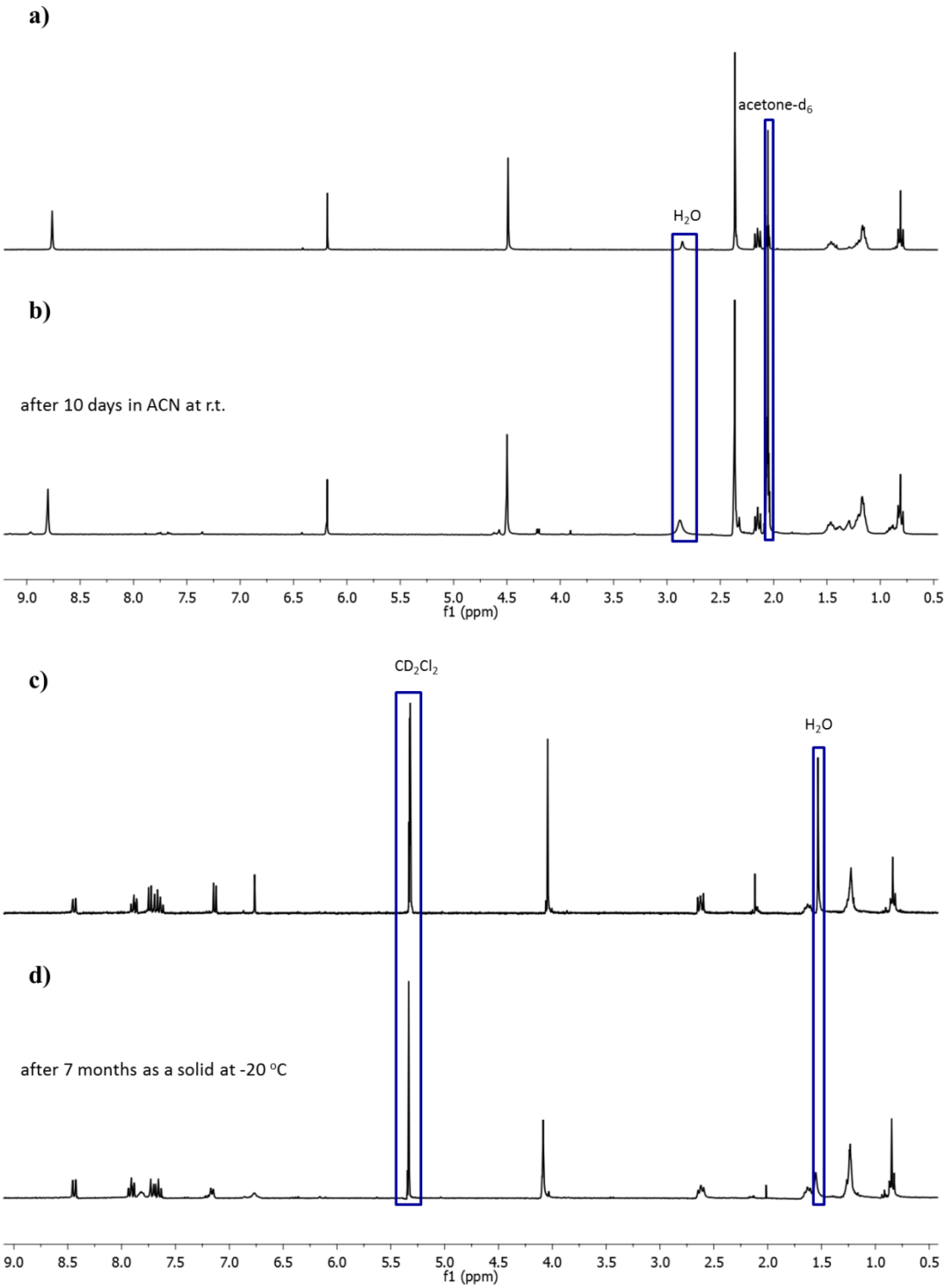

Figure 4.6. ^{1}H-NMR spectra of **$PMe_3TC_6(CN)_2$** upon synthesis (a), and after storing in CH_3CN solution for 10 days (b). ^{1}H-NMR spectra of **$QMeTC_6(CN)_2$** upon synthesis (c), and after storing in the solid state at −20 °C for 7 months (d).

a nonpolar environment.[230,233,234] In the solid state, FTIR spectroscopy allows the determination of the degree of negative charge carried by the dicyanomethanide group, while in solution, both NMR spectroscopy and absorption spectroscopy allow assessment of the contribution from the two canonical resonance forms. Structural analysis is also aided by the results of theoretical calculations performed by Dr. Alexander Baev (Prasad group, SUNY-Buffalo), shown in Table 4.4.

Table 4.4. Calculated properties of tictoid thiophene-based chromophores (HF/6-31G*; Dr. A. Baev, SUNY-Buffalo)

Compound	Vacuum			Polar Medium ($CHCl_3$)		
	Twist Angle	E_{ge}	μ_{gg}	Twist Angle	E_{ge}	μ_{gg}
$PMe_3TC_6(CN)_2$	40°	2.5	20.8	74°	1.2	35.4
$QMeTC_6(CN)_2$	18°	2.8	15.8	40°	2.0	32.1
$AHTC_6(CN)_2$	10°	3.1	12.0	68°	1.1	33.5
$PMeT(CN)_2$				0°	2.7	21.0

4.5.2.1. Solid State Structure from Infrared Spectroscopy

The FTIR spectra of the thiophene-based chromophores and their respective sodium salt precursors are shown in Figure 4.7. The strong peaks in the 700 – 1700 cm^{-1} region correspond to aromatic ring stretches, while the moderate to intense peaks in the 2800 - 3000 cm^{-1} region are observed for all chromophores containing the *n*-hexyl group on thiophene. Sharp bands are also observed in the 2100 – 2300 cm^{-1} region, corresponding to C≡N stretching vibrations.

The IR stretching frequency for the cyano group is well known to respond strongly to the changes in electron density around the nitrile groups.[83,258-260] The nitrile groups gain a partial double bond character with an increase in electron charge localization, leading to a longer bond with a weaker vibrational energy. In the case of

phenylmalononitrile, the conversion to its carbanion leads to a doublet of the $\nu_{C\equiv N}$ stretching frequencies with a splitting of 46 cm^{-1}, and an average decrease of 114 cm^{-1} in the $\nu_{C\equiv N}$ stretching frequencies compared to the neutral molecule.[259] The doublet character arises from a higher energy peak that is attributed to an in-phase stretching vibration, and a lower energy peak that corresponds to the out-of-phase motion of the C≡N bonds.[83] In zwitterionic tetracyanoquinodimethane (TCNQ) derivatives, the $\nu_{C\equiv N}$ stretching bands also take on a doublet character, and a splitting of 30-40 cm^{-1}.[254,261] In a series of thiophene-based push-pull chromophores, the intramolecular charge transfer that converts the quinonoid structure with a neutral dicyanomethane end group ($\nu_{C\equiv N}$ = 2222 cm^{-1}) to a zwitterionic structure that carries greater negative charge on this group, is accompanied by a decrease of 30 cm^{-1} on the $\nu_{C\equiv N}$ stretching frequencies, and a doublet character with a splitting of 27 cm^{-1}.[260] Thus, the $\nu_{C\equiv N}$ stretching frequencies are an appropriate vehicle by which to gauge the degree of negative charge or anion character in the dicyanomethanide group, both in the sodium salt precursors, and the final chromophores.

Figure 4.7a gives the FTIR spectra for the salt precursors **4.6a-d**, showing strong $\nu_{C\equiv N}$ bands with a doublet character comprising of a high-energy band at 2170 – 2180 cm^{-1}, and a low-energy band at 2110 – 2120 cm^{-1}. These frequencies are significantly lower than what is found for $CH_2(CN)_2$ (2270 cm^{-1}),[83] TCNQ (2225 ± 5 cm^{-1}),[83] or 2,5-bis(dicyanomethylene)-2,5-dihydrothiophene (2227 cm^{-1})[262] by 45 – 160 cm^{-1}. The splitting observed ranges from 50 – 60 cm^{-1}, indicating strong vibrational coupling. A third higher energy shoulder is also visible at 2235 – 2257 cm^{-1}, with medium intensity for **4.6b-d**, and only very weakly for **4.6a.** These observations indicate that the sodium

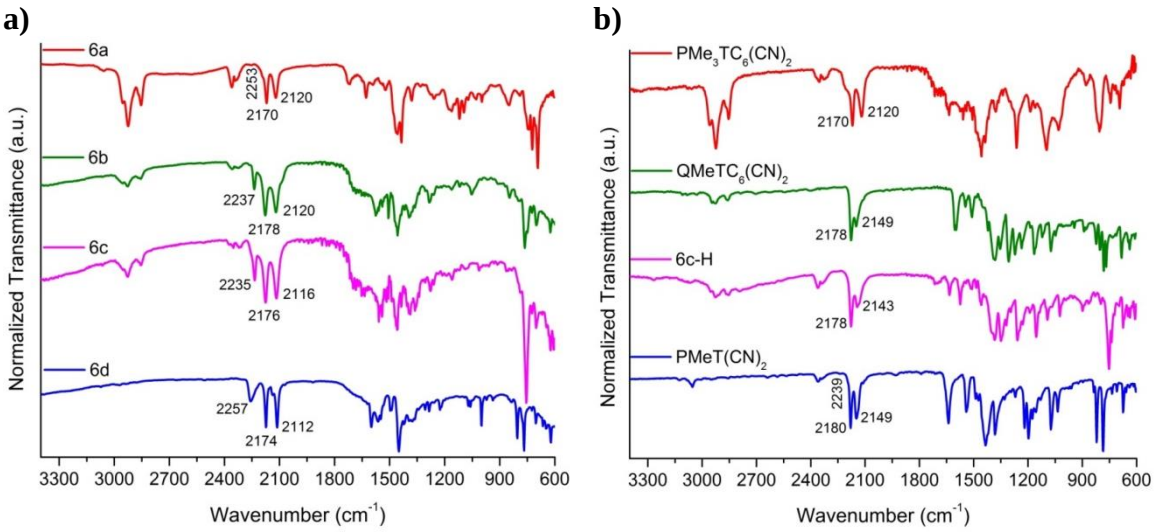

Figure 4.7. Normalized FTIR spectra of salt precursors **4.6a-d** (a), and final chromophores (b).

salts carry a significant density of negative charge on the dicyanomethanide group, with the higher energy shoulder pointing to a small contribution from the quinoidal structure.

The intensities of the high-energy shoulder increases from **4.6a** << **4.6b** < **4.6c** ~ **4.6d**, and indicates that the contribution from the quinoidal structure is practically negligible in **4.6a**, and significant in **4.6b**, **4.6c**, and **4.6d**. The ability to delocalize the charge depends on the degree of conjugation across the inter-aryl bond, which is dictated by the twist angle, and the relative stability of the neutral-quinoidal structure. Thus, this order also corresponds to the order of decreasing calculated twist angle (Table 4.4, polar medium), and the increasing annulation of benzene rings.

The $\nu_{C\equiv N}$ bands of the thiophene-based chromophores (Figure 4.7b) also show a strong high-energy band at 2170 – 2180 cm^{-1}, a moderate-to-strong intensity low-energy shoulder at 2120 – 2150 cm^{-1}, and a vibrational splitting of 29 – 50 cm^{-1}. No higher-energy shoulder attributable to a quinoidal contribution is observed for any chromophore, save for a very weak band for **PMeT(CN)$_2$**. The low frequencies, and significant

couplings for all chromophores point to the zwitterionic-aromatic structure (Chart 4.4) being the dominant contributor to the ground state structure in the solid state. The splitting is largest, and the frequencies (for both bands) are lowest for **$PMe_3TC_6(CN)_2$**, indicating negligible contribution from the neutral-quinoidal structure for this chromophore in the solid state. This can be rationalized from its large calculated twist angle, and lack of annulated benzene rings. The degree of contribution from the neutral-quinoidal structure remains minimal in the other chromophores, but the splitting and the frequencies of both $\nu_{C\equiv N}$ bands in these indicate lesser negative charge localization on their dicyanomethanide fragments.

Vibrational spectroscopy shows distinctly different behaviors for **$PMe_3TC_6(CN)_2$** and **$PMeT(CN)_2$**, despite the acceptor and donor fragments being equivalent in these two chromophores. The difference in behavior can thus be attributed to the steric factors that ultimately determine the electronic response in these chromophores. **$AHTC_6(CN)_2$**, with its significant twist angle, and the same degree of inter-ring substitution (pseudo-tri-*o*) as **$PMe_3TC_6(CN)_2$**, shows a weaker coupling of 35 cm^{-1}, and elevated band frequencies ($\Delta\nu_{C\equiv N}$ = 8 – 23 cm^{-1}), indicating some delocalization of the negative charge toward the acceptor fragment. This, along with the delocalization observed in its salt precursor **4.6c**, demonstrates that the annulated benzene rings can offset the energy cost of steric strain with a gain of aromatic stability in the neutral-quinoidal form.

4.5.2.2. Solution State Structure from Solvent-Dependent NMR Spectroscopy and Optical Absorption Spectroscopy

The contributions from the canonical resonance forms can be drastically affected by interactions from the surrounding environment. This is clear from the difference in

calculated properties (Table 4.4) in the gas phase/vacuum, and in a polarizable continuous medium (approximating $CHCl_3$). Solute-solvent interactions in a polar medium are expected to screen charges, and stabilize the charge-separated resonance form. Thus, an increase in ground state dipole moments is observed for all chromophores in a polar medium, pointing to an enhanced contribution from the zwitterionic-aromatic resonance form in the ground state. The solvent-dependent behavior of the chromophores was studied by NMR and optical absorption spectroscopy, and the solution structure is assessed for solvents used in characterizing nonlinear properties (CH_2Cl_2, CH_3CN, benzyl alcohol).

4.5.2.2.1. Solvent-Dependent NMR Spectroscopy

Differences in intermolecular interactions between solute and solvent can give rise to changes in the position of the solute's NMR signals.[263] This technique has been used to assess the contributions of benzenoid and quinoid resonance forms in merocyanines.[264,265] In order to isolate the effect of interactions with the solvent from interactions with other solute molecules, quantitative analyses of these interactions are most accurate at infinite dilution,[263] and often guided with theoretical calculations. However, qualitative assessments can be made by comparing the changes observed for the chromophore signals with the changes observed for tetramethylsilane (TMS), a nonpolar solute in the deuterated solvent. In the solvents compared, $CDCl_3$, CD_2Cl_2, and acetone-d_6, the ^{1}H-NMR signal for TMS occurs consistently at δ 0.07, 0.06, and -0.01 ppm, respectively. The different polarities of these NMR solvents are expected to induce different contributions from the zwitterionic-aromatic and neutral-quinoidal forms of the thiophene-based tictoid chromophores. The changes in ^{1}H-NMR signals of pertinent

protons of the chromophores and important precursors are summarized in Tables 4.5 to 4.8.

For **$PMe_3TC_6(CN)_2$** (Table 4.5), the acceptor ring proton undergoes a significant downfield shift in going from CD_2Cl_2 (ϵ_r = 8.9) to acetone-d_6 (ϵ_r = 20.7) of $\Delta\delta$ = 0.52 ppm ($\Delta\epsilon_r$ = 11.8), an indication of increased deshielding as the medium increases in polarity. This very strong response (*cf.* TMS shift $\Delta\delta$ = −0.07 ppm) can be attributed to an increase in positive charge localization around the acceptor ring. A similar downfield shift is also observed for the *N*-methyl proton ($\Delta\delta$ = 0.18 ppm), due to the inductive electron-withdrawing effect of the acceptor ring. The peak for hydrogen on the donor ring, on the other hand, undergoes an upfield shift of $\Delta\delta$ = −0.08 ppm, indicating increased shielding with a more polar solvent, and greater negative charge localization on the thiophene ring. These observations, coupled with the upfield positions of the thiophene peak in the chromophore, and its precursor salt (**4.6a**), as compared with the halide precursor (**4.5a**), and the strongly downfield position of the N-methyl protons (vs. δ_{CH3} (MeOTf) = 3.85 ppm, δ_{CH3} (trimethylamine, *N*-methylpiperidine) = 2.26), indicate a high degree of positive charge localization in the acceptor subfragment, and a high degree of negative charge localization in the donor subfragment. ^{13}C-NMR peak for the dicyanomethanide C*$(CN)_2$ central carbon are also located at δ 27.42 in CD_2Cl_2, corroborating the strong negative charge localized on this carbon. Thus, in this chromophore, the zwitterionic-aromatic resonance form is the predominant contributor in both solvents, and especially strongly in acetone. As in the solid state, the ground state solution structure of **$PMe_3TC_6(CN)_2$**, is best described by this resonance form that is enforced by its significant steric twist, with a calculated angle of 74°.

Table 4.5. Relevant ^{1}H-NMR peak changes in the synthesis of **$PMe_3TC_6(CN)_2$**.

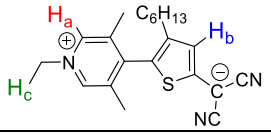

	4.5a	**4.6a**	**4.6a-H**	**$PMe_3TC_6(CN)_2$**	
	$CDCl_3$	**$(CD_3)_2CO$**	**$CDCl_3$**	**CD_2Cl_2**	**$(CD_3)_2CO$**
3,5-Lutidine 2 (or 6)-H (H_a)	8.34	8.30	8.39	8.24	8.76
Thiophene 3-H (H_b)	6.96	6.14	7.23	6.26	6.18
Dicyanomethanide-H	-	-	-	-	-
Pyridine *N*-methyl H (H_c)	-	-	-	4.31	4.49

For **$QMeTC_6(CN)_2$** (Table 4.6), the hydrogen on the 2-position of the acceptor ring undergoes a downfield shift of $\Delta\delta$ = 0.21 ppm in going from CD_2Cl_2 to acetone-d_6, while the hydrogen on the donor ring shifts upfield by $\Delta\delta$ = 0.13 ppm. These observations support increasing positive charge localization in the acceptor ring, and increasing negative charge localization in the donor ring. The *N*-methyl proton also undergoes a strong downfield shift of $\Delta\delta$ = 0.32 ppm in going from CD_2Cl_2 to acetone-d_6, again due to the electron-withdrawing effect of the acceptor ring, as it gains increasing partial positive charge. As in **$PMe_3TC_6(CN)_2$**, these observations, along with the upfield

Table 4.6. Relevant ^{1}H-NMR peak changes in the synthesis of **$QMeTC_6(CN)_2$**.

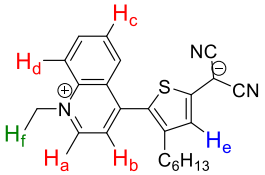

	4.5b	**4.6b**	**4.6b-H**	**$QMeTC_6(CN)_2$**		
	$CDCl_3$	**$(CD_3)_2CO$**	**$CDCl_3$**	**$CDCl_3$**	**CD_2Cl_2**	**$(CD_3)_2CO$**
Quinoline 2-H (H_a)	8.92	8.82	8.97	8.37	8.43	8.64
Quinoline 3-H (H_b)	7.82	8.03	7.76	7.85	7.89	8.52
Quinoline 6-H (H_c)*	7.53	7.71	7.57	7.58	7.64	7.87
Quinoline 8-H (H_d)*	7.33	7.31	7.37	7.01	7.14	7.50
Thiophene 3-H (H_e)	7.03	6.23	7.28	6.70	6.75	6.62
Dicyanomethanide-H	-	-	-	-	-	-
Quinoline *N*-methyl H (H_f)	-	-	-	4.07	4.07	4.45

*Assignments are tentative.

position of the thiophene hydrogen peak relative to the halide precursor (**4.5b**), and the downfield position of its *N*-methyl proton signal, support a predominant contribution from the zwitterionic-aromatic resonance form to its solution ground state structure in CH_2Cl_2, which increases further in acetone.

For **$AHTC_6(CN)_2$** (Table 4.7), a different trend is observed. All the acceptor ring protons undergo a slight to strong downfield shift ($\Delta\delta$ = 0.01 to 0.35 ppm) in going from CD_2Cl_2 to acetone-d_6, indicating deshielding, or a decrease in electron density. But, the thiophene proton also undergoes a downfield shift of $\Delta\delta$ = 0.26 ppm. The signal in acetone-d_6 for the chromophore (δ = 7.62 ppm) is also significantly downfield compared to the salt precursor **4.6c** (δ = 6.45 ppm). These observations indicate that the neutral-quinoidal resonance form is the main contributor to the solution ground state structure of **$AHTC_6(CN)_2$**. This is corroborated by the ^{13}C-NMR signal for the dicyanomethanide $C^*(CN)_2$ central carbon, which appears at δ = 52.62 ppm (CD_2Cl_2),versus δ = 28.35 ppm (acetone-d_6) for the precursor salt (where a dominant negative charge on the dicyanomethanide fragment is likely). In the neutral-quinoidal form, the acridine nitrogen lone pair becomes the donor, while the dicyanomethane group becomesthe acceptor. The observed downfield shift of $\Delta\delta$ > 1 ppm in the thiophene hydrogen peak can be rationalized by the electron-withdrawing effect of the dicyanomethane group as the structure is polarized by the solvent, and the change from a quinoidal to benzenoid structure:

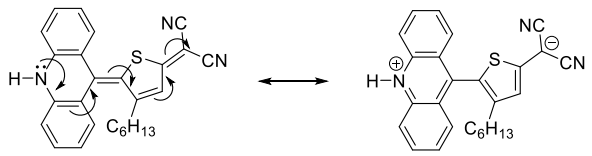

Table 4.7. Relevant ^{1}H-NMR peak changes in the synthesis of **AHTC$_6$(CN)$_2$**.

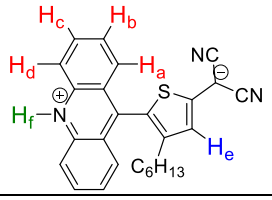

	4.5c	**4.6c**	**AHTC$_6$(CN)$_2$**		
	$CDCl_3$	**$(CD_3)_2CO$**	**$CDCl_3$**	**CD_2Cl_2**	**$(CD_3)_2CO$**
Acridine 1-H (H_a)*	7.48	7.51	7.57	7.55	7.66
Acridine 2-H (H_b)*	8.28	8.19	8.08	7.85	8.20
Acridine 3-H (H_c)*	7.77	7.79	7.88	7.85	7.92
Acridine 4-H (H_d)*	7.83	8.02	8.25	8.24	8.25
Thiophene 3-H (H_e)	7.15	6.45	7.40	7.36	7.62
Dicyanomethanide-H	-	-	-	-	-
Acridine *N*-H (H_f)	-	-	-	6.33	-

*Assignments are tentative.

For the sterically "relaxed" model compound **PMeT(CN)$_2$** (Table 4.8), the acceptor protons undergo a moderate downfield shift of $\Delta\delta \sim 0.12$ ppm with a large change in solvent polarity from acetone-d_6 to DMSO-d_6 ($\Delta\epsilon_r = 26.0$). The acceptor protons show well-resolved doublet signals in a DMSO-d_6, but the signal for the pyridine 3(5)-H is broad in acetone-d_6. This change in resolution indicates that the protons are becoming anisochronous in the less polar solvent acetone-d_6. If the acceptor and donor fragments can freely rotate through the inter-aryl bond, the 3 and 5 protons would be isochronous, thus, the loss of resolution can be attributed to a gain of double bond character in the inter-aryl bond.[244] The thiophene hydrogen in the 3-position (α to the dicyanomethanide group) undergoes a slight upfield shift, whereas the other hydrogen in the 2-position undergoes a slight downfield shift. The *N*-methyl protons undergo a modest upfield shift of $\Delta\delta = 0.16$ ppm with the change to a more polar solvent. The thiophene 3-H signal shifts downfield upon conversion from the salt precursor **4.6d** to **PMeT(CN)$_2$** by $\Delta\delta = 0.28$ ppm in acetone-d_6. The observations in DMSO-d_6, along with

the ^{13}C-NMR signal for the dicyanomethanide C*(CN)$_2$ central carbon at 35.80 ppm, point to a predominantly zwitterionic-aromatic ground state solution character in this solvent. But, in less polar acetone-d_6, the chromophore starts to favor a neutral-quinoidal structure.

Table 4.8. Relevant ^{1}H-NMR peak changes in the synthesis of **PMeT(CN)$_2$**.

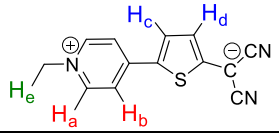

	4.6d	**PMeT(CN)$_2$**	
	(CD$_3$)$_2$CO	**(CD$_3$)$_2$CO**	**(CD$_3$)$_2$SO**
Pyridine 2 (or 6)-H (H_a)	8.32	8.14 (d, ^3J = 7.2 Hz)	8.25 (d, ^3J = 7.3 Hz)
Pyridine 3 (or 5)-H (H_b)	7.26	7.47 (br)	7.60 (d, ^3J = 6.4 Hz)
Thiophene 4-H (H_c)	7.32	7.80 (^3J = 4.6 Hz)	7.91 (d, ^3J = 4.4 Hz)
Thiophene 3-H (H_d)	6.19	6.47 (^3J = 4.6 Hz)	6.40 (d, ^3J = 4.4 Hz)
Pyridine *N*-methyl H (H_e)	-	4.12	3.96

Comparing the positions of the acceptor and donor signals, and their solvent dependence in the sterically twisted chromophore **PMe$_3$TC$_6$(CN)$_2$** and the sterically "relaxed" chromophore **PMeT(CN)$_2$**, it can be observed that the twisted/tictoid chromophore has significantly more upfield thiophene peaks, significantly more downfield pyridine peaks, and a stronger response to solvent polarity than the untwisted chromophore. Thus, as in the solid state (*vide supra*), the solution state structure is dictated by steric rather than electronic factors.

The ability of the inter-aryl steric strain to impede significant charge delocalization across the donor-acceptor linkage can be evaluated by monitoring the evolution of the peak shifts of pertinent aromatic protons during the addition of the charge-bearing groups (Figure 4.8). The introduction of the negative-charge bearing dicyanomethanide group (**4.5a-d → 4.6a-d**) causes a homogeneous upfield shift in the

thiophene 3-H peak for all compounds. But, non-negligible upfield shifts in the pertinent acceptor ring protons are observed only in **4.6b** and **4.6d**, with only a slight effect on **4.6c**. Thus, the large calculated solution twist angles in **4.6a** and **4.6c** hampers delocalization of the negative charge over the π-system toward the acceptor fragment. With the quaternization of nitrogen in the acceptor fragment, a moderate downfield shift is observed for the thiophene 3-H peak of **$QMeTC_6(CN)_2$**, and **$PMeT(CN)_2$**, whereas a slight upfield shift is observed for their acceptor ring protons. These modest responses demonstrate the significant delocalization of charge through the π-system that is accessible in these low twist angle chromophores. **$PMe_3TC_6(CN)_2$**, on the other hand, shows a substantial downfield shift in its acceptor ring protons, and a negligible downfield shift in its thiophene 3-H proton, upon quaternization of the acceptor ring nitrogen. This is attributed to the conjugation breaking enforced by its steric twist leading to shielding of the donor fragment from the charge build-up in the acceptor fragment. On the other hand, the much stronger $\Delta\delta > 1.0$ ppm shift in the thiophene 3-H peak observed

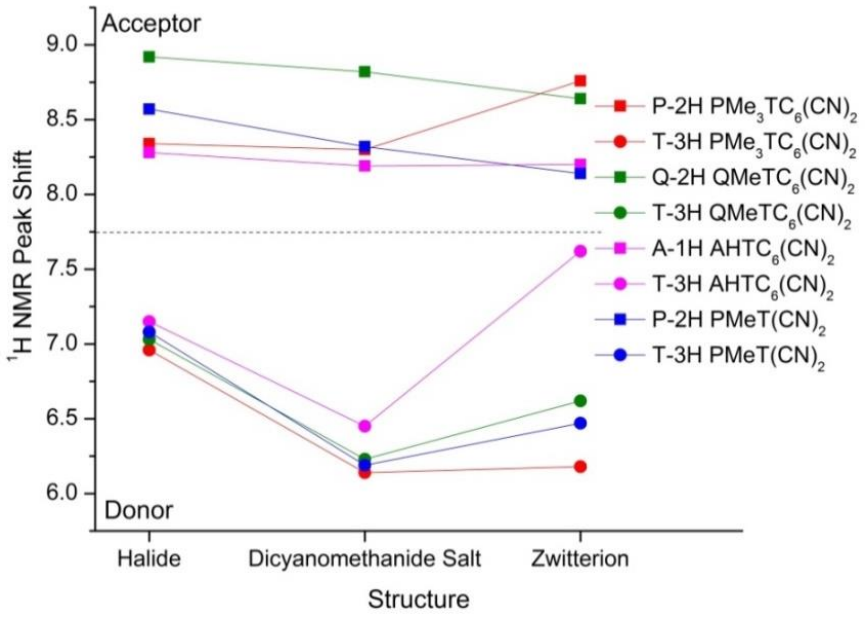

Figure 4.8. Changes in key NMR peaks with addition of charge-bearing groups.

in **$AHTC_6(CN)_2$**, which can be attributed to its adoption of the neutral-quinoidal structure,[257] demonstrates the gain in stability provided by the aromatization of the annulated benzene rings.

Thus, NMR spectroscopy results show that in solution, the zwitterionic-aromatic form is favored by **$PMe_3TC_6(CN)_2$**, **$QMeTC_6(CN)_2$**, and **$PMeT(CN)_2$** (with the ability to delocalize charge to some extent in the latter two), whereas the neutral-quinoidal form is adopted by **$AHTC_6(CN)_2$**.

4.5.2.2.2. Solution Absorption Spectroscopy

As described in the TICT mechanism outlined by Albert *et al.*,[227] the sterically enforced partitioning of the conjugated system leads to optical properties that are more aptly described by excitations arising from the donor subfragment, separate from another arising from the acceptor subfragment, and a distinct inter-subfragment charge-transfer excitation. These discrete transitions are observed in systems with significant twist angles, i.e. when the zwitterionic-aromatic form is the dominant resonance structure, but not in coplanar (neutral-quinoidal) systems. Thus, the absorption spectra of the thiophene-based chromophores can be used to evaluate their TICT response.

Figure 4.9a shows the optical absorption spectra of MeOH solutions of the thiophene-based chromophores. In the 400 to 1000 nm region, the chromophores show broad intramolecular charge transfer (ICT) peaks that vary greatly in their positions, and their molar extinction coefficients (ε). The λ_{max} of these ICT peaks are shown to red-shift with increasing strength of the acceptor ring: pyridine (λ_{max} 521, 537 nm) < quinoline (λ_{max} 633 nm) < acridine (λ_{max} 773 nm). **$PMe_3TC_6(CN)_2$**, **$QMeTC_6(CN)_2$**, and **$AHTC_6(CN)_2$** also show high-energy absorptions that can be assigned to the donor and

acceptor intra-ring excitations, as predicted for tictoid chromophores. These are particularly well-defined for **$PMe_3TC_6(CN)_2$** as shown in Figure 4.9b. The extinction coefficients are significantly lower for its inter-subfragment charge transfer absorption at ε = 2,745 M^{-1} cm^{-1}, versus the intra-subfragment bands with ε_{320nm} = 8,519 M^{-1} cm^{-1}. This is also observed in **$AHTC_6(CN)_2$**, with ε_{ICT} = 4,748 M^{-1} cm^{-1}, and ε_{360nm} = 14,135 M^{-1} cm^{-1}. The moderate strengths of the ICT absorptions suggest a modest overlap between their HOMO and LUMO orbitals. These can be expected from the large twist

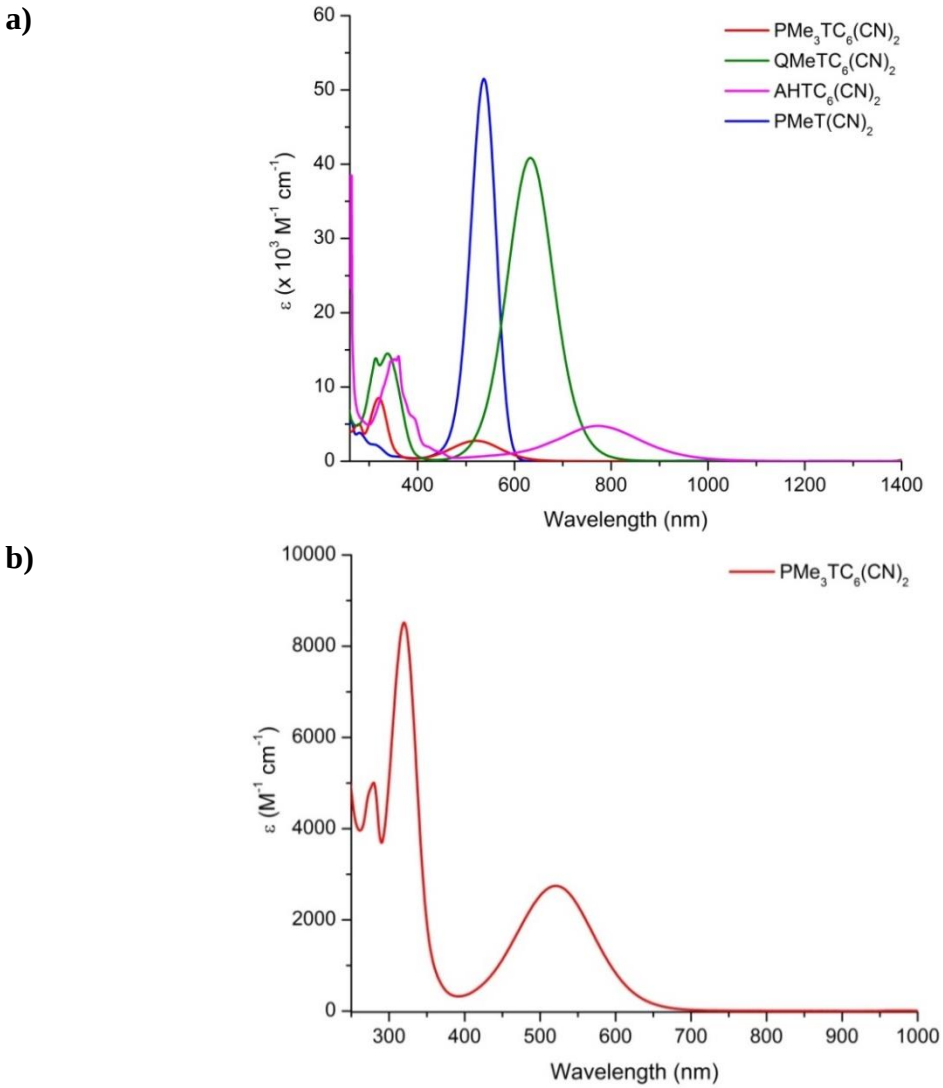

Figure 4.9. Optical absorption spectra of all chromophores (a) and **$PMe_3TC_6(CN)_2$** (b) in MeOH.

angles calculated for these two chromophores, and shown by their calculated orbital diagrams (Figure 4.10a and 4.10c), in which the HOMO is localized in the donor fragment, and the LUMO is localized in the acceptor fragment, with little orbital density around the inter-aryl linkage.

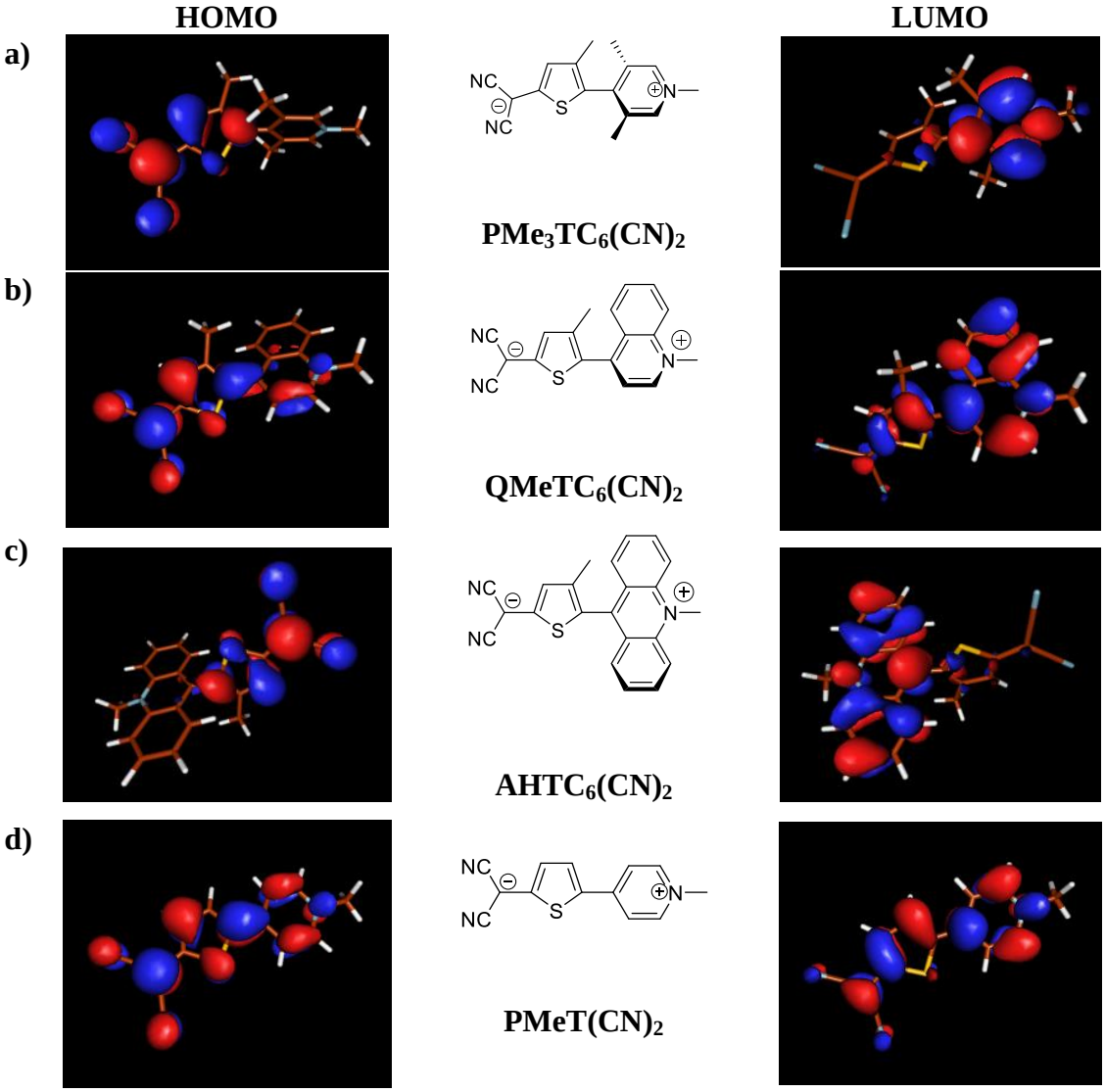

Figure 4.10. HOMO-LUMO orbital pictures of **$PMe_3TC_6(CN)_2$** (a), **$QMeTC_6(CN)_2$** (b), **$AHTC_6(CN)_2$** (c), and **$PMeT(CN)_2$** (d).

The other two chromophores, **$QMeTC_6(CN)_2$**, and **$PMeT(CN)_2$**, show significantly stronger molar extinction coefficients of their ICT bands, at ε = 40,850 M^{-1} cm^{-1} and 51,507 M^{-1} cm^{-1}, respectively. **$QMeTC_6(CN)_2$** also shows intra-subfragment peaks, but these are weaker than its ICT peak, with ε_{340nm} = 14,500 M^{-1} cm^{-1}. **$PMeT(CN)_2$**, on the other hand, shows poorly-defined intra-subfragment bands, indicating that it does not behave as a tictoid chromophore in its optical transitions. The stronger ICT bands of these latter two chromophores reflect their significantly smaller twist angles, allowing delocalization. Their orbital diagrams (Figure 4.10b and 4.10d) show substantial overlap of the HOMO and LUMO orbitals, and significant electron density around the inter-aryl bond.

Thus, the optical absorption spectra corroborate the conclusions drawn from solution NMR spectroscopy: **$PMe_3TC_6(CN)_2$** is significantly zwitterionic-aromatic in solution, especially in polar solvents, whereas **$QMeTC_6(CN)_2$** and **$PMeT(CN)_2$** show some delocalization due to their tolerant twist angles. **$AHTC_6(CN)_2$**, on the other hand, shows a response that reflects a dominant zwitterionic-aromatic form, similar to its solid state response, and different from what is described by its NMR spectra. These disparities can be attributed to its different behavior in solvents of significantly different polarities.

In fact, the optical absorption behavior of all chromophores changes in a less polar solvent, such as CH_2Cl_2 (Figure 4.11). The ICT peaks of **$PMe_3TC_6(CN)_2$** and **$QMeTC_6(CN)_2$** have larger molar extinction coefficients, and the increase is nearly five-fold in the former. But while the higher energy peaks change for **$QMeTC_6(CN)_2$**, the intra-subfragment peaks remain well-resolved for **$PMe_3TC_6(CN)_2$**, indicating that its

tictoid response can still be defined by a predominantly zwitterionic-aromatic ground state even in a medium that has a weaker ability to stabilize this structure.

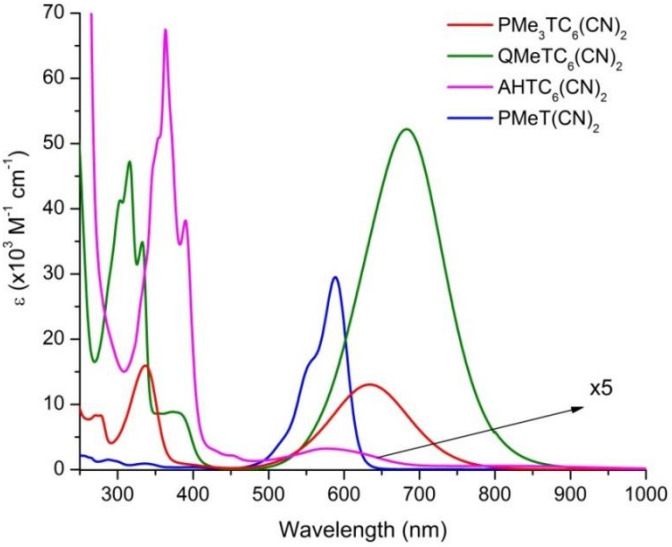

Figure 4.11. Optical absorption spectra of all chromophores in CH_2Cl_2.

PMeT(CN)$_2$ shows a different spectral shape for its ICT band, with two higher energy shoulders separated by ~ 40 nm (~ 1160 cm^{-1}), which can be attributed to vibronic transitions. This change is indicative of stronger intermolecular interactions, suggesting an increase in the contribution of the neutral-quinoidal structure in less polar solvents. The low coefficient for **AHTC$_6$(CN)$_2$** may be due to an n → π* character for this transition, and will be elucidated further in the succeeding sections.

4.5.3. Molecular Parameters from Absorption Spectroscopy and Electrochemistry

As defined in eq. 4.6, some of the molecular parameters that can be used to understand the structural effects on third-order nonlinear polarizability are $\boldsymbol{M}_{ge}$, $\boldsymbol{\Delta\mu}$, and $\boldsymbol{E}_{ge}$. These parameters can be obtained from optical absorption spectra, and derived relationships, as well as from electrochemical techniques. The analyses of these

calculated parameters are based on the structural pictures that have been elucidated for these chromophores, especially in solution, in the previous sections.

4.5.3.1. Solvatochromic Behavior and Estimation of $\Delta\mu$

The solvatochromic effect, in which a change in solvent brings about changes in the position of the maximum, the intensity, and the shape of an absorption band, arises from a differential solvation of the ground versus the excited state of an ICT excitation as the solvent polarity is changed.[263] A strong and measurable response occurs for chromophores for which the π-electron distribution in the ground and excited states are appreciably different. The strength of intermolecular interactions between the ground and excited states of the chromophore and the solvent, which in turn depend on the π-system structure of the chromophore, dictates the nature and extent of the response. For the case where $\boldsymbol{\mu}_{gg} > \boldsymbol{\mu}_{ee}$, an increase in polarity of the solvent leads to preferential solvation and stabilization of the charge separation in the relaxed ground state, whereas the Franck-Condon excited state, which is neutral, is only moderately stabilized (Figure 4.12a). This leads to an increase in transition energy, and a blue-shift (hypsochromic shift) of the λ_{max} with increasing solvent polarity, a response known as negative solvatochromism. For the case where $\boldsymbol{\mu}_{ee} > \boldsymbol{\mu}_{gg}$, the excited state energy decreases, while the ground state is only moderately stabilized, leading to a red-shift (bathochromic shift) (Figure 4.12b), or positive solvatochromism. Thus, the chromophore's solvatochromic response provides another method from which a structural picture of the ground and excited states of the chromophore can be obtained. In order to isolate the solute-solvent from the solute-solute interactions, dilute solutions (where no significant aggregation is observed) are considered.

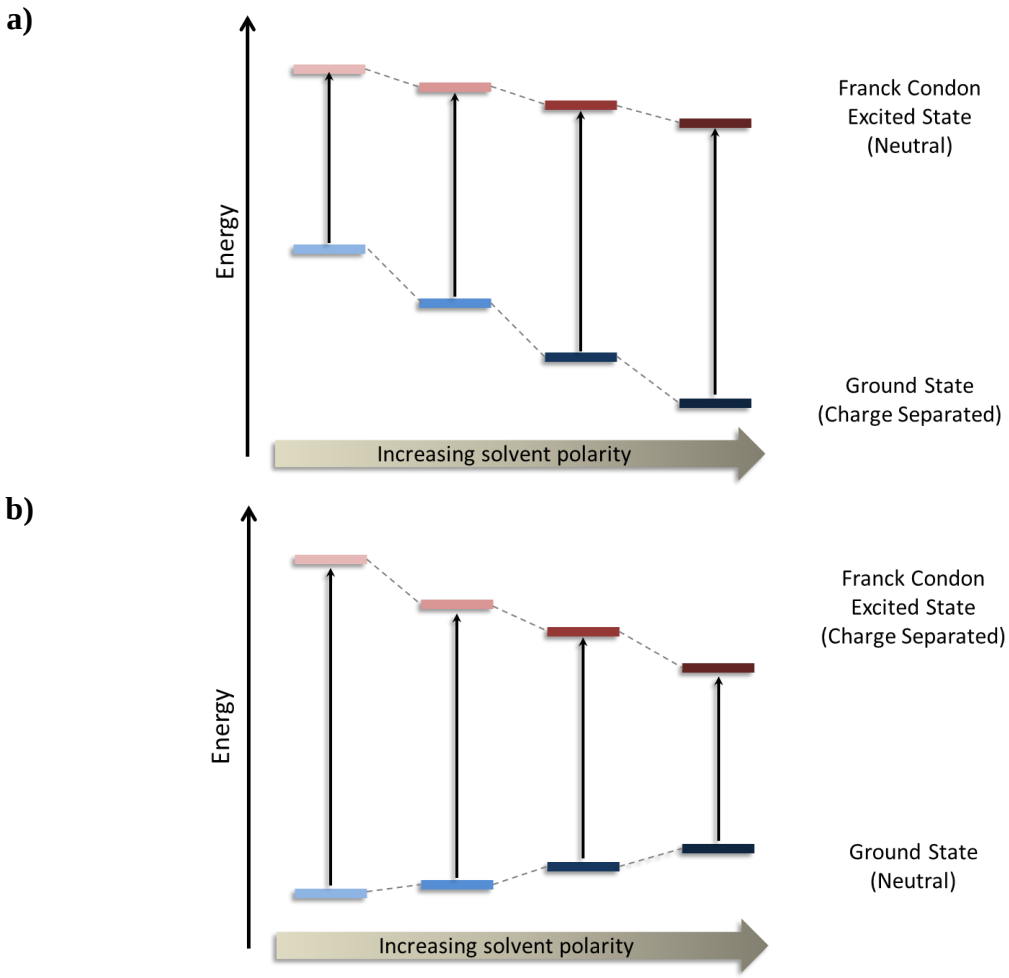

Figure 4.12. The effect of solvent polarity on the energies of the ground and Franck-Condon excited state, and the resultant transition energy for (a) $\boldsymbol{\mu_{gg} > \mu_{ee}}$; (b) $\boldsymbol{\mu_{ee} > \mu_{gg}}$.

Absorption spectra of the thiophene-based chromophores in solvents of varying polarity (Figure 4.13) shows a strong response of the ICT peak to the dielectric constant of the solvent (Table 4.9). The ICT peaks for **$PMe_3TC_6(CN)_2$**, **$QMeTC_6(CN)_2$**, and **$PMeT(CN)_2$** are increasingly blue-shifted with increasing polarity of the solvent medium. The ground state is thus more solvated than the excited state by a more polar solvent, and $\boldsymbol{\mu_{gg} > \mu_{ee}}$ or $\boldsymbol{\Delta\mu} < 0$. Thus, for the three aforementioned chromophores, their ground states are more appropriately described by the zwitterionic-aromatic resonance form.

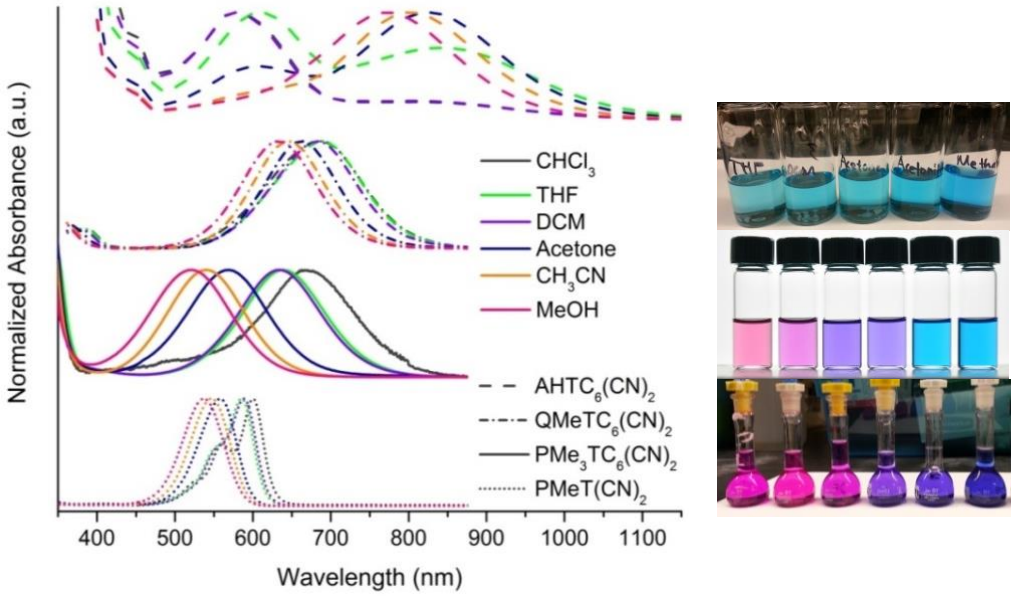

Figure 4.13. Solvatochromism of thiophene-based chromophores: **$AHTC_6(CN)_2$** (dashed lines), **$QMeTC_6(CN)_2$** (dash-dot lines), **$PMe_3TC_6(CN)_2$** (solid lines), and **$PMeT(CN)_2$** (dotted lines).

The extent of the negative solvatochromism of the ICT band is most pronounced for **$PMe_3TC_6(CN)_2$**, where the difference in λ_{max} between the most red-shifted spectra ($CHCl_3$, 671 nm), and the most blue-shifted one (MeOH, 521 nm), is $\Delta\lambda_{max}$ = 150 nm ($\Delta\epsilon_r$ = 27.9). The strength of this response is more conspicuous when compared with the much weaker response observed for the intra-subfragment peaks (Figure 4.14). Thus, the ground state of this chromophore has a significantly larger dipole moment than its excited state, and is more appropriately described by a zwitterionic-aromatic structure. This corresponds with the large calculated twist angle for this chromophore that is set by its pseudo-tri-*ortho* substitution pattern.

For **$QMeTC_6(CN)_2$**, the negative solvatochromism is only about a third of that for **$PMe_3TC_6(CN)_2$**, with the $\Delta\lambda_{max}$ between $CHCl_3$ and MeOH at 53 nm, reflecting the smaller $\boldsymbol{\Delta\mu}$. This can be attributed to the moderate twist angle for this chromophore that

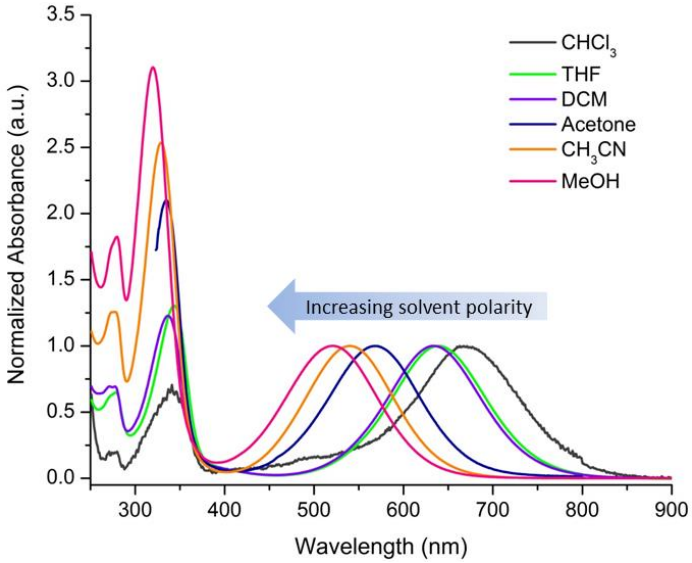

Figure 4.14. Significant **s**olvatochromism of the ICT peak of **$PMe_3TC_6(CN)_2$**, and negligible solvent-dependent behavior of the intra-subfragment peaks.

allows delocalization of the charges in the zwitterionic-aromatic structure to reduce the ground state dipole moment.

For **$PMeT(CN)_2$**, significant changes in the ICT band shape accompany its solvatochromic response (Figure 4.15). As in its CH_2Cl_2 spectra (Figure 4.11), **$PMeT(CN)_2$** shows two higher-energy bands attributed to vibronic transitions in other less polar solvents $CHCl_3$, and THF. In acetone, the ICT band loses its structure, but becomes more intense. In other more polar solvents, the absorption again loses intensity, while the λ_{max} continues to hypsochromically shift. This solvatochromic behavior reflects the responsiveness of the ground state structure to the medium, where the contributions of the two canonical resonance forms can vary strongly from a predominantly neutral-quinoidal form in less polar solvents, to a more zwitterionic-aromatic form in polar solvents.[266] This tunability of the structure was also noted from NMR spectroscopy.

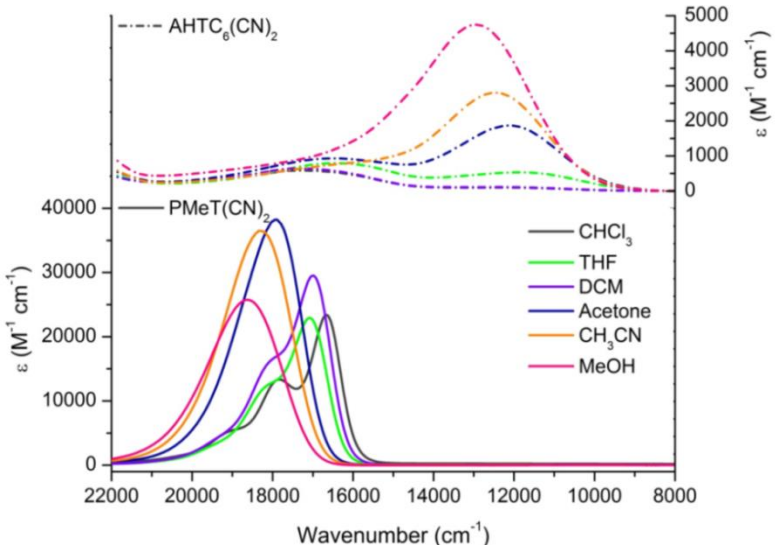

Figure 4.15. Changes in spectral shape for **$AHTC_6(CN)_2$** (dash-dot lines) and **$PMeT(CN)_2$** (solid lines) accompanying changes in position.

$AHTC_6(CN)_2$ also shows changes in spectral shape with changes in solvent (Figure 4.15). A shoulder band that is separated by ~ 230 nm (~ 4600 cm^{-1}) from the more intense peak is observed in all spectra, but the lack of differences in the absorption spectra at two different concentrations shows that the shoulder peak is not an aggregation peak (*vide infra*). The large gap between the peaks of the two bands also precludes a vibronic interpretation. It is thus likely that the two peaks arise from an n → π* transition, different from a π → π* transition, with the peak showing the stronger solvatochromic response being the π → π* transition that has a strong ICT character. The more intense ICT peak (π → π*) occurs at higher energy in less polar solvents, and undergoes a bathochromic shift in going from $CHCl_3$ to CH_2Cl_2. In more polar solvents, the stronger band occurs at much lower energies, and undergoes a hypsochromic shift in going from acetone to CH_3CN to MeOH, with the shoulder becoming less pronounced. This switch in response is termed solvatochromic reversal, and indicates that in less polar solvents, the neutral-quinoidal form of **$AHTC_6(CN)_2$** dominates and leads to positive

solvatochromism, but more polar solvents induce a change in the π-charge distribution toward the zwitterionic-aromatic structure, leading to a negative solvatochromic behavior.[263,267,268]

Table 4.9. Optical absorption properties of the intra-molecular charge transfer in the thiophene-based chromophores (λ_{max}, ε, $\Delta\lambda_{max}$).

Compound	λ_{max} (nm) (ε (M^{-1} cm^{-1}))[a]			$\Delta\lambda_{max}$ (nm)[c]
	MeOH	CH_3CN	CH_2Cl_2	
$PMe_3TC_6(CN)_2$	521 (2,740)	540 (5,260)	634 (12,075)	150
$QMeTC_6(CN)_2$	633 (40,850)	646 (43,500)	683 (52,200)	53
$AHTC_6(CN)_2$	773 (4,750)	803 (2,800)	577 (644)	248[d]
$PMeT(CN)_2$	537 (51,510)	545 (73,010)	589[b] (29,500)	63[d]

[a]Assigned to the ICT excitation. [b]Assigned to the lowest energy vibrational subband. [c]Taken as the difference between the most red-shifted and most blue-shifted spectra. [d]Disregards changes in spectral shape for simplicity.

Aside from the qualitative assessment of the relative magnitudes of the ground and excited state dipole moments, the solvatochromic shifts of a chromophore can also be correlated with solvent parameters such as the dielectric constant (effect of permanent dipoles), and the refractive index (effect of polarizability) to allow an estimation of $\boldsymbol{\Delta\mu}$ from many mathematical models.[269,270] Most models correlate the solvent parameters with the Stokes shift, but no fluorescence emission from the ICT transition is observed in these tictoid chromophores. A sufficient approximation of $\boldsymbol{\Delta\mu}$ can instead be obtained from the McRae equation,[59,269,271] which provides a simple relationship of the solvent parameters with the solvatochromic shifts in absorption maxima. The difference in absorption maxima (in wavenumbers) between the chromophore in solvent (ν_a), and in vacuum (ν_0) can be plotted against the solvent polarity function $f(\epsilon_r,n^2)$, according to:

$$\boldsymbol{v_a - v_0 \approx -mf(\epsilon_r, n^2)} \tag{4.11}$$

The slope of this relationship, *m*, is related to $\boldsymbol{\Delta\mu} = \mu_e - \mu_g$ by:

$$\boldsymbol{m = \frac{\mu_{gg}(\mu_{ee} - \mu_{gg})}{4\pi\epsilon_0 hca_0^3}} \tag{4.12}$$

where ϵ_0 is the vacuum permittivity (8.854×10^{-12} C V^{-1} m^{-1}), *h* is Planck's constant (6.626×10^{-34} J s), *c* is the speed of light (2.998×10^8 m s^{-1}), and $a_0 = (3M/4\pi\rho N)^{1/3}$ is the Onsager cavity radius. The solvent polarity function defined by McRae[269,271] based on the dielectric constant (ϵ_r) and the refractive index (*n*) of the solvent is:

$$\boldsymbol{f(\epsilon_r, n^2) = \frac{\epsilon - 1}{\epsilon + 2} - \frac{n^2 - 1}{n^2 + 2}} \tag{4.13}$$

The solvatochromic shifts in absorption versus the solvent polarity function are shown in Figure 4.16, and the results of the linear regression analysis are summarized in Table 4.10. The stronger solvatochromic response observed for **$PMe_3TC_6(CN)_2$** is apparent in the larger slope that gives rise to a greater $\boldsymbol{\Delta\mu}$ than for **$PMeT(CN)_2$** or **$QMeTC_6(CN)_2$**, despite quinoline being a stronger acceptor. This larger $\boldsymbol{\Delta\mu}$ can be correlated with the previous observations in which the ground state structure of **$PMe_3TC_6(CN)_2$** has a large contribution from the zwitterionic-aromatic resonance form. The greater isolation of charges in the individual rings facilitated by the larger inter-aryl twist leads to the larger ground state dipole moment.

The TICT response mechanism, as described by Albert *et al.*,[227] relies firmly on the sterically governed reduction of conjugation between donor and acceptor subfragments that results in charge localization, leading to large dipole moment changes between the charge separated ground state, and the neutral excited state. The calculated $\boldsymbol{\Delta\mu}$ values for the thiophene-based tictoid chromophores trend strongly with their

calculated twist angles, and the delocalization expected from annulated benzene rings. It must also be noted that the qualitative measure for $\Delta\mu$ using $\Delta\lambda_{max}$ gives nearly equivalent solvatochromic shifts between **$PMe_3TC_6(CN)_2$** and **TMC-2** (Chart 4.3),[234] despite the smaller calculated angle of the former (74°) than the latter (~90°). This is attributed to the gain in electron density afforded by the electron-rich thiophene ring acting as an auxiliary donor.[70]

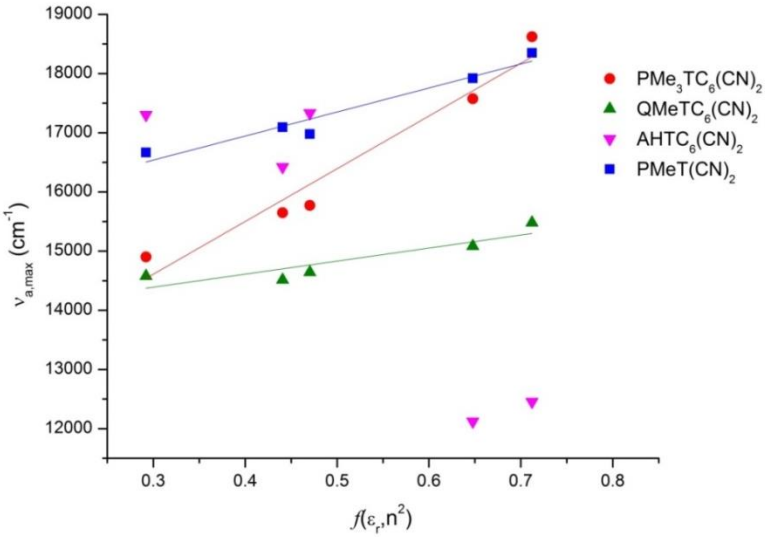

Figure 4.16. Linear regression analyses of the solvatochromic behavior in the thiophene-based chromophores *via* the McRae equation.

Table 4.10. Results of linear regression analysis according to eq. 4.11 (ν_0, slope (m), r^2, a_0, $\Delta\mu$, and μ_e,).

Compound	ν_0 (cm^{-1})	m	r^2	a_0 (Å)[b]	$\Delta\mu$ (D)	μ_{ee} (D)[c]
$PMe_3TC_6(CN)_2$	11,937 ± 604	8,910 ± 1131	0.94	5.2	−7.0	28.4
$QMeTC_6(CN)_2$	13,729 ± 330	2,203 ± 618	0.74	5.3	−2.0	30.1
$AHTC_6(CN)_2$[a]	6,389 ± 4666	8,859 ± 6754	0.79	5.4	8.5	25.0
$PMeT(CN)_2$	15,321 ± 302	4,059 ± 565	0.93	4.6	−3.6	17.4

[a] Only the values for polar solvents are considered (solvatochromic reversal not taken into account). [b]Calculated from $a_0 = (3M/4\pi\rho N)^{1/3}$ assuming ρ=1.0 g/cm^3 for all chromophores.[272] [c]Calculated from $\mu_{ee} = \mu_{gg} + \Delta\mu$, μ_{gg} values taken from DFT calculations.

4.5.3.2. Estimation of Transition Dipole Moments

The intensity of a transition depends on the oscillator strength, which gives a measure of the probability of the molecule to absorb light of a particular frequency. In quantum mechanical terms, this is equivalent to the square (probability) of the transition dipole moment, which gives a measure of how easily the electron distribution is distorted upon excitation.[6] Thus, the interaction of the electron cloud with the electric field of the light absorbed is closely related with the polarizability of the chromophore. This is evident in eqs. 4.4 to 4.6, where the transition dipole moment term ($\boldsymbol{M}_{\mathbf{ij}}$) appears in each equation.

Experimentally, the transition dipole moment can be determined from the area under the absorption band according to the relation:

$$\left|\boldsymbol{M}_{ij}\right|^2 = \mathbf{3\ln 10}\frac{\boldsymbol{hc\epsilon_0}}{\boldsymbol{2\pi^2 N_A}}\int \frac{\boldsymbol{\varepsilon}}{\boldsymbol{\nu}}\boldsymbol{d\nu} \qquad (4.14)$$

where h is Planck's constant, c is the speed of light, ϵ_0 is the permittivity of free space, N_A is Avogadro's number, ε is the molar absorptivity, and ν is the frequency in wavenumbers.[225] The areas considered for the thiophene-based chromophores are shown in Figure 4.17, and the calculated values in two different solvents (used for nonlinear characterizations) are listed in Table 4.11. The $\boldsymbol{M}_{\mathbf{ge}}$ values obtained for **$PMe_3TC_6(CN)_2$** and **$AHTC_6(CN)_2$** are 3.2 and 2.8 D, respectively, in CH_3CN (Figure 4.17a). These are modest due to the meager overlap of ground and excited state wavefunctions as shown by the theoretically calculated HOMO and LUMO orbitals (Figure 4.10), and reflecting the larger twist angles in these chromophores. In CH_2Cl_2, $\boldsymbol{M}_{\mathbf{ge}}$ for **$PMe_3TC_6(CN)_2$** increases to 5.2 D, due to the larger molar extinction coefficient observed in this solvent of ε = 12,075 M^{-1} cm^{-1} (Figure 4.17b), indicating a more significant overlap of ground and

excited state wavefunctions. The M_{ge} values for **PMeT(CN)$_2$**, and **QMeTC$_6$(CN)$_2$** are much higher at 8 to 10 D, due to the greater extent of conjugation and delocalization across the donor and acceptor subfragments from the sterically less hindered inter-aryl substitution, and lower calculated twist angles.

The experimental transition dipole moments for the thiophene-based chromophores strongly reflect the degree of overlap between their HOMO and LUMO orbitals, and are thus closely tied to the sterically induced twisting between the donor and acceptor subfragments in each molecule.

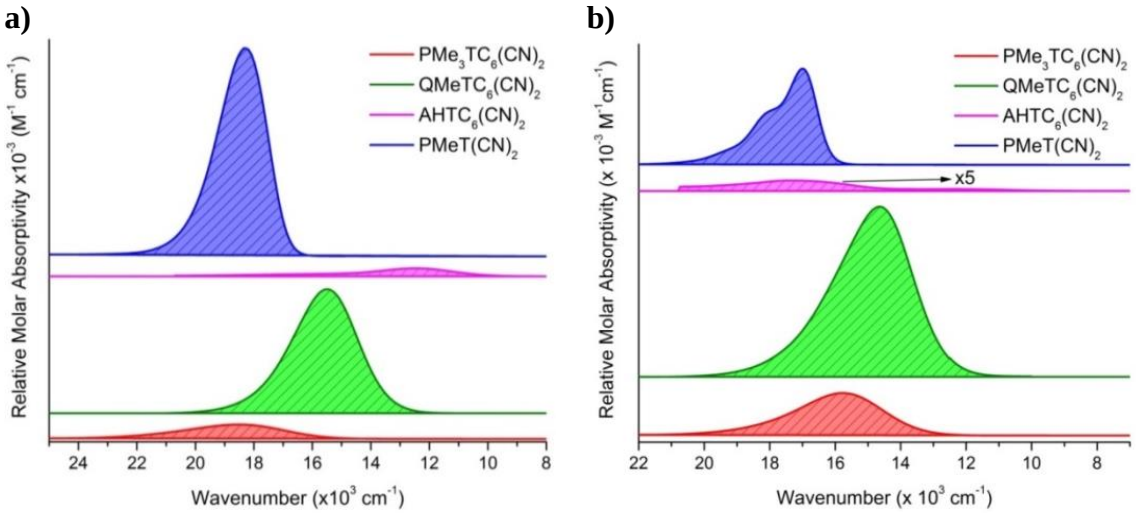

Figure 4.17. The areas of the ICT bands for the thiophene-based chromophores in CH_3CN (a); and in CH_2Cl_2 (b).

Table 4.11. Calculated M_{ge} in low and high polarity solvents.

Compound	M_{ge} (D)[a]	
	CH_3CN	**CH_2Cl_2**
PMe$_3$TC$_6$(CN)$_2$	3.2	5.2
QMeTC$_6$(CN)$_2$	8.6 (4.5)[b]	10.0
AHTC$_6$(CN)$_2$	2.8[c]	2.2[c]
PMeT(CN)$_2$	8.8	5.3[c]

[a]Calculated from eq. 4.14. [b]M_{ge} in benzyl alcohol. [c]Disregards changes in spectral shape for simplicity.

4.5.3.3. Ground-to-Excited State Energy Gap

The transition energy between ground and excited state is expected to be at a minimum when the dihedral twist angle in a TICT system approaches or is at 90° (Figure 4.1). Quantum chemical calculations performed by Dr. A. Baev (SUNY-Buffalo) on **P-T'-(CN)$_2$** (Chart 4.3) indeed show a strong dependence of the HOMO-LUMO energy gap on the twist angle (Table 4.12), with the minimum occurring at the largest twist angle.

Table 4.12. Twist angle dependence of the HOMO-LUMO energy for **P-T'-(CN)$_2$** (CAM-B3LYP/6-31+G*, Dr. A. Baev, SUNY-Buffalo).

Twist angle (°)	HOMO-LUMO gap (a.u.)
20	0.1372
30	0.1340
40	0.1292
50	0.1226
60	0.1143
70	0.1044
80	0.0936
90	0.0859
Optimized in $CHCl_3$ at HF/6-31G*	0.1057

The transition energies of the thiophene-based chromophores were experimentally determined from the onset of their absorptions in CH_3CN, and from electrochemical methods. As solutions in CH_3CN, the thiophene-based chromophores are expected to be more appropriately described by their zwitterionic-aromatic resonance forms in the ground state, and the neutral-quinoidal resonance form is expected to contribute strongly to the first excited state. Thus, the relative stabilities of these two structures are expected to help determine the energy gap. The results are summarized in Table 4.13.

Comparing the optical gaps ($\boldsymbol{E_{ge,opt}}$) of the tictoid thiophene-based chromophores, a decreasing trend is observed in the order: **PMe$_3$TC$_6$(CN)$_2$** < **QMeTC$_6$(CN)$_2$** <

AHTC$_6$(CN)$_2$. This trend follows the increasing annulation of benzene rings to the acceptor core. This structural modification is expected to stabilize the neutral-quinoidal form preferentially to the zwitterionic-aromatic form, and therefore lower the first excited state. Comparing $\boldsymbol{E}_{\mathbf{g,opt}}$ between **PMe$_3$TC$_6$(CN)$_2$** and **PMeT(CN)$_2$** allows isolation of the effects of the steric twist angle from the electronic effects. A lower transition energy is observed for the twisted molecule **PMe$_3$TC$_6$(CN)$_2$**, as predicted from theoretical calculations (Table 4.12). The $\boldsymbol{E}_{\mathbf{ge,opt}}$ of **PMe$_3$TC$_6$(CN)$_2$** is also 0.24 eV smaller than that for **TMC-2**,[234] an effect that can be attributed to the higher HOMO energies induced by an electron-rich thiophene donor (*vide infra*).

Cyclic voltammetry (Figure 4.18a) and differential pulse voltammetry (Figure 4.18b) in an Ar-filled glovebox with 0.1 M $TBAPF_6$ as a supporting electrolyte in anhydrous CH_3CN against a Ag/Ag^+ reference electrode show one reversible oxidation wave, and one irreversible reduction wave for each of the four thiophene-based chromophores. The electrochemical properties are summarized in Table 4.13. The oxidation potentials for the chromophores can be pinned to the donor fragment thiophenyldicyanomethanide, and are lower compared with those of the **TMC** chromophores.[234] Since electrochemistry was done in a polar solvent, the zwitterionic-aromatic structure is expected to be the dominant contributor, and the twist angles are similar or higher than those calculated for a $CHCl_3$ environment (Table 4.4). The oxidation potentials are expected to depend on the ease of removing an electron from the donor subfragment. This, in turn, depends on how well the negative charge is isolated in this fragment by the inter-aryl twist angle that reduces conjugation between the positively-charged acceptor ring and the donor ring. The oxidation potentials are

observed to increase from −0.21 for **$AHTC_6(CN)_2$** to −0.13 V for **$PMe_3TC_6(CN)_2$** to −0.03 V for **$QMeTC_6(CN)_2$**, and 0.10 V for **$PMeT(CN)_2$**, which roughly follows the calculated twist angles. The reduction potentials, on the other hand, are expected to correlate with the acceptor, with a stronger acceptor being able to more easily accommodate an added negative charge in each annulated aromatic ring, giving a less negative reduction potential. The reduction potentials are thus observed to increase from the strongest acceptor, acridine at −1.14 V, to quinoline at −1.32 V, to the weakest acceptor pyridine at −1.74 V for **$PMeT(CN)_2$**, and 3,5-lutidine at −1.75 V for **$PMe_3TC_6(CN)_2$**.

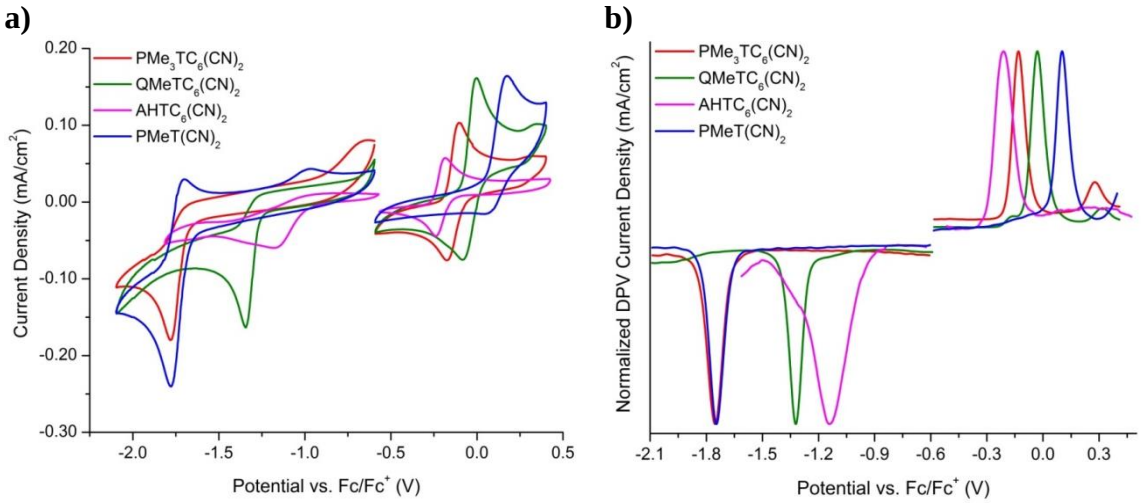

Figure 4.18. Cyclic voltammograms (a) and differential pulse voltammograms (b) of the thiophene-based chromophores.

The DPV potentials, referenced to ferrocene (−5.1 eV relative to vacuum), can be used to calculate the IP and EA, allowing calculation of electrochemical energy gaps ($\boldsymbol{E}_{\mathbf{ge,DPV}}$). Despite the expected deviation of the $\boldsymbol{E}_{\mathbf{ge,DPV}}$ from the fundamental gap,[10] comparison of the values across this family of chromophores shows strong correlation with the calculated optical energy gaps in CH_3CN, with the electrochemical energy gaps

being consistently 0.3 – 0.4 eV lower than the optical energy gaps. This difference arises from the exciton binding energy that is not accounted for by the optical transition energy values.

Table 4.13. Optical gap ($E_{ge,opt}$) and electrochemically-derived ionization potential (**IP**) and electron affinity (**EA**) energies, energy gap ($E_{ge,DPV}$), and oxidation (E_{ox}) and reduction (E_{red}) potentials of the thiophene-based chromophores in CH_3CN.

Compound	$E_{ge,opt}$ (eV)	E_{ox}[a] (V)	IP[b] (eV)	E_{red}[a] (V)	EA[b] (eV)	$E_{ge,DPV}$ (eV)
$PMe_3TC_6(CN)_2$	1.92	−0.13	−4.97	−1.75	−3.35	1.62
$QMeTC_6(CN)_2$	1.67	−0.03	−5.07	−1.32	−3.78	1.29
$AHTC_6(CN)_2$	1.23	−0.21	−4.89	−1.14	−3.96	0.93
$PMeT(CN)_2$	2.09	0.10	−5.20	−1.74	−3.36	1.82

[a]All values referenced to ferrocene $E_{½}$ = 0.067 V vs. Ag/Ag^+ in CH_3CN. [b]Values reported relative to vacuum (-5.1 eV).

Overall, the $E_{ge,opt}$ and $E_{ge,DPV}$ trend with the nature of the acceptor fragment, with higher values obtained for the weakest acceptor pyridine in chromophores **$PMeT(CN)_2$** and **$PMe_3TC_6(CN)_2$**, followed by quinoline in **$QMeTC_6(CN)_2$**, and the smallest value is found for acridine in **$AHTC_6(CN)_2$**. The annulation of one benzene ring in quinoline, and two in acridine, is expected to preferentially stabilize the neutral-quinoidal resonance form than the zwitterionic-aromatic form, leading to lower LUMO (EA) energies for **$QMeTC_6(CN)_2$**, and **$AHTC_6(CN)_2$**, and overall reduced E_{ge}. This annulation effect is also invoked in the trend in calculated E_{ge} values in vacuum (Table 4.4), in which the neutral-quinoidal form is expected to dominate the ground state. The E_{ge} values increase with increasing annulation, due to the preferential stabilization of the ground state over the excited state.

4.5.4. Aggregation Behavior from Optical Spectroscopy

The third order nonlinear susceptibility of a material depends not only on the intrinsic properties of the molecule that comprises it, but also on their macroscopic arrangement.[273] With the carefully engineered charge separation that enhances nonlinear properties *via* large dipole moment changes come substantial intermolecular interactions. These forces affect how molecular properties (normally determined at low concentrations) are translated into macroscopic properties in the bulk arrangement, and may either be augmented or prevented in order to achieve high performance materials.[274] In the case of materials for second-order nonlinear optics, for example, centrosymmetric arrangements lead to failures to translate promising molecular properties into satisfactory material performance.[8,275,276] Strong dipole-dipole interactions lead to aggregation of these chromophores at high concentration, where the thermodynamically favored molecular organization expected from the charge separation can counteract the kinetic structure introduced in poling, and other methods of device preparation.[277,278] In materials for third order nonlinear optics, intermolecular interactions can lead to mixing of excited states, and alteration of the molecular parameters that govern nonlinear properties, as detailed subsequently.

Without significant structural modifications that break up electrostatic interactions,[224,279] charge-separated molecules tend to dimerize in a centrosymmetric antiparallel fashion, which has been observed in many merocyanines.[280-282] These intermolecular interactions at the supramolecular level can be characterized based on the mixing of excited state wavefunctions that leads to changes in absorption properties.[88] A hypsochromic shift of the absorption band with increasing concentration indicates the

formation of H-aggregates. A bathochromic shift, on the other hand, indicates the formation of J-aggregates, with an end-to-end arrangement of dye molecules. (Chapter 1 gives an introduction of these phenomena.)

Strong van der Waals interactions are anticipated in the thiophene-based chromophores due to their large calculated ground state dipole moments in solution ($\boldsymbol{\mu_{gg}}$ > 30 D). In order to study the aggregation behavior of these molecules, concentration dependent absorption spectroscopy in several solvents were performed. The results are shown in Figures 4.19 to 4.22.

$PMe_3TC_6(CN)_2$ shows significant changes in its spectra upon increasing its concentration in $CHCl_3$ over three orders of magnitude (Figure 4.19). A 2.5×10^{-6} M solution shows an absorption band with maximum at ~ 668 nm, and a slight shoulder at higher energy values. Increasing the concentration of the chromophore incrementally to 5×10^{-4} M in this low polarity solvent causes a decrease in the intensity of the original absorption band at ~ 668 nm, while the high energy shoulder gradually intensifies to reveal a new blue-shifted absorption band with maximum at ~ 549 nm. This blue-shifted band at higher concentrations indicates the formation of H-aggregates. Furthermore, the spectra reveal a clear isosbestic point at ~ 596 nm that suggests the occurrence of an equilibrium between two species, the monomeric chromophore, and its dimer,[280] as given by the equation:

$$\mathbf{2M \rightleftharpoons D}.$$

The hypsochromic shift of ~ 119 nm in the dimer band denotes a parallel interaction between monomers, and the electrostatic nature of the interactions suggests an

anticentrosymmetric conformation,[234] thus allowing the positive center (acceptor) of one molecule to interact with the negative center (donor) of a nearby molecule:

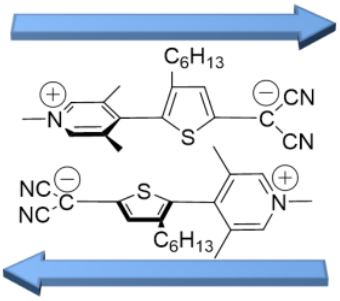

The presence of only one substituent on the donor ring (*n*-hexyl chain) will also allow the molecule to orient itself such that the substituents are on the opposite sides of the interacting faces of the two molecules in the dimer. This likely also stabilizes the dimer pair, while preventing higher order aggregates from forming. This limited aggregation may contribute to the difficulty of growing large single crystals of this chromophore described earlier.

The dimerization model implies an equilibrium constant, K_d, defined as:

$$\boldsymbol{K_d = \frac{c_D}{c_M^2} = \frac{1-\alpha}{2\alpha^2 c_{0M}}} \tag{4.14}$$

where c_M and c_D are the concentrations of the monomer, and the dimer, respectively, at equilibrium, c_0 is the initial concentration of the chromophore (the concentration of the solutions as prepared), and $\alpha = c_M/c_{0M}$ is the fraction of the monomeric chromophore in the solution. The observed or apparent molar absorption coefficient ε of the solutions may then be expressed as a function of ε_M and ε_D, the free monomer, and the dimer molar absorption coefficients, respectively:

$$\boldsymbol{\varepsilon = \varepsilon_M \alpha + \varepsilon_D (1-\alpha)} \tag{4.15}$$

ε can be related to K_d by combining the two equations, giving:

$$\boldsymbol{\varepsilon = \frac{\sqrt{8K_d c_0 + 1} - 1}{4K_d c_0}(\varepsilon_M - \varepsilon_D) + \varepsilon_D} \tag{4.16}$$

The K_d then gives the Gibbs dimerization energy by:

$$\boldsymbol{\Delta G_d^0 = -RT \ln K_d} \tag{4.17}$$

Since the pure monomer or dimer spectra could not be experimentally obtained, multi-parameter nonlinear regression analysis of ε at a specific wavelength as a function of c_0 (eq. 4.16) was used to calculate K_d, ε_M, and ε_D. One such analysis performed at 530 nm is shown in Figure 4.19b. Recursive analysis in the wavelength range 525 to 550 nm gives an average K_d = 59,300 ± 4,460 M^{-1}, and $\Delta G°_d$ = −27.2 ± 0.2 kJ mol^{-1}.

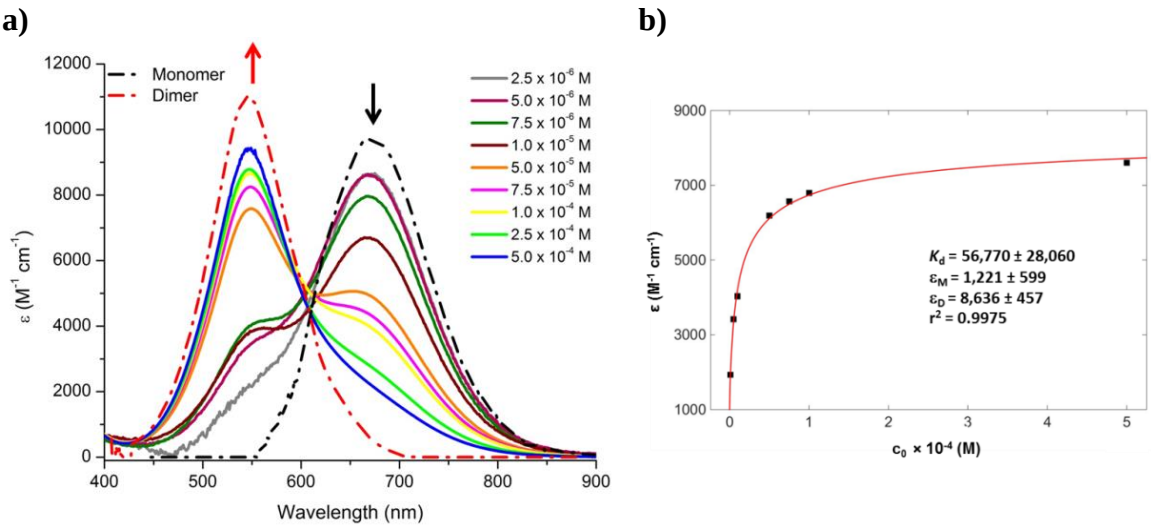

Figure 4.19. (a) Concentration-dependent absorption spectra of **$PMe_3TC_6(CN)_2$** in $CHCl_3$, with arrows indicating the evolution of the spectra with increasing concentration. The monomer and dimer spectra are derived from multi-parameter nonlinear regression analysis. (b) Example result of multi-parameter nonlinear regression analysis done at 530 nm. The red line represents the best fit curve.

The dimerization thermodynamics of **$PMe_3TC_6(CN)_2$** give values that are significantly larger than those for the **TMC** chromophores (**TMC-2** K_d = 13,300 ± 1420 M^{-1} and $\Delta G°_d$ = −23.5 ± 0.2 kJ mol^{-1} in $CHCl_3$),[234] and can be attributed to the larger

dipole moment of **$PMe_3TC_6(CN)_2$** (μ_g = 35.4 D vs. 27.0 D for **TMC-2**). The electrostatic nature of the interaction is further underscored by the observation that the same concentration-dependent absorption experiments did not yield a hypsochromic shift of the ICT band in solvents of higher polarity such as CH_2Cl_2, and CH_3CN (Figure 4.20). But the exergonic dimerization observed in $CHCl_3$ requires careful consideration of its measured nonlinear optical properties in these solvents at higher concentrations.

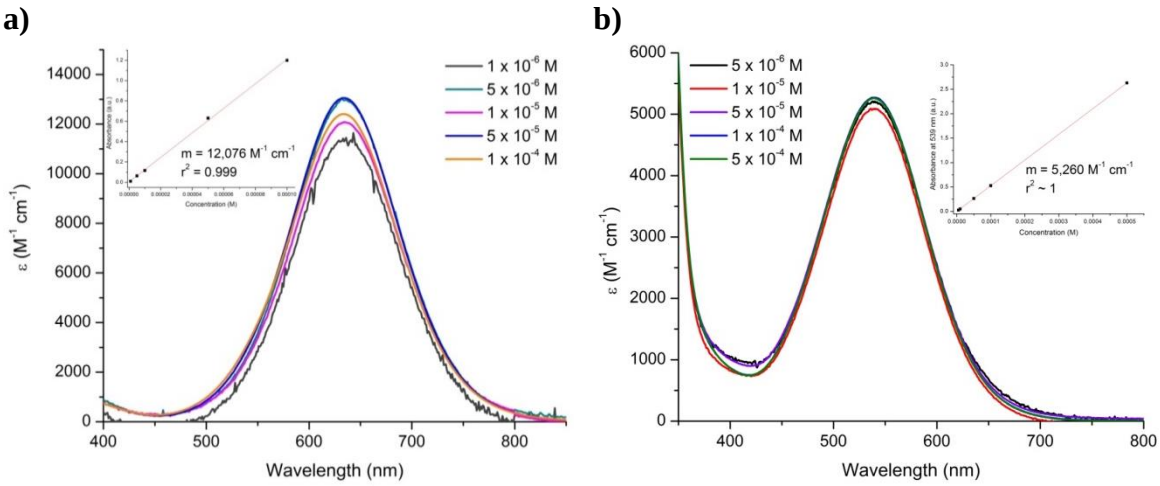

Figure 4.20. Concentration-dependent absorption spectra of **$PMe_3TC_6(CN)_2$** in CH_2Cl_2 (a); and CH_3CN (b). (Insets: Linear regression analysis of the data showing Beer's law dependence.)

$QMeTC_6(CN)_2$ shows a Beer's law relationship of its ICT peak in $CHCl_3$, and CH_2Cl_2 (Figure 4.21a and 4.21b) in the concentration ranges studied. Macroscopic particles were observed at elevated concentrations (Figure 4.21c), indicating aggregation phenomena at significantly higher concentrations than can be studied *via* absorption spectroscopy, and may or may not involve the ICT peak. The lack of clear spectral changes prevents a thermodynamic analysis of the aggregation phenomenon.

$PMeT(CN)_2$ also shows a Beer's law relationship of its ICT peak in CH_2Cl_2, but a nonlinear evolution of the absorption maximum with increasing concentration is observed

in $CHCl_3$ (Figure 4.22). The vibronic resolution in the ICT peak for this chromophore prevents a spectral analysis of aggregation, unlike in **$PMe_3TC_6(CN)_2$**.

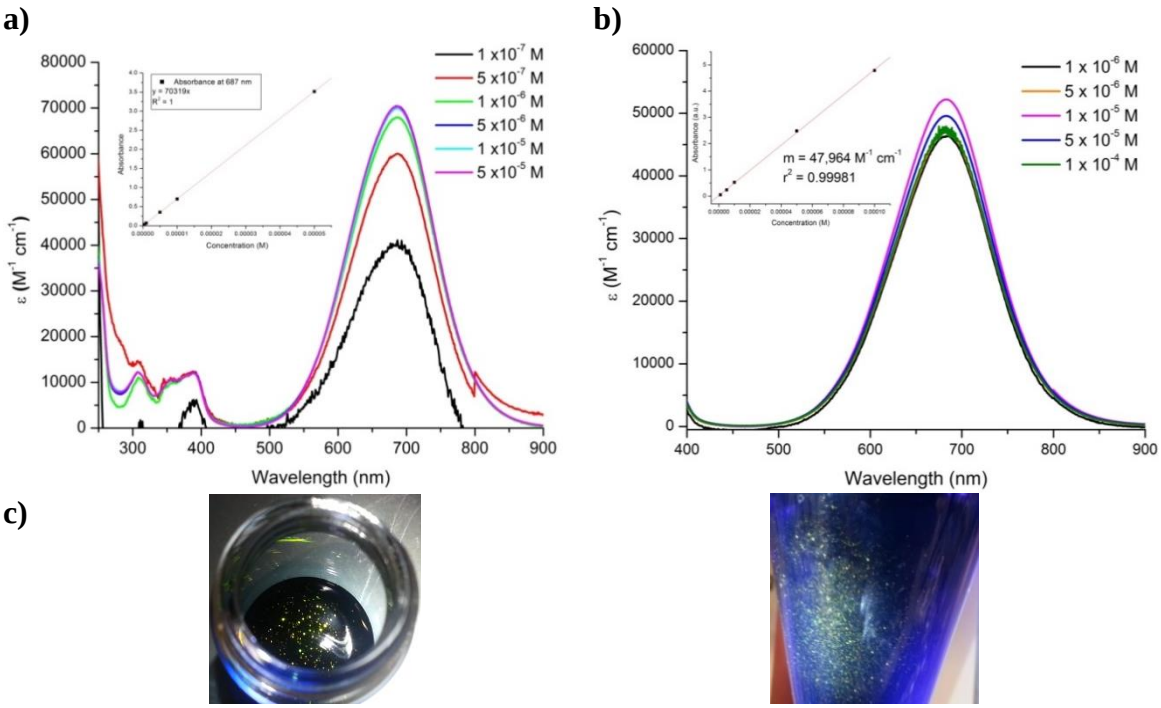

Figure 4.21. Concentration-dependent absorption spectra of **$QMeTC_6(CN)_2$** in CH_2Cl_2 (a); and CH_3CN (b). (Insets: Linear regression analysis of the data showing a Beer's law dependence.) (c) Macroscopic aggregation forming iridescent green particles in a blue solution of the chromophore observed in all solvents at concentrations ~ 10 mg mL^{-1}.

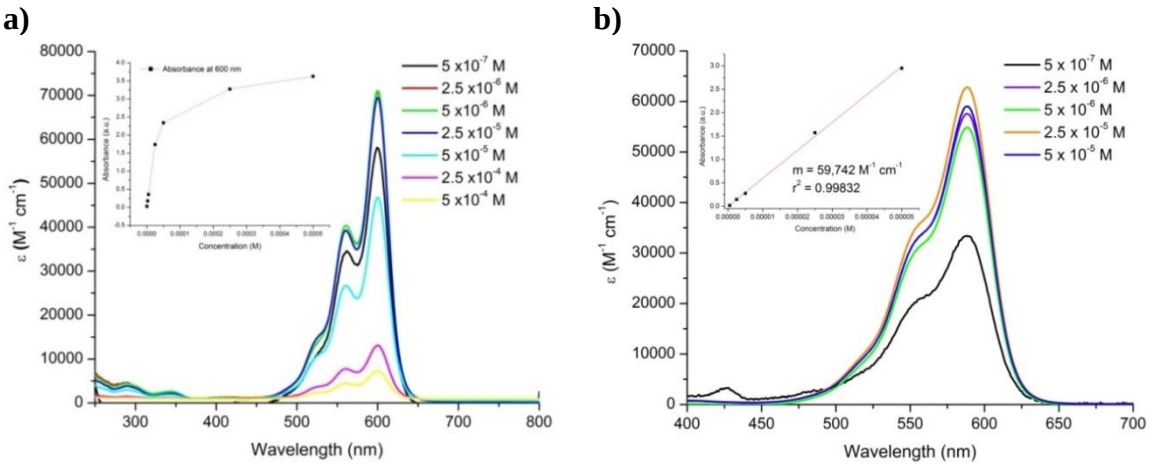

Figure 4.22. Concentration-dependent absorption spectra of **$PMeT(CN)_2$** in $CHCl_3$ (a); and CH_2Cl_2 (b). (Insets: Linear regression analysis of the data showing a Beer's law dependence in CH_2Cl_2, but a nonlinear dependence in $CHCl_3$.)

The concentration dependence of absorption spectra in these thiophene-based chromophores shows dimerization to be significant only for **$PMe_3TC_6(CN)_2$**. This correlates with the greater isolation of charges observed from its stronger solvatochromic behavior (absorption and NMR spectra). The stronger localization of charges allow for enhanced electrostatic interactions between two chromophore units, leading to the significant calculated K_d and $\Delta G°_d$ values.

4.5.5. Nonlinear Optical Properties

The key third order nonlinear optical properties, which are the real and imaginary parts of the third order polarizability, Re(γ) and Im (γ), respectively, can be determined from the intensity-dependent change in nonlinear refractive index, and nonlinear absorption. These properties can both be determined from the Z-scan method pioneered by Sheik-bahae *et al*.[283,284] The nonlinear refractive index change can be obtained from closed-aperture Z-scan measurements, whereas the nonlinear or two-photon absorption property can be determined from open-aperture measurements. For optical switching applications, the light-induced nonlinear refractive index change should be maximized for the optical power density necessary to induce the response to be kept low, while both linear and nonlinear absorptions should be minimized, to decrease the light-induced heating and improve light propagation lengths.[207]

Dr. Guang He (from the group of Prof. Paras Prasad at SUNY-Buffalo) performed Z-scan measurements at two wavelengths of interest for telecommunications applications, ~ 800 nm, and ~ 1300 nm. The laser beam source used is a Ti:sapphire oscillator/amplifier system with ~ 160 fs pulses for the ~ 800 nm case, and an optical parametric generator system for the ~ 1300 nm case, with ~ 160 fs pulses. Solutions in

two solvents of different polarities were studied, and compared with quartz plates, and the pure solvent. The results for **$PMe_3TC_6(CN)_2$** are shown in Figure 4.23 and 4.24, whereas those for **$QMeTC_6(CN)_2$** are in Figure 4.25.

The open-aperture Z-scan measurements for **$PMe_3TC_6(CN)_2$** in CH_3CN are shown in Figure 4.23a and 4.23c. It is clear from these plots that there is negligible intensity-dependent nonlinear absorption from this chromophore at both ~ 800 and ~ 1300 nm. The closed-aperture measurements, on the other hand, show that, at ~ 800 nm, **$PMe_3TC_6(CN)_2$** gives a nonlinear refractive index change that is half that of quartz (n_2(quartz) = 3 × 10^{-7} cm^2/GW), at 1.5 × 10^{-7} cm^2/GW. This gives a third order nonlinear susceptibility value of Re($\chi^{(3)}$) = 2.9 × 10^{-15} esu, and Re(γ) = 2.4 × 10^{-34} esu. At ~ 1300 nm, on the other hand, the nonlinear refractive index change overlaps with the pure

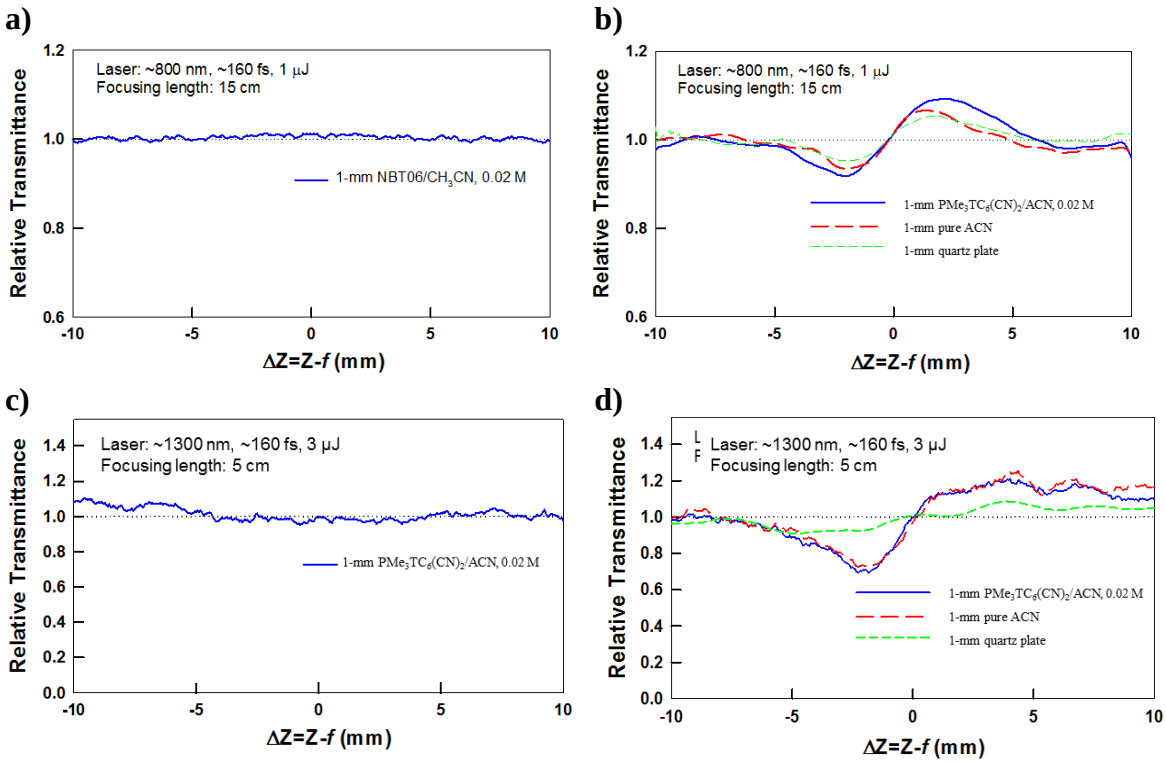

Figure 4.23. Z-scan measurements on **$PMe_3TC_6(CN)_2$** in CH_3CN at ~ 800 nm and at ~ 1300 nm in (a, c) open-aperture, and (b, d) closed-aperture configurations.

solvent, but due to the smaller quantity of the solute **$PMe_3TC_6(CN)_2$** than the solvent, values of $n_2 = 7.5 \times 10^{-8}$ cm^2/GW esu, and Re(γ) = 1.2×10^{-34} esu can be attributed to the chromophore. These properties are summarized in Table 4.14.

In CH_2Cl_2, the Z-scan measurements (Figure 4.24a and 4.24b) give a negligible nonlinear absorption for **$PMe_3TC_6(CN)_2$** at ~ 800 nm, and a nonlinear refractive index that is negative and significantly larger than that of quartz by about 30 times, giving an $n_2 = -9 \times 10^{-6}$ cm^2/GW, and Re(γ) = -1.42×10^{-32} esu.

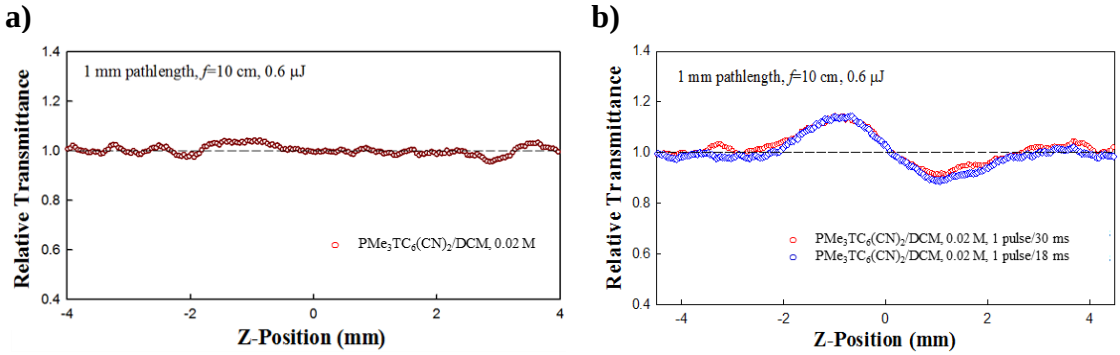

Figure 4.24. Z-scan measurements on **$PMe_3TC_6(CN)_2$** in CH_2Cl_2 at ~ 800 nm in open-aperture (a); and closed-aperture (b) configurations.

Table 4.14. Third-order nonlinear properties of **$PMe_3TC_6(CN)_2$** in CH_3CN at 0.02 M concentration (experimental uncertainty: ± 10 %).

Solvent	**CH_3CN**		**CH_2Cl_2**
Wavelength	**~800 nm**	**~1300 nm**	**~800 nm**
n_2 contribution from solute (cm^2/GW)	1.5×10^{-7}	0.75×10^{-7}	-9×10^{-6}
Re(γ) (esu)	0.24×10^{-33}	0.12×10^{-33}	-1.42×10^{-32}
Im(γ) (esu)	$\leq 1.63 \times 10^{-35}$	$\leq 1.63 \times 10^{-35}$	$\leq 1.63 \times 10^{-35}$ esu
T parameter	≤0.533	≤1.73	≤0.0089
FOM	29	15	
W (at 1 MW/cm^2 level)	0.375×10^{-3}	0.115×10^{-3}	
Linear transmittance: T≈0.995 (at ~800 nm and ~1300 nm, 1 cm path-length)			

The closed-aperture Z-scan measurements for **$QMeTC_6(CN)_2$** are shown in Figure 4.25, and the derived third-order nonlinear properties are summarized in Table

4.15. The Z-scan measurements show very little deviation of the chromophore solution from the pure solvent, but the molar concentration of the solvent is significantly larger than the chromophore, such that the nonlinear properties of the single chromophore molecule are expected to be larger than those of a solvent molecule.

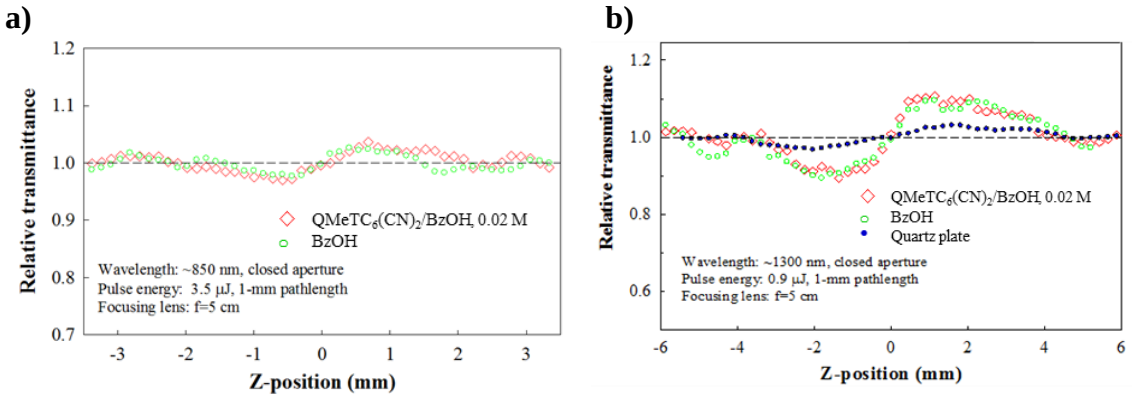

Figure 4.25. Closed aperture Z-scan measurements of **$QMeTC_6(CN)_2$** in benzyl alcohol at a) 850 nm, and b) 1300 nm.

Table 4.15. Third-order nonlinear properties of **$QMeTC_6(CN)_2$** in benzyl alcohol, at 0.02 M concentration (experimental uncertainty: ± 10 %)

Wavelength	**~850 nm**	**~1300 nm**
n_2 contribution from solute (cm^2/GW)	3×10^{-7}	1.2×10^{-7}
Re(γ) (esu)	0.47×10^{-33}	0.19×10^{-33}
Im(γ) (esu)	$\leq 1.63 \times 10^{-35}$	$\leq 1.63 \times 10^{-35}$
T parameter	≤0.283	≤1.08
FOM	29	12
W (at 1 MW/cm^2 level)	0.706×10^{-3}	0.185×10^{-3}

Onset of absorption in benzyl alcohol is 759 nm (1.63 eV). Linear transmittance: T≈0.995 (at ~850 nm and 1300 nm, 1 cm path-length)

The negligible nonlinear absorption coupled with the large Re (γ) values for these two chromophores at two different wavelengths of interest in telecommunications make them promising molecules for optical switching applications.

4.6. Summary

The relevant molecular parameters and third-order nonlinear properties for the thiophene-based chromophores are summarized in Table 4.16. It can be seen that the calculated twist angles follow the degree of substitution around the inter-aryl bond linking the donor and acceptor subfragments. Structural characterizations of these chromophores show that the ground state structure is strongly dictated by the sterically mandated diminution of delocalization between subfragments, and shows a strong response to the environment, with polar media favoring the zwitterionic-aromatic resonance form in all chromophores.

Table 4.16. Summary of molecular parameters and third-order nonlinear properties for the tictoid thiophene-based chromophores and **TMC-2**.

Chromophore	Twist Angle[b]	$\Delta\mu$ (D) ($\Delta\lambda_{max}$[c])	M_{ge}[f] (D)	$E_{ge,opt}$[f] (eV)	Re(γ)[g] (10^{-33} esu)	n_2[g] (10^{-7} cm^2/GW)
					CH_3CN	
$PMe_3TC_6(CN)_2$	74.0°	−7.0 (−113)	3.2	1.62	0.12 (2.4)	0.75 (1.5)
					CH_2Cl_2 (800 nm)	
					−14.2	−90
$QMeTC_6(CN)_2$	39.7°	−2.0 (−56)	8.6	1.29	0.19 (0.47)[h]	1.2 (3)[h]
$AHTC_6(CN)_2$	67.8°	8.5 (195[d])	2.8[e]	1.23		
$PMeT(CN)_2$	NA	(−52)[e]	6.3	1.84		
TMC-2[a]	89.6°	(−118)		1.95	1.4 (at 775 nm)	

[a] Values from reference [228]. [b]Calculated values for model compounds in Chart 4.4.1. [c]Taken as the difference in λ_{max} between CH_2Cl_2 and MeOH. [d]Neglects solvatochromic reversal. [e]Neglects changes in spectral band shape. [f]In CH_3CN. [g]Values outside of parentheses are for 1300 nm, values inside are for 800 nm. [h]Values for 850 nm.

The auxiliary donor effect of thiophene was shown to lead to enhanced solvatochromic response, and larger ground state dipole moments (leading to larger $\Delta\mu$), despite the lower calculated twist angles for these chromophores relative to the **TMC**

chromophores. The lower calculated twist angles also gave rise to higher oscillator strengths of the ICT absorption, leading to larger M_{ge}. The incorporation of an electron-rich thiophene ring has also been observed to result in lower transition energies, likely due to raised HOMO energy levels. Annulation of benzene rings in **QMeTC$_6$(CN)$_2$** and **AHTC$_6$(CN)$_2$** gave rise to greater delocalization and stabilization of the neutral-quinoidal form, leading to decreased transition energies. The greater charge localization afforded by the combination of the auxiliary donor effect of thiophene, and greater zwitterionic-aromatic character in **PMe$_3$TC$_6$(CN)$_2$** also led to a strong tendency for this chromophore to dimerize in low polarity solvents.

These factors are expected to give rise to the large intensity-dependent nonlinear refractive index change observed in **PMe$_3$TC$_6$(CN)$_2$** and **QMeTC$_6$(CN)$_2$**. Indeed, both chromophores show negligible nonlinear absorption, and significant nonlinear refractive index change. In particular, **PMe$_3$TC$_6$(CN)$_2$** has a large γ at 800 nm, surpassing that of **TMC-2** at 775 nm,[228] despite its lower twist angle. This enhancement can be attributed to the structural and electronic effects of the thiophene ring. These properties, along with the synthetic accessibility of the tictoid thiophene-based chromophores make them promising materials for optical switching applications.

4.7. Synthetic Details

General Procedure for Suzuki Couplings:

An oven-dried Schlenk tube equipped with a stir bar was charged with the bromide, $Pd_2(dba)_3$ (3 mol %), 2-dicyclohexylphosphino-2',6'-dimethoxy-1,1'-biphenyl (SPhos, 6 mol %), and K_3PO_4 (3.3eq). The Schlenk tube was then evacuated and backfilled with Ar three times. Then 3-hexylthiophene-2-boronic acid pinacol ester (**2**, 2.0 eq) was added *via*

syringe under Ar. Degassed toluene was then added *via* syringe under Ar. The sealed Schlenk tube was then stirred at 95 °C for 3 days. The reaction mixture was then cooled to room temperature, diluted with CH_2Cl_2 and filtered through a short silica plug and concentrated *in vacuo*. The product was then purified by flash chromatography on silica gel.

4-(3-hexylthiophen-2-yl)-3,5-dimethylpyridine 1-oxide (3a). 2.43 g (84 %) of a viscous brown oil. ^{1}H NMR (300 MHz, CDCl3) δ 7.70 (s, 2H), 6.96 (d, J = 5.1 Hz, 1H), 6.61 (d, J = 5.1 Hz, 1H), 1.84 (s, 2H), 1.62 (s, 6H), 1.15 – 0.95 (m, 2H), 0.94 – 0.62 (m, 6H), 0.51 – 0.24 (m, 3H); ^{13}C NMR (75 MHz, $CDCl_3$) 139.70, 136.21, 136.18, 132.10, 129.06, 127.88, 125.06, 30.66, 29.25, 28.18, 27.72, 21.67, 16.57, 13.20; HRMS (EI, $[M+H]^+$) *m/z* calcd. for $C_{17}H_{23}NOS$ 289.1500, found 289.1503.

4-(3-hexylthiophen-2-yl)quinoline (3b). 2.58 g (87 %) of a gummy brown solid. ^{1}H NMR (300 MHz, cdcl3) δ 8.93 (d, J = 4.4 Hz, 1H), 8.24 – 8.13 (m, 1H), 7.84 – 7.76 (m, 1H), 7.76 – 7.65 (m, 1H), 7.55 – 7.44 (m, 1H), 7.40 (d, J = 5.1 Hz, 1H), 7.36 (d, J = 4.4 Hz, 1H), 7.07 (d, J = 5.1 Hz, 1H), 2.38 (t, 2H), 1.54 – 1.37 (m, 2H), 1.20 – 1.00 (m, 6H), 0.80 – 0.69 (m, 3H); ^{13}C NMR (75 MHz, $CDCl_3$) δ 149.64, 148.43, 141.75, 141.64, 131.94, 129.71, 129.63, 128.88, 128.04, 126.89, 126.16, 125.68, 123.47, 31.50, 30.58, 29.79, 24.71, 22.52, 14.04.

4-(3-hexylthiophen-2-yl)acridine (3c). 2.46 g (71 %) of a light brown solid. ^{1}H NMR (300 MHz, cdcl3) δ 8.29 (dd, J = 8.8, 0.7 Hz, 2H), 7.77 (dd, J = 8.8, 0.7 Hz, 1H), 7.71 (dd, J = 6.6, 1.5 Hz, 1H), 7.70 (dd, J = 6.6, 1.5 Hz, 1H), 7.47 (d, J = 5.1 Hz, 1H), 7.40 (dd, J = 6.6, 1.2 Hz, 1H), 7.40 (dd, J = 6.6, 1.2 Hz, 1H), 7.12 (d, J = 5.1 Hz, 1H), 2.18 (t, 2H), 1.42 – 1.24 (m, 2H), 1.05 – 0.79 (m, 6H), 0.62 (t, 3H); ^{13}C NMR (75 MHz, $CDCl_3$)

δ 148.63, 142.83, 139.49, 129.91, 129.63, 129.39, 128.45, 126.62, 126.51, 126.15, 125.90, 31.18, 29.96, 28.62, 28.59, 22.22, 13.81; HRMS (EI, $[M+H]^+$) *m/z* calcd. for $C_{15}H_{27}NS$ 345.1551, found 345.1544. Anal. Calcd. C, 79.96; H, 6.71; N, 4.05; S, 9.28. Found: C, 79.51; H, 6.60; N, 3.88; S, 8.80.

4-(3-hexylthiophen-2-yl)-3,5-dimethylpyridine (4a). Palladium (10 wt. % on activated carbon, 0.026 g, 0.242 mmol) was added to a solution of **3a** (0.637 g, 2.2 mmol) in glacial acetic acid (15 mL) and the mixture stirred at 80 °C for several minutes. Then sodium hypophosphite hydrate (0.484 g, 5.5 mmol) was added in one portion and the set-up fitted with a condenser and the mixture refluxed under Ar overnight. The mixture was then cooled to room temperature, diluted with $CHCl_3$ (20 mL) and slowly quenched with aqueous $NaHCO_3$ (100 mL). The mixture was then transferred to a separatory funnel and the organic layer separated. The organic layer was then sequentially washed with aqueous $NaHCO_3$ (150mL), water (150mL), and brine (150mL). Then the organic layer was dried over $MgSO_4$, filtered and concentrated *in vacuo*. The resulting brown oil was then purified by flash chromatography on silica gel, eluting with 1:1 hexane: ethyl acetate, to give 0.59 g (98 %) of a light brown oil. ^{1}H NMR (300 MHz, $CDCl_3$) δ 8.32 (s, 2H), 7.28 (d, J = 5.1 Hz, 1H), 6.97 (d, J = 5.1 Hz, 1H), 2.19 (t, 2H), 2.03 (s, 6H), 1.49 – 1.36 (m, 2H), 1.26 – 1.08 (m, 6H), 0.84 – 0.71 (m, 3H); ^{13}C NMR (75 MHz, $CDCl_3$) δ 148.32, 141.98, 139.49, 133.34, 131.68, 128.53, 124.92, 31.53, 30.09, 29.03, 28.48, 22.51, 17.11, 14.02; HRMS (EI, $[M+H]^+$) *m/z* calcd. for $C_{17}H_{23}NS$ 273.1551, found 273.1553.

General Procedure for Brominations:

To a solution of the substrate cooled in an ice bath, N-bromosuccinimide (1.5 eq) dissolved in CH_3CN was added dropwise *via* syringe under Ar. The mixture was stirred

and allowed to come to room temperature over several hours, then heated to 60 °C and stirred for 6-12 hours. The mixture was then cooled to room temperature, diluted with CH_2Cl_2, then washed successively with two portions of water, then brine. The organic layer was then dried over Na_2SO_4 and concentrated *in vacuo*. The resulting product was then purified by flash chromatography on silica gel.

4-(5-bromo-3-hexylthiophen-2-yl)-3,5-dimethylpyridine (5a). 0.30 g (99 %) of a brown oil. 1H NMR (300 MHz, $CDCl_3$) δ 8.34 (s, 2H), 6.96 (s, 1H), 2.19 – 2.12 (m, 2H), 2.09 (s, 6H), 1.48 – 1.34 (m, 2H), 1.22 – 1.11 (m, 6H), 0.86 – 0.76 (m, 3H); ^{13}C NMR (75 MHz, $CDCl_3$) δ 148.15, 140.68, 140.42, 133.29, 133.30, 131.30, 111.75, 31.53, 29.97, 29.01, 28.58, 22.54, 17.19, 14.08; HRMS (EI, $[M+H]^+$) *m/z* calcd. for $C_{17}H_{22}NSBr$ 351.0656, found 351.0665.

4-(5-bromo-3-hexylthiophen-2-yl)quinoline (5b). 2.62 g (80 %) of a gummy dark brown solid. ^{1}H NMR (300 MHz, $CDCl_3$) δ 8.93 (d, J = 4.4 Hz, 1H), 8.23 – 8.14 (m, 1H), 7.85 – 7.78 (m, 1H), 7.78 – 7.68 (m, 1H), 7.61 – 7.45 (m, 2H), 7.33 (d, J = 4.4 Hz, 1H), 7.03 (s, 1H), 2.31 (t, 2H), 1.53 – 1.35 (m, 2H), 1.20 – 1.00 (m, 6H), 0.80 – 0.70 (m, 3H); ^{13}C NMR (75 MHz, $CDCl_3$) δ 149.50, 148.30, 142.50, 141.94, 140.31, 133.37, 131.65, 129.94, 129.70, 127.24, 125.87, 123.42, 112.61, 31.43, 30.39, 28.93, 28.78, 22.49, 14.05.

4-(5-bromo-3-hexylthiophen-2-yl)acridine (5c). 1.27 g (97 %) of a light brown solid. ^{1}H NMR (300 MHz, $CDCl_3$) δ 8.29 (dd, J = 8.8, 0.8 Hz, 2H), 7.82 (dd, J = 8.7, 0.7 Hz, 2H), 7.78 (dd, J = 6.6, 1.4 Hz, 1H), 7.75 (dd, J = 6.6, 1.4 Hz, 1H), 7.49 (dd, J = 6.6, 1.2 Hz, 1H), 7.46 (dd, J = 6.6, 1.2 Hz, 1H), 7.14 (s, 1H), 2.15 (t, 2H), 1.41 – 1.27 (m, 2H), 1.09 – 0.91 (m, 6H), 0.71 – 0.59 (m, 3H); ^{13}C NMR (75 MHz, $CDCl_3$) δ 148.76, 143.78, 137.96, 131.47, 131.20, 130.27, 129.85, 126.61, 126.46, 126.35, 113.11, 31.34, 29.76,

28.89, 28.73, 22.40, 13.99; HRMS (EI, $[M+H]^+$) *m/z* calcd. for $C_{23}H_{22}NSBr$ 423.0656, found 423.0663. Anal. Calcd. C, 65.09; H, 5.23; N, 3.30; S, 7.55. Found: C, 61.4; H, 4.95; N, 3.21; S, 6.66.

General Procedure for Dicyanomethanations:

NaH (95 % dispersion in mineral oil, 4.8 eq) was dispersed in degassed dry THF and cooled in an ice bath. Then a solution of malononitrile (2.4 eq) in THF was added dropwise *via* syringe under Ar. The mixture was allowed to come to room temperature and stirred for at least 1 h. Then, Pd_2dba_3•$CHCl_3$ (5 mol %) and 1,1′-bis(diphenylphosphino)ferrocene (15 mol %) was added, followed by a solution of the substrate in THF *via* syringe under Ar. The reaction mixture was then refluxed at 80 °C under Ar overnight. The mixture was then cooled to room temperature and then the solvent removed under vacuum. The resulting solid was taken up in benzene, filtered, and washed with CH_2Cl_2, $CHCl_3$, and toluene. The solid was then dissolved with acetone and filtered repeatedly, until catalyst byproducts were significantly reduced based on ^{1}H-NMR. The presence of the product was then confirmed by ^{1}H- and ^{13}C-NMR spectroscopy.

Sodium 2-[4-hexyl-5-[3,5-dimethylpyridin-4(*1H*)-ylidene]thiophen-2(*5H*)-ylidene]-malononitride (6a). ^{1}H NMR (300 MHz, acetone-d_6): δ 8.26 (s, 2H), 6.14 (s, 1H), 2.11 (s, 6H), 2.09 (m (under acetone-d_6 residual peaks, 2H), 1.42 (m, 2H), 1.17 (m, 6H), 0.79 (t, 3H); ^{13}C NMR (75 MHz, acetone-d_6) 148.83, 147.43, 143.64, 140.20, 134.55, 127.07, 118.86, 112.45, 32.16, 30.69, 29.63, 29.50, 25.71, 23.09, 17.31, 14.24.

Sodium 2-[4-hexyl-5-[quinolin-4(*1H*)-ylidene]thiophen-2(*5H*)-ylidene]-malononitride (5b). ^{1}H NMR (300 MHz, acetone-d_6) δ 8.82 (d, J = 4.4 Hz, 1H), 8.11 –

8.06 (m, 1H), 8.06 – 8.02 (m, 1H), 7.75 – 7.68 (m, 1H), 7.59 – 7.52 (m, 1H), 7.32 (d, J = 4.5 Hz, 1H), 6.24 (s, 1H), 2.33 (t, 2H), 1.54 – 1.41 (m, 2H), 1.20 – 0.98 (m, 6H), 0.79 – 0.66 (m, 3H). HRMS (ESI, $[M\text{-}Na]^-$) *m/z* calcd. for $C_{21}H_{25}N_3S$ 358.1381, found 358.1383.

Sodium 2-[4-hexyl-5-[acridin-4(*1H*)-ylidene]thiophen-2(*5H*)-ylidene]-malononitride (5c). ^{1}H NMR (300 MHz, acetone-d_6) δ 8.19 (d, J = 8.8 Hz, 2H), 8.02 (d, J = 8.8 Hz, 2H), 7.79 (dd, J = 6.7, 1.4 Hz, 1H), 7.77 (dd, J = 6.6, 1.5 Hz, 1H), 7.53 (dd, J = 6.6, 1.2 Hz, 1H), 7.51 (dd, J = 6.6, 1.2 Hz, 1H), 2.08 (t, 2H), 1.41 – 1.22 (m, 2H), 1.00 – 0.69 (m, 6H), 0.53 (t, 3H); ^{13}C NMR (75 MHz, acetone-d_6) δ 149.33, 148.86, 144.16, 141.99, 130.89, 129.82, 127.80, 127.57, 127.00, 126.46, 116.35, 113.59, 31.76, 30.52, 29.69, 29.10, 26.03, 22.76, 13.99.

General Procedure for Quaternization of Pyridinium Nitrogen:

Methyl triflate (0.9 eq) was added dropwise to a solution of the substrate in a mixture of CH_2Cl_2 and acetone. The mixture was then stirred for 2 h at room temperature, then quenched with water, and extracted with ethyl acetate. The organic layer was then separated and washed successively with two portions of water and brine. The organic layer was then dried over Na_2SO_4 and concentrated *in vacuo*. The resulting solid was then purified by flash column chromatography on silica gel, eluting with CH_2Cl_2:MeOH. Flash column chromatography was then repeated on neutral alumina, eluting with CH_2Cl_2:MeOH.

2-[4-hexyl-5-[1,3,5-trimethylpyridin-4(*1H*)-ylidene]thiophen-2(*5H*)-ylidene]-malononitrile ($PMe_3TC_6(CN)_2$). 0.19 g (33 % over two steps) of a dark purple solid. ^{1}H-NMR (300 MHz, acetone-d_6): δ 8.76 (s, 2H), 6.18 (s, 1H), 4.49 (s, 3H), 2.36 (s, 6H), 2.15

(t, 2H), 1.46 (m, 2H), 1.18 (m, 6H), 0.81 (m, 3H); ^{13}C NMR (75 MHz, acetone-d_6) 154.08, 153.18, 144.12, 143.32, 139.94, 125.10, 113.42, 112.29, 48.06, 32.25, 30.92, 29.64, 28.23, 23.22, 18.35, 14.30; HRMS (ESI, $[M-H]^+$) *m/z* calcd. for $C_{21}H_{25}N_3S$ 351.1763 found 351.1764

2-[4-hexyl-5-[1-methylquinolin-4(*1H*)-ylidene]thiophen-2(*5H*)-ylidene]-malononitrile ($QMeTC_6(CN)_2$). 0.11 g (28 % over two steps) of a shiny green solid. ^{1}H NMR (300 MHz, acetone-d_6) δ 8.64 (d, J = 6.8 Hz, 1H), 8.52 (dd, J = 8.5, 1.5 Hz, 1H), 8.21 (dd, J = 8.8, 1.2 Hz, 1H), 8.13 – 8.06 (m, 1H), 7.91 – 7.84 (m, 1H), 7.50 (d, J = 6.8 Hz, 1H), 6.62 (s, 1H), 4.45 (s, 3H), 2.66 (t, 2H), 1.70 – 1.53 (m, 2H), 1.32 – 1.08 (m, 6H), 0.86 – 0.74 (m, 3H); ^{13}C NMR (75 MHz, acetone-d_6) (insufficiently soluble); HRMS (EI, $[M-H]^+$) *m/z* calcd. for $C_{23}H_{23}N_3S$ 373.1613, found 409.1618; Anal. Calcd. C, 73.96; H, 6.21; N, 11.25; S, 8.85. Found: C, 73.34; H, 5.97; N, 11.17; S, 8.28.

2-(5-(acridin-9(10H)-ylidene)-4-hexylthiophen-2(5H)-ylidene)malononitrile ($AHTC_6(CN)_2$). 0.19 g (33 % over two steps) of a dark purple solid. ^{1}H NMR (300 MHz, CD_2Cl_2) δ 8.25 (d, J = 8.4 Hz, 2H), 7.94 – 7.76 (m, 4H), 7.61 – 7.50 (m, 2H), 7.36 (s, 1H), 6.33 (br, 1H), 3.93 (s, 3H), 2.20 (br, 2H), 1.53 – 1.21 (m, 2H), 1.18 – 0.80 (m, 6H), 0.68 (t, 3H). ^{13}C NMR (75 MHz, $CDCl_2$) 148.66, 147.48, 144.64, 135.04, 131.53, 130.86, 129.66, 128.26, 127.05, 126.99, 126.55, 113.68, 52.62, 31.59, 30.33, 30.19, 29.48, 29.04, 22.68, 14.03. HRMS (EI, $[M-H]^+$) *m/z* calcd. for $C_{26}H_{23}N_3S$ 409.1613, found 409.1600. Anal. Calcd. C, 76.25; H, 5.66; N, 10.26; S, 7.83. Found: C, 74.42; H, 5.87; N, 8.35; S, 7.51.

CHAPTER 5

DISCRETE DONOR-ACCEPTOR CONJUGATED SYSTEMS FOR HIGH CONTRAST ELECTROCHROMICS

5.1. Introduction to Electrochromism

One of the key advantages touted for π-conjugated organic materials is that their properties can be tailored with the molecular structure. This arises from the strong coupling between their electronic and geometric structures (electron-phonon coupling), an integral concept to the analysis of their properties. In this chapter, the focus will be on the simultaneous electronic and geometric changes that occur upon the introduction of charges in π-systems. Specifically, the change in electronic absorption properties upon oxidation (or p-doping – the introduction of positive charge or holes into the π-system) that leads to an observable color change in the material will be elucidated in materials with well-defined π-conjugated backbones. This will be done by understanding the electronic and magnetic characteristics of the oxidized states. This absorption change accompanying a redox reaction is called electrochromism. It finds application in display technologies, smart windows, optical filters, etc., in which a voltage applied to a material in a device can switch it from an opaque (colored) state, to a transmissive state.

To explore the underlying physical phenomena which govern these changes in electronic absorption, the process of ionization must be analyzed simultaneously with the geometric changes that occur with it. A clear demonstration of the paramount role of structure in determining the electronic band structure evolution with ionization is that polymers with degenerate or non-degenerate ground states generate completely different

responses.[1,20,21,285-289] A polymer such as all-*trans* polyacetylene can be described by two structures with exactly the same energy, i.e. it has a degenerate ground state (Figure 5.1a). Peierls distortion leads to a very small bond length alternation along the chain, and the transition from one structure to the other can be described by a defect where a single unpaired electron exists (Figure 5.1b). This defect, called a *soliton*, serves as a boundary between the two degenerate alternating single bond and double bond motifs, and has a slightly higher energy than these two ground state structures. Due to the strong electron-phonon coupling in organic systems, this geometric defect creates a localized state in the middle of the HOMO-LUMO gap of the polymer (Figure 5.1c). When an electron is added or removed from the π-system, the energetic disruption in the system can be reduced by localizing the charge in a geometric distortion, i.e. in the soliton. When the polymer is neutral, the state is singly occupied, and has a spin. When the polymer is p-doped, the intra-gap state is empty and there is no spin. When the polymer is n-doped, the intra-gap level is doubly occupied, and spinless.

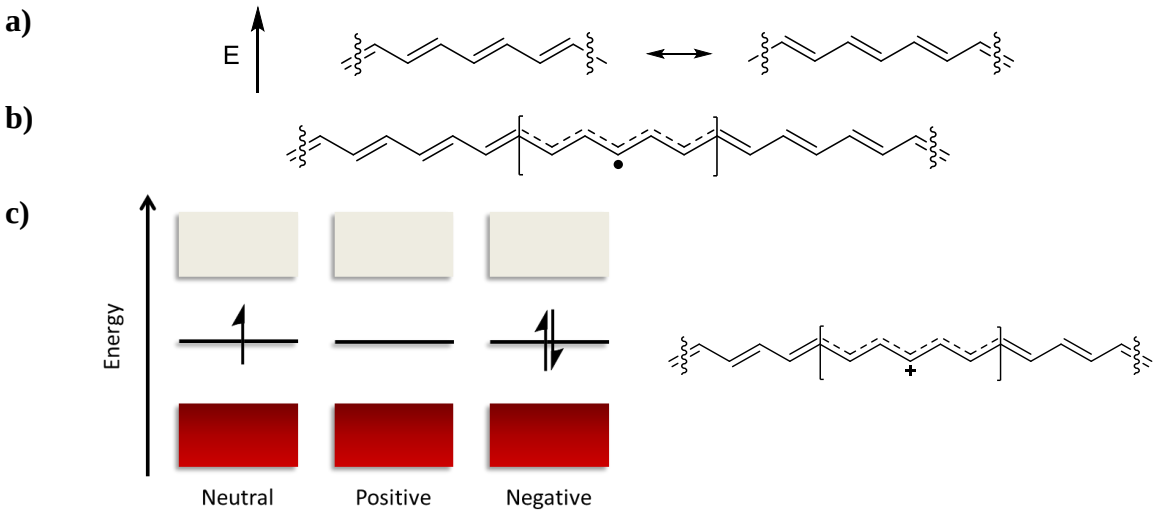

Figure 5.1. The degenerate ground state structure of all-*trans* polyacetylene (a), the soliton that serves as a domain boundary between the two resonance forms (b), and the evolution of its energetic structure with soliton formation around a charge (c). (Adapted from ref.[21])

The description for all-*trans* polyacetylene, however, fails for many conjugated polymers because the latter do not have a degenerate ground state structure. Polythiophene, one of the most ubiquitous and well-studied conjugated polymers, can be described by aromatic and quinoid resonance structures (Figure 5.2). The quinoid structure has a significantly higher energy than the aromatic structure, leading to a non-degenerate ground state. Furthermore, quantum chemical calculations have determined that the quinoid structure has a lower ionization potential and a higher electron affinity.[21] Thus, upon doping of either positive or negative charges, the π-system accommodates these charges on a quinoidal geometric distortion on the chain.

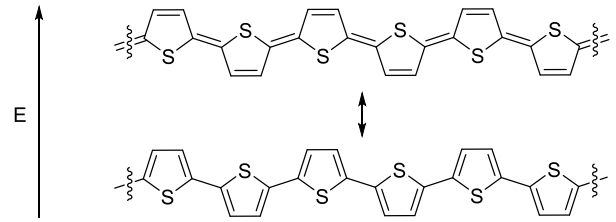

Figure 5.2. The resonance structures of polythiophene showing a non-degenerate ground state, with the aromatic structure (bottom) being less energetic than the quinoidal structure (top).

To further probe the ionization process for polymers with non-degenerate ground states, the case of p-doping (oxidation) will be examined.[20,42,290-293] An electron is removed from the polymer aromatic ground state structure (Figure 5.3a), which destabilizes the system *via* a vertical (Franck-Condon) ionization. The π-system regains some stability by distorting the lattice around the charge: a relaxation to the quinoidal geometry, which is favored by charged states (Figure 5.3b). Conversely, the process can be envisioned to occur (with equivalent energetic cost) by first destabilizing the system with a geometric deformation from the neutral state (to the quinoidal ground state structure), followed by ionization from the higher HOMO (IP level) of the quinoidal

state. The width of the quinoidal distortion varies with the polymer π-system, and the conditions of quinoidalization, but is considered to extend over four to five rings in many cases (~9 rings in oligothiophenes in some calculations[294]). The deformation maximizes in bond length alternation in the middle of the defect, and decreases as it progresses outward. At low doping levels, these localized deformations contain radical cations, and are called *polarons*, as introduced in Chapter 1. As with the soliton, the geometric distortion in the polaron creates electronic states within the HOMO-LUMO gap of the π-system (Figure 5.3b): a lower (P1) polaron level just above the valence (HOMO) band, and an upper polaron level (P2) below the conduction band. The radical cation will have a single unpaired electron in the lower polaron level. The generation of the lower and upper electronic states leads to new optical transitions different from the $\pi - \pi^*$ transition of the neutral system. Commonly, two transitions are observed, one transition between the valence band and the lower polaron level (HOMO → P1), and the other between the lower level and the upper unoccupied polaron level (P1 → P2). The HOMO → P1 transition tends to be weaker than the P1 → P2 transition in oligothiophenes, but the intensity of the former increases with increasing oligomer length.[290] The single occupancy of the lower polaron level is also expected to give rise to a signal by electron paramagnetic resonance (EPR) spectroscopy.

Thus, the process of p-doping such a polymer can be followed by the concomitant changes in its optical spectra (Figure 5.3a and 5.3b, third column). It must be noted, however, that the positions of the mid-gap states relative to the occupied (valence) and unoccupied (conduction) bands, as well as whether the band edges themselves move, are strongly dependent on the specific structure of the conjugated system, including their

length, heteroatoms, and substituents.[290,295] Strongly aromatic units (e.g. phenylene, isothianaphthene) can have weaker geometric distortions, leading to polaron levels close to the band edges, and large energy differences between the two transitions. Some electron-donating substituents, such as ethylenedioxy groups, tend to have an upper mid-gap state closer in energy to the conduction band edge, and a lower mid-gap state that is farther from the valence band edge.[295]

Further oxidation of the polymer to the dication state introduces some complexity. Two energetic costs must be considered: 1) geometric deformation in two sites, and 2) Coulombic repulsion between two charges. If the cost of geometric deformation is higher than the repulsion of putting two positive charges within four to five rings, then a *bipolaron* (Figure 5.3c) is created. If the cost of geometric deformation, on the other hand, is low, two separate polarons (a polaron pair) will be created to force the two repulsive charges apart. The latter case becomes significant in long oligomers, and has been proposed in oligothiophenes with 12 rings,[42,296,297] and in oligomers of other heterocycles[298] by theoretical calculations. In the case of a bipolaronic structure, both the lower and upper polaron levels will be empty, and all spins in the system will be paired. Thus, a bipolaronic structure tends to yield no EPR signal (a decrease in EPR signal from the polaron has also been attributed to partial formation of bipolarons). It must be noted, however, that the conditions for achieving the oxidized state participate in determining the dominant charge carrier. Chemical doping, for example, introduces counterions into the redox equation, and counterions can vary the conjugated system's ability to screen Coulombic repulsions between charges, and the number of rings in which to localize the geometric distortion.[3,291,296,299]

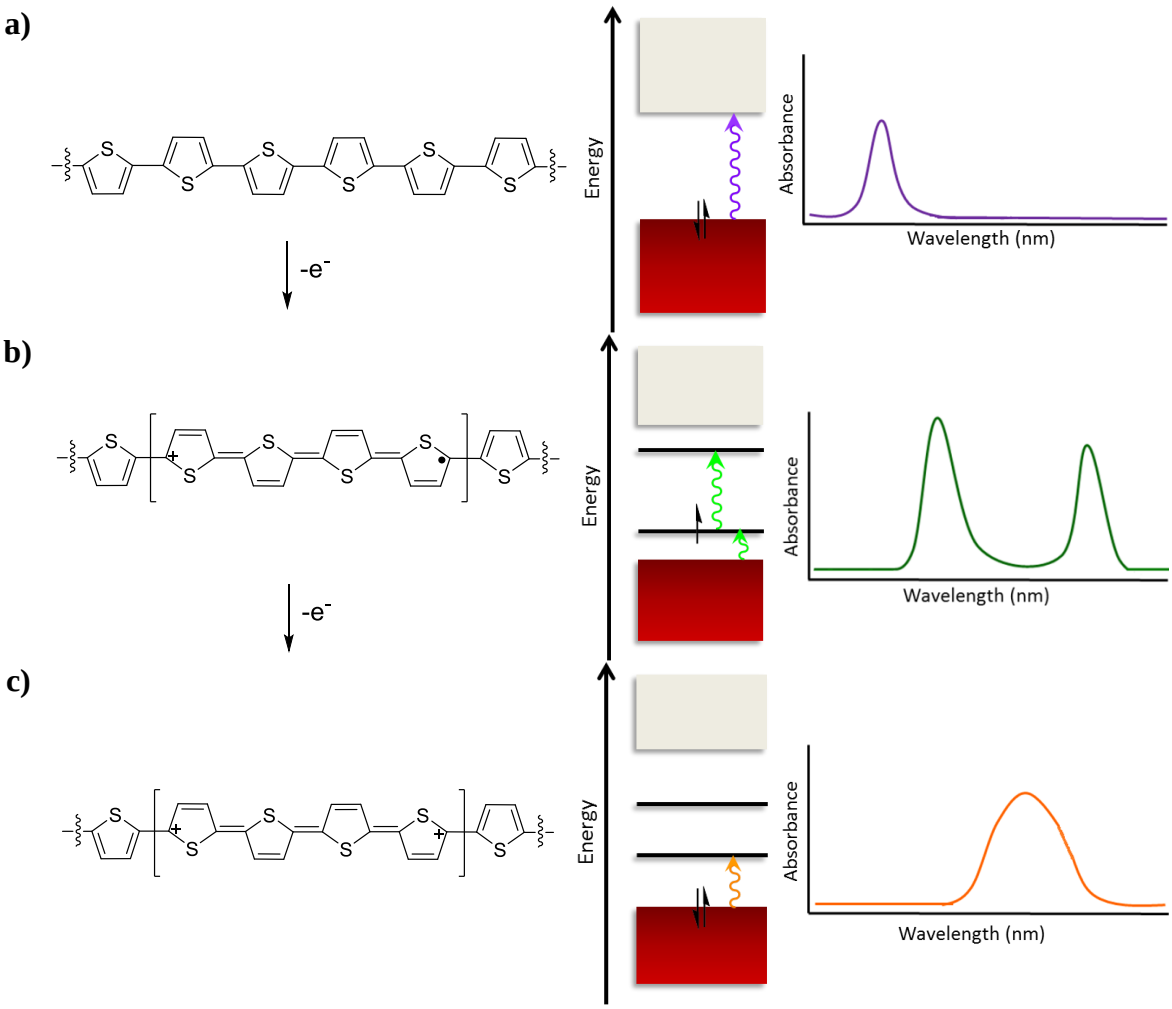

Figure 5.3. Representative structures (left), electronic band structure and transitions (middle), and typical optical spectra (right) of a neutral polthiophene (a), and its polaron (b), and bipolaron (c) formed upon oxidation.

By comparing the rightmost plots in Figure 5.3, it is easy to see how changes in observed color of conjugated materials can be induced upon their oxidation/reduction (or by application of a voltage). The absorption from the neutral polymer system (usually in the UV-vis region for $\pi - \pi^*$ transitions) tends to decrease or bleach out (some blue-shift as they decrease when the band edges widen with oxidation), and new absorptions that are lower in energy (in the near IR region) appear. This forms the physico-chemical basis of electrochromism in organic materials.

5.2. Characteristics of the Charged State: Electronic and Magnetic Properties

As explored in Chapter 1, the position of the neutral state absorption is determined by the electronic band structure of the conjugated material, which, in turn, is an intricate yet subtle interplay of steric and electronic factors in the π-system. Broadly speaking, the same is true for the oxidized state, with the added consideration that the structure adopted must stabilize, as best as it can, the charge it carries. This latter aspect is particularly significant because the energies of the mid-gap states of the oxidized system are tied to the geometric localization of the charge. For one oxidized state, several charge carrier species (an amalgam of the structure, the quantity of the charge, and spin) may be accessible. Each will have different stabilities, band structure, and electronic transitions. Furthermore, as mentioned in the previous section, the charge carriers formed are also a function of the conditions in which the charges are generated.

5.2.1. Radical Cations: Interactions Leading to Alternative Charge Carriers and Ramifications to the Condensed State

Radical cations have been shown to undergo associative interactions[300-302] at low temperature, and high concentration, conditions which approach the interactions expected in the condensed state potentially relevant in various applications. Some of the possible interactions that have been observed are schematically illustrated in Figure 5.4. An understanding of these interactions is required to analyze spectral and electrochemical changes with doping.

The first case in Figure 5.4a is an example of a disproportionation reaction, in which one radical cation oxidizes another to the dication, resulting in the former's reduction to the neutral state. This has been proposed to occur in long oligothiophenes,[42]

long oligothienylenevinylenes,[40] and in short oligoProDOTs,[43] as well as in oligomers containing electron-withdrawing heterocycles.[303] Bendikov, *et al*.[304,305] have shown from quantum chemical calculations that, in oligothiophenes, the energetics of the disproportionation reaction become favorable as the oligomer length increases, and in the presence of solvents and counterions. In both cases, the π-system becomes better able to stabilize two charges (by separating or shielding them). This has been experimentally observed by van Haare[42] in dodecamers of thiophene, and was deduced from a two-band absorption generated upon chemical doping. After addition of one equivalent of the dopant, spectral signatures from both the neutral oligomer, and the two-band signature of a polaronic species were observed, indicating the simultaneous presence of the neutral and radical cation species. In fact, the energies of the latter two peaks were found to be similar in energy to the polaronic signature of sexithiophene. In the case of oligoProDOTs,[43] addition of dopant past unit equivalence gave rise to spectra with signatures from neutral, radical cation, and dication species in tetramers of ProDOTs at room temperature. In longer oligomers, such as hexamers and octamers, the disproportionation reaction was observed only at low temperatures.

Figure 5.4b shows another interaction in which two radical cations homocouple to form a σ-bond (a similar interaction and bond formation occurs in the electrochemical polymerization of heterocyclic monomers). This has been observed in bithiophenes[306,307] and short oligomers of EDOTs.[308] In α-end-capped bithiophenes,[306] the formation of these σ-dimers were observed from temperature-, concentration-, and scan rate-dependent cyclic voltammetry. In these experiments, a second reduction wave was observed in the anodic scan, after the cathodic scan yields radical cations. The growth of

the reduction peaks coincided with a decrease in the peak current intensities of the oxidationwave, and quantitative analysis of these changes revealed a dimerization equilibrium with a large equilibrium constant of K_d = 17,000 M^{-1}, and $\Delta H°$ = −60 kJ mol^{-1}. The high exothermicity of this process points to a highly stable interaction despite the Coulombic repulsion of proximate positive charges, leading the authors to propose the formation of a covalent σ-bond. In hexyl-end-capped dimers of EDOTs, σ-dimerization was also invoked to explain irreversibility of electrochemical oxidation peaks, and the growth of a single absorption band on chemical oxidation, which reached maximum intensity after one equivalent of oxidant was added.[309]

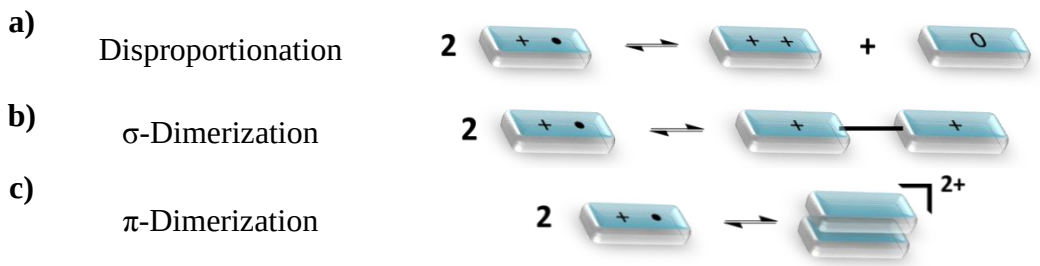

Figure 5.4. Possible interactions between radical cations yielding new species.

A third possible interaction between radical cations is illustrated in Figure 5.4c, in which a close face-to-face interaction of the π-system occurs. This interaction is called a *π-dimer*, and was first proposed by Hill, *et al.*[310,311] in end-capped terthiophenes, where spectroelectrochemistry revealed the growth of four peaks at 572 nm and >800 nm, and 466 nm and 708 nm, along with the depletion of the neutral terthiophene transition. The four peaks were shown to arise from two different species, the monomeric radical cation at 572 nm and > 800 nm, and the dimer at 466 nm and 708 nm. Increasing the concentration, or lowering the temperature favored the growth of the 466 nm and 708 nm pair of peaks at the expense of the 527 nm and >800 nm pair, leading to a dimerization

equilibrium. Also, decreased EPR activity was observed upon cooling below room temperature and at higher concentrations. Similarly, in a series of oligothiophenes, Bauerle *et al.*[312] showed that cooling caused the initial pair of radical cation peaks to blue-shift, and that the dimerization equilibria gave rise to more exothermic dimerization processes with increasing oligomer length. The blue-shifted dimer peaks relative to the monomer peaks were attributed to a Davydov splitting (see Chapter 1 for a thorough explanation),[86] illustrated in Figure 5.5, in which each monomeric non-degenerate energy level (most importantly the HOMO and polaronic levels) is split into two excited state levels due to the bonding interaction of the dimer. In some cases, a third charge-transfer transition from the HOMO → LUMO of the dimer is observed (orange arrow). π-Dimer formation has been observed in many types of conjugated systems, including non-oligomeric small molecules,[313] oligothiophenes,[42,311] oligothienylenevinylenes,[40,314] and oligodioxythiophenes.[41,43]

The energy level diagram shown in Figure 5.5 suggests a rationale for the interaction of two electrostatically repulsive monomers: the pairing of the two radicals to doubly occupy a bonding energy level provides energetic stabilization to counteract the Coulombic repulsion. This pairing of spins leads to the observed decrease in EPR activity at high concentrations or low temperatures. Aside from the stabilization from spin pairing, attractive π-π and van der Waals interactions are also expected to contribute to counteracting repulsive forces. Because of this, π-dimer formation is dependent on the medium in which radical cations are formed. Polar solvents can screen the Coulombic repulsions, thereby disfavoring dimerization.[315,316] This has been experimentally observed in unsubstituted oligomers.[316] In alkyl-substituted oligomers, van der Waals interactions

between alkyl chains and nonpolar solvents impede dimerization, leading to the opposite effect, with dimerization being observed in polar solvents.[316] Certain counterions, like hexafluorophosphate (PF_6^-), have also been shown to promote dimerization in oligothiophenes[317] and oligothienoacenes.[318]

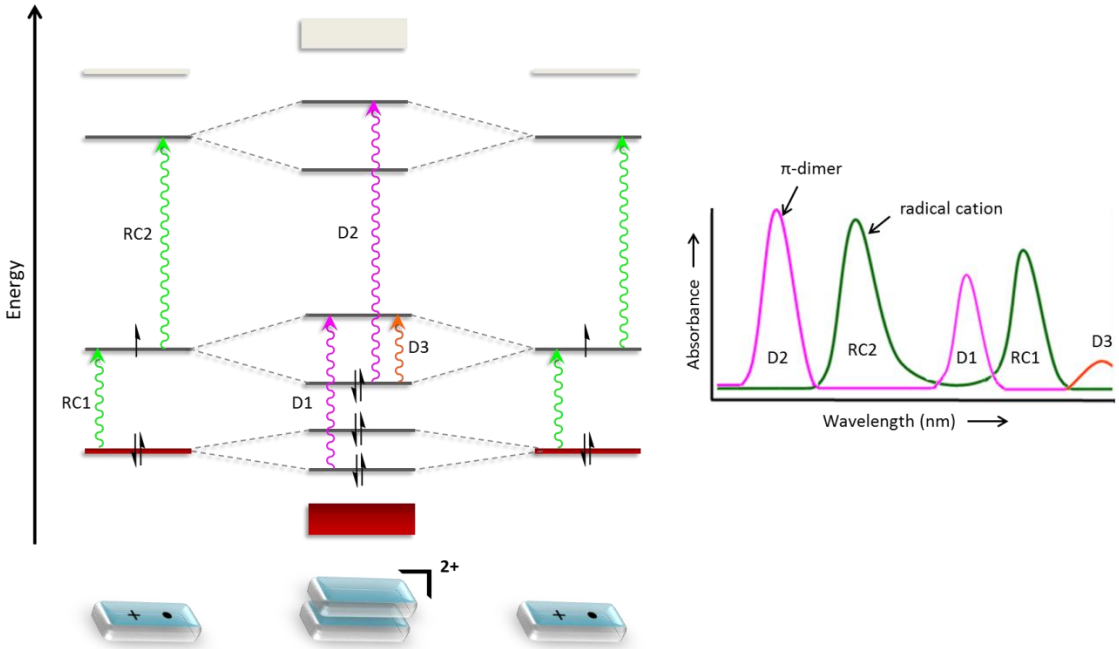

Figure 5.5. Evolution of energy levels and blue-shifted transitions in the π-dimer from the monomeric radical cation energy levels and transitions (Adapted from ref.[312]). The plot on the right shows the comparison of the idealized absorption bands of the two species.

5.2.2. Configurations for Dications: Bipolaron vs. Polaron Pair

The strong electron-phonon coupling in organic materials means that the perturbation induced by doping the material leads to a distortion of the lattice into a geometry that can better accommodate the charge. This, in turn, leads to the appearance of localized states in the electronic band structure. The higher affinity of the geometric distortion for charges offsets the energetic expense of creating the distortion. If a second unit of charge is to be added to the material, the question of where it will be most

energetically feasible to place the charge arises. There are two possibilities: i) the second unit of charge is introduced in the same geometric deformation as the first (Figure 5.6a); and ii) the second unit induces another distortion in a different region of the lattice (Figure 5.6b and 5.6c). The former entails having two like charges in close proximity, leading to Coulombic repulsion, but has no added energetic cost of distortion. The latter, on the other hand, can sidestep repulsion, but requires energy for two distortions. The first case leads to a bipolaron, whereas the second to a polaron pair. The electronic and magnetic signatures of the two may differ substantially, and allow them to be experimentally distinguished.

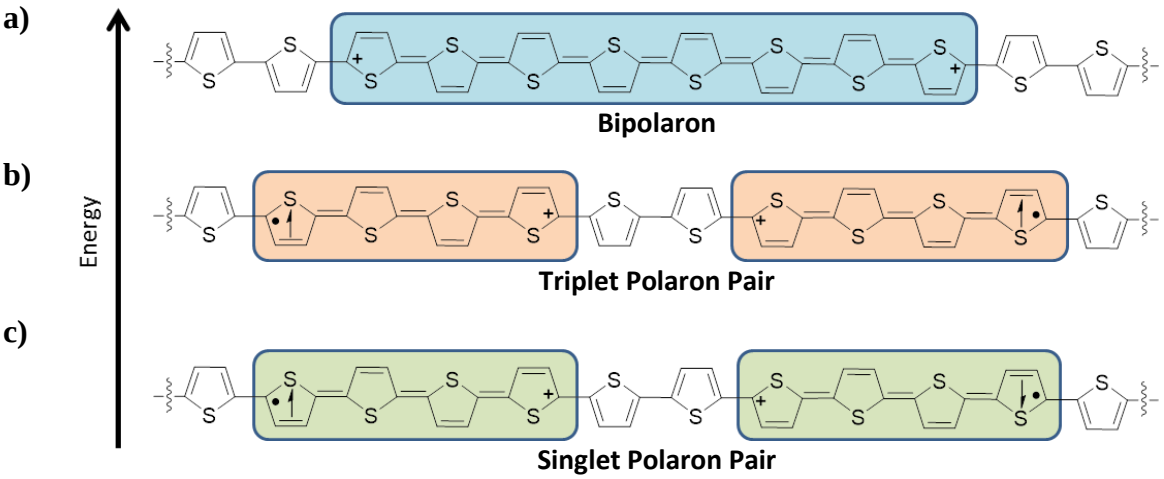

Figure 5.6. Cartoon representations of different dication charge carriers in long oligothiophenes, their geometric deformations and relative energies.

From early theoretical calculations, performed by Bredas, *et al.*,[20,21,288] it was shown that the bipolaron was energetically favorable over the polaron pair because the calculated distortion energy of the two were roughly the same, but the affinity of the bipolaron for charges was significantly higher (lower ionization energy, higher electron affinity, see mid-gap states in Figure 5.3). Subsequent theoretical work by Tol[319] on

oligothiophenes showed that the dication configuration was dependent on oligomer length, with oligomers with less than six units favoring the bipolaron, and longer oligomers a polaron pair. Geometric calculations showed that while the bipolaron structure has a quinoid geometry extending to around eight units in the middle of a decamer (Figure 5.6a), the polaron pair has two quinoid segments extending to four rings on either side of an aromatic middle (Figure 5.6b and 5.6c). In other heterocycles,[298] theoretical calculations show that the polaron pair is the favored charge carrier in longer oligomers, with oligoEDOTs[298] transitioning to the polaron pair at the nine-mer length, and methylthio-endcapped oligoProDOTs[43] favoring it at the hexamer length.

Further complexity is introduced when considering the configuration of a polaron pair (a diradical), which can have a singlet (Figure 5.6) or triplet state (Figure 5.6b). Theoretical calculations also show that the configuration is oligomer length dependent,[296,297,304,305] with short to medium length oligomers favoring the singlet state, and longer oligomers having a mixture of singlet and triplet states. In terms of their electronic transitions, Salzner[296] has shown in oligothiophenes that, while the bipolaron configuration leads to one higher-energy strong absorption and one significantly weaker lower-energy absorption, the polaron pair can have as many as three to four transitions of comparable oscillator strength. These results suggest that, while the polaron pair may consist of two separate geometric deformations, they can still weakly interact, making the experimental discrimination between dication charge carriers by absorption and/or EPR spectroscopy complex.

Zhang *et al*.[320] were able to unambiguously determine the charge carrier of the dication in a cyclo[10]thiophene by comparing its absorption and EPR spectra at various

oxidation states with linear quinque- and deci- thiophenes. They showed that chemical oxidation of the macrocycle to the dication gave rise to two low-energy absorptions, similar in energy to the radical cation peaks of the linear quinquethiophene. Whereas the linear quinquethiophene dication showed a single broad low-energy absorption attributable to a bipolaron, both the macrocycle and the decithiophene gave rise to two low-energy absorptions ascribed to polaron pairs. EPR spectroscopy showed a steady increase of the signal intensity upon doping with 0.5, 1.0, and 1.5 equivalents of oxidant, and decreases slightly at 2.0 equivalents, attributed to population of both singlet and triplet states of the diradical. Temperature-dependent EPR spectra of the diradical shows an increase in intensity at higher temperatures, which the authors attributed to population of the (slightly) higher-energy triplet state from the singlet state.

In other cases in which the polaron pair structure was invoked for the dication, the UV-vis-NIR absorption spectra show different behavior. In oligoProDOTs, Lin *et al.*[43] showed that the octa-, deca-, and dodeca- mers have significant biradical character (relative to the tetra- and hexa- mers). Their UV-vis-NIR absorption spectra showed only one strong and broad lower-energy absorption band, and a barely perceptible broad higher-energy absorption band, despite calculations predicting two strong bands. The lower-energy broad strong band from the polaron pair tends to build up in wavelength regions between the two transitions of the radical cation, making them difficult to distinguish from bipolarons by UV-vis-NIR spectroscopy alone.

5.3. Conjugated Materials for Electrochromics: Control of Neutral and Oxidized State Transitions

Among organic electrochromic materials, conjugated polymers have received significant research focus due to the ease with which their structures can be tailored for color and processing. The degree of delocalization and the electron richness or poorness of the π-system controls the energy gap and the electronic transitions, and therefore the resulting neutral state color of the polymer. In general, upon oxidation at low levels, conjugated polymers generate polaronic charge carriers as evidenced by a two-band absorption, usually in the near-IR region of the spectrum. Further oxidation leads to the formation of a broad band at energies between the two-band feature of the polaronic absorption. This is normally attributed to a bipolaron transition, although other charge carriers such as polaron pairs[321] have been invoked from both absorption spectroelectrochemistry and EPR spectroscopy. An example of the UV-vis-NIR spectra of a conjugated polymer at various oxidation states (attained with a positive applied voltage), and its associated color change in the film are shown in Figure 5.7.

In electrochromics for filtering applications (windows, sunglasses), the oxidized state absorptions must be placed outside of the visible range to yield a colored-to-transmissive switch upon application of a voltage. A survey of the spectroelectrochemistry of many conjugated polymers reported in the literature show broad absorptions for both the polaronic and bipolaronic species.[72,322,323] This broadness leads to a tailing of the bands into the red-region of the spectrum, and resulting in a blue tinted oxidized material. Residual absorptions in the visible region may also tentatively be attributed to incomplete conversion to the bipolaronic state through all conjugation

lengths of the polymer,[324] leaving residual segments in the polaronic or neutral states, and to overlapping absorptions. It is also possible that the disruption of conjugation as polymer chains twist generates different lengths of geometric deformations, leading to different associated energy levels and electronic transitions.

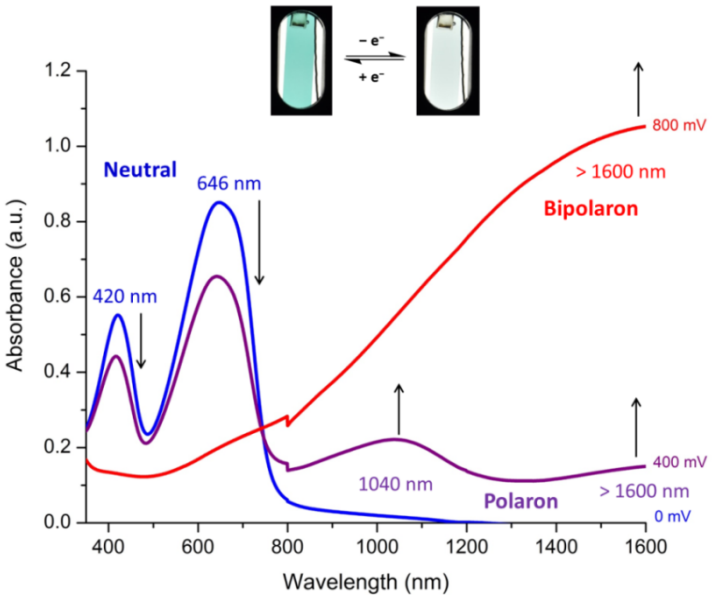

Figure 5.7. Absorption spectra of a fully conjugated polymer at the neutral state (blue), low p-doping levels (purple), and high p-doping levels (red). The applied voltages to attain the transitions are shown to the right of each plot. Top: Resulting color changes on the conjugated polymer film.

In small molecules, on the other hand, the absorptions of both the neutral and oxidized states (especially radical cation and dication states) are narrow and more well-defined. Because of this, some relationships can be established between oligomer structure, and neutral and oxidized state absorption characteristics. It must be noted, however, that a comparison of the absorption spectra of oxidized states of short and long oligothiophenes,[42] and oligoProDOTs[43] reveals increasingly broadened absorptions with longer oligomer chains. Overlapping absorptions from dimerization interactions in oligomers also contribute to broader observed spectra, but can be carefully isolated with

analysis of temperature- and concentration- dependence. Some examples of charge carrier structure elucidation in small molecules are given below.

The absorption energy maxima of charge carrier species were shown by Apperloo, *et al.*[41] to be strongly comparable in short phenyl-endcapped oligothiophenes, and oligoEDOTs, even though their consecutive oxidation potentials diverged significantly, and the neutral state absorptions for oligoEDOTs were red-shifted. The ter-ProDOTs studied by Lin, *et al.*[43] also show similar charge carrier peak energies for the same number of heterocycles. Thus, while electron donation from the β-oxygens in the dioxythiophenes serves to lower their oxidation potentials and neutral state absorption energies, their oxidized state transition energies show minimal response. Both studies also show the strong tendency of the short oligomers to form π-dimers, with some already present at micromolar concentrations, and at room temperature. Oligomers based on a mixture of thiophene, dioxyphenylene, and/or EDOT also form polarons and their π-dimers upon oxidation to the radical cation state. These are then converted to bipolarons upon further doping.[93] In these all-donor oligomer systems, a six-(hetero)cycle oligomer length (12 conjugated π-bonds) seems to be necessary to yield dication absorptions at wavelengths in the near-IR range.

A survey of the literature yields little in the way of analyses of charge carrier species in small molecule oligomers containing electron-poor units. Cao and Curtis[303] studied charge carriers in EDOT-bithiazole hexameric oligomers of acceptor-donor-acceptor (A-D-A) and donor-acceptor-donor (D-A-D) architectures. Solution p-doping experiments showed that while A-D-A oligomers generated two new transitions ascribable to radical cations and their π-dimers, D-A-D oligomers underwent a

disproportionation reaction of the radical cation into a neutral oligomer and a dication, characterized by a single absorption peak ascribed to a bipolaronic species. Further oxidation of the A-D-A oligomers to the dication state gave rise to a single bipolaron peak that was blue-shifted relative to the higher energy radical cation transition. Polander *et al.*[325] studied A-D-A and D-A-D trimeric oligomers of benzothiadiazole and dithienopyrrole units only to the radical cation state, and found two lower energy high oscillator strength transitions for either configuration, with two additional weaker transitions observed in the A-D-A oligomer. The high oscillator strength transitions of the D-A-D oligomer were shown to be red-shifted by about 0.6 eV compared to the A-D-A oligomer, and can be attributed to the greater electron density in the D-A-D oligomer, and the greater number of double bonds in that system. Karsten *et al.*[326] also studied trimers of cyclopentadithiophene and several different acceptors in a D-A-D architecture, and showed that the optical absorption spectra of their radical cations showed two transitions, and that these did not vary greatly across the different oligomers. The authors ascribed this to the localization of the charge in the donor segments. In these donor-acceptor systems, the transitions of the radical cations and dications were generally narrow and well-defined, but the 10 conjugated π-bonds seem insufficient to push the higher energy radical cation transition completely into the near-IR range.

5.4. Small Molecule Donor-Acceptor Systems with Discrete Chromophore Structures for High Contrast Electrochromics

The foregoing brief review shows that, while the structure property relationships that allow control of the neutral state color of conjugated polymers are well-understood,[74,322,323] the oxidized state, particularly those of donor-acceptor systems, does

not easily lend itself to the same type of analysis. Applications requiring high contrast, however, require an understanding of the structure-property relationships in charge carrier species so that materials with little to no absorption in the visible region can be generated upon electrochromic switching.

5.4.1. Design and Synthesis of Discrete Chromophores

The full color palette of electrochromic polymers (ECPs)[72,73] that has been developed by the Reynolds group has relied strongly on dioxythiophenes (Figure 5.8). The strong interest in dioxythiophenes can be attributed to two important properties: i) the electron richness of the heterocycle arising from electron donation by the two oxygen units in the β-positions makes them extremely suitable for redox chemistry at low applied voltages, and ii) the significant sulfur-oxygen interactions between adjacent rings that allow for enhanced planarization and conjugation.[43,47] The ProDOT unit, moreover, combines these desirable properties with the ability to attach solubilizing groups, without steric repulsions substantially hindering planarization. In order to induce absorptions in the low-energy end of the visible spectrum, the Reynolds group has also taken advantage of the electron-poor 2,1,3-benzothiadiazole (BTD) unit, as can be seen in the blue, cyan, and green polymers (Figure 5.8). For the same reasons, the ProDOT, and BTD units were incorporated in the discrete oligomers used in this study.

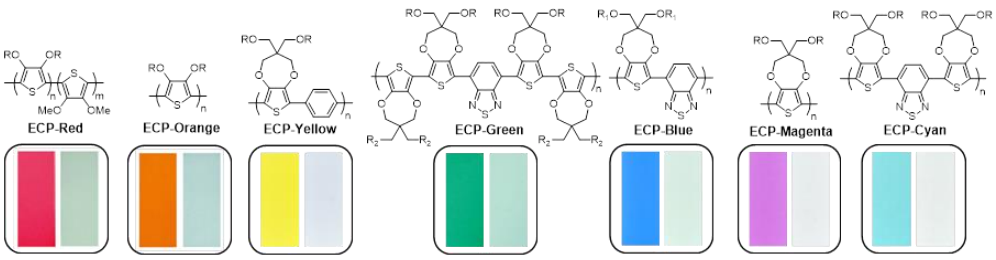

Figure 5.8. Structures, and neutral and oxidized state colors of the electrochromic polymers (ECPs) developed by the Reynolds group.[72,73]

The syntheses of the donor-acceptor small molecules with discrete chromophores are described in Schemes 5.1 and 5.2. The internal donor-acceptor trimer of ProDOT-BTD-ProDOT (**5.3**) was constructed with a one-step direct (hetero)arylation reaction of ProDOT-diethylhexyloxy (**5.1**), with 4,7-dibromobenzo[*c*][1,2,5]thiadiazole (**5.2**). Direct (hetero)arylation has been successfully utilized in dioxythiophene chemistries, especially in the construction of ECPs.[116,327] The dioxythiophene heterocycle is particularly appropriate because the lack of C-H selectivity in direct arylation is rendered a non-issue with the oxygen-blocked β-positions. The enhanced acidity of the α-C-H bonds due to the electron richness of the ring also contributes to its suitability. Here, although both reactants are difunctional heterocycles capable of reacting on both sides, trimer formation was favored over polymerization by careful control of the stoichiometry of the reactants and the catalyst loading (Table 5.1).

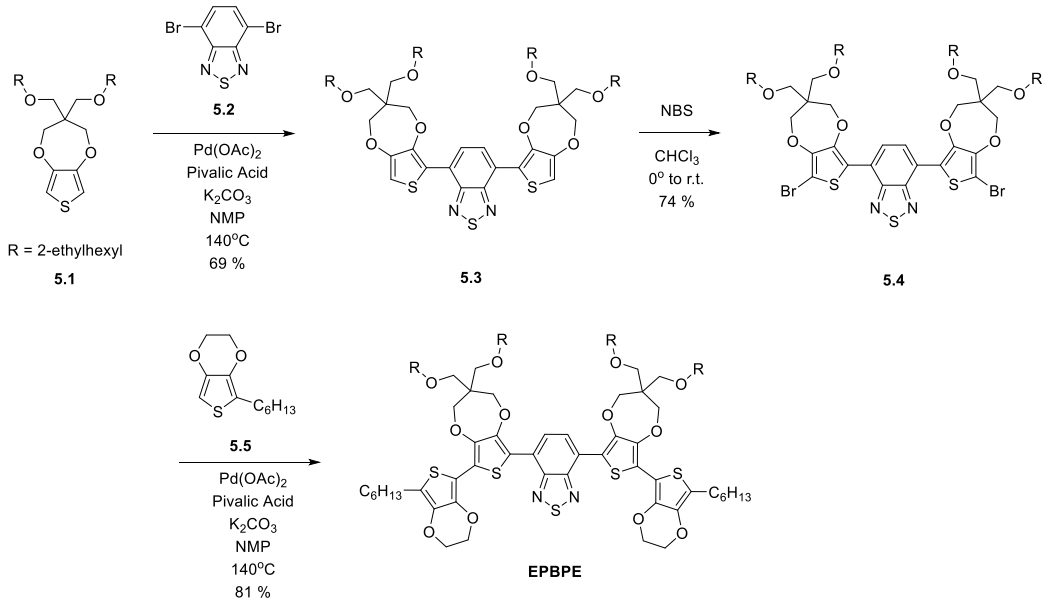

Scheme 5.1. Synthesis of **EPBPE**.

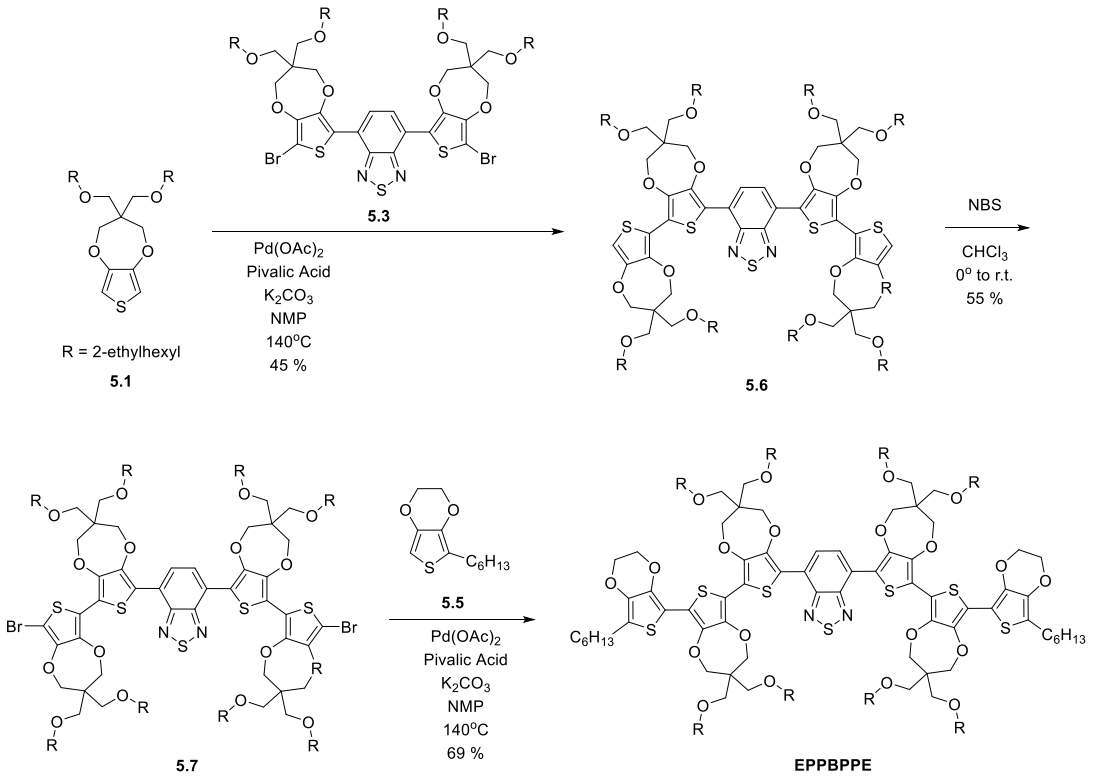

Scheme 5.2. Synthesis of **EPPBPPE**.

Table 5.1. Optimization of trimer formation in direct arylation of difunctional heterocycles.

		Equivalents				
	ProDOT	**BTD**	**$Pd(OAc)_2$**	**Pivalic Acid**	**Reaction Time**	**Yield (%)**
1	6	1	4 mol %	0.06	10 mins	47
2	6	1	4 mol %	0.06	10 mins	52
3	6	1[a]	8 mol %	0.12	20 mins	64
4	12	1	8 mol %	1.2	20 mins	69

[a]The BTD was dissolved in the solvent and added dropwise to the heated reaction mixture.

As shown in Table 5.1, trimer formation was made favorable by using a large excess of the capping ProDOT units. It can also be seen that the catalyst loading is double or more than what is commonly used for direct arylation polymerizations.[116,327] The higher catalyst loading is presumed to allow oxidative addition to both C-Br bonds in a significant fraction of the BTD units, making them susceptible to reaction with the large amount of ProDOT units available. This is unlike in polymerizations where the catalyst is

limited so that only a few oligomers are allowed to grow at a time. Although longer oligomers than the desired trimer were observed on TLC, their formation was arrested by quenching the reaction with a large amount of ethyl acetate as soon as **5.2** was completely consumed (determined by TLC taken at 5-minute intervals). Column chromatography on silica gel allowed near quantitative recovery of the excess ProDOT, making the reaction extremely efficient. The reaction conditions to favor the trimer have been shown to be applicable in other electron-poor units of interest in organic electronics, such as isoindigo. Furthermore, the optimized conditions were also shown to work in making longer oligomers, such as **5.6**, in one step from appropriate starting materials. More importantly, this stoichiometrically-controlled bi-coupling circumvents the need for borylation or stannylation, which involve toxic reagents, and usually entail tricky purification steps.

Finally, EDOT units were used to endcap the oligomers, and these were substituted with *n*-hexyl-chains on the open α-position to improve electrochemical stability. The syntheses of the 5- and 7-unit oligomers were thus accomplished in a few steps with moderate to good overall yields. The 2-ethylhexyl chains on the ProDOT units, along with the endcapping *n*-hexyl chains conferred high solubility to the oligomers, making them processable in a variety of solvents like CH_3CN, CH_2Cl_2, and toluene, among others.

5.4.2. Electronic and Magnetic Properties of Small Molecule Donor-Acceptor Systems in the Neutral and Charged States

The discrete oligomers synthesized here were characterized in their neutral and oxidized states to determine the physicochemical basis of their electrochromic properties.

Attempts to identify the charge carrier species at several oxidation states were made based on their electronic absorption spectra and electron paramagnetic resonance spectra. As described in the preceding sections, the dominant charge carrier species are influenced not only by the structure of the chromophore, but also by the medium in which they are created. Thus, multiple methods and conditions were explored in generating the oxidized states in these oligomers.

5.4.2.1. Optoelectronic Properties

The absorption spectra of the oligomers in the neutral state are shown in Figure 5.9, and summarized in Table 5.2. Two strong absorptions are observed in the visible region, a low-energy absorption attributed to a donor-acceptor charge transfer excitation, and a high-energy absorption attributed to a π-π* transition that is indicative of the extent of delocalization of the π-system.[69] Both peaks are narrow and well-defined, especially when compared with the donor-acceptor ECPs blue, cyan, and green (Figure 5.9 inset). This is expected from the discrete nature of the π-conjugated system. Their large molar absorption coefficients ($\varepsilon \sim 10^4\ M^{-1}\ cm^{-1}$) are also indicative of the strong delocalization of the π-system, likely due to the enhanced planarization induced by S-O interactions between the donor units. But the lack of vibronic structure on either peak points to the ability of the solubilizing branched alkyl chains on the ProDOT ring to prevent significant π-π stacking between molecules. The absorptions of the longer oligomer **EPPBPPE** are slightly red-shifted, and have higher absorption coefficients relative to **EPBPE**, and can be attributed to the more extended π-system, with a longer donor segment.

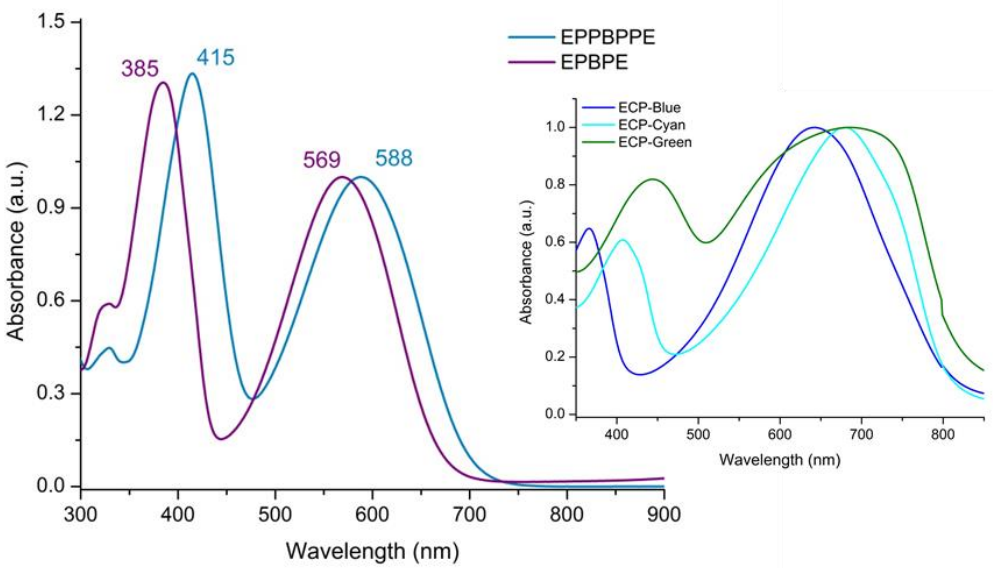

Figure 5.9. Neutral-state absorption spectra of the discrete oligomers. Inset shows the absorption spectra of donor-acceptor ECPs showing broad absorptions.

Cyclic and differential pulse voltammetry of the small molecules were performed in a glove box on 1 *mM* CH_2Cl_2 solutions of the chromophores, with 0.1 *M* $TBAPF_6$ as the supporting electrolyte. The results are shown in Figure 5.10, and summarized in Table 5.2. Both small molecules show reversible first and second oxidation steps, withstanding repeated cyclic voltammetry over 100 cycles (Figure 5.10b and 5.10c). This reversibility demonstrates the stability of the radical cation and dication states of both oligomers in CH_2Cl_2 solution under inert atmosphere. Both oxidized states are also made accessible at low voltages due to the low first ($\boldsymbol{E_{ox,1}}$) and second ($\boldsymbol{E_{ox,2}}$) oxidation potentials of both small molecules (Table 5.2). The addition of two ProDOT rings in **EPPBPPE** further lowers its first and second oxidation potential by about 0.3 V, and reduces the peak-to-peak separation ($\boldsymbol{\Delta E_{ox}}$) between the two oxidation curves by about 0.14 V. The latter behavior has also been observed with increasing length of oligoProDOTs,[43] oligoEDOTs,[41,47] and oligothiophenes,[41,47] and has been attributed to decreasing Coulombic repulsion between the two positive charges with increasing oligomer length.

The magnitude of ΔE_{ox} has been used to determine whether the small molecule can simultaneously exist at various oxidation states at a given potential,[42] and has also been related to the equilibrium constant for the disproportionation reaction of two radical cations into the neutral oligomer and dication (*vide infra*).[43,303,328]

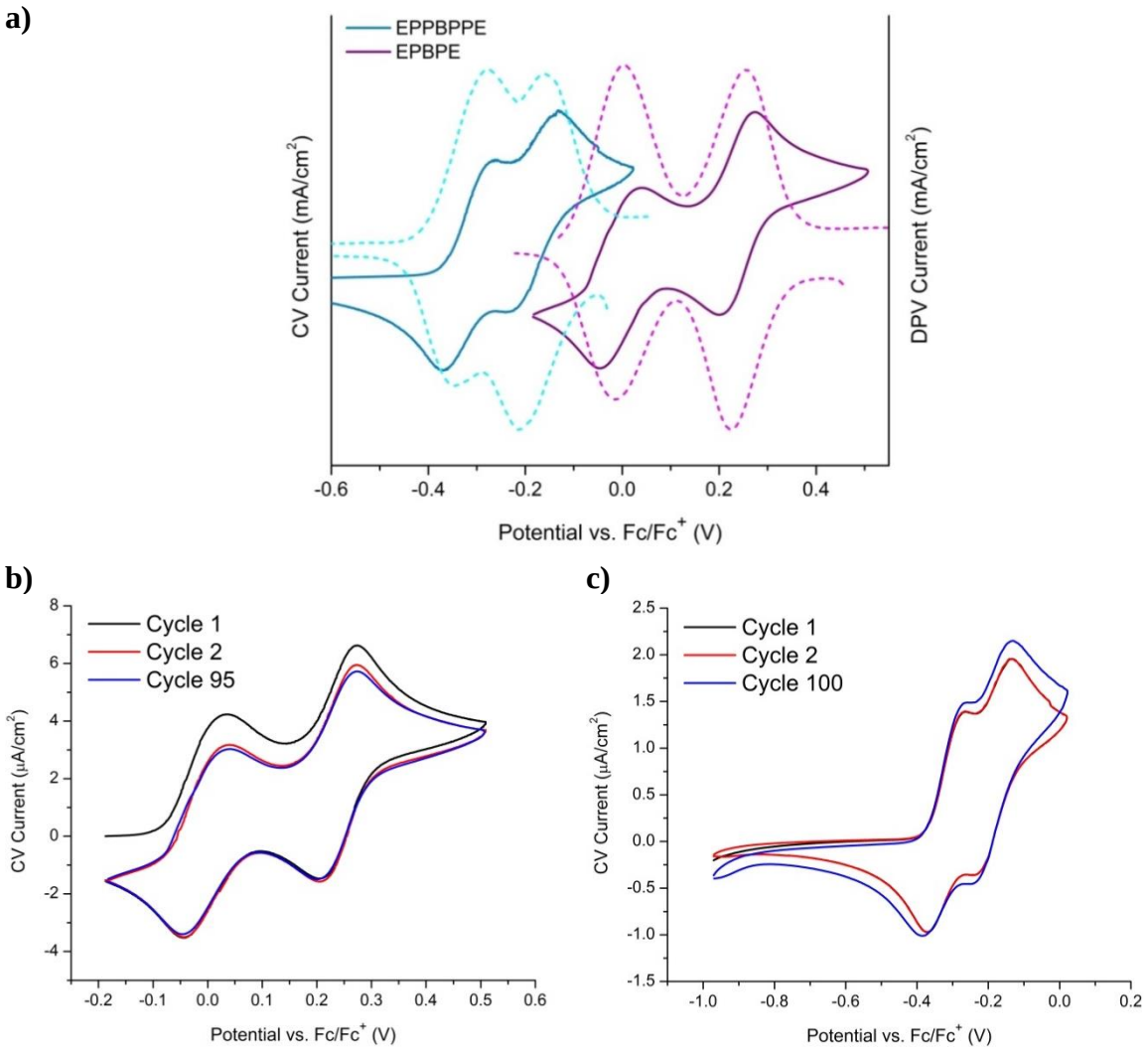

Figure 5.10. (a) Normalized cyclic (solid lines) and differential pulse (dashed lines) voltammograms of the two small molecule donor-acceptor systems showing reversible oxidation behavior. Repeated CV cycling shows the electrochemical stability of **EPBPE** (b), and **EPPBPPE** (c).

Table 5.2. Summary of optoelectronic properties of the small molecule donor-acceptor systems with discrete chromophore structures.

	Optical			Electrochemical				
	λ_{max} (nm) ($\varepsilon \times 10^4$ M^{-1} cm^{-1})		$E_{g,opt}$[a] (eV)	$E_{ox,1}$[b] (V)	$E_{ox,2}$[b] (V)	ΔE_{ox} (V)	IP / HOMO[c] (eV)	EA / LUMO[d] (eV)
	D-A	π-π*						
EPBPE	569 (4.0)	385 (5.3)	1.78	0.004	0.256	0.252	−5.10	−3.26
EPPBPPE	588 (5.5)	415 (7.3)	1.84	−0.276	−0.160	0.116	−4.82	−3.04

[a]Taken from the onset of the D-A charge transfer peak. [b]DPV peak potential; values referenced to ferrocene ($E_{½}$ = 0.185 V vs Ag/Ag^+ in CH_2Cl_2). [c]Values reported relative to vacuum (−5.1 eV). [d]Calculated from the sum of IP and $E_{g,opt}$.

5.4.2.2. Charge Carrier Species in Small Molecule Donor-Acceptor Systems

5.4.2.2.1. Charge Carriers in EPBPE

5.4.2.2.1.1. Chemical Oxidation

Chemical oxidation of **EPBPE** was performed on CH_2Cl_2 solutions of the chromophore at room temperature and inert atmospheres. The solutions were then gradually titrated with known amounts of the dopant solution (exposure to ambient oxygen was minimized), and the spectra of the resulting solution were obtained against a reference containing the same amount of dopant dissolved in the solvent. The chemical oxidants were selected based on the suitability of their formal potentials toward oxidizing the oligomers, and their solubility and stability in CH_2Cl_2. Thus, $AgPF_6$ ($E°$ = 0.65 V vs. Fc/Fc^+), and $NOBF_4$ ($E°$ = 1.00 V vs. Fc/Fc^+) were selected as strong oxidants expected to be able to generate the dication of both oligomers.[121]

The changes in optical absorption spectra in **EPBPE** upon doping with measured equivalents of $AgPF_6$ are shown in Figure 5.11a, along with photographs of the neutral and oxidized state. The difference spectra are also shown (Figures 5.11b and 5.11c) to aid

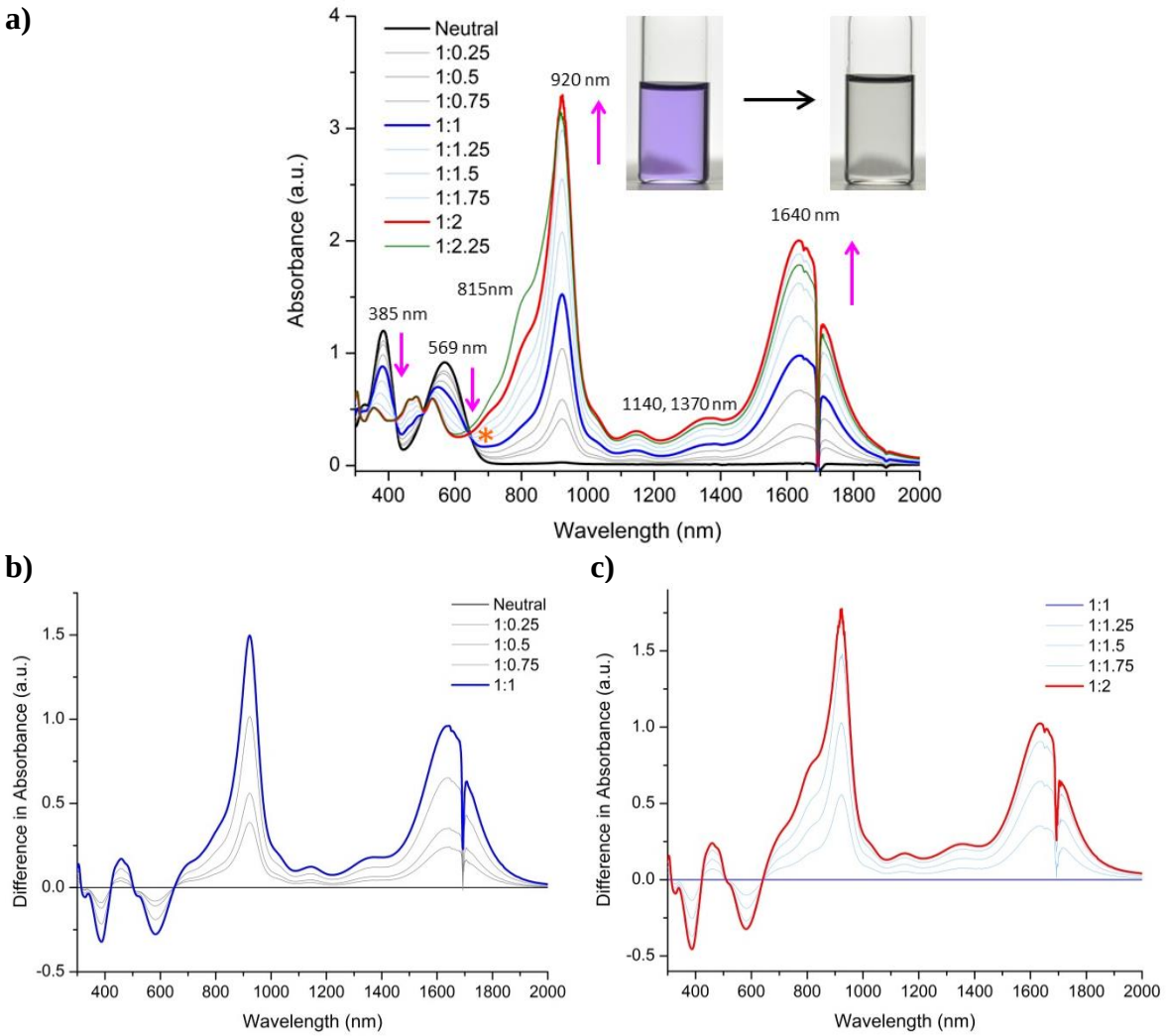

Figure 5.11. Solution chemical oxidation of **EPBPE** with $AgPF_6$ in CH_2Cl_2. (a) Changes in absorption spectra with doping (amounts of dopant are given in equivalents), and photographs of the neutral (left) and dication (right) solutions (inset). (b) Difference spectra showing conversion to the first oxidized state. (c) Difference spectra showing conversion to the second oxidized state.

in analysis. As shown in the plots, addition of $AgPF_6$ causes the depletion of the neutral state transitions at 385 nm and 569 nm, while generating two new strong, but narrow and well-resolved transitions at 920 nm and 1640 nm. This dual transition may be attributed to polaronic mid-gap states created as the molecule is oxidized and accommodates the charge in a quinoidal geometry. The oscillator strengths of the two transitions are also

significantly higher than the neutral transitions, which can be attributed to a quinoidal geometry of the charge carrier, allowing better delocalization in the π-system. The polaronic peaks gradually grow as more dopant is added, but surprisingly, after more than one equivalent of the dopant is added, their absorbances continue to increase with the amount of dopant, and no new transitions ascribable to a bipolaronic type of charge carrier are observed. The transitions at 386 nm and 569 nm, on the other hand, gradually diminish such that the solution changes in color from violet to a highly transmissive neutral hue (Figure 5.11a).

At the first equivalence point (1:1 **EPBPE**:$AgPF_6$, blue trace Figure 5.11a), the neutral state transitions are only about half-depleted, suggesting the presence of neutral molecules at equilibrium with the polaronic species. Since there is a clear isosbestic point in Figure 5.11a (orange asterisk), only these two species are likely present. In such a case, the following stoichiometric analysis[303] can be done in order to determine the possible redox chemistry leading to this equilibrium:

$$\mathbf{M} + y\mathbf{Ag^+} \longrightarrow \mathbf{M^{y+}} + y\mathbf{Ag} \tag{5.1}$$

The total absorbance ($A_{\lambda t}$) at a wavelength λ can be assumed to be the sum of weighted contributions from the two species, neutral (*n*) and polaronic (*p*):

$$\mathbf{A_{\lambda t}} = \boldsymbol{x_n}\mathbf{A_{\lambda n}} + \boldsymbol{x_p}\mathbf{A_{\lambda p}} \tag{5. 2}$$

where *x* gives the mole fractions of each species, and $A_{\lambda n}$ and $A_{\lambda p}$ are the absorbances of the neutral species before oxidation, and the polaronic species after complete oxidation, respectively. The mole fractions can then be rewritten as a function of the fraction (*f*) of dopant added relative to the starting concentration of the molecule:

$$f = \frac{mol\ \mathbf{Ag^+}}{mol\ \mathbf{M_0}} = x_p y \tag{5.3}$$

The total absorbance can therefore be written as:

$$\begin{aligned} \mathbf{A}_{\lambda t} &= \left(1 - \frac{f}{y}\right)\mathbf{A}_{\lambda n} + \frac{f}{y}\mathbf{A}_{\lambda p} = \mathbf{A}_{\lambda n} - \frac{f}{y}\mathbf{A}_{\lambda n} + \frac{f}{y}\mathbf{A}_{\lambda p} \\ &= f\left(\frac{\mathbf{A}_{\lambda p} - \mathbf{A}_{\lambda n}}{y}\right) + \mathbf{A}_{\lambda n} \end{aligned} \tag{5.4}$$

which gives a linear relationship of f and $A_{\lambda t}$, with the slope related to y. Thus, by plotting f vs. $A_{\lambda t}$, the stoichiometry of eq. 5.1, and the charge of the polaronic species M^{y+} can be deduced. The plots are shown in Figure 5.12, and are summarized in Table 5.3. It can be seen that for any chosen transition, the y value is approximately 2. Thus, eq. 5.1 can be rewritten as:

$$\mathbf{EPBPE} + 2\mathbf{Ag^+} \longrightarrow \mathbf{EPBPE^{2+}} + 2\mathbf{Ag} \tag{5.5}$$

The question then becomes: if the dication of **EPBPE** is being formed, why does it give rise to a dual transition ascribable to a polaronic type of charge carrier? It is thus proposed that the dication of **EPBPE** is a polaron pair, as shown in Scheme 5.3. The inference of a polaron pair is supported by the dication structure shown, which allows for the positive charges to be localized in the electron-rich dioxythiophene segments, with the electron-poor BTD ring serving as a conjugation break that prevents bipolaron formation.[326,329] This proposed structure is likely made favorable by S-O interactions that enhance conjugation between the dioxythiophene rings,[47,93,308,330,331] and the higher twist angle between the ProDOT and BTD rings due to steric torsion between the ProDOT rings and the phenyl C-H and C=N *ortho* substituents[332,333] that disrupt the conjugation between the donor rings and the BTD ring.

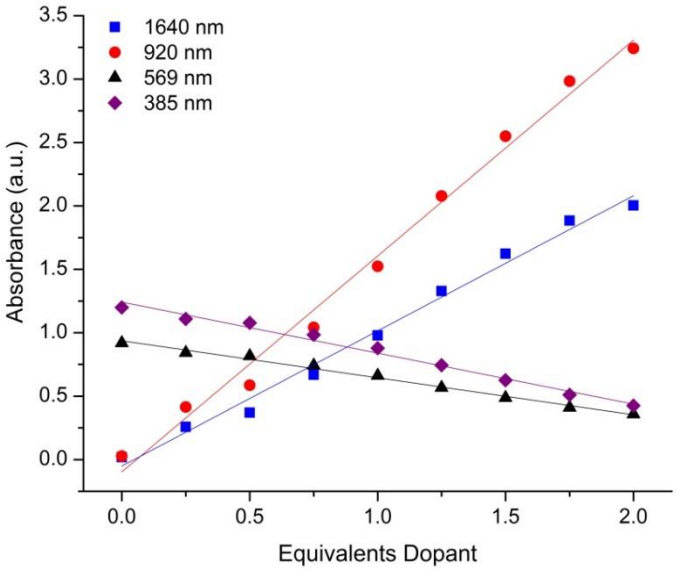

Figure 5.12. Plots of the absorbances of neutral and polaronic transitions against equivalents added dopant for **EPBPE**, and their best fit lines.

Table 5.3. Results of linear regression analysis of the absorbance changes of the different transitions against the equivalents added dopant, and the derived stoichiometric factor, *y*.

Transition	Slope	Standard Error (%)	$A_{\lambda n}$	$A_{\lambda p}$	*y*
385 nm	-0.40227	3	1.19916	0.42563	1.92
569 nm	-0.29147	4	0.91863	0.35843	1.92
920 nm	1.70196	4	0.02686	3.24142	1.89
1640 nm	1.06573	4	0.01882	2.00355	1.86

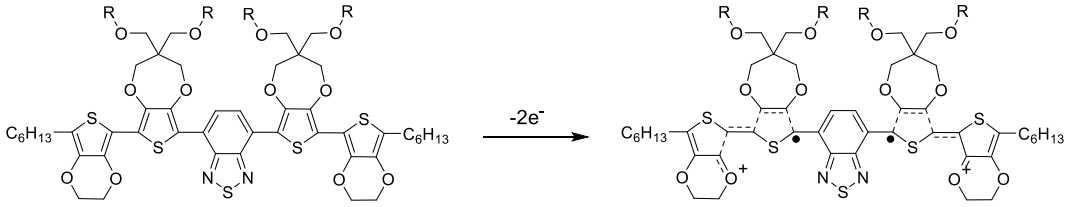

Scheme 5.3. Postulated structure of the polaron pair generated from the two-electron oxidation of **EPBPE**.

It can also be seen from Figure 5.11a and 5.11b that three other transitions at 815 nm, 1140 nm, and 1370 nm (which were present when 0.25 to 1.0 equivalents of the dopant were added) have become more pronounced in Figure 5.11b. In order to better elucidate the origin of these transitions, Figure 5.13a and 5.13b show the plots of the

absorbances of pertinent peaks with dopant amount, and the linear regression analysis results are summarized in Table 5.4. The results show that the absorbance of three transitions at 815 nm, 1140 nm, and 1370 nm are growing faster (significant increase in slope) during the conversion of the radical cation to the dication, than the conversion of the neutral molecule to the radical cation. These results show that these transitions are arising from species different from those giving rise to the absorptions at 920 nm and 1640 nm. Since these three transitions are at higher energies than the radical cation transitions, they are proposed to arise from π-dimers. The absorptions for these transitions are observed to increase faster after the first equivalence point due to the greater concentration of radical cations being forced to interact in a limited volume. Figure 5.14 shows a comparison of the normalized absorption spectra of the neutral molecule, the first equivalence point, and second equivalence point generated at two different concentrations, and it can be seen that while the plots for the neutral state, and the first equivalence point overlap, the plots for the second equivalence point do not. It can also

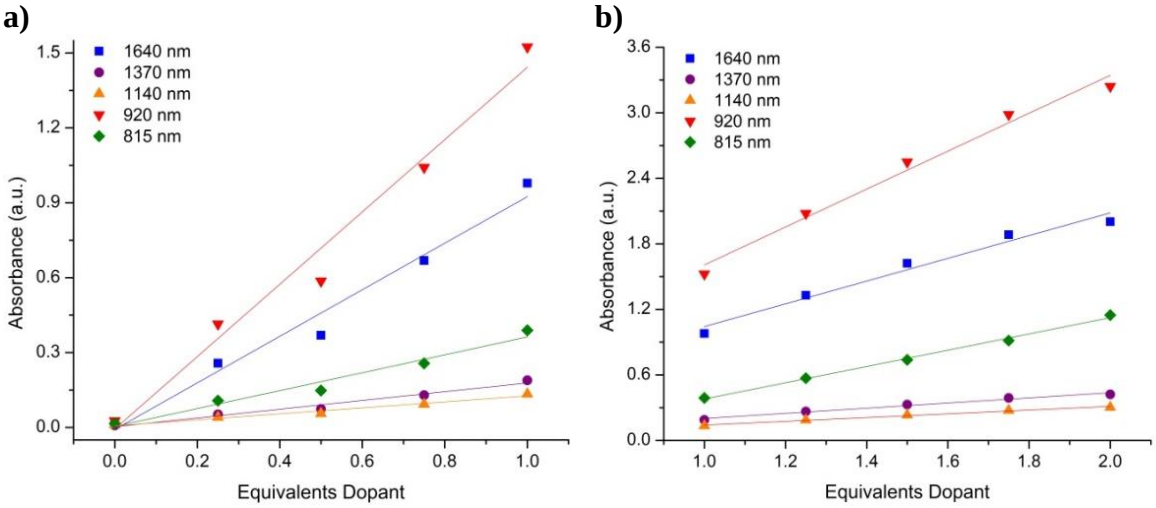

Figure 5.13. Linear regression analysis of absorbance changes of NIR peaks with increasing equivalents of $AgPF_6$. (a) Conversion to radical cation (a), and dication (b).

be seen that the peaks at 815 nm, 1140 nm, and 1370 nm are more pronounced when generated at the higher concentration, supporting the idea that they arise from π-dimers. Since the presence of π-dimers negates the assumption made in eq. 5.1, it is proposed that the slight deviation in the derived quantity *y* from two arises from the omitted contribution of the π-dimers to the monitored transitions.

Table 5.4. Summary of the linear regression analysis performed for the absorbance growth of NIR peaks during the titration of **EPBPE** with $AgPF_6$.

Peak Position	Conversion to Radical Cation (A)		Conversion to Dication (B)		Increase in Slope From A to B (%)
	Slope	Standard Error (%)	Slope	Standard Error (%)	
1640 nm	0.93249	8	1.04145	10	12
1370 nm	0.17526	2	0.23574	2	34
1140 nm	0.11951	1	0.17106	1	43
920 nm	1.44867	13	1.73601	12	20
815 nm	0.3584	4	0.74481	3	100

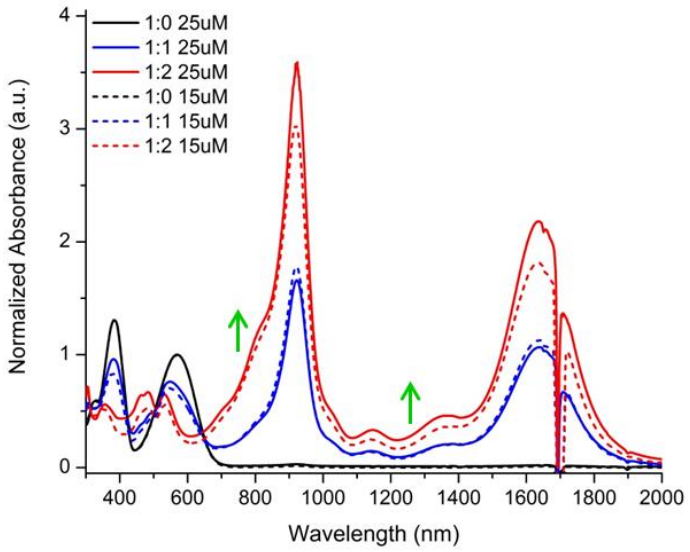

Figure 5.14. Concentration dependence of the charge carrier species formed in **EPBPE** titrated with $AgPF_6$.

EPR spectroscopy was also performed on 1 *mM* solutions of **EPBPE** in CH_2Cl_2 in the neutral state, and doped with one, and two equivalents of $AgPF_6$. The spectra are

shown in Figure 5.15. No EPR signal is observed from the neutral molecule solution, as expected from its closed-shell configuration. Doping with one equivalent of $AgPF_6$ leads to a strong EPR signal, with minimal fine structure. The *g* factor for this solution is 2.00581, with a peak-to-peak width (ΔH_{pp}) of 6.644 G. The *g* factor obtained is slightly higher than the free electron value (g_e = 2.0023), and close to many other EDOT-[41,93,303] and ProDOT-[43] containing oligomers. The slightly elevated value found in dioxythiophenes has been attributed to the delocalization of the radical species on the oxygen-substituents.[334] The lack of hyperfine coupling can be attributed to the delocalization of the radical cation between EDOT and ProDOT units, and the radical sampling the two different environments of the two heterocycles. The strong signal for the first equivalence point supports the formation of a large number of radical cations from polaron pairs in one molecule. This observation also supports the hypothesis that the acceptor ring prevents interaction between radicals in each pair. Upon addition of two equivalents of $AgPF_6$, a marked decrease in the intensity of the EPR signal is observed,

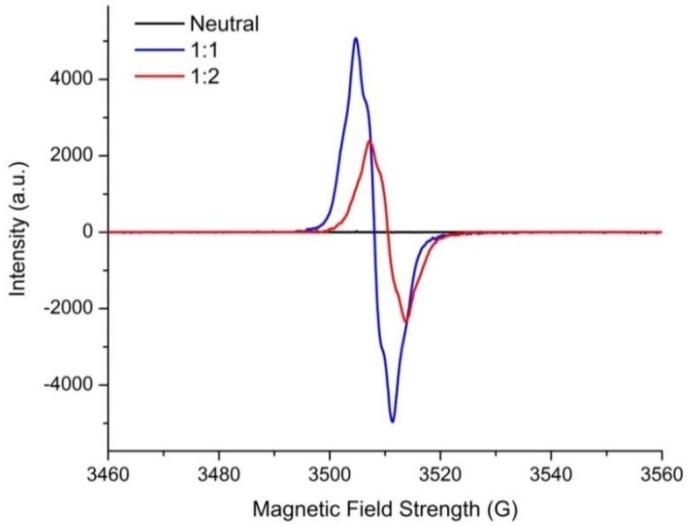

Figure 5.15. EPR spectra of 1 *mM* CH_2Cl_2 solutions of **EPBPE** with 0, 1, and 2 equivalents of $AgPF_6$.

but it is clear that there is still a significant amount of paramagnetic species in solution. Since the EPR samples are at a concentration 100 times that of those used for chemical doping, it can be expected that π-dimer formation becomes significant. Thus, for the second equivalence point, the decrease in EPR intensity is attributed to the formation of diamagnetic π-dimers, from the interaction of a larger concentration of polaron pairs. The *g* factor for the doubly oxidized solution is 2.00442, and the ΔH_{pp} is 6.546.

Chemical oxidation was also done with $NOBF_4$ as the oxidant to determine any oxidant or counterion effects. Figure 5.16 gives a comparison of the absorption spectra for the neutral and oxidized solutions for the two dopants. The spectra show that $NOBF_4$ behaves in essentially the same way as $AgPF_6$, with the formation of polaronic transitions at both the first and second equivalence points. However, the differences in the media do give rise to different molar extinction coefficients for the polaronic transitions. When a large excess of either dopant is added to **EPBPE**, it is also clear that higher oxidized states with higher-energy transitions (green traces) are formed, with peaks at 800 nm and

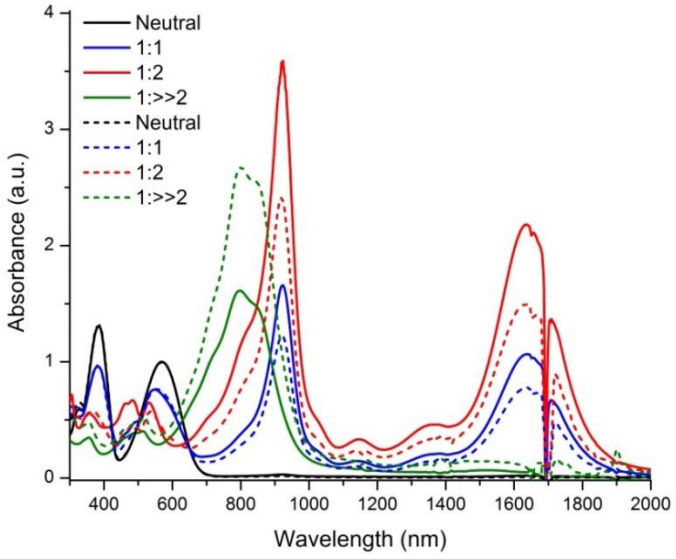

Figure 5.16. Comparison of the UV-vis-NIR absorption spectra of CH_2Cl_2 solutions of **EPBPE** chemically oxidized with $AgPF_6$ (solid lines) and $NOBF_4$ (dashed lines).

840 nm. It is proposed that these higher charged species (trication) are forced to delocalize the positive charge throughout the entire π-system, leading to further reduced electron density in the already electron-poor BTD ring. The decrease in transition peak wavelengths likely arises from the quinoidalization of a larger number of rings, leading to midgap states that are farther from the valence and conduction bands, and excitations between the valence band edge and the lower midgap state are thus higher in energy.

5.4.2.2.1.2. Electrochemical Oxidation

Positive charges were also introduced into the **EPBPE** π-system *via* electrochemical doping in CH_2Cl_2 solution. The changes in absorption spectra with oxidation were followed by spectroelectrochemistry in an OTTLE, with a Pt mesh working electrode and $TBAPF_6$ as the supporting electrolyte. The spectra are displayed in Figure 5.17, and show that as the potential is applied, the neutral transitions at 386 nm and 569 nm gradually decrease, while new transitions emerge. Sharp and narrow peaks are observed at 820 nm, 920 nm, and slightly broader and lower oscillator strength peaks are observed at 1320 nm and 1640 nm. These transitions are very similar to those observed in chemical doping, as shown by the comparison in Figure 5.18a. Thus, it can be proposed that the electrochemically generated charge carriers are also polaron pairs at the first and second oxidation waves. The transitions at 820 nm and 1320 nm can similarly be attributed to the π-dimer. Figure 5.18a also shows that the peak at 820 nm is more pronounced in electrochemical doping. This can be attributed to the larger concentration of PF_6^- counterions in electrochemical doping (100 *mM*) relative to chemical doping (100 μM). These and other counterions are known to facilitate π-dimer

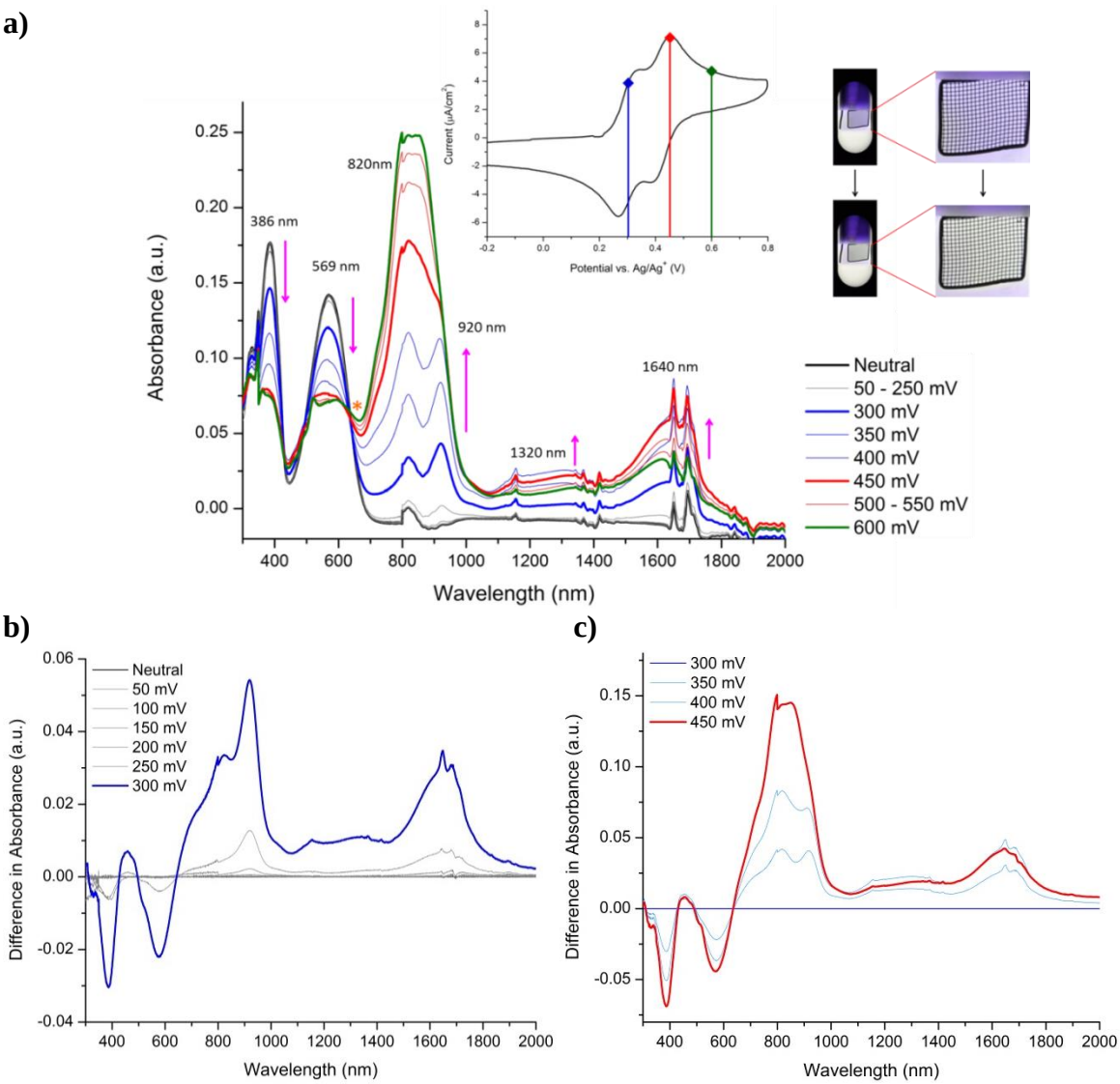

Figure 5.17. Spectroelectrochemistry of EPBPE in an OTTLE cell. (a) Changes in absorption spectra with electrochemical doping, (Inset: CV plot indicating the first and second oxidation peaks, and photographs of the OTTLE cell at 0 mV (top) and 600 mV (right) applied potentials). (b) Difference spectra showing conversion to polaronic radical cation. (c) Difference spectra showing conversion to polaronic dication.

formation by shielding some of the Coulombic repulsions between the positive charge centers.[305,317,318] This conclusion is further supported by Figure 5.18b, in which the spectroelectrochemistry of a higher **EPBPE** starting concentration shows more pronounced π-dimer peaks at 820 nm and 1260 nm.

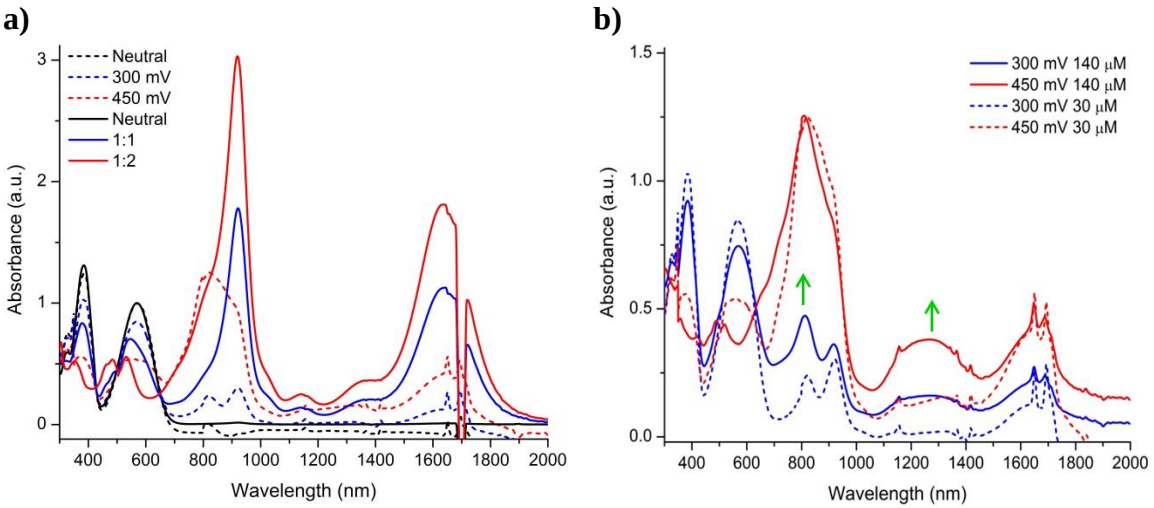

Figure 5.18. (a) Comparison of UV-vis-NIR spectra of neutral and oxidized states obtained *via* electrochemical vs. chemical doping. (b) Comparison of spectroelectrochemistry of two solutions of different concentration.

The kinetics of the electrochemical doping process was studied by comparing the spectra obtained after the application of a static potential for 30 s, and in a separate experiment, for 720 s. The results are shown in Figure 5.19. No new peaks are observed for the longer experiment, indicating that the formation of the charged species is fast. The higher extinction coefficients obtained for the slower experiment are attributed to unavoidable concentration changes that occur in a significantly longer experiment with a low boiling solvent.

As demonstrated in Scheme 5.3, the redox reaction that yields a polaron pair in **EPBPE** likely arises from a two-electron oxidation of the neutral molecule. How does this occur in an electrochemical cell? In order to understand this process, it must first be pointed out that the difference in set-up, electrode area and geometry between the OTTLE cell used in spectroelectrochemistry, and the bulk electrochemical cell used in the CV and DPV plots shown in Figure 5.10a gives rise to significant changes in oxidation behavior. Constraints of the OTTLE cell set-up prevent reproducible placement

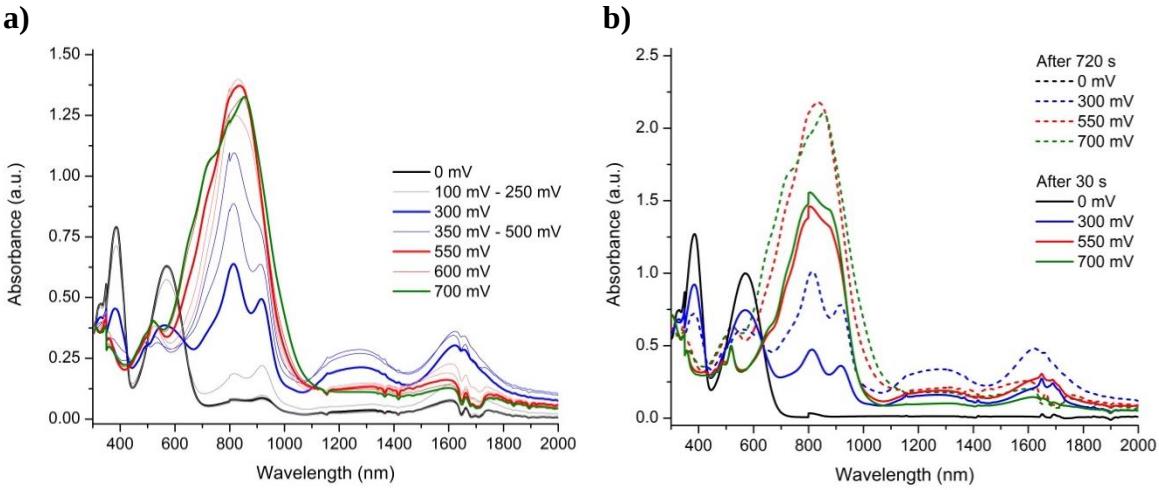

Figure 5.19. (a) Spectroelectrochemistry of **EPBPE**, with spectra taken after indicated potential was applied for 720 s. (b) Comparison of the spectra for the two different time scales.

of the counter and reference electrodes relative to the working electrode. Significant distances between these electrodes can lead to substantial resistive effects, which can increase the potential necessary to induce oxidation of the conjugated material.[335] Thus, the resulting OTTLE cyclic voltammogram looks significantly different from the one obtained with a bulk electrochemical cell using Pt button as working electrode, as shown in Figure 5.20. The first oxidation peak occurs at potentials about 120 mV higher in the

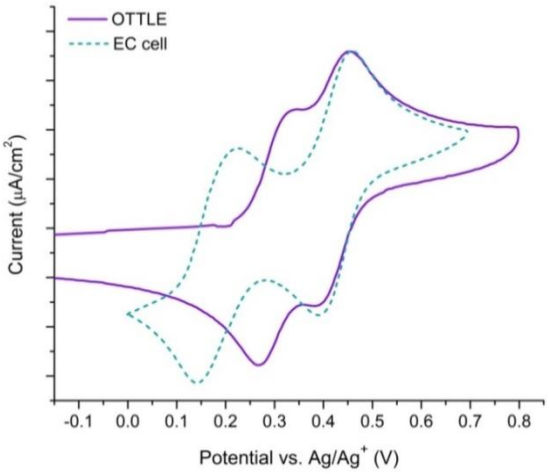

Figure 5.20. Comparison of cyclic voltammograms obtained in a bulk electrochemical cell with a Pt button electrode, and an OTTLE cell with a Pt mesh electrode.

OTTLE cell, leading to a smaller peak-to-peak separation between the first and second oxidation waves. This difference is significant as it contributes to determining the possible charge carrier species that can exist at each potential, as discussed below.

The stepwise oxidation of a neutral oligomer (M) to the dication state (M^{2+}) can be envisioned to occur in two one-electron oxidation steps, as shown in equations 5.6 to 5.7. Each reversible one electron oxidation has an associated equilibrium constant, K_1 and K_2. These equilibrium constants are related to the cell potentials by the Nernst equation. The disproportionation reaction, in which one radical cation ($M^{+\bullet}$) oxidizes another to yield a dication, and a neutral oligomer, can be written as the sum of the two one-electron equations, as shown in eq. 5.8 to 5.10. The corresponding derived equilibrium constant, K_d, gives a measure of the favorability of the disproportionation reaction, and increases with a smaller $\boldsymbol{\Delta E_{ox}}$.[43,328]

$$M \rightleftharpoons M^{+\bullet} \qquad \boldsymbol{K_1 = exp\left(\frac{-nFE_{ox,1}}{RT}\right)} \tag{5.6}$$

$$M^{+\bullet} \rightleftharpoons M^{2+} \qquad \boldsymbol{K_2 = exp\left(\frac{-nFE_{ox,2}}{RT}\right)} \tag{5.7}$$

$$\boldsymbol{K_d = \frac{[M^{2+}][M]}{[M^{+\bullet}]^2}} \tag{5.8}$$

$$2M^{+\bullet} \rightleftharpoons M^{2+} + M \qquad \boldsymbol{K_d = \frac{K_2}{K_1} = \exp\left[\frac{-nF\left(E_{ox.2} - E_{ox,1}\right)}{RT}\right]} \tag{5.9}$$

$$\boldsymbol{\Delta E_{ox} = E_{ox.2} - E_{ox,1}} \tag{5.10}$$

In these equations, n is the number of electrons in each step (n = 1 in both steps), and F is Faraday's constant, R is the ideal gas law constant, and T is the temperature.

As shown in Figure 5.17, while in the bulk electrochemical cell measurements, $\boldsymbol{\Delta E_{ox}}$ for **EPBPE** is around 250 mV (Table 5.2), in the OTTLE cell it is reduced to

around 100 mV. The resulting K_d values at room temperature are 6.0×10^{-5}, and 2.0×10^{-2}, respectively. Thus, while the disproportionation reaction is highly unlikely in the bulk measurement, it is a likely mechanism for generating charge carrier species in the OTTLE cell. The polaron pair formation during electrochemical doping can thus be envisioned to occur by first generating the radical cations from the neutral molecules. Then the radical cations bimolecularly react to give one neutral molecule, and one dication (a polaron pair). The radical cations can be considered to be unstable under the conditions of both chemical and electrochemical doping, and can, again, be rationalized by the BTD ring serving as a conjugation break due to its electron-deficient character and steric bulk.

5.4.2.2.2. Charge Carriers in EPPBPPE

Since the positive charge carriers in **EPBPE** were shown to be predominantly localized in the donor segments of the molecule, the **EPPBPPE** molecule was designed to explore the effect of a more extended donor segment on the charge carriers generated. Similar to **EPBPE**, the charge carriers are generated by both chemical and electrochemical doping, and their transitions studied with UV-vis-NIR absorption spectroscopy and EPR spectroscopy.

5.4.2.2.2.1. Chemical Oxidation

Chemical doping of **EPPBPPE** was carried out with $AgPF_6$ in CH_2Cl_2 solutions. The accompanying spectral changes are shown in Figure 5.21. As expected, the neutral state transitions of **EPPBPPE** at 414 nm and 587 nm gradually decrease as increasing amounts of dopant are added. At the same time, two strong transitions are observed at

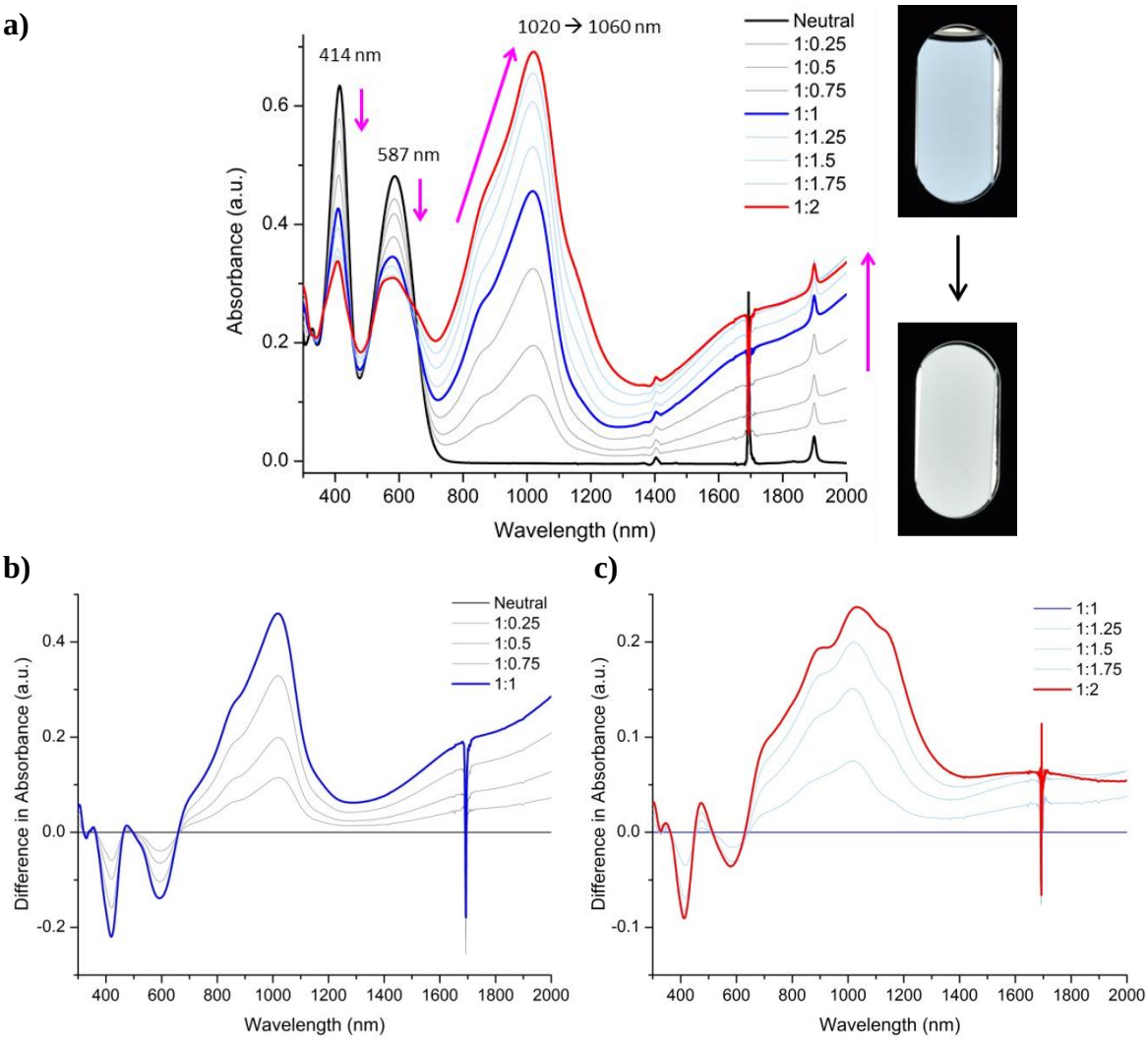

Figure 5.21. Solution chemical oxidation of **EPPBPPE** with $AgPF_6$ in CH_2Cl_2. (a) Changes in absorption spectra with doping (amounts of dopant are given in equivalents), and photographs of the neutral (left) and dication (right) solutions (inset). (b) Difference spectra showing conversion to the first oxidized state. (c) Difference spectra showing conversion to the second oxidized state.

higher wavelengths, one at 1020 nm, and another above 2000 nm (Figure 5.21b). These two transitions can be ascribed to a polaronic type of charge carrier. Both transitions are also accompanied by high-energy shoulders at 880 nm, and 1680 nm, which can be attributed to a π-dimer interaction. The polaronic transitions are red-shifted by at least 100 nm relative to those of **EPBPE** due to the more extended and electron-rich π-system

with the added ProDOT ring. With two equivalents of $AgPF_6$ added, the same transitions are still observed, with the transitions at 1020 nm undergoing a slight red-shift, and the high-energy shoulders becoming more pronounced (Figure 5.21c). These observations mirror those made for **EPBPE**, and as such it is reasonable to propose a polaron pair structure for the oxidized state of **EPPBPPE** as well. But, because of the red-shift in the polaronic transitions, **EPPBPPE** gives rise to oxidized state transitions that are predominantly outside of the visible, and its color changes from dark cyan to transmissive.

Performing the same chemical doping experiment on a more concentrated solution (50 vs. 25 μM solutions) gave rise to different absorption changes, as shown in Figure 5.22. Two polaronic transitions are observed up to the first equivalence point, but further doping reveals a new transition at 1140 nm. A new isosbestic point is also observed at 1490 nm. This new transition, occurring during the addition of the second equivalent of $AgPF_6$, occurs at energies between the two polaronic transitions, and likely

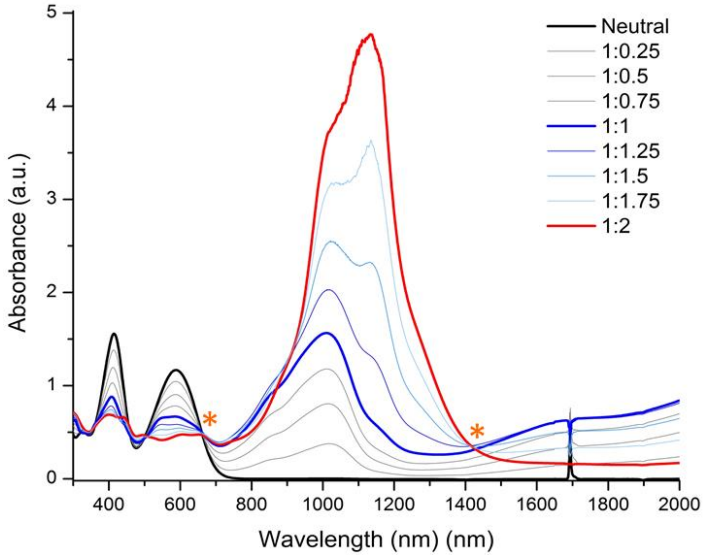

Figure 5.22. Spectral changes in a more concentrated (50 μM) solution of **EPPBPPE** in CH_2Cl_2 with $AgPF_6$ doping.

arises from a bipolaronic type of charge carrier. The depletion of the transitions attributed to π-dimers is also observed. The change in response at higher starting concentrations has also been observed in oligoProDOTs, in which the bipolaronic dication is observed simultaneously with the radical cation (polaron) and its π-dimer.[43] In **EPPBPPE**, however, the π-dimer peaks decrease in favor of the bipolaron.

How then is the bipolaron structure stabilized in **EPPBPPE**, but not in **EPBPE**? It is probable that the additional ProDOT ring allows the positive charges to be predominantly centered in the electron-rich rings, while extending the geometric deformation to the BTD ring. The quinoidalization of a larger number of rings also explains the substantial increase in oscillator strength of the bipolaronic transition. The possible structures of the polaron pair and bipolaron are shown in Chart 5.1.

Chart 5.1. Possible Structures of Charge Carriers in **EPPBPPE**

Polaron Pair

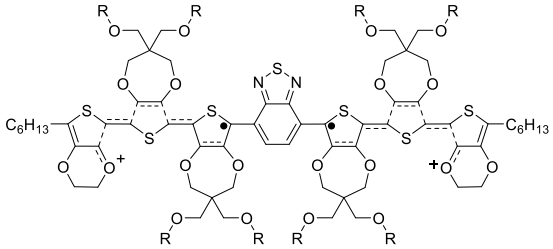

Bipolaron

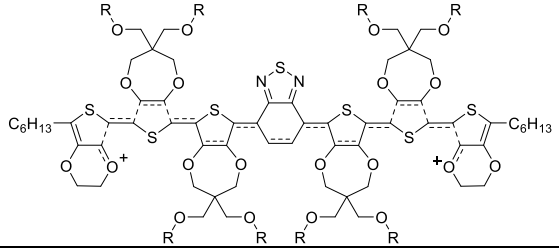

Chemical oxidation was also brought about with a molybdenum-based oxidant $Mo(tfd\text{-}CO_2Me)_3$,[122] chosen for its improved stability to air in the solid state. Figure 5.23 shows a comparison of the absorption spectra of the neutral state, and the first and second equivalence points for $AgPF_6$ and $Mo(tfd\text{-}CO_2Me)_3$. The plot shows that the same

polaronic transitions are observed from Mo(tfd-CO_2Me)$_3$, and the π-dimer transitions are more pronounced, while the bipolaronic transition (observed as a slight shoulder with $AgPF_6$) is suppressed. Unfortunately, the neutral and reduced states of Mo(tfd-CO_2Me)$_3$ absorb in the visible region, preventing the investigation of the changes in the neutral transition peaks.

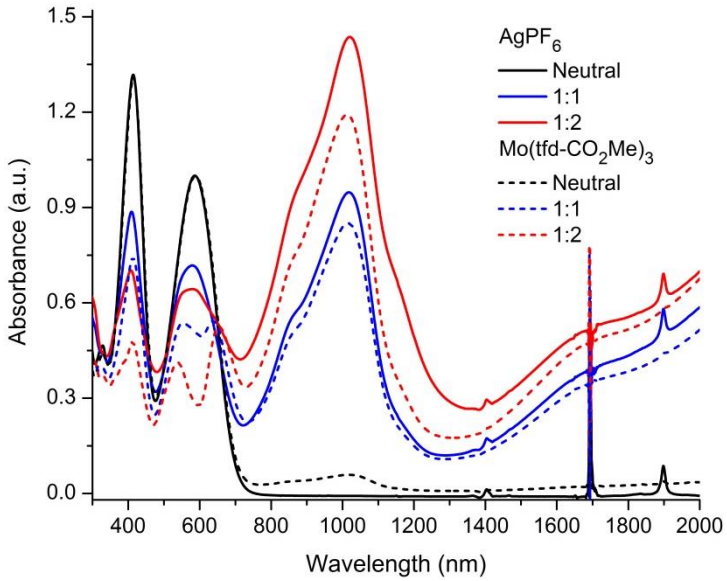

Figure 5.23. Comparison of the absorption spectra of the oxidized states attained with $AgPF_6$ (solid lines) and Mo(tfd-CO_2Me)$_3$ (dashed lines).

EPR spectroscopy was also performed on 1 *mM* solutions of **EPPBPPE** in CH_2Cl_2, oxidized with $AgPF_6$. The spectra shown in Figure 5.24 show that paramagnetic species are present in both solutions oxidized with one and two equivalents of $AgPF_6$. The *g* factors are 2.00509 and 2.00434 for the first and second equivalence points, and the ΔH_{pp} are 4.006 and 4.348, respectively. The EPR signals also do not show hyperfine coupling, again due to the differences in EDOT and ProDOT environments, which the radical may sample in the timescale of the experiment. It can also be noted that the intensities observed in the EPR spectra of **EPPBPPE** are significantly lower than for

EPBPE (for the same volume and concentration of the small molecules). This can be ascribed to the participation of the EPR-silent bipolaronic species in **EPPBPPE**, which has also been shown to become significant at higher concentrations. Thus, the EPR studies also support the charge carriers species suggested by the results of absorption spectroscopy.

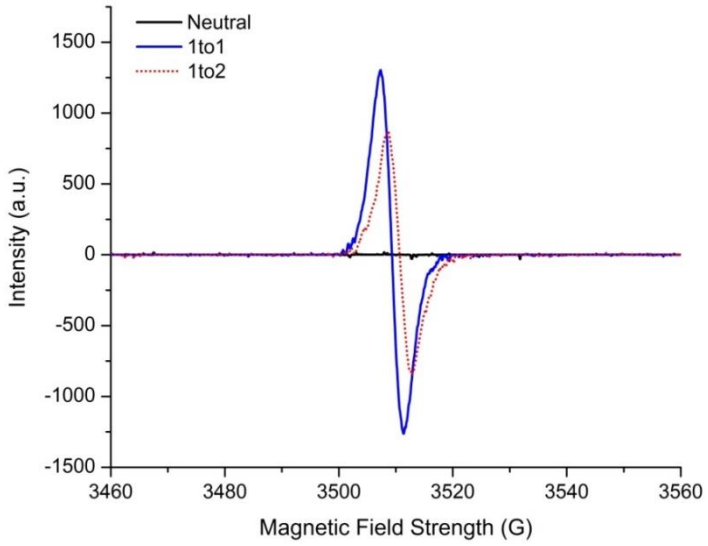

Figure 5.24. EPR spectra of neutral and $AgPF_6$-oxidized **EPPBPPE** solutions in CH_2Cl_2.

5.4.2.2.2.2. Electrochemical Oxidation

The oxidized states of **EPPBPPE** were also studied *via* electrochemical doping in an OTTLE cell. Again, the different cell set-up and electrode geometries in the OTTLE gives rise to a change in the CV behavior of **EPPBPPE**. Figure 5.25 shows that the separation between the first and second oxidation waves are reduced when obtained in an OTTLE cell. Although the peak potentials are difficult to extract from the OTTLE CV, a ΔE_{ox} value of 95 mV is a good approximation. This corresponds to a K_d of 2.5×10^{-2}, making the disproportionation reaction an important process to consider in electrochemically generating charge carriers.

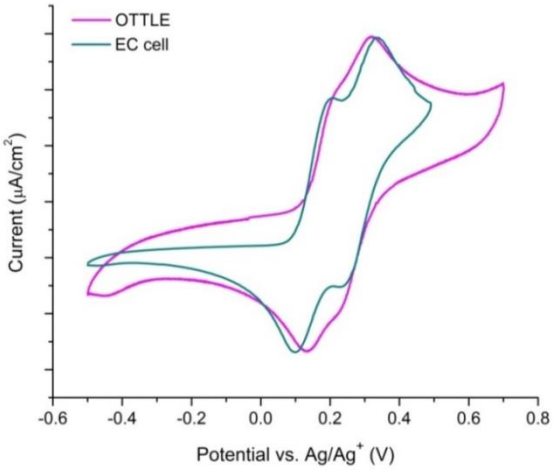

Figure 5.25. Comparison of cyclic voltammograms obtained in a bulk electrochemical cell and an OTTLE cell.

The results of the spectroelectrochemistry of **EPPBPPE** are shown in Figure 5.26. Electrochemical oxidation gives rise to two new transitions at around 940 nm and 1620 nm (Figure 5.26b) that undergo a slight red-shift with increasing oxidation. Compared with the results from chemical doping, these transitions can be assigned to the π-dimer species, which are stabilized by the higher concentration of PF_6^- counterions, similar to what is observed in **EPBPE**. A slight shoulder at around 1140 nm is also observed at 250 mV, which corresponds to the bipolaron species. This peak then continues to grow at oxidation potentials above 250 mV (Figure 5.26c). The simultaneous observation of the polaron and bipolaron can be attributed to the significant disproportionation constant brought about by the small peak-to-peak separation. The substantially higher concentration (130 μM) of **EPPBPPE** required by the OTTLE set-up is also expected to contribute to generating bipolaron species.

Figure 5.27 shows the absorption spectra of the neutral and oxidized states obtained through chemical and electrochemical doping. The comparison shows that while the polaronic radical cation is observed on chemical doping to the first equivalence point,

the dominant charge carrier generated through electrochemical doping is its π-dimer. At higher doping levels, the π-dimer and the bipolaron coexist, along with the neutral molecule, due to the disproportionation reaction made favorable by the small ΔE_{ox}.

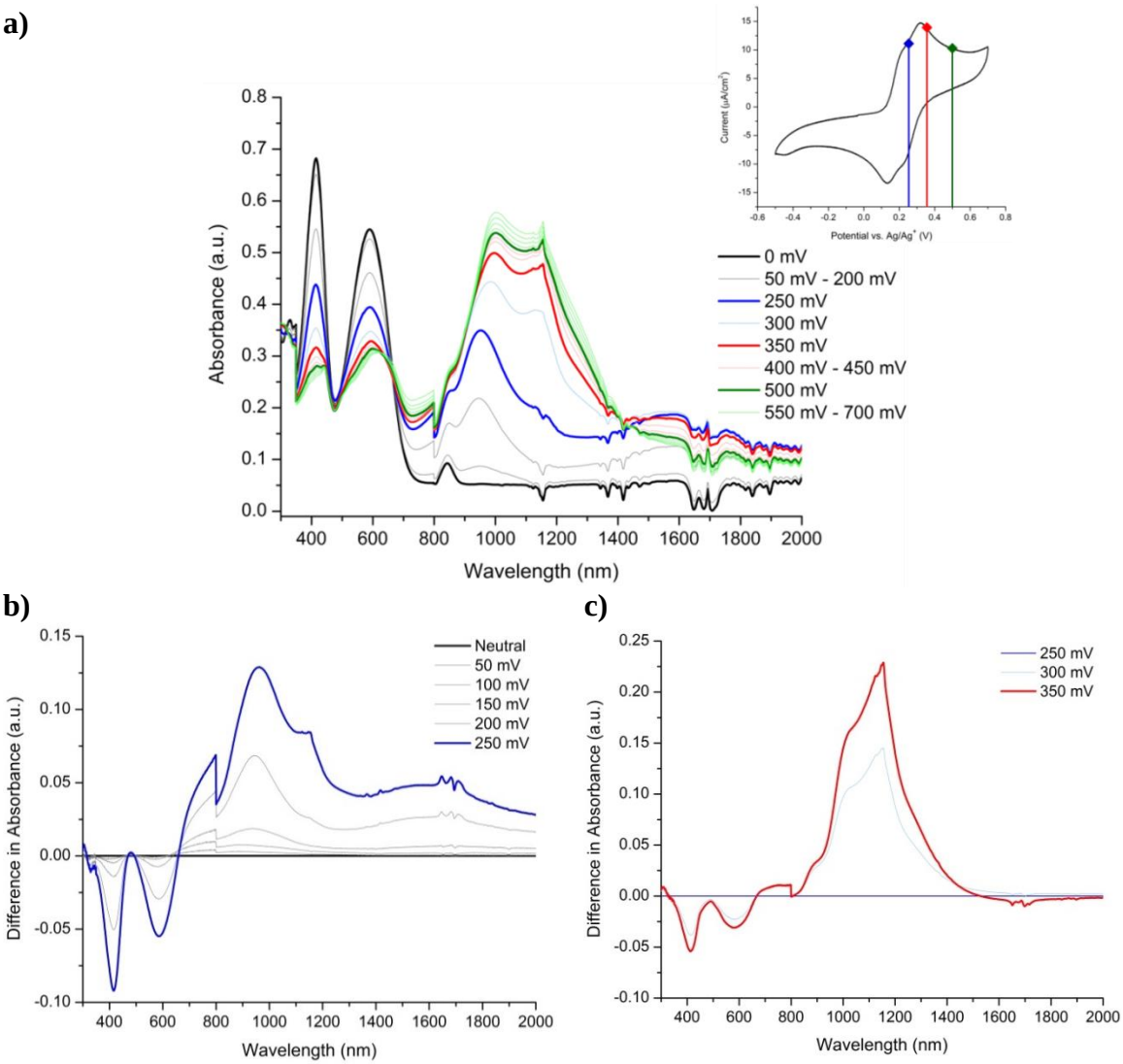

Figure 5.26. Spectroelectrochemistry of **EPPBPPE** in CH_2Cl_2. (a) Changes in absorption spectra with electrochemical doping (Inset: CV plot indicating the first and second oxidation peaks). (b) Difference spectra showing conversion to polaron and π-dimer at potentials below 250 mV. (c) Difference spectra showing conversion to the bipolaronic dication past 250 mV.

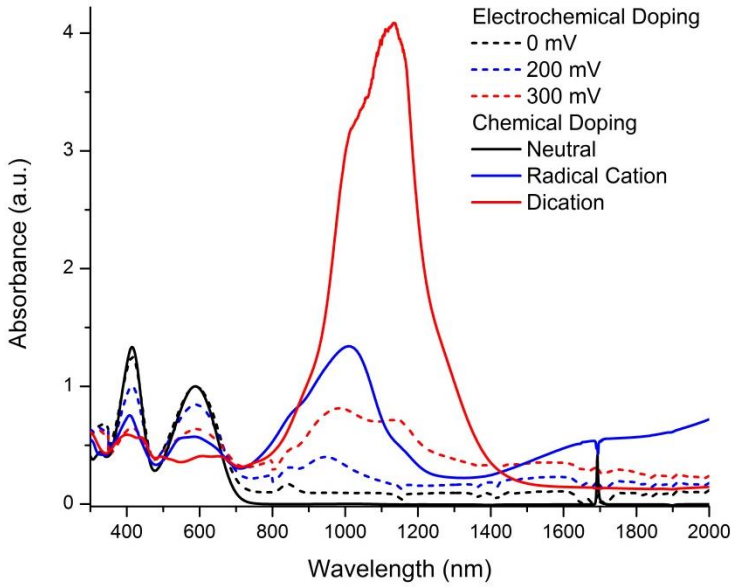

Figure 5.27. Comparison of transitions observed from charge carrier generation *via* chemical doping (solid lines) and electrochemical doping (dashed lines) in **EPPBPPE**.

The addition of a ProDOT unit in **EPPBPPE** allows the positive charge to be delocalized to three electron-rich rings in the polaron pair structure, leading to significantly lower-energy transitions (Figure 5.28). It also perturbs the balance of charge delocalization, Coulombic repulsion, and geometric deformation through the electron-

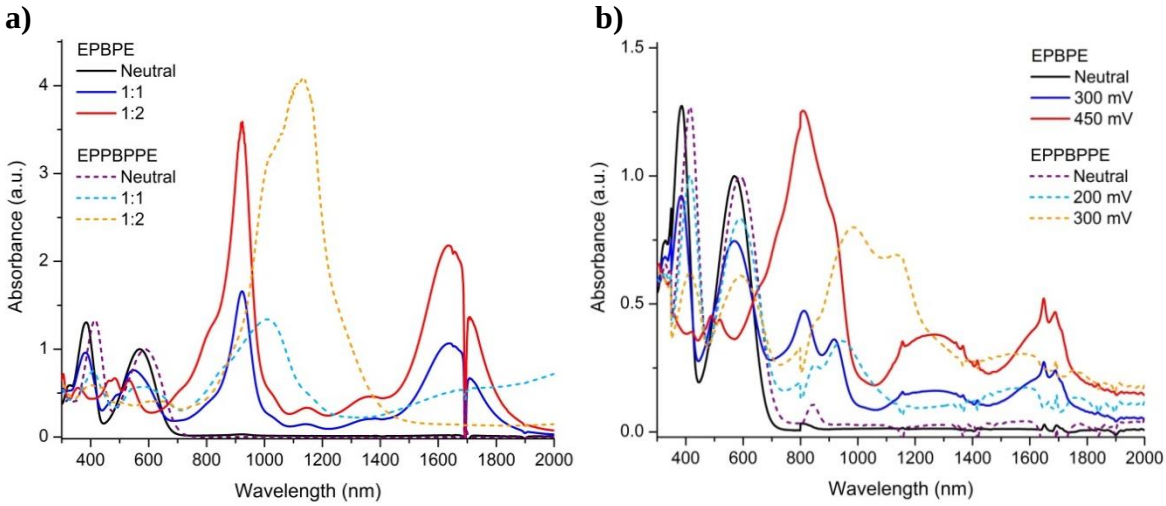

Figure 5.28. UV-vis-NIR spectra of neutral and oxidized states of **EPBPE** and **EPPBPPE** generated *via* chemical (a) and electrochemical (b) p-doping.

poor ring, such that the type of charge carrier formed is strongly dependent on the conditions and medium. While **EPBPE** consistently generates polaron pairs and π-dimers in chemical and electrochemical doping, **EPPBPPE** generates a mixture of polaron pairs, π-dimers, and bipolarons at high oxidation levels.

5.4.3. Path to Materials: Donor-Acceptor Polymer with Discrete Conjugated Structure

The small molecules described above have shown narrow and well-defined transitions that are promising for high-contrast electrochromic applications. However, in order to be useful materials for electrochromic devices, these need to be solution-cast as thin films that can maintain their structural integrity in a device during operation. While the small molecules studied here can be spray-cast as thin films from solution, their oxidized states are soluble in many solvents used for electrolyte systems. To address this, some groups have incorporated chromophores into non-conjugated polymer structures, thereby combining the discrete molecular properties of small molecules with the mechanical properties of polymers.[93,336,337] Nawa, *et al.*,[336] for example, functionalized oligothiophenes with vinyl groups on one terminus, and then radically polymerized the vinyl end groups. This led to a polyvinyl chain from which pendant oligothiophenes were attached. The resultant polymers retained their electrochromic properties. Ohsedo, *et al.*,[337] on the other hand, used methacrylate termini to create polymers with different lengths of oligothiophenes pendant to the methacrylate chains. The unfunctionalized terminus of the polymers with short pendant oligothiophene, however, was shown to undergo coupling reactions under cyclic voltammetry, causing crosslinking of chains. The methacrylate polymers of the quinque- and sexi- thiophenes, on the other hand,

showed CVs that were similar to the monomeric oligothiophenes. More importantly, the absorption spectra of their neutral and oxidized states showed narrow polaronic and bipolaronic transitions, with significant contributions from π-dimers of the radical cations. The polymers showed reversible and well-defined color changes as a result of the disconnected π-systems. Nielsen, *et al*.[93] developed this approach further with thiophene-, EDOT-, and dialkoxyphenyl- containing oligomers that were functionalized at the termini with acrylate groups. The small molecules could be dissolved in solution (Figure 5.29, step 1), and spray-cast onto conducting substrates (step 2), then UV-polymerized over a mask to crosslink the acrylate groups and create an insoluble crosslinked network (step 3). The uncrosslinked monomers remain soluble, and can be washed off with the appropriate solvent to leave a patterned film (step 4). The rod-coil nature of the conjugated system coupled with the aliphatic segments allowed strong secondary interactions such that the acrylate termini can polymerize, as depicted in the boxed

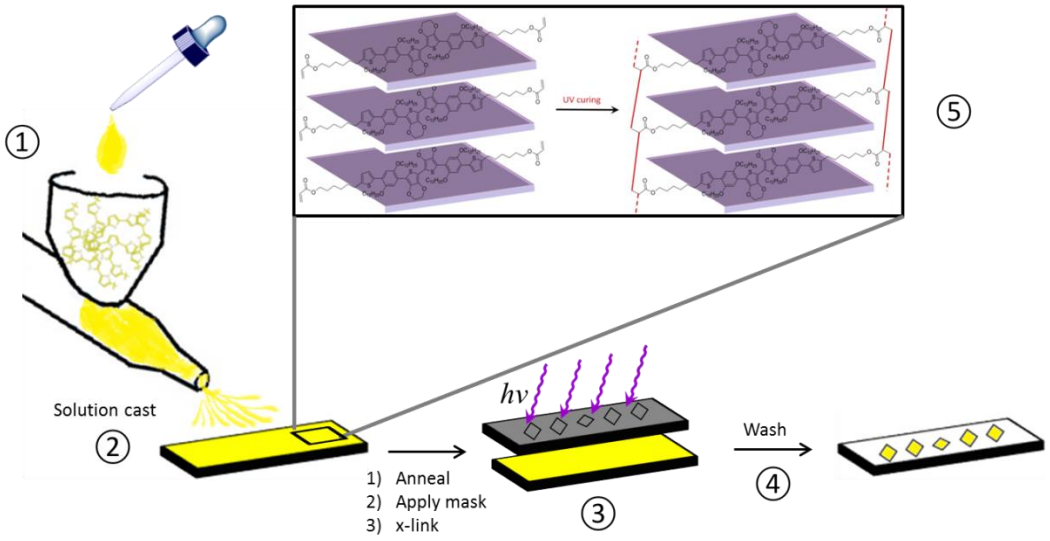

Figure 5.29. Diagram of solution processing and formation of an insoluble electroactive polymer film in acrylate-terminated conjugated oligomers.

reaction scheme (5) in Figure 5.29. The resulting polymer films retained the narrow absorptions of the radical cation and dications observed in the monomers, and showed reversible electrochromic behavior with distinct color changes.

Another approach to polymeric materials with discrete electroactive chromophores is to have the conjugated units connected by aliphatic segments along the main chain of the polymer (Figure 5.30). This approach allows the polymer to be solution processable and cast as a film, and has been employed to polymerize many oligothiophene derivatives resulting in electrochromic materials with distinct color changes.[338-340]

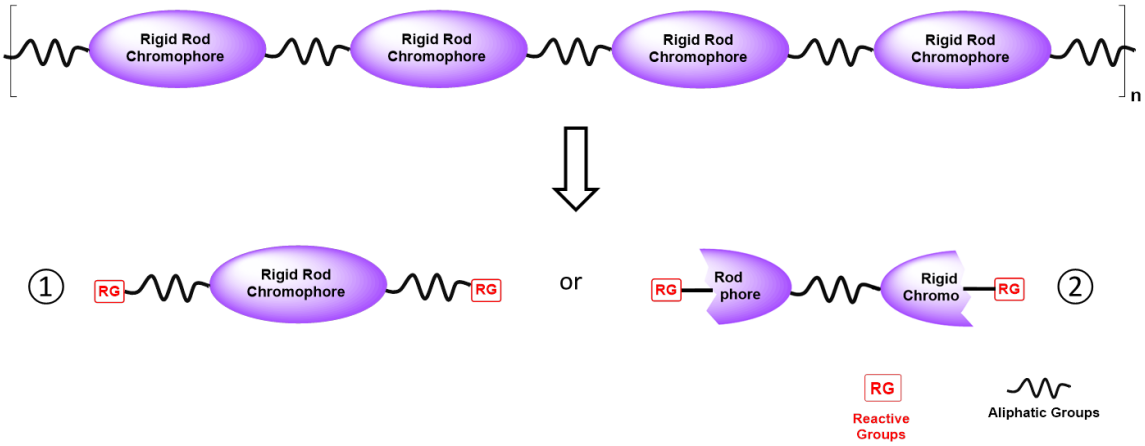

Figure 5.30. Structure and retrosynthesis of a polymer with discrete conjugated segments linked together by aliphatic groups in the main chain.

5.4.3.1. Design and Synthesis of Polymer with Discrete Chromophores in the Main Chain

As shown in Figure 5.30, two approaches are identified to synthesize polymers with discrete conjugated segments in the main chain. Here, the second approach was selected to take advantage of direct (hetero)arylation as a versatile yet efficient polymerization method. The synthesis of the polymer is shown in Scheme 5.4. A long

alkyl chain was selected as a linker between the conjugated units to contribute to solubility and processability of the resulting polymer. The polymer was end-capped with 2-*n*-hexyl-EDOT to improve electrochemical stability. The characterized polymer was obtained from the $CHCl_3$ fraction from Soxhlet extraction, which gave M_w = 54 kDa, M_n = 23 kDa, and PDI = 2.33. The resulting polymer was found to have good solubility in solvents commonly used for processing and characterization (toluene, THF, $CHCl_3$, CH_2Cl_2).

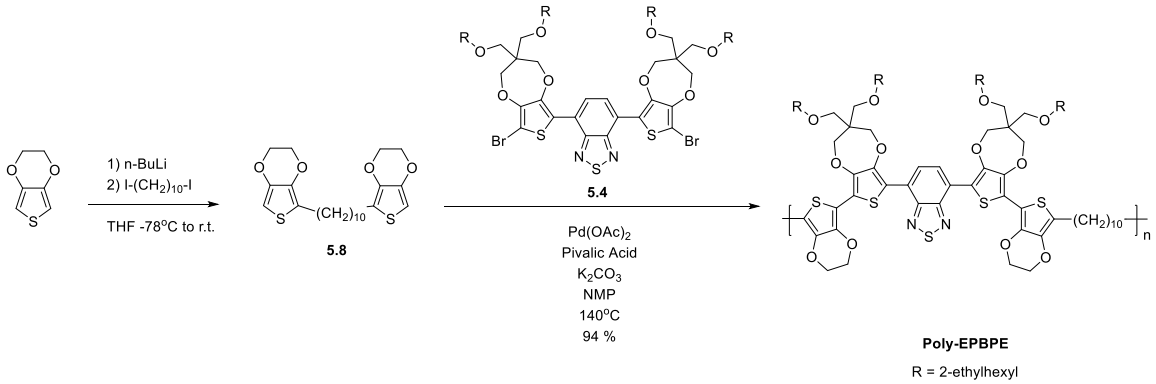

Scheme 5.4. Synthesis of a polymer with discrete **EPBPE** segments coupled by aliphatic *n*-decyl chains.

5.4.3.2. Optoelectronic Properties of the Discrete Conjugated System in Poly-EPBPE

To determine if **Poly-EPBPE** retains the discrete nature of the conjugated system in its main chain, its optoelectronic properties are compared with those of **EPBPE**. The absorption spectra of the neutral materials are shown in Figure 5.31. In solution, the polymer has narrow and well-defined absorptions, with a donor-acceptor charge transfer band peaking at 576 nm, and a high energy π-π* band peaking at 385 nm. Its absorption spectrum nearly overlaps that of the small molecule, showing that the polymer predominantly preserves the discrete character of the π-system in the main chain in

solution. The small red-shift in the polymer (~ 5 nm) may be due to a small amount of π-stacking interactions occurring in solution. The polymer film, on the other hand, is red-shifted by around 10 nm, due to aggregation. There is also some slight scattering that elevates the baseline, which can be attributed to the rod-coil nature of the polymer structure leading to inhomogeneities in the film (*vide infra*).

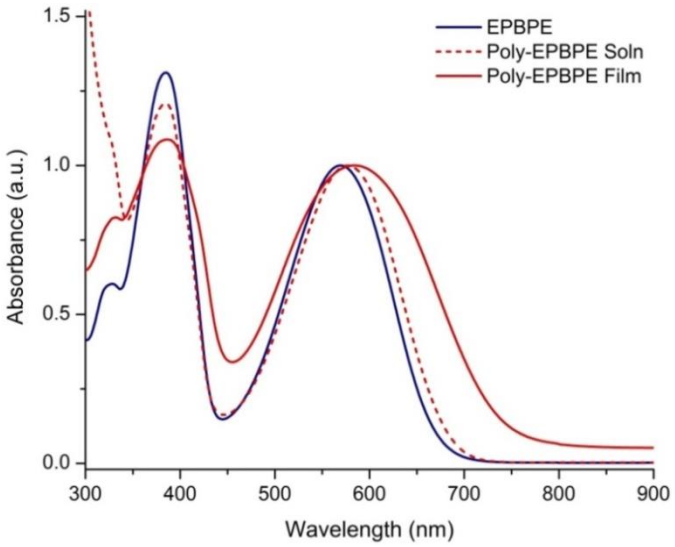

Figure 5.31. Absorption spectra of neutral **EPBPE** and **Poly-EPBPE**.

Electrochemistry of the polymer was done in both film and solution states, and the results are shown in Figures 5.32 to 5.34. The electrochemistry of a 5 mg mL^{-1} solution of **Poly-EPBPE** in CH_2Cl_2 shows two resolved peaks (Figure 5.32a), with the first wave overlapping well with that of the small molecule. The second oxidation wave of the polymer is broader, has a higher current, and the peak occurs at a higher potential than that for the small molecule, although the onset is at lower potentials. The cathodic wave is similarly broad and unresolved for the second step. DPV shows the first oxidation step as only a small shoulder to the second oxidation process. The polymer solution shows stability toward repetitive cycling, with only slight changes occurring after 50 cycles

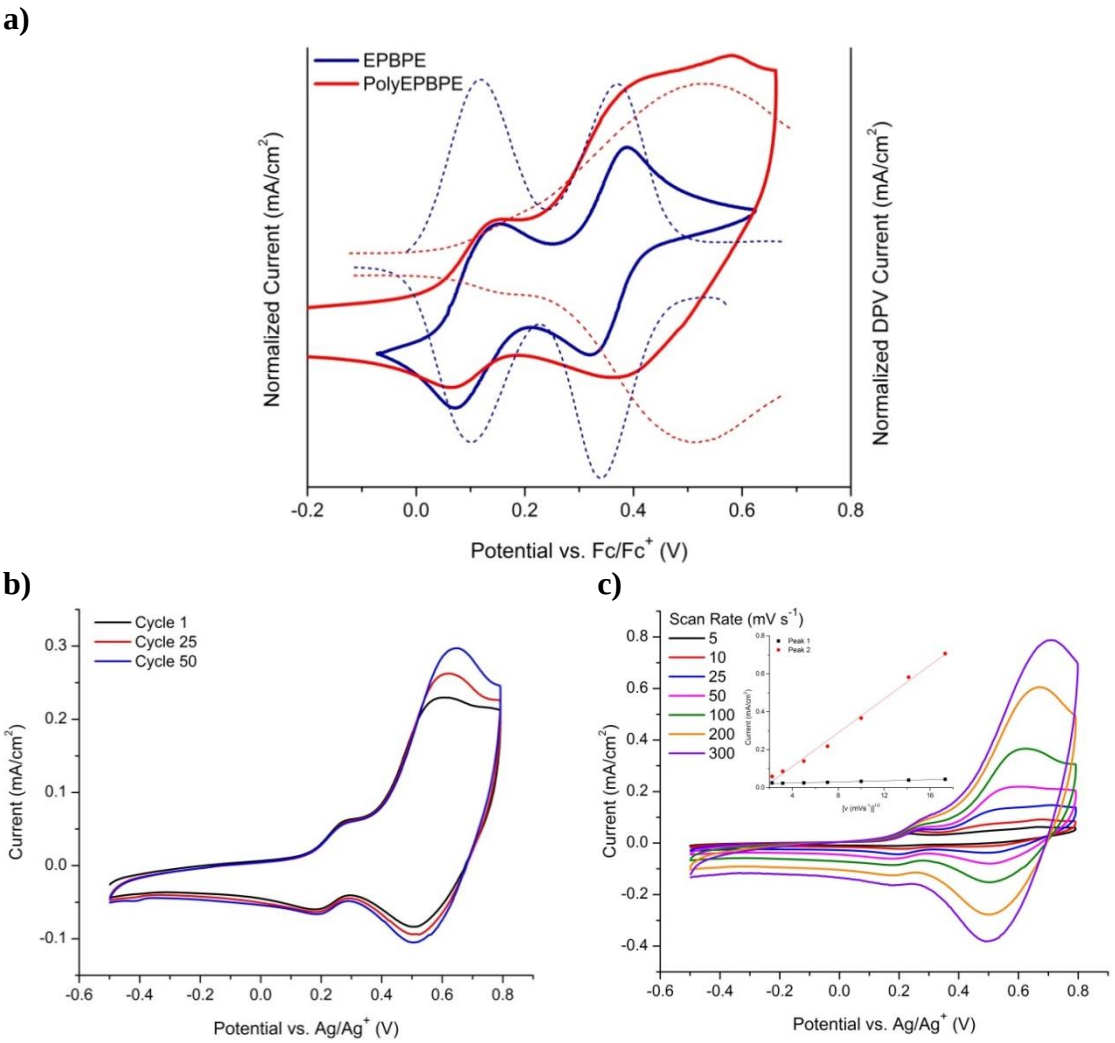

Figure 5.32. Comparative solution electrochemistry of **EPBPE** and **Poly-EPBPE** in CH_2Cl_2. (a) Cyclic voltammetry and differential pulse voltammetry. (b) Electrochemical stability. (c) Scan rate dependence of first and second oxidation waves.

(Figure 5.32b). Varying the scan rate also shows a Cottrell dependence of the current at both peaks (Figure 5.32c), but with different slopes (Figure 5.32c inset), leading to a significant change in the CV wave shape. These differences can be attributed to a variation in the diffusion coefficients of the mono- and di- cationic species.

In the solid state, it can be seen that the two oxidation processes of **Poly-EPBPE** can only be resolved in the first CV cycle (Figure 5.33a) of a pristine film. Thereafter, the two waves coalesce into one broad peak. This is likely due to the instability of the radical

cation state toward disproportionation to the dication state. The dication has been shown in small molecules to take many forms in the condensed state (π-dimer, polaron pair, bipolaron), which can explain the broadness of the second oxidation wave (relative to the first wave) seen in solution electrochemistry of **Poly-EPBPE**. It has also been shown in the small molecule that PF_6^- promotes dimerization. Thus, upon break-in of the polymer film, in which electrolyte salts are expected to intercalate between chains, the likely formation of π-dimers causes the first wave to broaden and overlap with the second wave. The stability of the film to electrochemical switching is shown in Figure 5.33b, in which a minimal change in the trace is observed over 50 CV cycles.

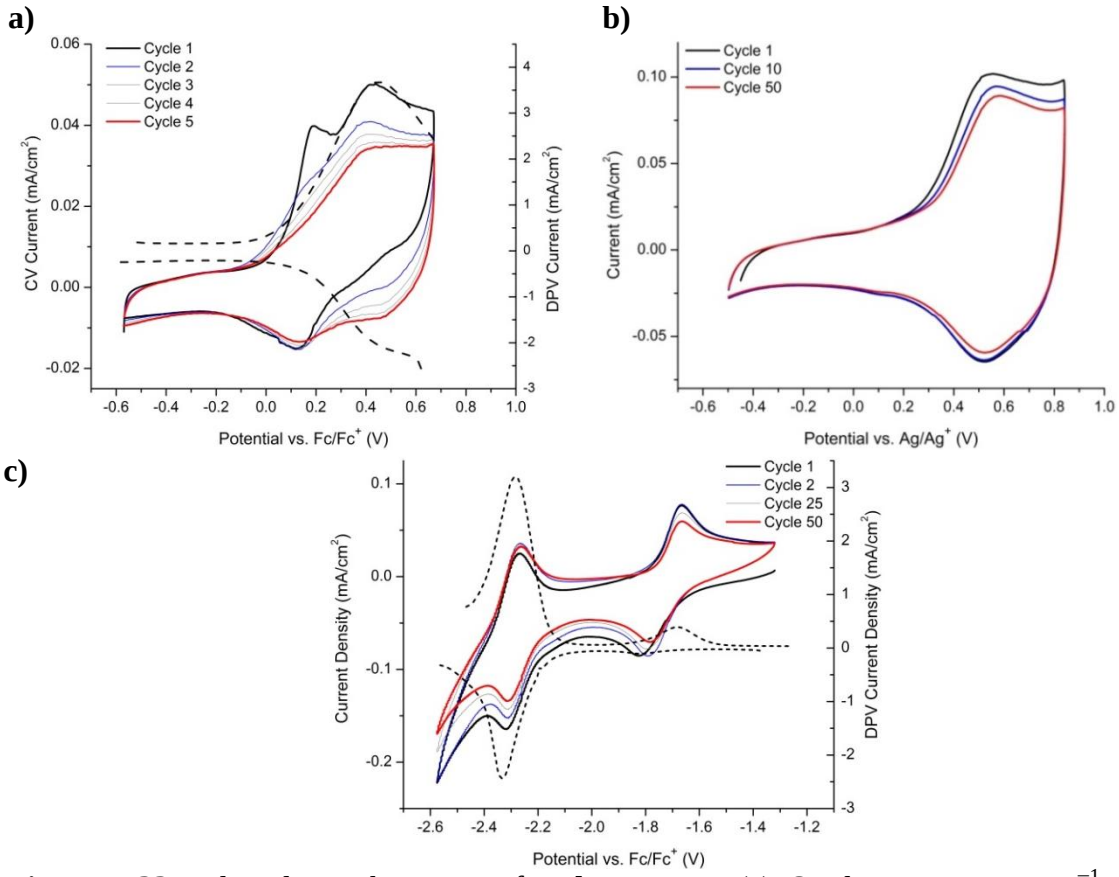

Figure 5.33. Film electrochemistry of **Poly-EPBPE**. (a) Oxidation at 5 mV s^{-1}. (b) Stability to repeated cycling at 50 mV s^{-1}. (c) Reduction behavior.

The reduction behavior of the polymer can be studied in the solid state due to the larger potential window of the supporting electrolyte solution. As shown in Figure 5.33c, the polymer shows two well-resolved reduction waves at substantially negative potentials. This can be attributed to the electron-richness of the dioxythiophenes destabilizing n-doping of the polymer.

The optoelectronic properties of the polymer and its small molecule equivalent are summarized in Table 5.5. The small molecule and polymer show very similar optoelectronic properties, owing to the discrete nature of the π-system in both materials.

Table 5.5. Optoelectronic properties of **EPBPE** and **Poly-EPBPE**.

	Optical			Electrochemical						
	λ_{max} (nm)		$E_{g,o}$[b]	E_{ox1}[d]	E_{ox2}[e]	E_{re1}[f]	E_{re2}[f]	IP[g]	EA[g]	$E_{g,ec}$
	D-A	π-π*	(eV)	(V)	(V)	(V)	(V)	(eV)	(eV)	(eV)
Poly-EPBPE	576 (585[a])	385	1.69[c]	0.11 (0.16[e])	0.52 (0.45[f])	-1.73	-2.29	-5.26	-3.37	1.89
EPBPE	569	385	1.78	0.11[d]	0.35			-5.21	-3.26[h]	1.95

[a]Film absorption onset. [b]Taken from the onset of the D-A charge transfer peak. [c]Onset of the polymer film. [d]Difference in CV anodic and cathodic peak potentials; values referenced to ferrocene ($E_{½}$ = 0.013 V vs Ag/Ag^+ in CH_2Cl_2). [e]Taken from DPV peak potentials. [f]Film electrochemistry values (referenced to ferrocene ($E_{½}$ = 0.085 V vs Ag/Ag^+ in CH_3CN). [g]Values taken from the first wave, and reported relative to vacuum (−5.1 eV). [h]Calculated from the sum of IP and $E_{g,opt}$.

5.4.3.3. Charge Carriers in Poly-EPBPE

The chemical and electrochemical doping of **Poly-EPBPE** were studied in solution, and solid state, respectively, with absorption spectroscopy used to identify possible charge carriers. Figure 5.34a shows the evolution of the absorption spectra of the polymer in CH_2Cl_2 solution upon doping with $AgPF_6$. Addition of the oxidant causes a gradual decrease of the neutral polymer transitions at 385 nm and 576 nm, followed by

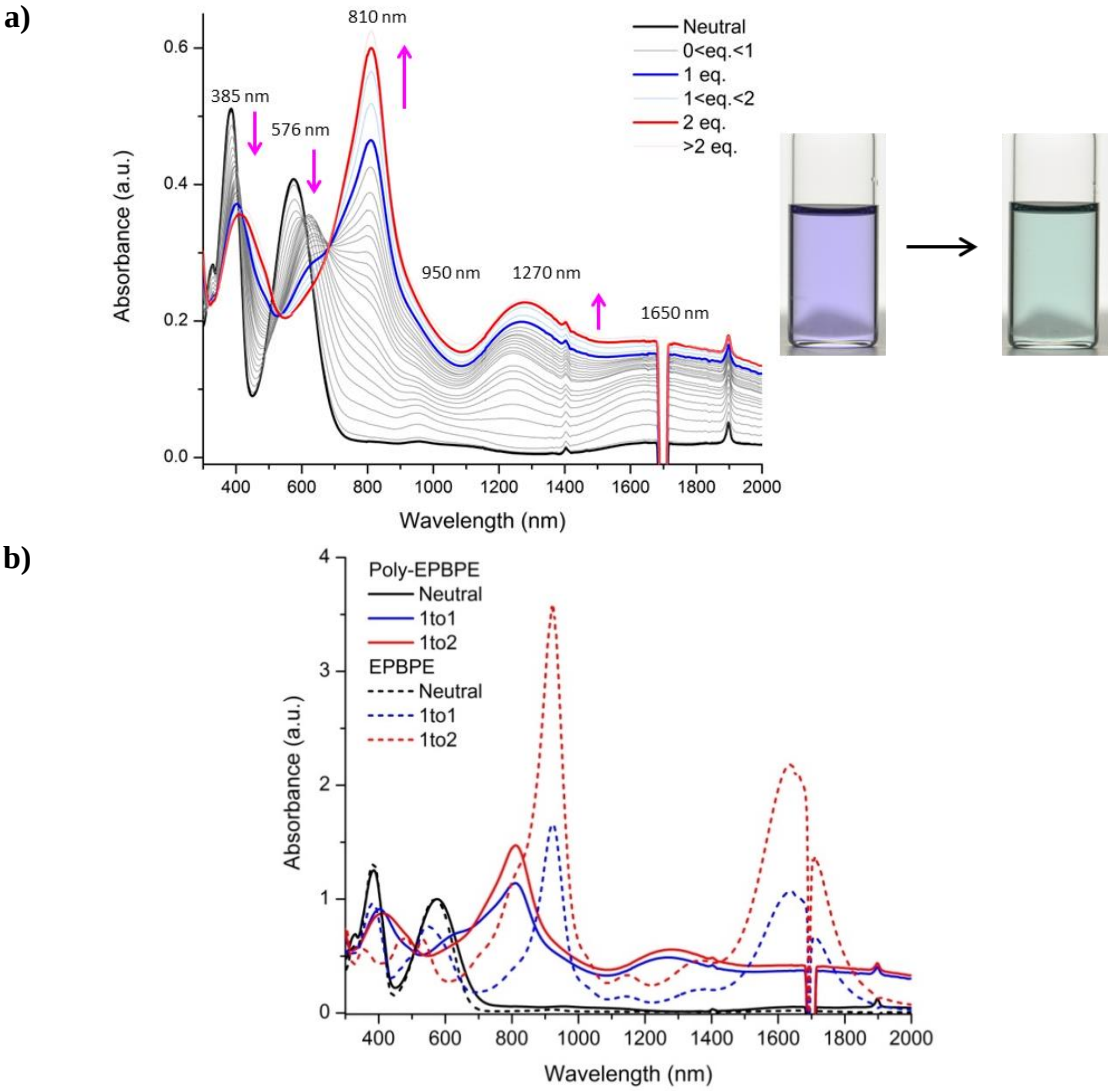

Figure 5.34. (a) Solution chemical oxidation of **Poly-EPBPE** with $AgPF_6$ (Inset: Photographs of the neutral and oxidized polymer solutions). (b) Comparison with chemical oxidation of **EPBPE**.

the growth of new transitions at 950 nm and 1650 nm. These latter two transitions then quickly become shoulders of transitions at 810 nm and 1270 nm, which predominate well below the first equivalence point. Continued p-doping increases the absorbance from the latter transitions without yielding any new transitions, even at the second equivalence point. Comparison of the transitions at the first and second equivalence points of $AgPF_6$ oxidation with those of **EPBPE** (Figure 5.34b) shows that the transitions at 950 nm and

1650 nm are polaronic transitions, likely arising from the formation of polaron pairs. Furthermore, the transitions at 810 nm and 1270 nm are likely due to their π-dimers. In the polymer, it can be seen that these dimers are the dominant charge carrier at both the first and second equivalence points. This can be attributed to the strong π-stacking of conjugated segments in the polymer, which is likely promoted by the rod-coil nature of the polymer.

Electrochemical doping of **Poly-EPBPE** was done on a film of polymer spray-coated from toluene solution onto a conductive ITO substrate. The spectroelectrochemistry results are shown in Figure 5.35. The pristine polymer film shows some scattering due to inhomogeneities in the film (*vide infra*). Upon electrochemical break-in, the film undergoes irreversible spectral changes (purple trace). Electrochemical oxidation of this film to 300 mV leads initially to the formation of polarons (Figure 5.35b), with transitions at 910 nm, and 1650 nm. Increasing the potential then causes a blue-shift of the transitions to 720 nm, and 1240 nm, which are due to the formation of π-dimers (Figure 5.35c). The transitions are considerably broader than those observed on solution doping, and can be attributed to the conjunction of different charge carriers in different environments, along with their interactions. The neutral absorptions of the polymer are not significantly reduced by the process, leading to a substantial residual color in the oxidized film (Figure 5.35a, inset).

Film electrochemistry of **Poly-EPBPE** (Figure 5.33a) has been shown to yield two well-resolved peaks only on the first oxidation cycle. Thus, spectroelectrochemistry was done on a pristine film (without prior break-in). As shown in Figure 5.36, the pristine film required oxidation to 350 mV to show significant changes in spectra. This higher

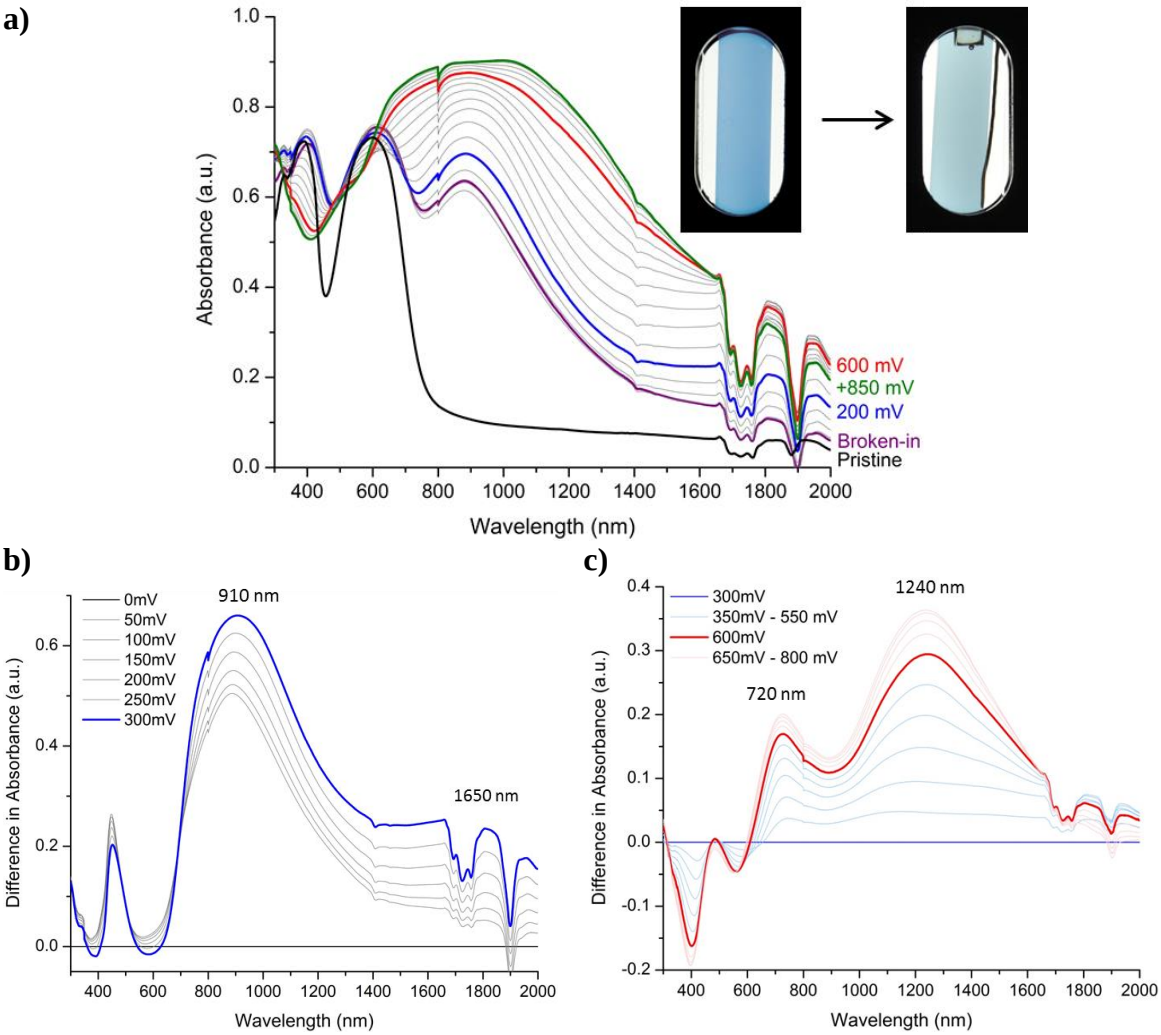

Figure 5.35. Electrochemical doping of a broken-in film of **Poly-EPBPE**. (a) Spectroelectrochemistry and photographs of the neutral and oxidized films. (b) Difference spectra of the film oxidized step-wise to 300 mV. (c) Difference spectra at higher oxidation potentials.

potential is required for solvent and electrolyte to diffuse into the film and intercalate between chains. The difference spectra show that the same charge carriers are produced at lower potentials: polarons (shoulder at 940 nm, and 1650 nm), and their π-dimers (840 nm, and 1290 nm). At higher potentials, transitions are observed at 700 nm, and 1030 nm, and may be due to other dication charge carriers, such as higher orders of polaron interactions, and bipolarons.

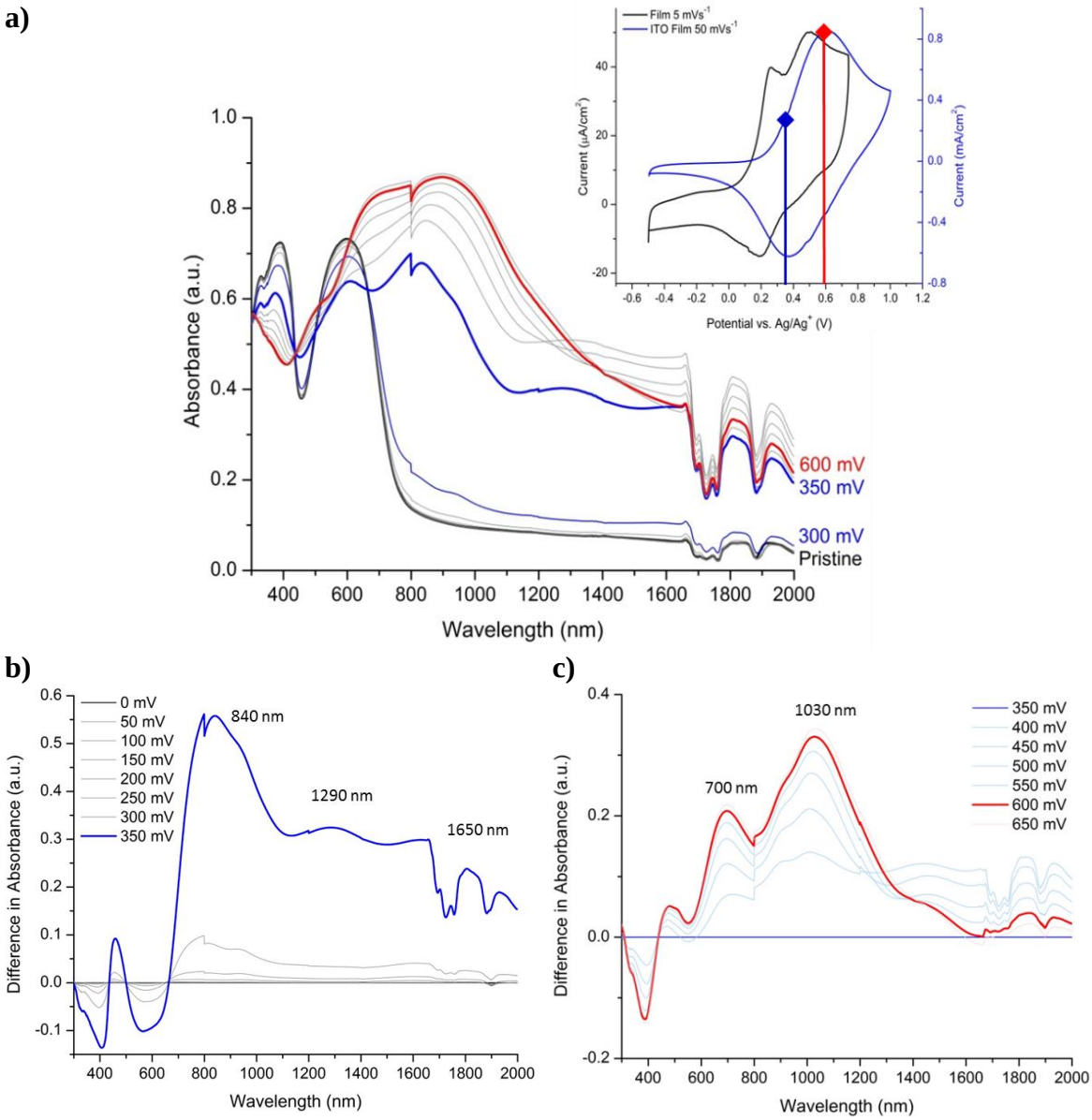

Figure 5.36. Electrochemical oxidation of a pristine film of **Poly-EPBPE**. (a) Spectroelectrochemistry (Inset: CV of a film on Pt button and on ITO.). (b) Difference spectra of the oxidation process to 350 mV. (c) Difference spectra at higher potentials.

The chemical and electrochemical doping of **Poly-EPBPE** shows significant differences in behavior between the solution and solid state, owing to the importance of secondary interactions in determining the charge carriers that are energetically favorable at each oxidation state.

5.4.3.4. Condensed State Characteristics

For many applications which require the active material to be cast as a thin film with good optical quality, an amorphous material is desired. In this respect, polymeric materials are favored over small molecules for their reduced tendency to crystallize, and generally superior mechanical properties. An understanding of the film and other solid-state characteristics of a polymer is also essential in its design for electrochromic applications.

5.4.3.4.1. Film Morphology

In the foregoing sections, it has been demonstrated that the condensed state interactions of small molecules and polymers can influence their oxidized state transitions. For example, the contribution from π-dimers becomes more important at higher concentrations and in the films of **Poly-EPBPE**. The polymer films have also consistently shown signs of optical inhomogeneity, observed as scattering in their absorption spectra. The spray-cast films were thus studied by optical and atomic force microscopy to discover the origin of the reduced optical quality.

Figure 5.37 shows optical micrographs of **Poly-EPBPE** films. The pristine film spray-cast from toluene (Figure 5.37a) shows a network of colored active material interspersed with uncovered areas exposing the ITO surface. This can be due to incomplete wetting by the solution of the polar ITO surface. By comparison, a fully-conjugated polymer (ECP-Magenta) film (Figure 5.37b) shows full coverage of the ITO surface. After electrochemical break-in, in which electrolyte solution is expected to diffuse into the polymer matrix, the **Poly-EPBPE** film still showed significant areas without active material (Figure 5.37c). Overoxidation (to 950 mV) of the film also led to

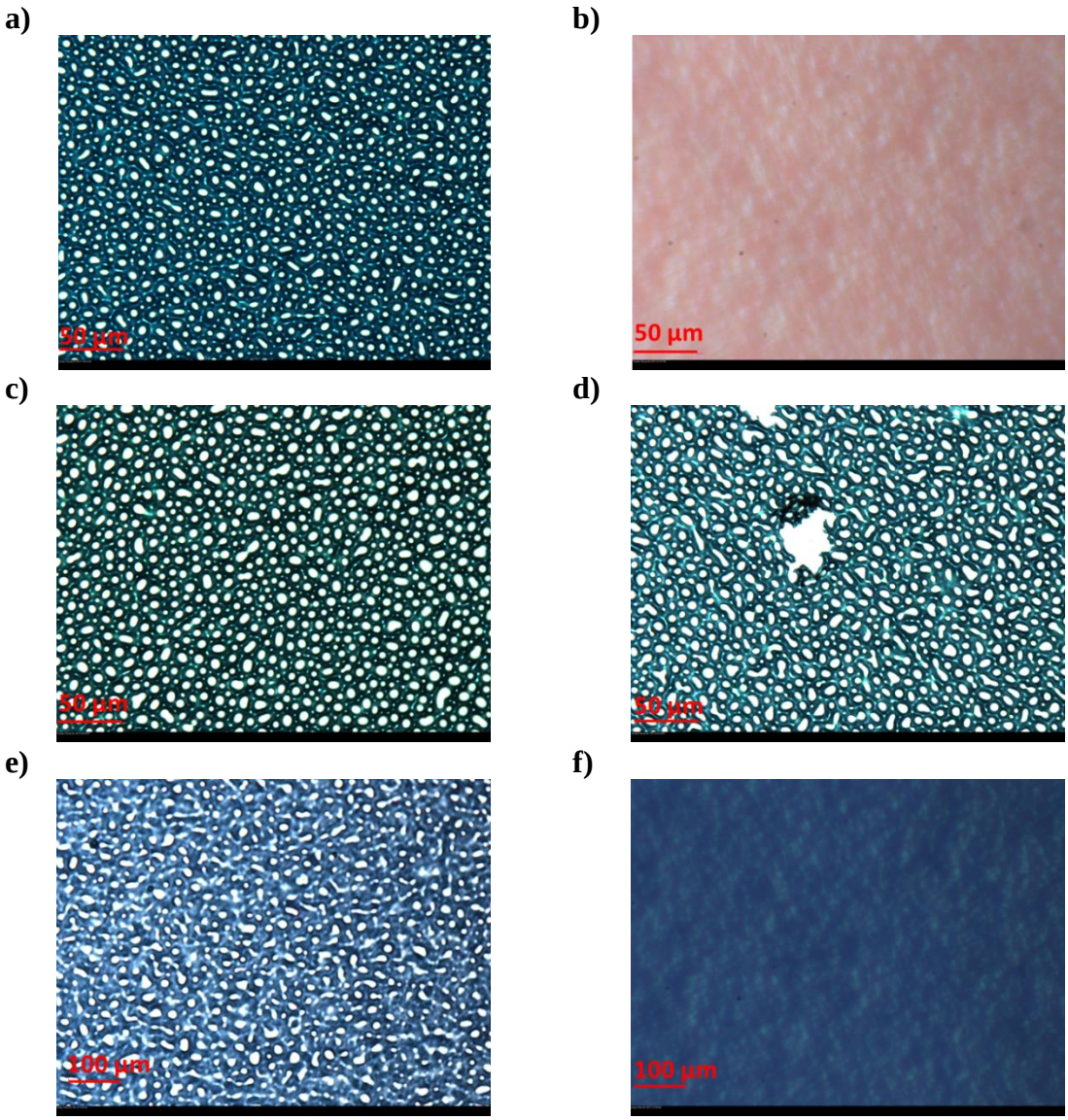

Figure 5.37. Optical micrographs of **Poly-EPBPE** spray-cast films on ITO. (a) Pristine film sprayed from toluene solution. (b) Micrograph of a fully conjugated polymer for comparison. (c) Toluene-sprayed film after break-in. (d) Over-oxidized film. (e) Pristine film sprayed from 9:1 toluene:$CHCl_3$. (f) Pristine film on phosphonic-acid treated ITO (spray-cast by Keith Johnson).

delamination, as shown by the "torn" holes in Figure 5.37d.

The polymer was also sprayed from solutions in mixed solvents to modify the wetting of the ITO surface. The polymer was cast using mixtures of toluene and $CHCl_3$, but the resulting film still showed insufficient coverage of the ITO surface (Figure 5.37e).

A pre-treatment of the ITO surface with octadecyl-functionalized phosphonic acid to reduce the polarity of the surface, enabled the polymer to uniformly wet the conductive surface. This film did yield improved coverage of the ITO surface (Figure 5.37f), but scattering was not reduced on the pristine film absorption spectra. Thus, inhomogeneities still likely exist within the polymer-covered areas, and were studied with atomic force microscopy.

Figure 5.38 shows the height and phase AFM images (obtained by Dr. Caroline Grand) of **Poly-EPBPE** drop-cast from toluene solution onto a glass slide. Close inspection of the images show fibrillar structures that presumably constitute the networks observed on optical microscopy. These fibrils may be due to the rod-coil structure of the polymer that can lead to selective interactions between the π-conjugated segments, separate from the interactions between the long aliphatic linkers. If amorphous films with better optical quality are to be obtained from polymers with discrete conjugated segments and aliphatic linkers, one or both of these interactions must be disrupted.

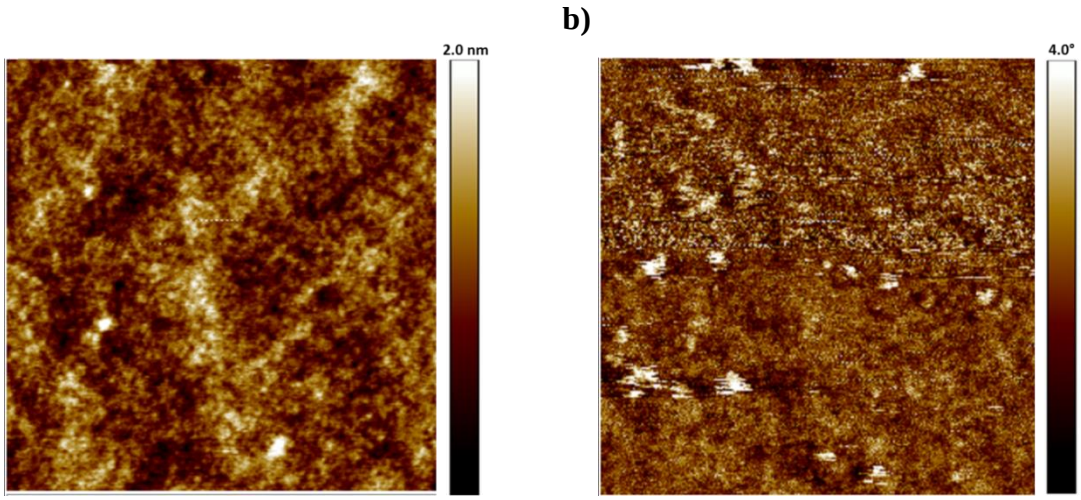

Figure 5.38. Atomic force micrographs of a **Poly-EPBPE** film drop-cast from toluene: (a) height, and (b) phase images (1 × 1 μm). (Taken by Dr. Caroline Grand)

5.4.3.4.2. Thermal Properties

The thermal transitions and overall stability of the small molecule and polymer were also compared. Figure 5.39a shows the results of thermogravimetric analysis of the materials, whereas Figure 5.39b shows their differential scanning calorimetry traces. The materials show excellent stability, with degradation temperatures (threshold of 5 % weight loss) at 363 °C for **EPBPE**, and 389 °C for the polymer. The DSC plots show

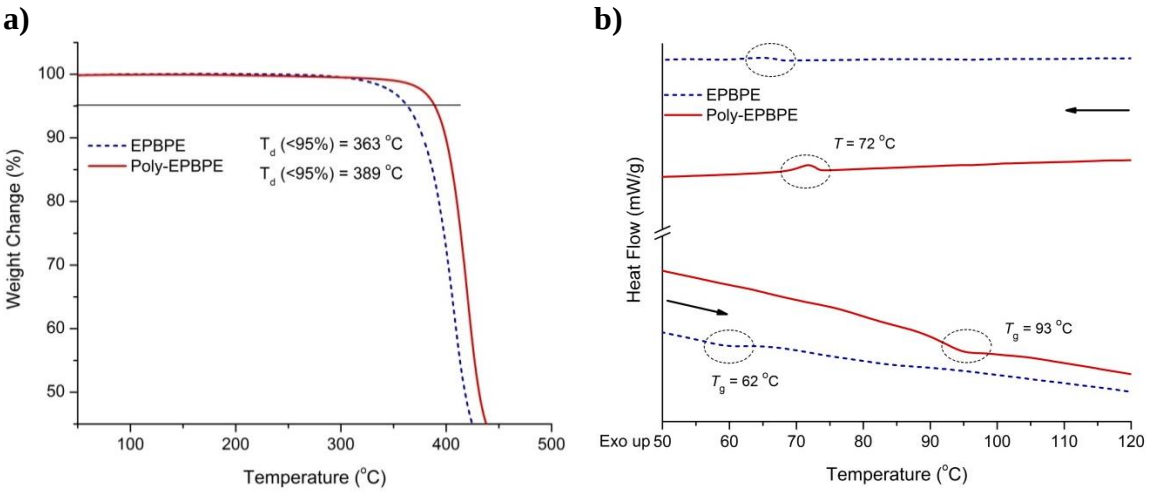

Figure 5.39. Thermal properties of **EPBPE** and **Poly-EPBPE**: (a) TGA curves, and (b) DSC traces.

glass transition temperatures for both materials, with the small molecule at 62 °C, and the polymer at a higher temperature of 93 °C. The polymer also shows a broad exothermic transition on cooling at 72 °C. This indicates a transition to a more ordered structure, which may be related to the fibrillar structures observed on AFM.

5.5. Summary

Donor-acceptor small molecules and polymers based on dioxythiophenes and an electron-poor heterocycle, BTD, were conveniently synthesized through a direct (hetero)arylation methods. Stoichiometric control of this cross coupling method allowed

access to donor-acceptor-donor trimers in high yields from difunctional heterocycles, eliminating the need for boronic or stannic derivatives that are often difficult to purify and require toxic precursors. The five- and seven-heterocycle small molecules were thus obtained in four or fewer steps.

The neutral and oxidized state properties of the donor-acceptor small molecules and the polymer are summarized in Table 5.6. All materials gave narrow and well-defined dual-band absorptions in the neutral state, due to the donor-acceptor charge-transfer interaction, and the π-π* high-energy excitation. The transitions had high molar extinction coefficients, attributed to the enhanced π-delocalization enabled by S-O interactions in the dioxythiophene units. The electron donation from the β-oxygens in these also allowed access to the mono- and dication states at low applied voltages. The donor-acceptor nature of the materials resulted in low ionization potentials, high electron affinities, and overall low energy gaps.

The well-defined π-system of the small molecules allowed analysis of the potential structures of charge carriers in dioxythiophene- and BTD-containing donor-

Table 5.6. Summary of properties of neutral and oxidized states of the donor-acceptor small molecules and polymer in this work.

	Neutral State Properties					**Oxidized State Properties**		
	λ_{max} **(nm)**	E_{ox} **(V)**	**IP (eV)**	**EA (eV)**	E_g **(eV)**	λ_{max} **(nm)** **Polaron**	**π-Dimer**	**Bipolaron**
EPBPE	569, 385	0.11, 0.35	−5.10	−3.26	1.78	920, 1640	820, 1260	
EPPBPPE	588, 415	-0.28, -0.16	−4.82	−3.04	1.84	1020, >2000	880, 1680	1140
Poly-EPBPE	576, 385	0.11, 0.52	−5.26	−3.37	1.89	950, 1650	810, 1270	1030

acceptor systems. Oxidized states generated *via* chemical and electrochemical doping gave rise to structures in which the positive charge is localized in the donor segments, with the BTD ring serving as a conjugation break. In **EPBPE**, this led to the polaron pair and its π-dimer being the dominant charge carriers at both low and high oxidation states. Both charge carriers had transitions peaking outside the visible range, leading to a violet to transmissive color change. In **EPPBPPE**, the longer donor segment produced polaron pairs that have significantly red-shifted absorptions, peaking well outside of the visible region. The extended structure also allowed bipolarons to be formed at high concentrations. All the charge carriers observed had absorptions with maxima in the near-IR, leading to a dark cyan to transmissive color change. Thus, donor-acceptor π-conjugated structures have been identified that can give rise to high contrast electrochromic materials.

In order to study the applicability of these donor-acceptor chromophores as electrochromic films, a polymer that retains the discrete nature of the π-system by linking these with aliphatic chains was developed. **Poly-EPBPE** was found to have well-defined and narrow transitions in its absorption spectra, and resolved oxidation waves, relative to fully-conjugated polymers. However, in higher oxidation states, the effect of interchain π-π interactions becomes pronounced, and the polymer's properties reflects this distribution of electronic environments. Thus, the polymer oxidized state absorption spectra were dominated by π-dimer transitions. In developing polymeric materials from discrete chromophores, the linkers must thus be designed such that undesired interactions are obstructed, such as by sterically bulky aliphatic moieties.

The polymer showed improved mechanical properties, yielding solution processable films that remained intact in the oxidized state. The polymer also showed higher glass transition and decomposition temperatures. However, the rod-coil structure of the conjugated segments linked with aliphatic chains gave rise to fibrillar networks that caused incomplete coverage of the ITO surface and scattering. These interactions must be disrupted to improve the amorphous nature of the resulting film.

The analyses of charge carriers are best supported with theoretical calculations to better elucidate the geometric deformations, and the accompanying evolution of the electronic configuration that determine oxidized state transitions. These calculations are currently being performed by collaborators, and are guided by the results obtained in this work.

5.6. Synthetic Details

4,7-bis(3,3-bis(((2-ethylhexyl)oxy)methyl)-3,4-dihydro-2H-thieno[3,4-b][1,4]dioxepin-6-yl)benzo[c][1,2,5]thiadiazole (5.3). 5.1 (ProDOT-diethylhexyl) (36 mmol, 15.86 g), **5.2** (dibromo-BTD) (3 mmol, 0.88 g), $Pd(OAc)_2$ (8 mol %, 0.05 g), pivalic acid (3.6 mmol, 0.37 g), and K_2CO_3 (4.5 mmol, 0.62 g) were charged into an oven-dried Schlenk tube fitted with a stir bar, and pumped for 30 min, then purged with Ar three times. Then Ar-bubbled *N*,*N*-dimethylacetamide (15 mL) was added to the mixture. The reaction was then placed in an oil bat at 140 °C and stirred until all of the dibromo-BTD is judged consumed by TLC (~ 20 mins). The reaction was then removed from the oil bath, quenched with ethyl acetate (~ 50 mL) and allowed to come to r.t.. The mixture is then poured into water and extracted with ethyl acetate. The organics were separated, washed with H_2O twice, then brine. The organic layer was separated, dried

over $MgSO_4$, filtered, and concentrated. The product was purified *via* column chromatography, eluting with 3:2 hexanes:CH_2Cl_2, to yield 2.11 g (69 %) of the pure product. ^{1}H NMR (300 MHz, $CDCl_3$) δ 8.31 (s, 2H), 6.66 (s, 2H), 4.21 (s, 4H), 4.09 (s, 4H), 3.55 (s, 8H), 3.31 (d, J = 7.7 Hz, 8H), 1.58 – 1.44 (m, 4H), 1.44 – 1.19 (m, 32H), 0.98 – 0.78 (m, 24H). ^{13}C NMR (75 MHz, $CDCl_3$) δ 152.76, 149.86, 147.97, 127.66, 124.31, 117.70, 106.62, 77.58, 77.16, 76.74, 74.40, 73.96, 70.07, 48.03, 39.75, 30.79, 29.25, 24.14, 23.25, 14.27, 11.31. MS (MALDI, $[M+H]^+$) *m/z* calcd. for $C_{56}H_{88}N_2O_8S_3$ 1012.57; found 1013.53.

4,7-bis(8-bromo-3,3-bis(((2-ethylhexyl)oxy)methyl)-3,4-dihydro-2H-thieno[3,4-b][1,4]dioxepin-6-yl)benzo[c][1,2,5]thiadiazole (5.4). 5.3 (0.26 mmol, 0.26 g) was dissolved in $CHCl_3$ (25 mL) and cooled to 0 °C in an ice bath. Then *N*-bromosuccinimide (0.56 mmol, 0.10 g) was added in one portion as a solid. The reaction mixture was protected from light, stirred, and allowed to come to r.t. overnight. The solvent was removed *in vacuo* and the concentrate was passed through a short pad of silica, eluting with 3:2 hexanes:CH_2Cl_2, to yield 0.22 g (74 %) of the pure product. ^{1}H NMR (300 MHz, $CDCl_3$) δ 8.30 (s, 8H), 4.20 (d, J = 13.6 Hz, 8H), 3.68 – 3.43 (m, 4H), 3.31 (d, J = 7.4 Hz, 8H), 1.57 – 1.44 (m, 4H), 1.44 – 1.19 (m, 32H), 0.98 – 0.79 (m, 24H). ^{13}C NMR (75 MHz, $CDCl_3$) δ 152.26, 147.69, 147.13, 127.29, 123.58, 117.41, 96.33, 74.40, 74.21, 70.00, 48.05, 39.76, 30.79, 29.26, 24.14, 23.26, 14.29, 11.33. MS (MALDI, $[M+H]^+$) *m/z* calcd. for $C_{56}H_{86}Br_2N_2O_8S_3$ 1168.39; found 1170.38.

4,7-bis(3,3-bis(((2-ethylhexyl)oxy)methyl)-8-(7-hexyl-2,3-dihydrothieno[3,4-b][1,4]dioxin-5-yl)-3,4-dihydro-2H-thieno[3,4-b][1,4]dioxepin-6-yl)benzo[c][1,2,5]thiadiazole (EPBPE). 5.4 (0.15 mmol, 0.17 g), **5.5** (0.34 mmol, 0.08

g), $Pd(OAc)_2$ (2 mol %, 0.0021 g), pivalic acid (0.3 mmol, 0.005 g), and K_2CO_3 (0.3 mmol, 0.041 g) were charged into an oven dried Schlenk tube fitted with a stir bar, and pumped for 30 min, then purged with Ar three times. Then Ar-bubbled *N*,*N*-dimethylacetamide (5 mL) was added, and the mixture was placed in an oil bath at 140 °C, and stirred for 12 hrs. The reaction mixture was then cooled to r.t. and precipitated in cold methanol. Then the product was collected and redissolved in 1:1 hexanes:CH_2Cl_2. Column chromatography in silica gel was done to purifiy the product, eluting with 1:1 hexanes:CH_2Cl_2, to yield 0.18 g (81 %) of pure product. ^{1}H NMR (300 MHz, $CDCl_3$) δ 8.35 (s, 2H), 4.38 (s, 4H), 4.24 (s, 8H), 4.20 (s, 4H), 3.68 – 3.51 (m, 8H), 3.33 (d, J = 5.6 Hz, 8H), 2.66 (s, 4H), 1.71 – 1.56 (m, 4H), 1.56 – 1.45 (m, 4H), 1.45 – 1.20 (m, 44H), 0.99 – 0.80 (m, 30H). ^{13}C NMR (75 MHz, $CDCl_3$) δ 152.72, 148.02, 144.26, 138.01, 137.19, 127.10, 123.79, 117.96, 117.31, 114.73, 106.36, 74.39, 74.17, 70.27, 65.44, 64.71, 48.06, 39.77, 31.72, 30.82, 30.79, 29.27, 29.25, 29.07, 24.16, 23.28, 22.76, 14.31, 14.26, 11.33. MS (MALDI, $[M+H]^+$) *m/z* calcd. for $C_{80}H_{120}N_2O_{12}S_5$ 1460.74; found 1461.75. Elem. Anal. calcd. C, 65.72; H, 8.27; N, 1.92; S, 10.96 found: C, 65.71; H, 8.13; N, 1.97; S, 10.95.

4,7-bis(3,3,3',3'-tetrakis(((2-ethylhexyl)oxy)methyl)-3,3',4,4'-tetrahydro-2H,2'H-[6,6'-bithieno[3,4-b][1,4]dioxepin]-8-yl)benzo[c][1,2,5]thiadiazole (5.6). 5.3 (0.59 mmol, 0.6 g), **5.1** (7.0 mmol, 3.19 g), $Pd(OAc)_2$ (8 mol %, 0.010 g), pivalic acid (0.70 mmol, 0.072 g), and K_2CO_3 (0.88 mmol, 0.12 g) were charged into an oven dried Schlenk tube fitted with a stir bar, and pumped for 30 min, then purged with Ar three times. Then Ar-bubbled *N*,*N*-dimethylacetamide (3 mL) was added, and the mixture was placed in an oil bath at 140 °C, and stirred for 12 hrs. The reaction mixture was then cooled to r.t. and

precipitated in cold methanol. Then the product was collected and redissolved in 1:1 hexanes:CH_2Cl_2. Column chromatography in silica gel was done to purifiy the product, eluting with 1:1 hexanes:CH_2Cl_2, to yield 0.49 g (45 %) of pure product. ^{1}H NMR (300 MHz, $CDCl_3$) δ 8.30 (s, 2H), 6.43 (s, 2H), 4.24 (s, 4H), 4.18 (s, 8H), 4.07 (s, 4H), 3.61 (s, 8H), 3.54 (s, 8H), 3.32 (dd, J = 5.3, 3.4 Hz, 16H), 1.59 – 1.45 (m, 8H), 1.44 – 1.15 (m, 64H), 1.01 – 0.76 (m, 48H). ^{13}C NMR (75 MHz, $CDCl_3$) δ 152.84, 149.54, 147.78, 145.62, 145.39, 127.63, 124.12, 117.06, 115.81, 115.36, 103.71, 74.39, 74.19, 70.21, 39.75, 30.79, 29.27, 26.96, 24.15, 23.26, 14.28, 11.30. MS (MALDI, $[M+H]^+$) *m/z* calcd. for $C_{106}H_{172}N_2O_{16}S_5$ 1889.13; found 1890.08.

4,7-bis(8'-bromo-3,3,3',3'-tetrakis(((2-ethylhexyl)oxy)methyl)-3,3',4,4'-tetrahydro-2H,2'H-[6,6'-bithieno[3,4-b][1,4]dioxepin]-8-yl)benzo[c][1,2,5]thiadiazole (5.7). 5.6 (0.11 mmol, 0.22 g) was dissolved in $CHCl_3$ and cooled to 0 °C in an ice bath, and stirred for 20 mins under light protection. Then *N*-bromosuccinimide (0.25 mmol, 0.045 g) was added as a solid in one portion. Then the reaction mixture was stirred at 0 °C under light protection for 40 mins. Then the reaction mixture was concentrated at reduced pressure and filtered through a silica plug, eluting with 1:1 hexanes:CH_2Cl_2. Then column chromatography in silica gel was repeated, eluting with 7:3 hexanes:CH_2Cl_2, to yield 0.12 g (55 %) of the pure product. ^{1}H NMR (300 MHz, $CDCl_3$) δ 8.30 (s, 2H), 4.18 (d, J = 20.7 Hz, 16H), 3.58 (d, J = 5.3 Hz, 16H), 3.31 (dd, J = 12.6, 8.7 Hz, 16H), 1.54 (t, J = 13.3 Hz, 8H), 1.45 – 1.17 (m, 64H), 1.04 – 0.78 (m, 48H). ^{13}C NMR (75 MHz, CDCl3) δ aromatic protons were not resolved, 74.42, 70.43, 69.89, 39.78, 30.80, 29.91, 29.27, 24.16, 23.27, 14.30, 11.32. MS (MALDI, $[M+H]^+$) *m/z* calcd. for $C_{106}H_{170}Br_2N_2O_{16}S_5$ 2044.95 found 2048.87.

4,7-bis(3,3,3',3'-tetrakis(((2-ethylhexyl)oxy)methyl)-8'-(7-hexyl-2,3-dihydrothieno[3,4-b][1,4]dioxin-5-yl)-3,3',4,4'-tetrahydro-2H,2'H-[6,6'-bithieno[3,4-b][1,4]dioxepin]-8-yl)benzo[c][1,2,5]thiadiazole (EPPBPPE). **5.7** (0.044 mmol, 0.09 g), **5.5** (0.11 mmol, 0.026 g), $Pd(OAc)_2$ (8 mol %, 0.001 g), pivalic acid (0.013 mmol, 0.002 g), and K_2CO_3 (0.09 mmol, 0.012 g) were charged into an oven dried Schlenk tube fitted with a stir bar, and pumped for 30 min, then purged with Ar three times. Then Ar-bubbled *N*,*N*-dimethylacetamide (2.5 mL) was added, and the mixture was placed in an oil bath at 140 °C, and stirred for 16 hrs. The reaction mixture was then cooled to r.t. and precipitated in cold methanol. Then the product was collected and redissolved in 1:1 hexanes:CH_2Cl_2. Column chromatography in silica gel was done to purifiy the product, eluting with 1:1 hexanes:CH_2Cl_2, to give 0.07 g (69 %) of pure product. ^{1}H NMR (300 MHz, CD_2Cl_2) δ 8.38 (s, 2H), 4.47 – 3.96 (m, 24H), 3.75 – 3.50 (m, 16H), 3.35 (d, J = 3.7 Hz, 16H), 2.64 (s, 4H), 1.61 (d, J = 7.5 Hz, 4H), 1.54 (s, 8H), 1.47 – 1.13 (m, 76H), 1.02 – 0.76 (m, 54H). ^{13}C NMR (75 MHz, CD_2Cl_2) δ 153.04, 148.39, 146.10, 145.37, 144.37, 137.87, 137.51, 133.84, 127.44, 124.19, 117.82, 116.02, 114.93, 112.66, 106.33, 74.70, 70.37, 65.72, 65.01, 48.36, 40.08, 31.98, 31.08, 31.05, 30.09, 29.53, 29.25, 24.41, 23.53, 23.02, 14.30, 11.39, 11.36. MS (MALDI, $[M+H]^+$) *m/z* calcd. for $C_{130}H_{204}N_2O_{20}S_7$ 2337.31; found 2338.29. Elem. Anal. calcd. C, 66.74; H, 8.79; N, 1.20; S, 9.59; found: C, 68.13; H, 9.27; N, 1.33; S, 8.31.

1,10-bis(2,3-dihydrothieno[3,4-b][1,4]dioxin-5-yl)decane (5.8). EDOT (2.3 mmol, 0.33 g) was dissolved in anhydrous THF (10 mL) and the solution was cooled to −78 °C in an isopropyl/dry ice bath, and stirred for 15 mins. Then n-BuLi (1.6 M, 2.41 mmol, 1.51 mL) was added dropwise and the reaction mixture stirred at −78 °C for 1 hr. Then 1,10-

diiododecane (1 mmol, 0.39 g) dissolved in anhydrous THF (5 mL) was added dropwise to the deprotonated EDOT solution at −78 °C. Then the reaction mixture was allowed to come to r.t. slowly. The reaction mixture was allowed to come to r.t. overnight. Then the reaction was quenched with H_2O, and the organics were extracted with ethyl acetate, washed with NH_4Cl, H_2O, then brine. The organic layer was separated, dried over Na_2SO_4, and concentrated. The product was purified *via* column chromatography in silica gel, eluting with 95:5 hexanes:ethyl acetate, to yield 0.070 g (17%) of pure product. ^{1}H NMR (300 MHz, CD_2Cl_2) δ 6.08 (s, 2H), 4.20 – 4.10 (m, 8H), 2.61 (t, J = 15.1, 7.4 Hz, 4H), 1.68 – 1.50 (m, 4H), 1.29 (d, J = 3.7 Hz, 12H). ^{13}C NMR (75 MHz, CD_2Cl2) δ 142.00, 137.92, 118.70, 95.14, 65.11, 30.91, 29.92, 29.70, 29.51, 26.23. MS (EI, [M+H]) *m/z* calcd. for $C_{22}H_{30}O_4S_2$ 422.16; found 422.1.

Poly-EPBPE. 5.4 (0.45 mmol, 0.53 g), **5.8** (0.445 mmol, 0.19 g), $Pd(OAc)_2$ (2 mol %, 0.006 g), pivalic acid (0.013 mmol, 0.014 g), and K_2CO_3 (0.89 mmol, 0. 12 g) were charged into an oven dried Schlenk tube fitted with a stir bar, and pumped for 30 min, then purged with Ar three times. Then Ar-bubbled *N*-methylpyrrolidone (2.5 mL) was added, and the mixture was placed in an oil bath at 145 °C, and stirred for 24 hrs. Then **5.5** (0.048 g) was added to the reaction mixture, and stirred for 1.5 hrs. Then the reaction was cooled to r.t., and precipitated in methanol, and stirred for 1.5 hrs. Then the solids were filtered out, and air-dried under vacuum overnight. Then the solids were transferred to a cellulose thimble and placed in a Soxhlet extraction set-up. The solids were washed successively with methanol, acetone, hexanes, and $CHCl_3$. The $CHCl_3$ fraction was concentrated, then redissolved in toluene (25 mL). Then diethylammonium diethyldithiocarbamate (Pd scavenger), and 18-Crown-6 (K^+ scavenger) were added, and

the mixture was stirred at 65 °C overnight. Then the reaction mixture was cooled to room temperature, and the solvent reduced *in vacuo*. The mixture was then reprecipitated in methanol, filtered, and dried under vaccum, to yield 0.46 g (72 %) of polymer. ^{1}H NMR (300 MHz, CD_2Cl_2) δ 8.40 (s, 2H), 4.54 – 3.97 (m, 16H), 3.73 – 3.46 (m, 8H), 3.35 (d, J = 5.5 Hz, 8H), 2.66 (t, J = 7.2 Hz, 4H), 1.72 – 1.58 (m, 4H), 1.58 – 1.46 (m, 4H), 1.46 – 1.19 (m, 48H), 1.01 – 0.79 (m, 24H). 1^{3}C NMR (75 MHz, CD_2Cl_2) δ 152.94, 148.44, 144.54, 138.34, 137.59, 127.17, 123.98, 118.27, 117.62, 114.79, 106.42, 74.60, 74.53 – 74.14, 70.32, 65.87, 65.03, 48.31, 40.11, 31.06, 30.94, 30.01, 29.77, 29.64, 29.52, 26.24, 24.44, 23.55, 14.35, 11.39. Elem. Anal. calcd. for $(C_{78}H_{114}N_2O_{12}S_5)_n$ C, 65.42; H, 8.02; N, 1.96; S, 11.19; found: C, 65.13; H, 7.93; N, 2.14; S, 10.54. GPC: M_n: 23.1 kDa, M_w: 54.0 kDa, PDI: 2.33, in $CHCl_3$ vs. PS.

CHAPTER 6

CONCLUSIONS AND PERSPECTIVES

In this dissertation, the versatility of the conjugated π-system is demonstrated in the design of three sets of functional materials for different electronic applications. The π-systems were structurally tailored in terms of their extent of conjugation, and electron density (Figure 6.1). The extent of conjugation was varied by the size or length of the π-system and its planarity. The planarity was tuned by the use of fused ring systems, the balance between aromatic and quinoidal contributing resonance forms, and secondary interactions such as S-O interactions. Conjugation breaking was also enforced with the inter-aryl steric crowding that regulated torsion angles, the substitution pattern in aromatic rings (*meta*, *ortho*, *para*), and non-conjugated linkers. The electron density, on the other hand, was modulated with electron -rich and -poor heterocycles, and electron -donating and -withdrawing substituents.

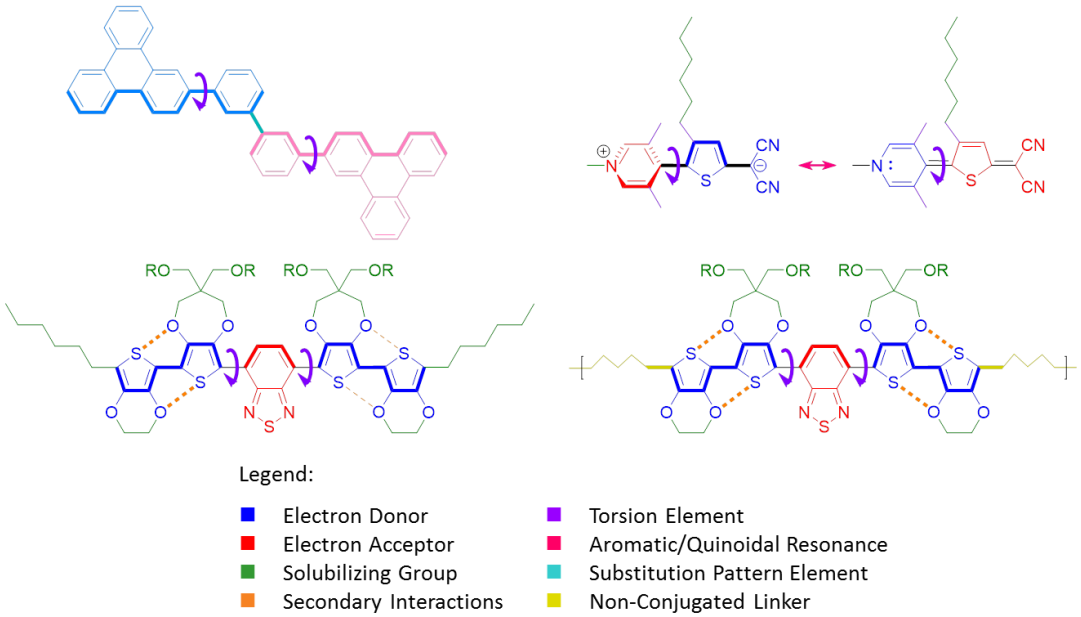

Figure 6.1. Elements of structural control for tailoring the π-systems in this dissertation.

Access to this wide variety of π-systems took advantage of developments in cross-coupling techniques, and careful optimization of the synthetic conditions ensured moderate to high yields. Judicious selection of heteroaromatic units already functionalized with appropriate solubilizing groups or torsional elements, and modification of existing protocols to control oligomer vs. polymer formation allowed the synthesis of all molecules in five or fewer steps.

In Chapter 3, triphenylene-based hosts were designed to have large energy gaps, high triplet energies, ambipolar transport characteristics, and to form stable amorphous films through high glass transition temperatures. The *meta* substitution pattern around the biphenyl linker, and the lack of any electron -withdrawing or -donating groups in the triphenylene core or the biphenyl linker gave the desired large energy gaps, but the *p*-terphenyl fragment in the structure led to a large singlet-triplet splitting, and lower triplet energy than the triphenylene core. All host materials showed low to moderate mobilities, with hole mobilities being higher than electron mobilities. All host materials showed moderate to high $\boldsymbol{T_g}$'s. The low transport characteristics of the alkylated host materials were due to the disorder induced by a regio-isomeric mixture. However, this disorder allowed the formation of solution processable, yet thermally stable films, despite their low $\boldsymbol{T_g}$. All optoelectronic and film forming properties of the host materials contributed to highly efficient green OLED devices, comparable in performance to well-known materials in the literature.

In order to improve the transport characteristics of the host materials, they can be functionalized with electron-donating units in the linker, such as carbazole, to lower their IP's, and stabilize their radical cations. Weak electron-accepting units can also be

implemented as side groups to stabilize radical anions and enhance electron mobilities. However, the placement of these groups must be such that there is no conjugation between them that can induce an ICT interaction. Selection of electron- donating and withdrawing heterocycles must also consider fused rings and spiro-linkages to reduce disorder and maintain or enhance their $\boldsymbol{T_g}$'s.

The unalkylated host **DTPBP** showed mesogenic properties, owing to the strong tendency of the triphenylene core to form discs. However, the rotational elements in the biphenyl linker induced enough disorder to yield a liquid crystalline material, with spherulitic or mosaic textures, depending on the processing conditions. The material also yielded birefringent fibers with high aspect ratios. This strong propensity toward order can be taken advantage of by growing single crystals of the material, and studying their mobilities in transistor devices.

In Chapter 4, donor-acceptor π-systems with sterically enforced large inter-aryl twist angles, and benzene-annulation modulated aromatic/quinoidal resonance distribution were designed and synthesized. Rigorous structural characterization showed the steric and electronic basis of the chromophore ground-state structure, and the strong response of the ground state structure to the condensed state environment. The electron-rich and less-aromatic thiophene ring served as an auxiliary donor, leading to large ground state dipole moments, and significantly reduced ground-to-excited state energy gaps. These properties, and the large twist angle in $\mathbf{PMe_3TC_6(CN)_2}$, arising from its higher inter-aryl steric bulk, gave rise to large γ. Thus, the incorporation of thiophene is an effective approach toward enhancing tictoid nonlinear optical properties, and should be further pursued.

The results of theoretical calculations on other proposed twisted donor-acceptor structures (Table 4.2) also show other promising structures, such as the π-extended derivatives of **$PMe_3TC_6(X)_2$**, where X is changed from CN to (CNPhS), $(PhS)_2$, and $(TFS)_2$. Other π-extended thiophene-based donor heterocycles, such as DTS and DTG, also show promising calculated γ.

In Chapter 5, donor-acceptor small molecules and polymer with discrete π-conjugated chromophores were designed and synthesized. The well-defined nature of their π-systems allowed sharp absorption bands in both their neutral and charged states, in contrast with fully conjugated ECPs. The strong charge-transfer and π-π* transitions in the neutral state gave the materials intense colors. The red-shifted charged state absorptions due to polaron localization gave rise to absorptions in the near-IR. Thus, these discrete chromophores are viable materials for study in high-contrast electrochromics.

A comprehensive characterization of their charged states allowed structures for their polaron, polaron pair, and bipolaron to be proposed. The D-A-D pattern, the enhanced conjugation between the donor rings (from S-O interactions), and the strongly electron-poor and sterically more-demanding BTD ring contributed to the favorability of disproportionation toward the polaron pair. The localization of the charges in the donor segments in the polaron pair structure can be further studied by varying the acceptor ring can be varied in the D-A-D structure. This will allow structure-property relationships such as the effect of the acceptor strength, and the effect of inter-ring torsion, to be determined. With sufficiently electron-poor and sterically bulky acceptors, it is expected that a family of D-A-D structures with similar charged state absorptions in the near-IR

can be generated. This will allow a mechanism for tuning the neutral state color independently from the oxidized state color, giving a variety of color-to-highly-transmissive materials for electrochromics.

The polaron pair structure in both small molecules and the polymer was also observed to form π-dimers. The Davydov-blue-shifted absorptions for these dimers indicate that their interactions arise from a cofacial stacking. Thus, if this dimer formation is to be disrupted, structural elements that hinder cofacial stacking must be introduced into the side chains of the molecules and polymers. Large bulky aliphatic units are expected to accomplish this purpose, and can serve as linkers in the polymer structure. The bulky units must also be able to disrupt the rod-coil structure of the polymer, to enhance its amorphous nature, and reduce scattering in spray-cast films.

It must also be noted that the characterization of charge carriers in any conjugated system can benefit from well-designed and thorough theoretical calculations. At present, the small molecules reported in this dissertation are being studied to determine computational methodologies that will best elucidate the orbital structure and electronic states that govern the optical transitions in both neutral and charged states. The results of these computational studies, conducted by collaborators at the University of North Georgia, will inform the structure elucidation of the charge carrier species proposed in this dissertation.

REFERENCES

(1) Su, W. P.; Schrieffer, J. R.; Heeger, A. J. Solitons in Polyacetylene. *Phys. Rev. Lett.* **1979**, *42*, 1698.

(2) Kertesz, M.; Choi, C. H.; Yang, S. Conjugated Polymers and Aromaticity. *Chem. Rev.* **2005**, *105*, 3448.

(3) Salaneck, W. R.; Friend, R. H.; Brédas, J. L. Electronic structure of conjugated polymers: consequences of electron–lattice coupling. *Physics Reports* **1999**, *319*, 231.

(4) Salzner, U.; Lagowski, J. B.; Pickup, P. G.; Poirier, R. A. Comparison of geometries and electronic structures of polyacetylene, polyborole, polycyclopentadiene, polypyrrole, polyfuran, polysilole, polyphosphole, polythiophene, polyselenophene and polytellurophene. *Synth. Met.* **1998**, *96*, 177.

(5) Hofmann, P. *Solid State Physics: An Introduction*; 2nd ed.; Wiley-VCH: Weinheim, Germany, 2015.

(6) Turro, N. J. *Modern molecular photochemistry of organic molecules*; Sausalito, Calif.: University Science Books, 2010.

(7) Köhler, A.; Bässler, H. In *Electronic Processes in Organic Semiconductors*; Wiley-VCH Verlag GmbH & Co. KGaA: 2015, p 1.

(8) Stucky, G. D.; Marder, S. R.; Sohn, J. E. In *Materials for Nonlinear Optics : Chemical Perspectives*; Marder, S. R., Sohn, J. E., Stucky, G. D., Eds.; Washington, DC: American Chemical Society, 1991, p 2.

(9) Knupfer, M. Exciton binding energies in organic semiconductors. *Appl. Phys. A* **2003**, *77*, 623.

(10) Bredas, J.-L. Mind the gap! *Mater. Horiz.* **2014**, *1*, 17.

(11) Bässler, H.; Arkhipov, V. I.; Emelianova, E. V.; Gerhard, A.; Hayer, A.; Im, C.; Rissler, J. Excitons in π-conjugated polymers. *Synth. Met.* **2003**, *135–136*, 377.

(12) Lüssem, B.; Riede, M.; Leo, K. Doping of organic semiconductors. *Physica Status Solidi A* **2013**, *210*, 9.

(13) Sun, S.-S.; Zhang, C. In *Introduction to organic electronic and optoelectronic materials and devices*; Sun, S.-S., Dalton, L. R., Eds.; CRC Press: Boca Raton, 2008, p 401.

(14) Köhler, A.; Beljonne, D. The Singlet–Triplet Exchange Energy in Conjugated Polymers. *Adv. Funct. Mater.* **2004**, *14*, 11.

(15) Milián-Medina, B.; Gierschner, J. Computational design of low singlet–triplet gap all-organic molecules for OLED application. *Org. Electron.* **2012**, *13*, 985.

(16) Bässler, H.; Köhler, A. In *Unimolecular and Supramolecular Electronics I*; Metzger, R. M., Ed.; Springer Berlin Heidelberg: 2012; Vol. 312, p 1.

(17) Heeger, A. J. Semiconducting and metallic polymers: the fourth generation of polymeric materials. *Synth. Met.* **2001**, *125*, 23.

(18) MacDiarmid, A. G.; Mammone, R. J.; Kaner, R. B.; Porter, S. J.; Pethig, R.; Heeger, A. J.; Rosseinsky, D. R. The Concept of `Doping' of Conducting Polymers: The Role of Reduction Potentials [and Discussion]. *Philosophical Transactions of the Royal Society of London A: Mathematical, Physical and Engineering Sciences* **1985**, *314*, 3.

(19) Mityashin, A.; Olivier, Y.; Van Regemorter, T.; Rolin, C.; Verlaak, S.; Martinelli, N. G.; Beljonne, D.; Cornil, J.; Genoe, J.; Heremans, P. Unraveling the Mechanism of Molecular Doping in Organic Semiconductors. *Adv. Mater.* **2012**, *24*, 1535.

(20) Brédas, J. L.; Thémans, B.; Fripiat, J. G.; André, J. M.; Chance, R. R. Highly conducting polyparaphenylene, polypyrrole, and polythiophene chains: An \textit{ab initio} study of the geometry and electronic-structure modifications upon doping. *Phys. Rev. B* **1984**, *29*, 6761.

(21) Bredas, J. L.; Street, G. B. Polarons, bipolarons, and solitons in conducting polymers. *Acc. Chem. Res.* **1985**, *18*, 309.

(22) Nishinaga, T.; Wakamiya, A.; Yamazaki, D.; Komatsu, K. Crystal Structures and Spectroscopic Characterization of Radical Cations and Dications of Oligothiophenes Stabilized by Annelation with Bicyclo[2.2.2]octene Units: Sterically Segregated Cationic Oligothiophenes. *J. Am. Chem. Soc.* **2004**, *126*, 3163.

(23) Yamazaki, D.; Nishinaga, T.; Komatsu, K. Radical Cation of Dibenzothiophene Fully Annelated with Bicyclo[2.2.2]octene Units: X-ray Crystal Structure and Electronic Properties. *Org. Lett.* **2004**, *6*, 4179.

(24) Natali, D.; Caironi, M. Charge Injection in Solution-Processed Organic Field-Effect Transistors: Physics, Models and Characterization Methods. *Adv. Mater.* **2012**, *24*, 1357.

(25) Bässler, H. Injection, transport and recombination of charge carriers in organic light-emitting diodes. *Polym. Adv. Technol.* **1998**, *9*, 402.

(26) Ishii, H.; Sugiyama, K.; Ito, E.; Seki, K. Energy Level Alignment and Interfacial Electronic Structures at Organic/Metal and Organic/Organic Interfaces. *Adv. Mater.* **1999**, *11*, 605.

(27) Kahn, A.; Koch, N.; Gao, W. Electronic structure and electrical properties of interfaces between metals and π-conjugated molecular films. *J. Polym. Sci., Part B: Polym. Phys.* **2003**, *41*, 2529.

(28) Scott, J. C. Metal–organic interface and charge injection in organic electronic devices. *Journal of Vacuum Science & Technology A* **2003**, *21*, 521.

(29) Norbert, K. Energy levels at interfaces between metals and conjugated organic molecules. *J. Phys.: Condens. Matter* **2008**, *20*, 184008.

(30) Karl, N. Charge carrier transport in organic semiconductors. *Synth. Met.* **2003**, *133–134*, 649.

(31) Brédas, J.-L.; Beljonne, D.; Coropceanu, V.; Cornil, J. Charge-Transfer and Energy-Transfer Processes in π-Conjugated Oligomers and Polymers: A Molecular Picture. *Chem. Rev.* **2004**, *104*, 4971.

(32) Zaumseil, J.; Sirringhaus, H. Electron and Ambipolar Transport in Organic Field-Effect Transistors. *Chem. Rev.* **2007**, *107*, 1296.

(33) Coropceanu, V.; Cornil, J.; da Silva Filho, D. A.; Olivier, Y.; Silbey, R.; Brédas, J.-L. Charge Transport in Organic Semiconductors. *Chem. Rev.* **2007**, *107*, 926.

(34) Stafstrom, S. Electron localization and the transition from adiabatic to nonadiabatic charge transport in organic conductors. *Chem. Soc. Rev.* **2010**, *39*, 2484.

(35) Baranovskii, S. D. Theoretical description of charge transport in disordered organic semiconductors. *physica status solidi (b)* **2014**, *251*, 487.

(36) Cornil, J.; Lemaur, V.; Calbert, J. P.; Brédas, J. L. Charge Transport in Discotic Liquid Crystals: A Molecular Scale Description. *Adv. Mater.* **2002**, *14*, 726.

(37) Kuppermann, A.; Flicker, W. M.; Mosher, O. A. Electronic spectroscopy of polyatomic molecules by low-energy, variable-angle electron impact. *Chem. Rev.* **1979**, *79*, 77.

(38) Roncali, J. Synthetic Principles for Bandgap Control in Linear π-Conjugated Systems. *Chem. Rev.* **1997**, *97*, 173.

(39) Meier, H.; Stalmach, U.; Kolshorn, H. Effective conjugation length and UV/vis spectra of oligomers. *Acta Polym.* **1997**, *48*, 379.

(40) Apperloo, J. J.; Raimundo, J.-M.; Frère, P.; Roncali, J.; Janssen, R. A. J. Redox States and Associated Interchain Processes of Thienylenevinylene Oligomers. *Chem. Eur. J.* **2000**, *6*, 1698.

(41) Apperloo, J. J.; Groenendaal, L. B.; Verheyen, H.; Jayakannan, M.; Janssen, R. A. J.; Dkhissi, A.; Beljonne, D.; Lazzaroni, R.; Brédas, J.-L. Optical and Redox Properties of a Series of 3,4-Ethylenedioxythiophene Oligomers. *Chem. Eur. J.* **2002**, *8*, 2384.

(42) van Haare, J. A. E. H.; Havinga, E. E.; van Dongen, J. L. J.; Janssen, R. A. J.; Cornil, J.; Brédas, J.-L. Redox States of Long Oligothiophenes: Two Polarons on a Single Chain. *Chem. Eur. J.* **1998**, *4*, 1509.

(43) Lin, C.; Endo, T.; Takase, M.; Iyoda, M.; Nishinaga, T. Structural, Optical, and Electronic Properties of a Series of 3,4-Propylenedioxythiophene Oligomers in Neutral and Various Oxidation States. *J. Am. Chem. Soc.* **2011**, *133*, 11339.

(44) Hermann, J. P.; Ducuing, J. Third-order Polarizabilities of Long-Chain Molecules. *J. Appl. Phys.* **1974**, *45*, 5100.

(45) Nalwa, H. S. Organic Materials for Third-Order Nonlinear Optics. *Adv. Mater.* **1993**, *5*, 341.

(46) Beljonne, D.; Shuai, Z.; Brédas, J. L. Theoretical study of thiophene oligomers: Electronic excitations, relaxation energies, and nonlinear optical properties. *J. Chem. Phys.* **1993**, *98*, 8819.

(47) Turbiez, M.; Frère, P.; Roncali, J. Stable and Soluble Oligo(3,4-ethylenedioxythiophene)s End-Capped with Alkyl Chains. *J. Org. Chem.* **2003**, *68*, 5357.

(48) Baughman, R. H.; Shacklette, L. W. Conductivity as a function of conjugation length: Theory and experiment for conducting polymer complexes. *Phys. Rev. B* **1989**, *39*, 5872.

(49) Baughman, R. H.; Shacklette, L. W. Conjugation length dependent transport in conducting polymers from a resistor network model. *J. Chem. Phys.* **1989**, *90*, 7492.

(50) Roncali, J. Conjugated poly(thiophenes): synthesis, functionalization, and applications. *Chem. Rev.* **1992**, *92*, 711.

(51) Coppo, P.; Turner, M. L. Cyclopentadithiophene based electroactive materials. *J. Mater. Chem.* **2005**, *15*, 1123.

(52) Yum, S.; An, T. K.; Wang, X.; Lee, W.; Uddin, M. A.; Kim, Y. J.; Nguyen, T. L.; Xu, S.; Hwang, S.; Park, C. E.; Woo, H. Y. Benzotriazole-Containing Planar Conjugated Polymers with Noncovalent Conformational Locks for Thermally

Stable and Efficient Polymer Field-Effect Transistors. *Chem. Mater.* **2014**, *26*, 2147.

(53) Wijsboom, Y. H.; Sheynin, Y.; Patra, A.; Zamoshchik, N.; Vardimon, R.; Leitus, G.; Bendikov, M. Tuning of electronic properties and rigidity in PEDOT analogs. *J. Mater. Chem.* **2011**, *21*, 1368.

(54) Breza, M.; Lukeš, V.; Vrábel, I. On the dependence of optical properties on conformational changes in oligothiophenes I. Electron absorption spectra. *Journal of Molecular Structure: THEOCHEM* **2001**, *572*, 151.

(55) Barbarella, G.; Zambianchi, M.; Bongini, A. Conformation and optical absorption properties of thiophene oligomers: 13C-NMR, UV, and MMP2 calculations of Di- and tetramethyl-quaterthiophenes. *Adv. Mater.* **1991**, *3*, 494.

(56) Brédas, J. L.; Street, G. B.; Thémans, B.; André, J. M. Organic polymers based on aromatic rings (polyparaphenylene, polypyrrole, polythiophene): Evolution of the electronic properties as a function of the torsion angle between adjacent rings. *J. Chem. Phys.* **1985**, *83*, 1323.

(57) Koch, N.; Heimel, G.; Wu, J.; Zojer, E.; Johnson, R. L.; Brédas, J.-L.; Müllen, K.; Rabe, J. P. Influence of molecular conformation on organic/metal interface energetics. *Chem. Phys. Lett.* **2005**, *413*, 390.

(58) Darling, S. B. Isolating the Effect of Torsional Defects on Mobility and Band Gap in Conjugated Polymers. *J. Phys. Chem. B* **2008**, *112*, 8891.

(59) Grabowski, Z. R.; Rotkiewicz, K.; Rettig, W. Structural Changes Accompanying Intramolecular Electron Transfer: Focus on Twisted Intramolecular Charge-Transfer States and Structures. *Chem. Rev.* **2003**, *103*, 3899.

(60) Sen, R.; Majumdar, D.; Bhattacharyya, S. P.; Bhattacharyya, S. N. MODELING HYPERPOLARIZABILITIES OF SOME TICT MOLECULES AND THEIR ANALOGS. *J. Phys. Chem.* **1993**, *97*, 7491.

(61) Albert, I. D. L.; Marks, T. J.; Ratner, M. A. Conformationally-Induced Geometric Electron Localization. Interrupted Conjugation, Very Large Hyperpolarizabilities, and Sizable Infrared Absorption in Simple Twisted Molecular Chromophores. *J. Am. Chem. Soc.* **1997**, *119*, 3155.

(62) Zhou, H.; Yang, L.; You, W. Rational Design of High Performance Conjugated Polymers for Organic Solar Cells. *Macromolecules* **2012**, *45*, 607.

(63) Roncali, J.; Blanchard, P.; Frere, P. 3,4-Ethylenedioxythiophene (EDOT) as a versatile building block for advanced functional [small pi]-conjugated systems. *J. Mater. Chem.* **2005**, *15*, 1589.

(64) Groenendaal, L.; Jonas, F.; Freitag, D.; Pielartzik, H.; Reynolds, J. R. Poly(3,4-ethylenedioxythiophene) and Its Derivatives: Past, Present, and Future. *Adv. Mater.* **2000**, *12*, 481.

(65) Groenendaal, L.; Zotti, G.; Aubert, P. H.; Waybright, S. M.; Reynolds, J. R. Electrochemistry of Poly(3,4-alkylenedioxythiophene) Derivatives. *Adv. Mater.* **2003**, *15*, 855.

(66) Havinga, E. E.; ten Hoeve, W.; Wynberg, H. A new class of small band gap organic polymer conductors. *Polym. Bull.* **1992**, *29*, 119.

(67) Havinga, E. E.; ten Hoeve, W.; Wynberg, H. Alternate donor-acceptor small-band-gap semiconducting polymers; Polysquaraines and polycroconaines. *Synth. Met.* **1993**, *55*, 299.

(68) van Mullekom, H. A. M.; Vekemans, J. A. J. M.; Havinga, E. E.; Meijer, E. W. Developments in the chemistry and band gap engineering of donor–acceptor substituted conjugated polymers. *Materials Science and Engineering: R: Reports* **2001**, *32*, 1.

(69) Salzner, U. Effect of Donor–Acceptor Substitution on Optoelectronic Properties of Conducting Organic Polymers. *Journal of Chemical Theory and Computation* **2014**, *10*, 4921.

(70) Albert, I. D. L.; Marks, T. J.; Ratner, M. A. Large molecular hyperpolarizabilities. Quantitative analysis of aromaticity and auxiliary donor-acceptor effects. *J. Am. Chem. Soc.* **1997**, *119*, 6575.

(71) Ellinger, S.; Graham, K. R.; Shi, P.; Farley, R. T.; Steckler, T. T.; Brookins, R. N.; Taranekar, P.; Mei, J.; Padilha, L. A.; Ensley, T. R.; Hu, H.; Webster, S.; Hagan, D. J.; Van Stryland, E. W.; Schanze, K. S.; Reynolds, J. R. Donor–Acceptor–Donor-based π-Conjugated Oligomers for Nonlinear Optics and Near-IR Emission. *Chem. Mater.* **2011**, *23*, 3805.

(72) Amb, C. M.; Dyer, A. L.; Reynolds, J. R. Navigating the Color Palette of Solution-Processable Electrochromic Polymers†. *Chem. Mater.* **2011**, *23*, 397.

(73) Dyer, A. L.; Thompson, E. J.; Reynolds, J. R. Completing the Color Palette with Spray-Processable Polymer Electrochromics. *ACS Appl. Mater. Interfaces* **2011**, *3*, 1787.

(74) Beaujuge, P. M.; Vasilyeva, S. V.; Liu, D. Y.; Ellinger, S.; McCarley, T. D.; Reynolds, J. R. Structure-Performance Correlations in Spray-Processable Green Dioxythiophene-Benzothiadiazole Donor–Acceptor Polymer Electrochromes. *Chem. Mater.* **2012**, *24*, 255.

(75) Beaujuge, P. M.; Ellinger, S.; Reynolds, J. R. The donor-acceptor approach allows a black-to-transmissive switching polymeric electrochrome. *Nature materials* **2008**, *7*, 795.

(76) Shi, P.; Amb, C. M.; Knott, E. P.; Thompson, E. J.; Liu, D. Y.; Mei, J.; Dyer, A. L.; Reynolds, J. R. Broadly Absorbing Black to Transmissive Switching Electrochromic Polymers. *Adv. Mater.* **2010**, *22*, 4949.

(77) Brédas, J. L. Relationship between band gap and bond length alternation in organic conjugated polymers. *J. Chem. Phys.* **1985**, *82*, 3808.

(78) Casado, J.; Ortiz, R. P.; Ruiz Delgado, M. C.; Hernández, V.; López Navarrete, J. T.; Raimundo, J.-M.; Blanchard, P.; Allain, M.; Roncali, J. Alternated Quinoid/Aromatic Units in Terthiophenes Building Blocks for Electroactive Narrow Band Gap Polymers. Extended Spectroscopic, Solid State, Electrochemical, and Theoretical Study. *J. Phys. Chem. B* **2005**, *109*, 16616.

(79) Bérubé, N.; Gaudreau, J.; Côté, M. Low Band Gap Polymers Design Approach Based on a Mix of Aromatic and Quinoid Structures. *Macromolecules* **2013**, *46*, 6873.

(80) Roncali, J. Molecular Engineering of the Band Gap of π-Conjugated Systems: Facing Technological Applications. *Macromol. Rapid Commun.* **2007**, *28*, 1761.

(81) Wudl, F.; Kobayashi, M.; Heeger, A. J. Poly(isothianaphthene). *J. Org. Chem.* **1984**, *49*, 3382.

(82) Kobayashi, M.; Colaneri, N.; Boysel, M.; Wudl, F.; Heeger, A. J. The electronic and electrochemical properties of poly(isothianaphthene). *J. Chem. Phys.* **1985**, *82*, 5717.

(83) Andreu, R.; Blesa, M. J.; Carrasquer, L.; Garin, J.; Orduna, J.; Villacampa, B.; Alcala, R.; Casado, J.; Delgado, M. C. R.; Navarrete, J. T. L.; Allain, M. Tuning first molecular hyperpolarizabilities through the use of proaromatic spacers. *J. Am. Chem. Soc.* **2005**, *127*, 8835.

(84) Hoeben, F. J. M.; Jonkheijm, P.; Meijer, E. W.; Schenning, A. P. H. J. About Supramolecular Assemblies of π-Conjugated Systems. *Chem. Rev.* **2005**, *105*, 1491.

(85) Garnier, F. Organic-Based Electronics à la Carte. *Acc. Chem. Res.* **1999**, *32*, 209.

(86) Davydov, A. S. THE THEORY OF MOLECULAR EXCITONS. *Soviet Physics Uspekhi* **1964**, *7*, 145.

(87) Kirstein, S.; Möhwald, H. Herringbone structure in two-dimensional single crystals of cyanine dyes. II. Optical properties. *J. Chem. Phys.* **1995**, *103*, 826.

(88) Mishra, A.; Behera, R. K.; Behera, P. K.; Mishra, B. K.; Behera, G. B. Cyanines during the 1990s: A Review. *Chem. Rev.* **2000**, *100*, 1973.

(89) Grenier, C. R. G. Ph.D. Dissertation, University of Florida, 2006.

(90) Nguyen, T.-Q.; Doan, V.; Schwartz, B. J. Conjugated polymer aggregates in solution: Control of interchain interactions. *J. Chem. Phys.* **1999**, *110*, 4068.

(91) Brown, P. J.; Thomas, D. S.; Köhler, A.; Wilson, J. S.; Kim, J.-S.; Ramsdale, C. M.; Sirringhaus, H.; Friend, R. H. Effect of interchain interactions on the absorption and emission of poly(3-hexylthiophene). *Phys. Rev. B* **2003**, *67*, 064203.

(92) Beaujuge, P. M.; Amb, C. M.; Reynolds, J. R. A Side-Chain Defunctionalization Approach Yields a Polymer Electrochrome Spray-Processable from Water. *Adv. Mater.* **2010**, *22*, 5383.

(93) Nielsen, C. B.; Angerhofer, A.; Abboud, K. A.; Reynolds, J. R. Discrete photopatternable pi-conjugated oligomers for electrochromic devices. *J. Am. Chem. Soc.* **2008**, *130*, 9734.

(94) Shirota, Y. Organic materials for electronic and optoelectronic devices. *J. Mater. Chem.* **2000**, *10*, 1.

(95) Saragi, T. P. I.; Spehr, T.; Siebert, A.; Fuhrmann-Lieker, T.; Salbeck, J. Spiro Compounds for Organic Optoelectronics. *Chem. Rev.* **2007**, *107*, 1011.

(96) Jørgensen, M.; Norrman, K.; Krebs, F. C. Stability/degradation of polymer solar cells. *Sol. Energy Mater. Sol. Cells* **2008**, *92*, 686.

(97) Katz, H. E.; Bao, Z.; Gilat, S. L. Synthetic Chemistry for Ultrapure, Processable, and High-Mobility Organic Transistor Semiconductors. *Acc. Chem. Res.* **2001**, *34*, 359.

(98) Cheng, Y.-J.; Luh, T.-Y. Synthesizing optoelectronic heteroaromatic conjugated polymers by cross-coupling reactions. *J. Organomet. Chem.* **2004**, *689*, 4137.

(99) Cheng, Y.-J.; Yang, S.-H.; Hsu, C.-S. Synthesis of Conjugated Polymers for Organic Solar Cell Applications. *Chem. Rev.* **2009**, *109*, 5868.

(100) Pron, A.; Gawrys, P.; Zagorska, M.; Djurado, D.; Demadrille, R. Electroactive materials for organic electronics: preparation strategies, structural aspects and characterization techniques. *Chem. Soc. Rev.* **2010**, *39*, 2577.

(101) Miyaura, N.; Suzuki, A. PALLADIUM-CATALYZED CROSS-COUPLING REACTIONS OF ORGANOBORON COMPOUNDS. *Chem. Rev.* **1995**, *95*, 2457.

(102) Suzuki, A. Recent advances in the cross-coupling reactions of organoboron derivatives with organic electrophiles, 1995–1998. *J. Organomet. Chem.* **1999**, *576*, 147.

(103) Suzuki, A. Organoborane coupling reactions (Suzuki coupling). *Proceedings of the Japan Academy Series B-Physical and Biological Sciences* **2004**, *80*, 359.

(104) Martin, R.; Buchwald, S. L. Palladium-Catalyzed Suzuki−Miyaura Cross-Coupling Reactions Employing Dialkylbiaryl Phosphine Ligands. *Acc. Chem. Res.* **2008**, *41*, 1461.

(105) Beaumard, F.; Dauban, P.; Dodd, R. H. One-Pot Double Suzuki−Miyaura Couplings: Rapid Access to Nonsymmetrical Tri(hetero)aryl Derivatives. *Org. Lett.* **2009**, *11*, 1801.

(106) Suzuki, A. Cross-Coupling Reactions Of Organoboranes: An Easy Way To Construct C□C Bonds (Nobel Lecture). *Angew. Chem. Int. Ed.* **2011**, *50*, 6722.

(107) Bao, Z.; Chan, W. K.; Yu, L. Exploration of the Stille Coupling Reaction for the Synthesis of Functional Polymers. *J. Am. Chem. Soc.* **1995**, *117*, 12426.

(108) Carsten, B.; He, F.; Son, H. J.; Xu, T.; Yu, L. Stille Polycondensation for Synthesis of Functional Materials. *Chem. Rev.* **2011**, *111*, 1493.

(109) Mkhalid, I. A. I.; Barnard, J. H.; Marder, T. B.; Murphy, J. M.; Hartwig, J. F. C−H Activation for the Construction of C−B Bonds. *Chem. Rev.* **2009**, *110*, 890.

(110) Wencel-Delord, J.; Glorius, F. C-H bond activation enables the rapid construction and late-stage diversification of functional molecules. *Nat Chem* **2013**, *5*, 369.

(111) Alberico, D.; Scott, M. E.; Lautens, M. Aryl−Aryl Bond Formation by Transition-Metal-Catalyzed Direct Arylation. *Chem. Rev.* **2007**, *107*, 174.

(112) McGlacken, G. P.; Bateman, L. M. Recent advances in aryl-aryl bond formation by direct arylation. *Chem. Soc. Rev.* **2009**, *38*, 2447.

(113) Schipper, D. J.; Fagnou, K. Direct Arylation as a Synthetic Tool for the Synthesis of Thiophene-Based Organic Electronic Materials. *Chem. Mater.* **2011**, *23*, 1594.

(114) Facchetti, A.; Vaccaro, L.; Marrocchi, A. Semiconducting Polymers Prepared by Direct Arylation Polycondensation. *Angew. Chem. Int. Ed.* **2012**, *51*, 3520.

(115) Okamoto, K.; Zhang, J.; Housekeeper, J. B.; Marder, S. R.; Luscombe, C. K. C–H Arylation Reaction: Atom Efficient and Greener Syntheses of π-Conjugated Small Molecules and Macromolecules for Organic Electronic Materials. *Macromolecules* **2013**, *46*, 8059.

(116) Estrada, L. A.; Deininger, J. J.; Kamenov, G. D.; Reynolds, J. R. Direct (Hetero)arylation Polymerization: An Effective Route to 3,4-Propylenedioxythiophene-Based Polymers with Low Residual Metal Content. *ACS Macro Letters* **2013**, *2*, 869.

(117) Kerszulis, J. A., Atlanta, Ga., 2014.

(118) Cardona, C. M.; Li, W.; Kaifer, A. E.; Stockdale, D.; Bazan, G. C. Electrochemical Considerations for Determining Absolute Frontier Orbital Energy Levels of Conjugated Polymers for Solar Cell Applications. *Adv. Mater.* **2011**, *23*, 2367.

(119) Djurovich, P. I.; Mayo, E. I.; Forrest, S. R.; Thompson, M. E. Measurement of the lowest unoccupied molecular orbital energies of molecular organic semiconductors. *Org. Electron.* **2009**, *10*, 515.

(120) Bard, A. J. *Electrochemical methods : fundamentals and applications*; 2nd ed. ed.; New York: Wiley, 2001.

(121) Connelly, N. G.; Geiger, W. E. Chemical Redox Agents for Organometallic Chemistry. *Chem. Rev.* **1996**, *96*, 877.

(122) Dai, A.; Zhou, Y.; Shu, A. L.; Mohapatra, S. K.; Wang, H.; Fuentes-Hernandez, C.; Zhang, Y.; Barlow, S.; Loo, Y.-L.; Marder, S. R.; Kippelen, B.; Kahn, A. Enhanced Charge-Carrier Injection and Collection Via Lamination of Doped Polymer Layers p-Doped with a Solution-Processible Molybdenum Complex. *Adv. Funct. Mater.* **2014**, *24*, 2197.

(123) Tsujimura, T. In *OLED Displays*; John Wiley & Sons, Inc.: 2012, p 5.

(124) Helfrich, W.; Schneider, W. G. Recombination Radiation in Anthracene Crystals. *Phys. Rev. Lett.* **1965**, *14*, 229.

(125) Vincett, P. S.; Barlow, W. A.; Hann, R. A.; Roberts, G. G. Electrical conduction and low voltage blue electroluminescence in vacuum-deposited organic films. *Thin Solid Films* **1982**, *94*, 171.

(126) Tang, C. W.; VanSlyke, S. A. Organic electroluminescent diodes. *Appl. Phys. Lett.* **1987**, *51*, 913.

(127) Chihaya, A.; Shizuo, T.; Tetsuo, T.; Shogo, S. Electroluminescence in Organic Films with Three-Layer Structure. *Jpn. J. Appl. Phys.* **1988**, *27*, L269.

(128) Chihaya, A.; Shizuo, T.; Tetsuo, T.; Shogo, S. Organic Electroluminescent Device with a Three-Layer Structure. *Jpn. J. Appl. Phys.* **1988**, *27*, L713.

(129) Herron, N.; Meng, H. In *Organic Light-Emitting Materials and Devices*; Li, Z. R., Meng, H., Eds.; CRC Press: Boca Raton, FL, 2006, p 296.

(130) Kalinowski, J. In *Organic Light-Emitting Diodes: Principles, Characteristics, and Processes*; CRC Press: New York, NY, 2004, p 171.

(131) Meth, J.; Li, Z.-R. In *Organic Light-Emitting Materials and Devices*; Li, Z.-R., Meng, H., Eds.; CRC Press: Boca Raton, FL, 2006, p 626.

(132) Forrest, S. R.; Bradley, D. D. C.; Thompson, M. E. Measuring the Efficiency of Organic Light-Emitting Devices. *Adv. Mater.* **2003**, *15*, 1043.

(133) Tsutsui, T.; Takada, N. Progress in Emission Efficiency of Organic Light-Emitting Diodes: Basic Understanding and Its Technical Application. *Jpn. J. Appl. Phys.* **2013**, *52*, 110001.

(134) Kalinowski, J. In *Organic Light-Emitting Diodes*; CRC Press: 2004, p 273.

(135) Burrows, P. E.; Shen, Z.; Bulovic, V.; McCarty, D. M.; Forrest, S. R.; Cronin, J. A.; Thompson, M. E. Relationship between electroluminescence and current transport in organic heterojunction light-emitting devices. *J. Appl. Phys.* **1996**, *79*, 7991.

(136) Cornil, J.; Beljonne, D.; Calbert, J. P.; Brédas, J. L. Interchain Interactions in Organic π-Conjugated Materials: Impact on Electronic Structure, Optical Response, and Charge Transport. *Adv. Mater.* **2001**, *13*, 1053.

(137) Hutchison, G. R.; Ratner, M. A.; Marks, T. J. Intermolecular Charge Transfer between Heterocyclic Oligomers. Effects of Heteroatom and Molecular Packing on Hopping Transport in Organic Semiconductors. *J. Am. Chem. Soc.* **2005**, *127*, 16866.

(138) Hutchison, G. R.; Ratner, M. A.; Marks, T. J. Hopping Transport in Conductive Heterocyclic Oligomers: Reorganization Energies and Substituent Effects. *J. Am. Chem. Soc.* **2005**, *127*, 2339.

(139) Perepichka, D. F.; Ling, M.-M.; Meng, H. In *Organic Light-Emitting Materials and Devices*; CRC Press: 2006, p 413.

(140) Marcus, R. A. Electron transfer reactions in chemistry. Theory and experiment. *Rev. Mod. Phys.* **1993**, *65*, 599.

(141) Tatsuo, H.; Jun, T. Organic field-effect transistors using single crystals. *Science and Technology of Advanced Materials* **2009**, *10*, 024314.

(142) Giri, G.; Park, S.; Vosgueritchian, M.; Shulaker, M. M.; Bao, Z. High-Mobility, Aligned Crystalline Domains of TIPS-Pentacene with Metastable Polymorphs Through Lateral Confinement of Crystal Growth. *Adv. Mater.* **2014**, *26*, 487.

(143) Sundar, V. C.; Zaumseil, J.; Podzorov, V.; Menard, E.; Willett, R. L.; Someya, T.; Gershenson, M. E.; Rogers, J. A. Elastomeric Transistor Stamps: Reversible Probing of Charge Transport in Organic Crystals. *Science* **2004**, *303*, 1644.

(144) Feng, X.; Marcon, V.; Pisula, W.; Hansen, M. R.; Kirkpatrick, J.; Grozema, F.; Andrienko, D.; Kremer, K.; Mullen, K. Towards high charge-carrier mobilities by rational design of the shape and periphery of discotics. *Nat. Mater.* **2009**, *8*, 421.

(145) Haddon, R. C.; Perel, A. S.; Morris, R. C.; Palstra, T. T. M.; Hebard, A. F.; Fleming, R. M. C60 thin film transistors. *Appl. Phys. Lett.* **1995**, *67*, 121.

(146) Shirota, Y.; Kageyama, H. Charge Carrier Transporting Molecular Materials and Their Applications in Devices. *Chem. Rev.* **2007**, *107*, 953.

(147) Tao, Y.; Yang, C.; Qin, J. Organic host materials for phosphorescent organic light-emitting diodes. *Chem. Soc. Rev.* **2011**, *40*, 2943.

(148) Thejokalyani, N.; Dhoble, S. J. Novel approaches for energy efficient solid state lighting by RGB organic light emitting diodes – A review. *Renewable and Sustainable Energy Reviews* **2014**, *32*, 448.

(149) Bach, U.; De Cloedt, K.; Spreitzer, H.; Grätzel, M. Characterization of Hole Transport in a New Class of Spiro-Linked Oligotriphenylamine Compounds. *Adv. Mater.* **2000**, *12*, 1060.

(150) Xiao, L.; Chen, Z.; Qu, B.; Luo, J.; Kong, S.; Gong, Q.; Kido, J. Recent Progresses on Materials for Electrophosphorescent Organic Light-Emitting Devices. *Adv. Mater.* **2011**, *23*, 926.

(151) Sasabe, H.; Kido, J. Multifunctional Materials in High-Performance OLEDs: Challenges for Solid-State Lighting. *Chem. Mater.* **2011**, *23*, 621.

(152) Su, S.-J.; Gonmori, E.; Sasabe, H.; Kido, J. Highly Efficient Organic Blue-and White-Light-Emitting Devices Having a Carrier- and Exciton-Confining Structure for Reduced Efficiency Roll-Off. *Adv. Mater.* **2008**, NA.

(153) Baldo, M. A.; Lamansky, S.; Burrows, P. E.; Thompson, M. E.; Forrest, S. R. Very high-efficiency green organic light-emitting devices based on electrophosphorescence. *Appl. Phys. Lett.* **1999**, *75*, 4.

(154) Adachi, C.; Baldo, M. A.; Thompson, M. E.; Forrest, S. R. Nearly 100% internal phosphorescence efficiency in an organic light-emitting device. *J. Appl. Phys.* **2001**, *90*, 5048.

(155) Yeh, S. J.; Wu, M. F.; Chen, C. T.; Song, Y. H.; Chi, Y.; Ho, M. H.; Hsu, S. F.; Chen, C. H. New Dopant and Host Materials for Blue-Light-Emitting Phosphorescent Organic Electroluminescent Devices. *Adv. Mater.* **2005**, *17*, 285.

(156) Reineke, S.; Rosenow, T. C.; Lüssem, B.; Leo, K. Improved High-Brightness Efficiency of Phosphorescent Organic LEDs Comprising Emitter Molecules with Small Permanent Dipole Moments. *Adv. Mater.* **2010**, *22*, 3189.

(157) Yook, K. S.; Lee, J. Y. Small Molecule Host Materials for Solution Processed Phosphorescent Organic Light-Emitting Diodes. *Adv. Mater.* **2014**, *26*, 4218.

(158) Thiessen, A.; Wettach, H.; Meerholz, K.; Neese, F.; Hoger, S.; Hertel, D. Control of electronic properties of triphenylene by substitution. *Org. Electron.* **2012**, *13*, 71.

(159) Kijima, Y.; Asai, N.; Tamura, S.-i. A Blue Organic Light Emitting Diode. *Jpn. J. Appl. Phys.* **1999**, *38*, 5274.

(160) Chaskar, A.; Chen, H. F.; Wong, K. T. Bipolar host materials: a chemical approach for highly efficient electrophosphorescent devices. *Adv. Mater.* **2011**, *23*, 3876.

(161) Brunner, K.; van Dijken, A.; Börner, H.; Bastiaansen, J. J. A. M.; Kiggen, N. M. M.; Langeveld, B. M. W. Carbazole Compounds as Host Materials for Triplet Emitters in Organic Light-Emitting Diodes: Tuning the HOMO Level without Influencing the Triplet Energy in Small Molecules. *J. Am. Chem. Soc.* **2004**, *126*, 6035.

(162) Chaskar, A.; Chen, H.-F.; Wong, K.-T. Bipolar Host Materials: A Chemical Approach for Highly Efficient Electrophosphorescent Devices. *Adv. Mater.* **2011**, *23*, 3876.

(163) Tsuboi, T.; Liu, S.-W.; Wu, M.-F.; Chen, C.-T. Spectroscopic and electrical characteristics of highly efficient tetraphenylsilane-carbazole organic compound as host material for blue organic light emitting diodes. *Org. Electron.* **2009**, *10*, 1372.

(164) Ren, X.; Li, J.; Holmes, R. J.; Djurovich, P. I.; Forrest, S. R.; Thompson, M. E. Ultrahigh Energy Gap Hosts in Deep Blue Organic Electrophosphorescent Devices. *Chem. Mater.* **2004**, *16*, 4743.

(165) Hung, W.-Y.; Wang, T.-C.; Chiu, H.-C.; Chen, H.-F.; Wong, K.-T. A spiro-configured ambipolar host material for impressively efficient single-layer green electrophosphorescent devices. *PCCP* **2010**, *12*, 10685.

(166) Tsuji, H.; Mitsui, C.; Sato, Y.; Nakamura, E. Bis(carbazolyl)benzodifuran: A High-Mobility Ambipolar Material for Homojunction Organic Light-Emitting Diode Devices. *Adv. Mater.* **2009**, *21*, 3776.

(167) Pal, S. K.; Setia, S.; Avinash, B. S.; Kumar, S. Triphenylene-based discotic liquid crystals: recent advances. *Liq. Cryst.* **2013**, *40*, 1769.

(168) Togashi, K.; Nomura, S.; Yokoyama, N.; Yasuda, T.; Adachi, C. Low driving voltage characteristics of triphenylene derivatives as electron transport materials in organic light-emitting diodes. *J. Mater. Chem.* **2012**, *22*, 20689.

(169) Saleh, M.; Park, Y.-S.; Baumgarten, M.; Kim, J.-J.; Müllen, K. Conjugated Triphenylene Polymers for Blue OLED Devices. *Macromol. Rapid Commun.* **2009**, *30*, 1279.

(170) Lemaur, V.; da Silva Filho, D. A.; Coropceanu, V.; Lehmann, M.; Geerts, Y.; Piris, J.; Debije, M. G.; van de Craats, A. M.; Senthilkumar, K.; Siebbeles, L. D. A.; Warman, J. M.; Brédas, J.-L.; Cornil, J. Charge Transport Properties in Discotic Liquid Crystals: A Quantum-Chemical Insight into Structure−Property Relationships. *J. Am. Chem. Soc.* **2004**, *126*, 3271.

(171) Bock, H.; Rajaoarivelo, M.; Clavaguera, S.; Grelet, É. An Efficient Route to Stable Room-Temperature Liquid-Crystalline Triphenylenes. *Eur. J. Org. Chem.* **2006**, *2006*, 2889.

(172) Kumar, S. Triphenylene-based discotic liquid crystal dimers, oligomers and polymers. *Liq. Cryst.* **2005**, *32*, 1089.

(173) El Mansoury, A.; Bushby, R. J.; Karodia, N. Triphenylene-based discotic liquid crystals: star-shaped oligomers and branched-chain polymers. *Liq. Cryst.* **2012**, *39*, 1222.

(174) Adam, D.; Schuhmacher, P.; Simmerer, J.; Haussling, L.; Siemensmeyer, K.; Etzbachi, K. H.; Ringsdorf, H.; Haarer, D. Fast photoconduction in the highly ordered columnar phase of a discotic liquid crystal. *Nature* **1994**, *371*, 141.

(175) Iino, H.; Takayashiki, Y.; Hanna, J.-i.; Bushby, R. J.; Haarer, D. High electron mobility of 0.1cm2V−1s−1 in the highly ordered columnar phase of hexahexylthiotriphenylene. *Appl. Phys. Lett.* **2005**, *87*, 192105.

(176) Herkstroeter, W. G.; Lamola, A. A.; Hammond, G. S. Mechaisms of Photochemical Reactions in Solution. XXVIII.1 Values of Triplet Excitation energies of Selected Sensitizers. *J. Am. Chem. Soc.* **1964**, *86*, 4537.

(177) Murov, S. L.; Hug, G. L.; Carmichael, I. *Handbook of Photochemistry*; M. Dekker: New York, 1993.

(178) Watson, M. D.; Fechtenkötter, A.; Müllen, K. Big Is Beautiful−"Aromaticity" Revisited from the Viewpoint of Macromolecular and Supramolecular Benzene Chemistry. *Chem. Rev.* **2001**, *101*, 1267.

(179) Togashi, K.; Yasuda, T.; Adachi, C. Triphenylene-based Host Materials for Low-voltage, Highly Efficient Red Phosphorescent Organic Light-emitting Diodes. *Chem. Lett.* **2013**, *42*, 383.

(180) Lee, N.-J.; Jeon, J. H.; In, I.; Lee, J.-H.; Suh, M. C. Triphenylene containing host materials with high thermal stability for green phosphorescent organic light emitting diode. *Dyes and Pigments* **2014**, *101*, 221.

(181) Adamovich, V.; Weaver, M. S.; D'Andrade, B. (Universal Display Corporation). Long lifetime phosphorescent organic light emitting device (OLED) structures. Pat. Appl. WO 2007-IB4687, 2009.

(182) Miyake, Y.; Wu, M.; Rahman, M. J.; Kuwatani, Y.; Iyoda, M. Efficient construction of biaryls and macrocyclic cyclophanes via electron-transfer oxidation of Lipshutz cuprates. *J. Org. Chem.* **2006**, *71*, 6110.

(183) Perez, D.; Guitian, E. Selected strategies for the synthesis of triphenylenes. *Chem. Soc. Rev.* **2004**, *33*, 274.

(184) Jayanth, T. T.; Cheng, C.-H. Palladium-catalyzed carbopalladation and carbocyclization of arynes with aryl halides: a highly efficient route to functionalized triphenylenes. *Chem. Commun.* **2006**, 894.

(185) Iwasaki, M.; Iino, S.; Nishihara, Y. Palladium-Catalyzed Annulation of o-Iodobiphenyls with o-Bromobenzyl Alcohols: Synthesis of Functionalized Triphenylenes via C–C and C–H Bond Cleavages. *Org. Lett.* **2013**, *15*, 5326.

(186) Romero, C.; Peña, D.; Pérez, D.; Guitián, E. Synthesis of Extended Triphenylenes by Palladium-Catalyzed [2+2+2] Cycloaddition of Triphenylynes. *Chem. Eur. J.* **2006**, *12*, 5677.

(187) Tamura, H.; Yamazaki, H.; Sato, H.; Sakaki, S. Iridium-Catalyzed Borylation of Benzene with Diboron. Theoretical Elucidation of Catalytic Cycle Including Unusual Iridium(V) Intermediate. *J. Am. Chem. Soc.* **2003**, *125*, 16114.

(188) Vanchura, I. I. B. A.; Preshlock, S. M.; Roosen, P. C.; Kallepalli, V. A.; Staples, R. J.; Maleczka, J. R. E.; Singleton, D. A.; Smith, I. I. I. M. R. Electronic effects in iridium C-H borylations: insights from unencumbered substrates and variation of boryl ligand substituents. *Chem. Commun.* **2010**, *46*, 7724.

(189) Liao, Y. Z.; Strong, V.; Wang, Y.; Li, X.-G.; Wang, X.; Kaner, R. B. Oligotriphenylene Nanofiber Sensors for Detection of Nitro-Based Explosives. *Adv. Funct. Mater.* **2012**, *22*, 726.

(190) Hitosugi, S.; Tanimoto, D.; Nakanishi, W.; Isobe, H. A Facile Chromatographic Method for Purification of Pinacol Boronic Esters. *Chem. Lett.* **2012**, *41*, 972.

(191) Coventry, D. N.; Batsanov, A. S.; Goeta, A. E.; Howard, J. A. K.; Marder, T. B.; Perutz, R. N. Selective Ir-catalysed borylation of polycyclic aromatic hydrocarbons: structures of naphthalene-2,6-bis(boronate), pyrene-2,7-bis(boronate) and perylene-2,5,8,11-tetra(boronate) esters. *Chem. Commun.* **2005**, 2172.

(192) Chaudhuri, D.; Wettach, H.; van Schooten, K. J.; Liu, S.; Sigmund, E.; Hoger, S.; Lupton, J. M. Tuning the singlet-triplet gap in metal-free phosphorescent pi-conjugated polymers. *Angew. Chem. Int. Ed. Engl.* **2010**, *49*, 7714.

(193) Salman, S.; Kim, D.; Coropceanu, V.; Brédas, J.-L. Theoretical Investigation of Triscarbazole Derivatives As Host Materials for Blue Electrophosphorescence: Effects of Topology. *Chem. Mater.* **2011**, *23*, 5223.

(194) Su, S.-J.; Cai, C.; Takamatsu, J.; Kido, J. A host material with a small singlet–triplet exchange energy for phosphorescent organic light-emitting diodes: Guest, host, and exciplex emission. *Org. Electron.* **2012**, *13*, 1937.

(195) Hashimoto, S.; Ikuta, T.; Shiren, K.; Nakatsuka, S.; Ni, J.; Nakamura, M.; Hatakeyama, T. Triplet-Energy Control of Polycyclic Aromatic Hydrocarbons by BN Replacement: Development of Ambipolar Host Materials for Phosphorescent Organic Light-Emitting Diodes. *Chem. Mater.* **2014**, *26*, 6265.

(196) Ban, X.; Jiang, W.; Sun, K.; Yang, H.; Miao, Y.; Yang, F.; Sun, Y.; Huang, B.; Duan, L. Systematically tuning the [capital Delta]EST and charge balance property of bipolar hosts for low operating voltage and high power efficiency solution-processed electrophosphorescent devices. *J. Mater. Chem. C* **2015**, *3*, 5004.

(197) Kociper, B.; Niehaus, T. A. Spatial Extension of Excitons in Triphenylene-Based Polymers Given by Range-Separated Functionals. *J. Phys. Chem. C* **2013**, *117*, 26213.

(198) Cai, M.; Xiao, T.; Hellerich, E.; Chen, Y.; Shinar, R.; Shinar, J. High-Efficiency Solution-Processed Small Molecule Electrophosphorescent Organic Light-Emitting Diodes. *Adv. Mater.* **2011**, *23*, 3590.

(199) Sasabe, H.; Kido, J. Recent Progress in Phosphorescent Organic Light-Emitting Devices. *Eur. J. Org. Chem.* **2013**, *2013*, 7653.

(200) Baldo, M. A.; Adachi, C.; Forrest, S. R. Transient analysis of organic electrophosphorescence. II. Transient analysis of triplet-triplet annihilation. *Phys. Rev. B* **2000**, *62*, 10967.

(201) Adamovich, V. I.; Cordero, S. R.; Djurovich, P. I.; Tamayo, A.; Thompson, M. E.; D'Andrade, B. W.; Forrest, S. R. New charge-carrier blocking materials for high efficiency OLEDs. *Org. Electron.* **2003**, *4*, 77.

(202) Goushi, K.; Yoshida, K.; Sato, K.; Adachi, C. Organic light-emitting diodes employing efficient reverse intersystem crossing for triplet-to-singlet state conversion. *Nature Photonics* **2012**, *6*, 253.

(203) Rehmann, N.; Hertel, D.; Meerholz, K.; Becker, H.; Heun, S. Highly efficient solution-processed phosphorescent multilayer organic light-emitting diodes based on small-molecule hosts. *Appl. Phys. Lett.* **2007**, *91*, 103507.

(204) New, G. *Introduction to Nonlinear Optics*; Cambridge University Press: Cambridge, UK, 2011.

(205) Franken, P. A.; Hill, A. E.; Peters, C. W.; Weinreich, G. Generation of Optical Harmonics. *Phys. Rev. Lett.* **1961**, *7*, 118.

(206) Meyers, F.; Marder, S. R.; Perry, J. W. In *Chemistry of Advanced Materials : An Overview*; Interrante, L. V., Hampden-Smith, M. J., Eds.; New York: Wiley-VCH, 1998, p 207.

(207) Bredas, J. L.; Adant, C.; Tackx, P.; Persoons, A.; Pierce, B. M. Third-Order Nonlinear Optical Response in Organic Materials: Theoretical and Experimental Aspects. *Chem. Rev.* **1994**, *94*, 243.

(208) Prasad, P. N.; Reinhardt, B. A. Is there a role for organic materials chemistry in nonlinear optics and photonics? *Chem. Mater.* **1990**, *2*, 660.

(209) Bosshard, C.; Sutter, K.; Pretre, P.; Hulliger, J.; Florsheimer, M.; Kaatz, P.; Gunter, P. In *Advances in Nonlinear Optics* Garito, A. F., Ed.; Gordon and Breach: Basel, Switzerland, 1995; Vol. 1.

(210) Hermann, J. P.; Ricard, D.; Ducuing, J. Optical Nonlinearities in Conjugated Systems: Beta-Carotene. *Appl. Phys. Lett.* **1973**, *23*, 178.

(211) Hermann, J. P.; Rustagi, K. C.; Ducuing, J. Third-order Optical Polarizability of Conjugated Organic Molecules. *IEEE J. Quantum Electron.* **1974**, *QE10*, 769.

(212) Zhao, M. T.; Singh, B. P.; Prasad, P. N. A systematic study of polarizability and microscopic third-order optical nonlinearity in thiophene oligomers. *J. Chem. Phys.* **1988**, *89*, 5535.

(213) Jenekhe, S. A.; Lo, S. K.; Flom, S. R. Third-order nonlinear optical properties of a soluble conjugated polythiophene derivative. *Appl. Phys. Lett.* **1989**, *54*, 2524.

(214) Torruellas, W. E.; Neher, D.; Zanoni, R.; Stegeman, G. I.; Kajzar, F.; Leclerc, M. Dispersion measurements of the third-order nonlinear susceptibility of polythiophene thin films. *Chem. Phys. Lett.* **1990**, *175*, 11.

(215) Singh, B. P.; Prasad, P. N.; Karasz, F. E. Third-order non-linear optical properties of oriented films of poly(p-phenylene vinylene) investigated by femtosecond degenerate four wave mixing. *Polymer* **1988**, *29*, 1940.

(216) Samoc, A.; Samoc, M.; Woodruff, M.; Luther-Davies, B. Tuning the properties of poly(p-phenylenevinylene) for use in all-optical switching. *Opt. Lett.* **1995**, *20*, 1241.

(217) Oudar, J. L.; Chemla, D. S. Hyperpolarizabilities of Nitroanilines and Their Relations to Excited-State Dipole Moment. *J. Chem. Phys.* **1977**, *66*, 2664.

(218) Oudar, J. L. Optical Nonlinearities of Conjugated Molecules: Stilbene Dervatives and Highly Polar Aromatic Compounds. *J. Chem. Phys.* **1977**, *67*, 446.

(219) Marder, S. R.; Beratan, D. N.; Cheng, L. T. Approaches fo Optimizing the First Electronic Hyperpolarizability of Conjugated Organic Molecules. *Science* **1991**, *252*, 103.

(220) Meyers, F.; Marder, S. R.; Pierce, B. M.; Bredas, J. L. Electric Field Modulated Nonlinear Optical Properties of Donor-Acceptor Polyenes: Sum-Over-States Investigation of the Relationship Between Molecular Polarizabilities (a, b, and c) and Bond Length Alternation. *J. Am. Chem. Soc.* **1994**, *116*, 10703.

(221) Gorman, C. B.; Marder, S. R. Effect of Molecular Polarization on Bond-Length Alternation, Linear Polarizability, First and Second Hyperpolarizability In Donor-Acceptor Polyenes as a Function of Chain Length. *Chem. Mater.* **1995**, *7*, 215.

(222) Marder, S. R.; Kippelen, B.; Jen, A. K. Y.; Peyghambarian, N. Design and synthesis of chromophores and polymers for electro-optic and photorefractive applications. *Nature* **1997**, *388*.

(223) Ahlheim, M.; Barzoukas, M.; Bedworth, P. V.; Blanchard-Desce, M.; Fort, A.; Hu, Z.-Y.; Marder, S. R.; Perry, J. W.; Runser, C.; Staehelin, M.; Zysset, B. Chromophores with Strong Heterocyclic Acceptors: A Poled Polymer with a Large Electro-Optic Coefficient. *Science* **1996**, *271*, 335.

(224) Hales, J. M.; Barlow, S.; Kim, H.; Mukhopadhyay, S.; Brédas, J.-L.; Perry, J. W.; Marder, S. R. Design of Organic Chromophores for All-Optical Signal Processing Applications. *Chem. Mater.* **2014**, *26*, 549.

(225) Hales, J. M.; Matichak, J.; Barlow, S.; Ohira, S.; Yesudas, K.; Bredas, J. L.; Perry, J. W.; Marder, S. R. Design of Polymethine Dyes with Large Third-Order Optical Nonlinearities and Loss Figures of Merit. *Science* **2010**, *327*, 1485.

(226) Albert, I. D. L.; Marks, T. J.; Ratner, M. A. Large Molecular Hyperpolarizabilities in "Push−Pull" Porphyrins. Molecular Planarity and Auxiliary Donor−Acceptor Effects. *Chem. Mater.* **1998**, *10*, 753.

(227) Albert, I. D. L.; Marks, T. J.; Ratner, M. A. Remarkable NLO response and infrared absorption in simple twisted molecular pi-chromophores. *J. Am. Chem. Soc.* **1998**, *120*, 11174.

(228) He, G. S.; Zhu, J.; Baev, A.; Samoc, M.; Frattarelli, D. L.; Watanabe, N.; Facchetti, A.; Agren, H.; Marks, T. J.; Prasad, P. N. Twisted pi-System Chromophores for All-Optical Switching. *J. Am. Chem. Soc.* **2011**, *133*, 6675.

(229) Shi, Y.; Lou, A. J. T.; He, G. S.; Baev, A.; Swihart, M. T.; Prasad, P. N.; Marks, T. J. Cooperative Coupling of Cyanine and Tictoid Twisted π-Systems to Amplify Organic Chromophore Cubic Nonlinearities. *J. Am. Chem. Soc.* **2015**, *137*, 4622.

(230) Keinan, S.; Zojer, E.; Bredas, J. L.; Ratner, M. A.; Marks, T. J. Twisted pi-system electro-optic chromophores. A CIS vs. MRD-CI theoretical investigation. *Theochem-J. Mol. Struct.* **2003**, *633*, 227.

(231) Isborn, C. M.; Davidson, E. R.; Robinson, B. H. Ab Initio Diradical/Zwitterionic Polarizabilities and Hyperpolarizabilities in Twisted Double Bonds. *J. Phys. Chem. A* **2006**, *110*, 7189.

(232) Brown, E. C.; Marks, T. J.; Ratner, M. A. Nonlinear response properties of ultralarge hyperpolarizability twisted pi-system donor-acceptor chromophores. Dramatic environmental effects on response. *J. Phys. Chem. B* **2008**, *112*, 44.

(233) Nakano, M.; Kishi, R.; Nitta, T.; Kubo, T.; Nakasuji, K.; Kamada, K.; Ohta, K.; Champagne, B.; Botek, E.; Yamaguchi, K. Second Hyperpolarizability (γ) of Singlet Diradical System: Dependence of γ on the Diradical Character. *J. Phys. Chem. A* **2005**, *109*, 885.

(234) Kang, H.; Facchetti, A.; Jiang, H.; Cariati, E.; Righetto, S.; Ugo, R.; Zuccaccia, C.; Macchioni, A.; Stern, C. L.; Liu, Z. F.; Ho, S. T.; Brown, E. C.; Ratner, M. A.; Marks, T. J. Ultralarge hyperpolarizability twisted pi-electron system electro-optic chromophores: Synthesis, solid-state and solution-phase structural characteristics, electronic structures, linear and nonlinear optical properties, and computational studies. *J. Am. Chem. Soc.* **2007**, *129*, 3267.

(235) Albert, I. D. L.; Marks, T. J.; Ratner, M. A. Large Molecular Hyperpolarizabilities. Quantitative Analysis of Aromaticity and Auxiliary Donor−Acceptor Effects. *J. Am. Chem. Soc.* **1997**, *119*, 6575.

(236) Gorman, C. B.; Marder, S. R. An investigation of the interrelationships between linear and nonlinear polarizabilities and bond-length alternation in conjugated organic molecules. *Proc. Natl. Acad. Sci.* **1993**, *90*, 11297.

(237) Marder, S. R.; Gorman, C. B.; Meyers, F.; Perry, J. W.; Bourhill, G.; Brédas, J.-L.; Pierce, B. M. A Unified Description of Linear and Nonlinear Polarization in Organic Polymethine Dyes. *Science* **1994**, *265*, 632.

(238) Marder, S. R.; Cheng, L.-T.; Tiemann, B. G.; Friedli, A. C.; Blanchard-Desce, M.; Perry, J. W.; Skindhøj, J. Large First Hyperpolarizabilities in Push-Pull Polyenes by Tuning of the Bond Length Alternation and Aromaticity. *Science* **1994**, *263*, 511.

(239) Meier, H. Conjugated Oligomers with Terminal Donor–Acceptor Substitution. *Angew. Chem. Int. Ed.* **2005**, *44*, 2482.

(240) Rao, V. P.; Jen, A. K. Y.; Wong, K. Y.; Drost, K. J. NOVEL PUSH-PULL THIOPHENES FOR 2ND-ORDER NONLINEAR OPTICAL APPLICATIONS. *Tetrahedron Lett.* **1993**, *34*, 1747.

(241) Morley, J. O. Non-linear optical properties of organic molecules. Part 20. Calculation of the structure, electronic properties and hyperpolarizabilities of donor-acceptor heterocycles containing sulfur, oxygen and nitrogen. *J. Chem. Soc. Perkin Trans. 2* **1995**, 177.

(242) Hutchings, M. G.; Ferguson, I.; McGeein, D. J.; Morley, J. O.; Zyss, J.; Ledoux, I. Quadratic non-linear optical properties of some donor-acceptor substituted thiophenes. *J. Chem. Soc. Perkin Trans. 2* **1995**, 171.

(243) Varanasi, P. R.; Jen, A. K. Y.; Chandrasekhar, J.; Namboothiri, I. N. N.; Rathna, A. The Important Role of Heteroaromatics in the Design of Efficient Second-Order Nonlinear Optical Molecules: Theoretical Investigation on Push−Pull Heteroaromatic Stilbenes. *J. Am. Chem. Soc.* **1996**, *118*, 12443.

(244) Abbotto, A.; Bradamante, S.; Facchetti, A.; Pagani, G. A. Facile, Regioselective Synthesis of Highly Solvatochromic Thiophene-Spaced N-Alkylpyridinium Dicyanomethanides for Second-Harmonic Generation. *J. Org. Chem.* **1997**, *62*, 5755.

(245) Dai, C.; Fu, G. C. The First General Method for Palladium-Catalyzed Negishi Cross-Coupling of Aryl and Vinyl Chlorides: Use of Commercially Available Pd(P(t-Bu)3)2 as a Catalyst. *J. Am. Chem. Soc.* **2001**, *123*, 2719.

(246) Su, W.; Urgaonkar, S.; McLaughlin, P. A.; Verkade, J. G. Highly Active Palladium Catalysts Supported by Bulky Proazaphosphatrane Ligands for Stille Cross-Coupling: Coupling of Aryl and Vinyl Chlorides, Room Temperature Coupling of Aryl Bromides, Coupling of Aryl Triflates, and Synthesis of Sterically Hindered Biaryls. *J. Am. Chem. Soc.* **2004**, *126*, 16433.

(247) Barder, T. E.; Walker, S. D.; Martinelli, J. R.; Buchwald, S. L. Catalysts for Suzuki−Miyaura Coupling Processes: Scope and Studies of the Effect of Ligand Structure. *J. Am. Chem. Soc.* **2005**, *127*, 4685.

(248) Klán, P. Effect of metal ions on the bromination of 3,5-dimethylpyridine-N-oxide in acetic acid. *Monatshefte für Chemie / Chemical Monthly* **1993**, *124*, 327.

(249) Billingsley, K.; Buchwald, S. L. Highly efficient monophosphine-based catalyst for the palladium-catalyzed Suzuki-Miyaura reaction of heteroaryl halides and heteroaryl boronic acids and esters. *J. Am. Chem. Soc.* **2007**, *129*, 3358.

(250) Yin, J.; Rainka, M. P.; Zhang, X.-X.; Buchwald, S. L. A Highly Active Suzuki Catalyst for the Synthesis of Sterically Hindered Biaryls: Novel Ligand Coordination. *J. Am. Chem. Soc.* **2002**, *124*, 1162.

(251) Hartwig, J. F.; Paul, F. Oxidative Addition of Aryl Bromide after Dissociation of Phosphine from a Two-Coordinate Palladium(0) Complex, Bis(tri-o-tolylphosphine)Palladium(0). *J. Am. Chem. Soc.* **1995**, *117*, 5373.

(252) Watanabe, T.; Miyaura, N.; Suzuki, A. Synthesis of Sterically Hindered Biaryls via the Palladium-Catalyzed Cross-Coupling Reaction of Arylboronic Acids or their Esters with Haloarenes. *Synlett* **1992**, *1992*, 207.

(253) Cammidge, A. N.; Crépy, K. V. L. Application of the Suzuki Reaction as the Key Step in the Synthesis of a Novel Atropisomeric Biphenyl Derivative for Use as a Liquid Crystal Dopant. *J. Org. Chem.* **2003**, *68*, 6832.

(254) Szablewski, M. Novel Reactions of TCNQ: Formation of Zwitterions for Nonlinear Optics by Reaction with Enamines. *J. Org. Chem.* **1994**, *59*, 954.

(255) Ashwell, G. J. Photochromic and non-linear optical properties of C16H33P3CNQ and C16H33Q3CNQ Langmuir-Blodgett films. *Thin Solid Films* **1990**, *186*, 155.

(256) Mitin, A. V.; Kashin, A. N.; Beletskaya, I. P. Role of base in palladium-catalyzed arylation of carbanions. *J. Organomet. Chem.* **2004**, *689*, 1085.

(257) Abbotto, A.; Beverina, L.; Bradamante, S.; Facchetti, A.; Klein, C.; Pagani, G. A.; Redi-Abshiro, M.; Wortmann, R. A distinctive example of the cooperative interplay of structure and environment in tuning of intramolecular charge transfer in second-order nonlinear optical chromophores. *Chem. Eur. J.* **2003**, *9*, 1991.

(258) Juchnovski, I. N.; Radomirska, V. B.; Binev, I. G.; Grekova, E. A. Infrared spectra and structure of carbanions : VIII. Mono- and di-alkali metal derivatives of some bis(cyanomethyl)arenes. *J. Organomet. Chem.* **1977**, *128*, 139.

(259) Binev, Y. I.; Georgieva, M. K.; Novkova, S. I. The conversion of phenylpropanedinitrile (phenylmalononitrile) into the carbanion, followed by IR spectra, ab initio and DFT force field calculations. *Spectrochim. Acta A Mol. Biomol. Spectrosc.* **2003**, *59*, 3041.

(260) Milián, B.; Ortí, E.; Hernández, V.; López Navarrete, J. T.; Otsubo, T. Spectroscopic and Theoretical Study of Push−Pull Chromophores Containing Thiophene-Based Quinonoid Structures as Electron Spacers. *J. Phys. Chem. B* **2003**, *107*, 12175.

(261) Ashwell, G. J.; Dawnay, E. J. C.; Kuczynski, A. P.; Szablewski, M.; Sandy, I. M.; Bryce, M. R.; Grainger, A. M.; Hasan, M. Langmuir-Blodgett alignment of zwitterionic optically non-linear D-[small pi]-A materials. *J. Chem. Soc., Faraday Trans.* **1990**, *86*, 1117.

(262) Inoue, S.; Mikami, S.; Aso, Y.; Otsubo, T.; Wada, T.; Sasabe, H. Donor-acceptor-substituted heteroquinoid chromophores as novel nonlinear optics. *Synth. Met.* **1997**, *84*, 395.

(263) Reichardt, C.; Welton, T. In *Solvents and Solvent Effects in Organic Chemistry*; Wiley-VCH Verlag GmbH & Co. KGaA: 2010, p 359.

(264) Benson, H. G.; Murrell, J. N. Some studies of benzenoid-quinonoid resonance. Part 2.-The effect of solvent polarity on the structure and properties of merocyanine dyes. *Journal of the Chemical Society, Faraday Transactions 2: Molecular and Chemical Physics* **1972**, *68*, 137.

(265) Patel, D. G.; Paquette, M. M.; Kopelman, R. A.; Kaminsky, W.; Ferguson, M. J.; Frank, N. L. A Solution- and Solid-State Investigation of Medium Effects on Charge Separation in Metastable Photomerocyanines. *J. Am. Chem. Soc.* **2010**, *132*, 12568.

(266) Wurthner, F.; Archetti, G.; Schmidt, R.; Kuball, H. G. Solvent effect on color, band shape, and charge-density distribution for merocyanine dyes close to the cyanine limit. *Angew. Chem. Int. Edit.* **2008**, *47*, 4529.

(267) Rezende, M. C.; Aracena, A. Electrophilicity and solvatochromic reversal of pyridinium phenolate betaine dyes. *Chem. Phys. Lett.* **2012**, *542*, 147.

(268) Beverina, L.; Pagani, G. A. π-Conjugated Zwitterions as Paradigm of Donor–Acceptor Building Blocks in Organic-Based Materials. *Acc. Chem. Res.* **2013**.

(269) McRae, E. G. Theory of Solvent Effects on Molecular Electronic Spectra. Frequency Shifts. *J. Phys. Chem.* **1957**, *61*, 562.

(270) Suppan, P. Invited review solvatochromic shifts: The influence of the medium on the energy of electronic states. *Journal of Photochemistry and Photobiology A: Chemistry* **1990**, *50*, 293.

(271) Manohara, S. R.; Kumar, V. U.; Shivakumaraiah; Gerward, L. Estimation of ground and excited-state dipole moments of 1, 2-diazines by solvatochromic method and quantum-chemical calculation. *J. Mol. Liq.* **2013**, *181*, 97.

(272) Husain, M. M.; Sindhu, R.; Tandon, H. C. Photophysical properties and estimation of ground and excited state dipole moments of 7-diethylamino and 7-diethylamino-4-methyl coumarin dyes from absorption and emission spectra. *European Journal of Chemistry; Vol 3, No 1 (2012): March 2012* **2012**.

(273) Lehn, J. M. In *Materials for Nonlinear Optics*; American Chemical Society: 1991; Vol. 455, p 436.

(274) Cole, J. M.; Waddell, P. G.; Wilson, C. C.; Howard, J. A. K. Molecular and Supramolecular Origins of Optical Nonlinearity in N-Methylurea. *J. Phys. Chem. C* **2013**, *117*, 25669.

(275) Yitzchaik, S.; Di Bella, S.; Lundquist, P. M.; Wong, G. K.; Marks, T. J. Anomalous Second-Order Nonlinear Optical Response of In-Plane Poled Glassy Polymers. Spectroscopic and Theoretical Support for the Importance of Charged Chromophore Aggregates. *J. Am. Chem. Soc.* **1997**, *119*, 2995.

(276) Dalton, L. R.; Harper, A. W.; Robinson, B. H. The role of London forces in defining noncentrosymmetric order of high dipole moment high hyperpolarizability chromophores in electrically poled polymeric thin films. *Proc. Natl. Acad. Sci. U.S.A.* **1997**, *94*, 4842.

(277) Wurthner, F.; Yao, S. Dipolar dye aggregates: A problem for nonlinear optics, but a chance for supramolecular chemistry. *Angew. Chem. Int. Edit.* **2000**, *39*, 1978.

(278) Wortmann, R.; Rosch, U.; Redi-Abshiro, M.; Wurthner, F. Large electric-field effects on the dipolar aggregation of merocyanine dyes. *Angew. Chem. Int. Edit.* **2003**, *42*, 2080.

(279) Wu, W.; Li, C.; Yu, G.; Liu, Y.; Ye, C.; Qin, J.; Li, Z. High-Generation Second-Order Nonlinear Optical (NLO) Dendrimers that Contain Isolation Chromophores: Convenient Synthesis by Using Click Chemistry and their Increased NLO Effects. *Chem. Eur. J.* **2012**, *18*, 11019.

(280) Wurthner, F.; Yao, S.; Debaerdemaeker, T.; Wortmann, R. Dimerization of merocyanine dyes. Structural and energetic characterization of dipolar dye aggregates and implications for nonlinear optical materials. *J. Am. Chem. Soc.* **2002**, *124*, 9431.

(281) Ashwell, G. J.; Skjonnemand, K.; Paxton, G. A. N.; Allen, D. W.; Mifflin, J. P. L.; Li, X. Merocyanine dyes: dimeric aggregation in solution, film structure and pH sensing. *J. Mater. Chem.* **2001**, *11*, 1351.

(282) Liao, Y.; Eichinger, B. E.; Firestone, K. A.; Haller, M.; Luo, J.; Kaminsky, W.; Benedict, J. B.; Reid, P. J.; Jen, A. K. Y.; Dalton, L. R.; Robinson, B. H. Systematic Study of the Structure−Property Relationship of a Series of Ferrocenyl Nonlinear Optical Chromophores. *J. Am. Chem. Soc.* **2005**, *127*, 2758.

(283) Sheik-bahae, M.; Said, A. A.; Van Stryland, E. W. High-sensitivity, single-beam n2 measurements. *Opt. Lett.* **1989**, *14*, 955.

(284) Sheik-Bahae, M.; Said, A. A.; Wei, T. H.; Hagan, D. J.; Van Stryland, E. W. Sensitive measurement of optical nonlinearities using a single beam. *Quantum Electronics, IEEE Journal of* **1990**, *26*, 760.

(285) Brédas, J. L.; Chance, R. R.; Silbey, R. Comparative theoretical study of the doping of conjugated polymers: Polarons in polyacetylene and polyparaphenylene. *Phys. Rev. B* **1982**, *26*, 5843.

(286) Fesser, K.; Bishop, A. R.; Campbell, D. K. Optical absorption from polarons in a model of polyacetylene. *Phys. Rev. B* **1983**, *27*, 4804.

(287) Boudreaux, D.; Chance, R.; Brédas, J.; Silbey, R. Solitons and polarons in polyacetylene: Self-consistent-field calculations of the effect of neutral and charged defects on molecular geometry. *Phys. Rev. B* **1983**, *28*, 6927.

(288) Brédas, J. L.; Scott, J. C.; Yakushi, K.; Street, G. B. Polarons and bipolarons in polypyrrole: Evolution of the band structure and optical spectrum upon doing. *Phys. Rev. B* **1984**, *30*, 1023.

(289) Heeger, A. J.; Pethig, R. Charge Storage and Charge Transport in Conducting Polymers: Solitons, Polarons and Bipolarons [and Discussion]. *Philosophical Transactions of the Royal Society of London A: Mathematical, Physical and Engineering Sciences* **1985**, *314*, 17.

(290) Ye, A.; Shuai, Z.; Kwon, O.; Brédas, J. L.; Beljonne, D. Optical properties of singly charged conjugated oligomers: A coupled-cluster equation of motion study. *J. Chem. Phys.* **2004**, *121*, 5567.

(291) Alkan, F.; Salzner, U. Theoretical Investigation of Excited States of Oligothiophene Anions. *J. Phys. Chem. A* **2008**, *112*, 6053.

(292) Furukawa, Y. Electronic Absorption and Vibrational Spectroscopies of Conjugated Conducting Polymers. *J. Phys. Chem.* **1996**, *100*, 15644.

(293) Fichou, D.; Horowitz, G.; Xu, B.; Garnier, F. Stoichiometric control of the successive generation of the radical cation and dication of extended α-conjugated oligothiophenes: a quantitative model for doped polythiophene. *Synth. Met.* **1990**, *39*, 243.

(294) Takeda, N.; Miller, J. R. Poly(3-decylthiophene) Radical Anions and Cations in Solution: Single and Multiple Polarons and Their Delocalization Lengths in Conjugated Polymers. *J. Phys. Chem. B* **2012**, *116*, 14715.

(295) Hutchison, G. R.; Ratner, M. A.; Marks, T. J. Electronic Structure and Band Gaps in Cationic Heterocyclic Oligomers. Multidimensional Analysis of the Interplay of Heteroatoms, Substituents, Molecular Length, and Charge on Redox and Transparency Characteristics. *J. Phys. Chem. B* **2005**, *109*, 3126.

(296) Salzner, U. Investigation of Charge Carriers in Doped Thiophene Oligomers through Theoretical Modeling of their UV/Vis Spectra. *J. Phys. Chem. A* **2008**, *112*, 5458.

(297) Geskin, V. M.; Brédas, J.-L. Polaron Pair versus Bipolaron on Oligothiophene Chains: A Theoretical Study of the Singlet and Triplet States. *Chem. Phys. Chem.* **2003**, *4*, 498.

(298) Casanovas, J.; Alemán, C. Comparative Theoretical Study of Heterocyclic Conducting Oligomers: Neutral and Oxidized Forms. *J. Phys. Chem. C* **2007**, *111*, 4823.

(299) Okur, S.; Salzner, U. Theoretical Modeling of the Doping Process in Polypyrrole by Calculating UV/Vis Absorption Spectra of Neutral and Charged Oligomers. *J. Phys. Chem. A* **2008**, *112*, 11842.

(300) Miller, L. L.; Mann, K. R. π-Dimers and π-Stacks in Solution and in Conducting Polymers. *Acc. Chem. Res.* **1996**, *29*, 417.

(301) Collard, D. In *π-Stacked Polymers and Molecules*; Nakano, T., Ed.; Springer Japan: 2014, p 185.

(302) Nishinaga, T.; Komatsu, K. Persistent [small pi] radical cations: self-association and its steric control in the condensed phase. *Organic & Biomolecular Chemistry* **2005**, *3*, 561.

(303) Cao, J.; Curtis, M. D. Polarons, Bipolarons, and π-Dimers of Bis(3,4-ethylene-dioxythiophene)-(4,4‘-dialkyl-2,2‘-bithiazole)- co-Oligomers. Direct Measure of the Intermolecular Exciton Transfer Interaction. *Chem. Mater.* **2003**, *15*, 4424.

(304) Zade, S. S.; Zamoshchik, N.; Bendikov, M. From Short Conjugated Oligomers to Conjugated Polymers. Lessons from Studies on Long Conjugated Oligomers. *Acc. Chem. Res.* **2011**, *44*, 14.

(305) Zamoshchik, N.; Salzner, U.; Bendikov, M. Nature of Charge Carriers in Long Doped Oligothiophenes: The Effect of Counterions. *J. Phys. Chem. C* **2008**, *112*, 8408.

(306) Tschuncky, P.; Heinze, J.; Smie, A.; Engelmann, G.; Koßmehl, G. Reversible dimerization of 3,3′,5,5′,-tetramethyl-2,2′-bithiophene cations. *J. Electroanal. Chem.* **1997**, *433*, 223.

(307) Heinze, J.; John, H.; Dietrich, M.; Tschuncky, P. σ-“Dimers” – key intermediates and products during generation and redox switching of conjugated oligomers and polymers. *Synth. Met.* **2001**, *119*, 49.

(308) Turbiez, M.; Hergué, N.; Leriche, P.; Frère, P. Rigid oligomers based on the combination of 3,6-dimethoxythieno[3,2-b]thiophene and 3,4-ethylenedioxythiophene. *Tetrahedron Lett.* **2009**, *50*, 7148.

(309) Turbiez, M.; Faye, D.; Leriche, P.; Frere, P. Bis-EDOT end capped by n-hexyl or n-hexylsulfanyl groups: the effect of the substituents on the stability of the oxidized states. *New J. Chem.* **2015**, *39*, 1678.

(310) Hill, M. G.; Mann, K. R.; Miller, L. L.; Penneau, J. F. Oligothiophene cation radical dimers. An alternative to bipolarons in oxidized polythiophene. *J. Am. Chem. Soc.* **1992**, *114*, 2728.

(311) Hill, M. G.; Penneau, J. F.; Zinger, B.; Mann, K. R.; Miller, L. L. Oligothiophene cation radicals. .pi.-Dimers as alternatives to bipolarons in oxidized polythiophenes. *Chem. Mater.* **1992**, *4*, 1106.

(312) Baeuerle, P.; Segelbacher, U.; Maier, A.; Mehring, M. Electronic structure of mono- and dimeric cation radicals in end-capped oligothiophenes. *J. Am. Chem. Soc.* **1993**, *115*, 10217.

(313) Lü, J.-M.; Rosokha, S. V.; Kochi, J. K. Stable (Long-Bonded) Dimers via the Quantitative Self-Association of Different Cationic, Anionic, and Uncharged π-Radicals: Structures, Energetics, and Optical Transitions. *J. Am. Chem. Soc.* **2003**, *125*, 12161.

(314) Levillain, E.; Roncali, J. Structural Control of the Reversible Dimerization of π-Conjugated Oligomeric Cation Radicals. *J. Am. Chem. Soc.* **1999**, *121*, 8760.

(315) Scherlis, D. A.; Marzari, N. π-Stacking in Charged Thiophene Oligomers. *J. Phys. Chem. B* **2004**, *108*, 17791.

(316) Apperloo, J. J.; Janssen, R. A. J. Solvent effects on the π-dimerization of cation radicals of conjugated oligomers. *Synth. Met.* **1999**, *101*, 373.

(317) Singh-Miller, N. E.; Scherlis, D. A.; Marzari, N. Effect of Counterions on the Interactions of Charged Oligothiophenes. *J. Phys. Chem. B* **2006**, *110*, 24822.

(318) Ferron, C. C.; Delgado, M. C. R.; Hernandez, V.; Navarrete, J. T. L.; Vercelli, B.; Zotti, G.; Cortada, M. C.; Novoa, J. J.; Niu, W.; He, M.; Hartl, F. Substituent and counterion effects on the formation of [small pi]-dimer dications of end-capped heptathienoacenes. *Chem. Commun.* **2011**, *47*, 12622.

(319) Tol, A. J. W. The electronic and geometric structure of dications of oligo-thiophenes. *Chem. Phys.* **1996**, *208*, 73.

(320) Zhang, F.; Gotz, G.; Mena-Osteritz, E.; Weil, M.; Sarkar, B.; Kaim, W.; Bauerle, P. Molecular and electronic structure of cyclo[10]thiophene in various oxidation states: polaron pair vs. bipolaron. *Chemical Science* **2011**, *2*, 781.

(321) Österholm, A.; Petr, A.; Kvarnström, C.; Ivaska, A.; Dunsch, L. The Nature of the Charge Carriers in Polyazulene as Studied by in Situ Electron Spin

Resonance−UV−Visible−Near-Infrared Spectroscopy. *J. Phys. Chem. B* **2008**, *112*, 14149.

(322) Beaujuge, P. M.; Amb, C. M.; Reynolds, J. R. Spectral Engineering in π-Conjugated Polymers with Intramolecular Donor−Acceptor Interactions. *Acc. Chem. Res.* **2010**, *43*, 1396.

(323) Beaujuge, P. M.; Reynolds, J. R. Color Control in π-Conjugated Organic Polymers for Use in Electrochromic Devices. *Chem. Rev.* **2010**, *110*, 268.

(324) Domagala, W.; Pilawa, B.; Lapkowski, M. Quantitative in-situ EPR spectroelectrochemical studies of doping processes in poly(3,4-alkylenedioxythiophene)s: Part 1: PEDOT. *Electrochim. Acta* **2008**, *53*, 4580.

(325) Polander, L. E.; Pandey, L.; Barlow, S.; Tiwari, S. P.; Risko, C.; Kippelen, B.; Brédas, J.-L.; Marder, S. R. Benzothiadiazole-Dithienopyrrole Donor–Acceptor–Donor and Acceptor–Donor–Acceptor Triads: Synthesis and Optical, Electrochemical, and Charge-Transport Properties. *J. Phys. Chem. C* **2011**, *115*, 23149.

(326) Karsten, B. P.; Bijleveld, J. C.; Viani, L.; Cornil, J.; Gierschner, J.; Janssen, R. A. J. Electronic structure of small band gap oligomers based on cyclopentadithiophenes and acceptor units. *J. Mater. Chem.* **2009**, *19*, 5343.

(327) Kerszulis, J. A. *Reading the rainbow: tailoring the properties of electrochromic polymers*; Atlanta, Ga.: Georgia Institute of Technology, 2014.

(328) Richardson, D. E.; Taube, H. Determination of E20-E10 in multistep charge transfer by stationary-electrode pulse and cyclic voltammetry: application to binuclear ruthenium ammines. *Inorg. Chem.* **1981**, *20*, 1278.

(329) Kurowska, A.; Kostyuchenko, A. S.; Zassowski, P.; Skorka, L.; Yurpalov, V. L.; Fisyuk, A. S.; Pron, A.; Domagala, W. Symmetrically Disubstituted Bithiophene Derivatives of 1,3,4-Oxadiazole, 1,3,4-Thiadiazole, and 1,2,4-Triazole – Spectroscopic, Electrochemical, and Spectroelectrochemical Properties. *J. Phys. Chem. C* **2014**, *118*, 25176.

(330) Raimundo, J.-M.; Blanchard, P.; Frère, P.; Mercier, N.; Ledoux-Rak, I.; Hierle, R.; Roncali, J. Push–pull chromophores based on 2,2′-bi(3,4-ethylenedioxythiophene) (BEDOT) π-conjugating spacer. *Tetrahedron Lett.* **2001**, *42*, 1507.

(331) Turbiez, M.; Frère, P.; Allain, M.; Videlot, C.; Ackermann, J.; Roncali, J. Design of Organic Semiconductors: Tuning the Electronic Properties of π-Conjugated Oligothiophenes with the 3,4-Ethylenedioxythiophene (EDOT) Building Block. *Chem. Eur. J.* **2005**, *11*, 3742.

(332) Amb, C. M.; Kerszulis, J. A.; Thompson, E. J.; Dyer, A. L.; Reynolds, J. R. Propylenedioxythiophene (ProDOT)-phenylene copolymers allow a yellow-to-transmissive electrochrome. *Polym. Chem.* **2011**, *2*, 812.

(333) Kerszulis, J. A.; Amb, C. M.; Dyer, A. L.; Reynolds, J. R. Follow the Yellow Brick Road: Structural Optimization of Vibrant Yellow-to-Transmissive Electrochromic Conjugated Polymers. *Macromolecules* **2014**, *47*, 5462.

(334) Zotti, G.; Zecchin, S.; Schiavon, G.; Groenendaal, L. B. Conductive and Magnetic Properties of 3,4-Dimethoxy- and 3,4-Ethylenedioxy-Capped Polypyrrole and Polythiophene. *Chem. Mater.* **2000**, *12*, 2996.

(335) Zhang, C.; Park, S. M. Simple technique for constructing thin-layer electrochemical cells. *Anal. Chem.* **1988**, *60*, 1639.

(336) Nawa, K.; Miyawaki, K.; Imae, I.; Noma, N.; Shirota, Y. Polymers containing pendant oligothiophenes as a novel class of electrochromic materials. *J. Mater. Chem.* **1993**, *3*, 113.

(337) Ohsedo, Y.; Imae, I.; Shirota, Y. Synthesis and electrochromic properties of a new family of methacrylate polymers containing pendant oligothiophenes. *J. Polym. Sci., Part B: Polym. Phys.* **2003**, *41*, 2471.

(338) Hong, Y.; Miller, L. L. An Electrically Conducting Polyester That Has Isolated Quatrathiophene Units in the Main Chain. *Chem. Mater.* **1995**, *7*, 1999.

(339) Donat-Bouillud, A.; Mazerolle, L.; Gagnon, P.; Goldenberg, L.; Petty, M. C.; Leclerc, M. Synthesis, Characterization, and Processing of New Electroactive and Photoactive Polyesters Derived from Oligothiophenes. *Chem. Mater.* **1997**, *9*, 2815.

(340) Stalder, R.; Mavrinskiy, A.; Grand, C.; Imaram, W.; Angerhofer, A.; Pisula, W.; Mullen, K.; Reynolds, J. R. Electrochromic and liquid crystalline polycarbonates based on telechelic oligothiophenes. *Polym. Chem.* **2015**, *6*, 1230.

VITA

NATASHA B. TERAN

Natasha B. Teran was born in Iloilo, Philippines. She earned her bachelor's degree in Chemistry from the Ateneo de Manila University, with an undergraduate thesis in natural products isolation. Natasha then pursued a career as a college instructor, teaching at the University of the Philippines for one year, and at her *alma mater*, the Ateneo de Manila University for five years. While teaching at the Ateneo, Natasha also pursued several masters-level courses focused on Materials Chemistry. She also began doing research on quantum-dot sensitized solar cells, under the guidance of Dr. Erwin Enriquez. Her mother's sudden and catastrophic illness forced Natasha to move back to Iloilo, and abort her pursuit of a Master's degree. After a year, Natasha enrolled in the graduate program of the Department of Chemistry at the University of Florida, and made the difficult move from the Philippines to Gainesville, FL in January 2010. Natasha then joined the group of Prof. John Reynolds at UF in April of the same year, and began her training in the synthesis lab with Dr. Romain Stalder, working on donor-acceptor oligomers. In December of 2011, Natasha moved with the Reynolds group to the Georgia Institute of Technology, where she helped setup the synthesis laboratories. Natasha then began working on the synthesis of nonlinear optics chromophores, and continued with her work on donor-acceptor oligomers. In August 2013, Natasha began her work on host and charge transport materials for OLEDs. She expects to graduate in December 2015 with a doctoral degree in Chemistry.